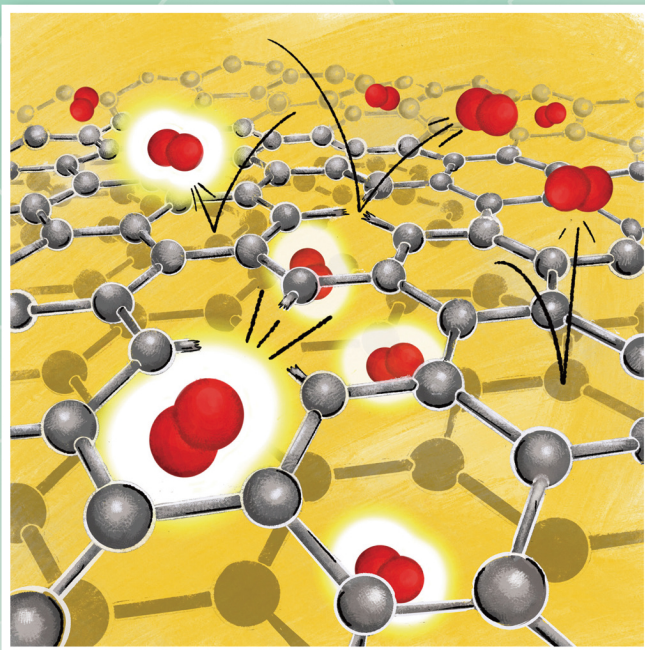
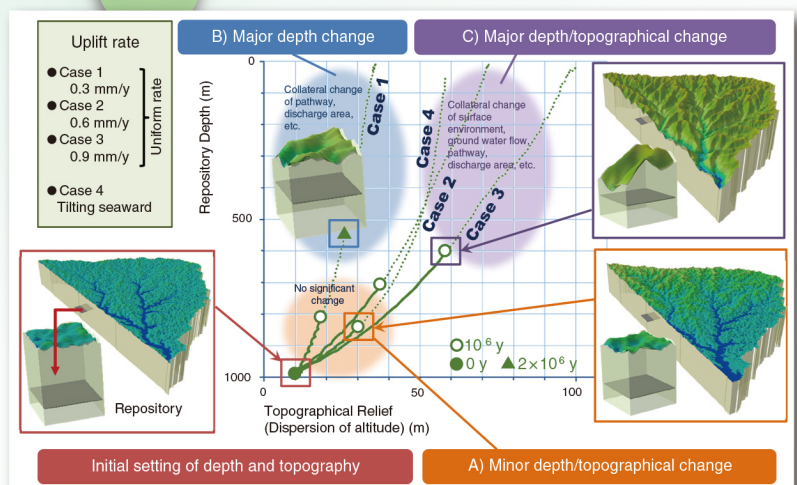


JAEA R&D Review

2021-22



An image of an oxygen molecule passing through graphene (a net made of a single layer of carbon atoms) (Topic 5-6)



Example of topographical and repository depth change calculated using the developed tool (Topic 8-9)



Message from the President

児玉敏雄

President, JAEA, Toshio KODAMA

We sincerely thank you for your understanding and continuous support for the research and development (R&D) activities of the Japan Atomic Energy Agency (JAEA).

As Japan's sole comprehensive nuclear R&D institution, the mission of the JAEA is to contribute to the welfare and prosperity of human society through nuclear science and technology (S&T). Since last year, the JAEA has been working toward this mission, while prioritizing safety, taking measures against COVID-19, and adopting novel ways of working, such as telecommuting.

In response to the accident at the Fukushima Daiichi Nuclear Power Station, we are working on the R&D of both decommissioning and environmental recovery, such as the preparation for the analysis of fuel debris. In the field of nuclear safety research and emergency preparedness—in addition to technical support for the nuclear safety regulatory administration (e.g., evaluation of nuclear safety)—we are engaged in research on advanced nuclear safety and emergency preparedness. In the development of fast reactors and advanced reactors, we are working on technical issues related to fast reactor development in accordance with the national strategic roadmap. Further, we are undertaking R&D on high-temperature gas-cooled reactor technology, which is expected to contribute to carbon neutrality by 2050. Furthermore, we are proceeding with R&D on the nuclear fuel cycle, as well as radioactive waste treatment and disposal technology. In the area of decommissioning, the decommissioning of Monju, Fugen, and Tokai Reprocessing Plants, is proceeding on the basis of the “Backend Roadmap”. As for basic and fundamental research in the nuclear field, we are advancing efforts aimed at creating new applications of atomic energy, developing unexplored research fields, and promoting academic progress and cutting-edge S&T. In May 2021, we started operation of the “Open Facility Platform”. This provides related information and accepts applications with the aim of improving researchers' usability of large-scale service facilities and equipment provided by the JAEA. Further, in February 2021, we resumed in-service operation of the research reactor JRR-3. We are working to establish a system for further cooperation and collaboration with industry, academia, and government.

In the Future Vision “JAEA 2050+”, JAEA intends to achieve a “New Era Nuclear S&T” that facilitates the resolution of global climate change, securing energy supply, and achieving the ideal future society (Society 5.0). This will be attained through the promotion of synergies between the nuclear energy field and other fields. Based on the “Innovation Creation Strategy”—revised in November 2020—we will promote our contribution to social change through open innovation initiatives via synergies with various fields.

In this publication, we introduce the latest R&D results obtained from studies undertaken by the JAEA. We hope this publication will further your understanding of our R&D activities.

We would appreciate your continued encouragement and support.

About This Publication and the JAEA Organizational Outline	10
--	----

1

Research and Development Related to the Accident at TEPCO's Fukushima Daiichi NPS

Highlight	Assistance in Environmental Restoration and Decommissioning	13
1-1	Revealing the Characteristics of Fuel Debris – Formation Mechanisms of Metallic Fuel Debris Originating from Control Rods – Takehiro Sumita	14
1-2	Development of Radiation Detector for Non-Destructive Assay of Nuclear Fuel Debris – γ -ray Spectrometry System Specific to High Dose-Rate Measurements Using CeBr ₃ – Masaaki Kaburagi	15
1-3	Chemical Forms of Radionuclides in Fuel Debris – Structure of Concrete Interaction Products and Distribution of Sr and Ba – Ayako Sudo	16
1-4	To Establish Safer Criticality Management of Fuel Debris – Optimization of the Core Configuration of the New STACY for Debris Simulation – Satoshi Gunji	17
1-5	Methodology to Remove Cs from Soil – Preparation for the Treatment of Contaminated Soil – Xiangbiao Yin, Yoshikazu Koma	18
1-6	Toward Understanding Core Melting Behavior in RPVs – Evaluation of RPV Failure Mechanism – Hiroshi Madokoro	19
1-7	Laser Ultrasonic Approach to Detect Corrosion of Reinforced Concrete – Toward Nondestructive Testing Technology for Decommissioning – Akinori Furusawa	20
1-8	Aiming to Predict PCV Corrosion – Development of Corrosion Database under Varying Irradiation Conditions – Tomonori Sato	21
1-9	Radiation Position Detection under High Dose Rate Using Optical Fibers – An Approach to Detect the Position of Radiation Focusing on the Wavelength Information of Light – Yuta Terasaka	22
1-10	Impact of Large Typhoons on the Estuary Mass Flux – Observation of Radioactive Cesium in the Estuary in 2019 – Toshiharu Misonou	23
1-11	Visualization of Radiological Map Using Machine Learning – Analytical Method Using Big Data of Radiation Measurements in Fukushima – Miyuki Sasaki	24
1-12	Improving the Accuracy in Estimation of Air Dose Rate Decrease – A New Model for Simulation of Temporal Changes Due to an Environmental Effect – Masaki Andoh	25

1-13	Sediment Characteristics Determine the Behavior of Cesium in Rivers – Adsorption/Desorption Mechanism of Radioactive Cesium onto River Sediments – Kenso Fujiwara	26
1-14	Remobilization of Radiocesium from Sediments – Mass Balance of Dissolved ¹³⁷ Cs in an Artificial Reservoir in Fukushima – Hironori Funaki	27
1-15	Rapid Analysis of ⁹⁰Sr in Small Bone Samples – Applicability of Sr Resin for ICP-MS of ⁹⁰ Sr in Hard Tissues – Kazuma Koarai	28
1-16	Speciation of Cs in Tree Tissues – Elucidation of the Mobility of Cs inside Trees Using Synchrotron Radiation – Kazuya Tanaka	29
1-17	Where Does the Radiation Determining Air Dose Rates in Forests Originate? – Simulations Reveal the Connection between the Movement of Radioactive Cesium and Air Dose Rate Trends – Minsik Kim	30
1-18	Understanding the Cesium Adsorption Behavior in Concrete – Accurate Simulation of Cement Hydrate Using Machine Learning Molecular Dynamics – Keita Kobayashi	31

2 Research on Nuclear Safety and Emergency Preparedness

Highlight	Implementing Continuous Improvements in Safety and Emergency Preparedness	32
2-1	Reliable Thyroid Dose Measurement after a Severe Nuclear Accident – Developing a Portable Thyroid Dose Monitor – Sho Nishino	33
2-2	Can Contaminated Monitoring Posts Measure Accurately in a Nuclear Accident? – Influence of Contamination on Measured Dose Rates at Monitoring Posts – Hirokazu Hiraoka	34
2-3	Prediction of Structural Damage from Projectile Impacts – Numerical Evaluation of Penetration Damage under Realistic Conditions – Zuoyi Kang	35
2-4	Accident Simulation: HLLW Evaporation to Dryness – Evaluating the Restraint Effect on the Release of Volatile Ruthenium – Ryoichiro Yoshida	36
2-5	A Nonparametric Bayesian Method for Predicting the Embrittlement of Reactor Pressure Vessels – Toward Further Reliability of Integrity Assessment in Long-Term Operation – Hisashi Takamizawa	37
2-6	Migration of Radionuclides from Radioactive Wastes of Reactor Core Structures in Underground Environments – Modeling Niobium Sorption onto Clay Minerals in the Presence of Calcium – Saki Ohira	38

2-7	Detection of Undeclared Uranium Purification Activities – $^{230}\text{Th}/^{234}\text{U}$ Radio-Chronometry with a Single Uranium Particle – Daisuke Suzuki	39
------------	---	----

2-8	Operating Robots Entering the Accident Site on Behalf of a Person – Training of Robot Operators for Nuclear Disaster Response – Yusuke Chiba	40
------------	---	----

3 Advanced Scientific Research

Highlight	Advanced Science Explores the Future	41
------------------	--------------------------------------	----

3-1	Nuclear Fission Unveiled via Multinucleon Transfer Reaction – Opening Fission Research in Unexplored Region of the Chart of Nuclei – Katsuhisa Nishio	42
------------	--	----

3-2	Determination of the Mass of a Ξ Hypernucleus – New Information to Understand the Structure of Neutron Stars – Kiyoshi Tanida	43
------------	---	----

3-3	Magnetic Cooling to Near Absolute Zero Temperatures – Cooling to Extremely Low Temperature Realized by Quantum Fluctuations in “Ytterbium Magnet” – Yoshifumi Tokiwa	44
------------	---	----

3-4	For a Radio-Resistant Thermoelectric Generation System – Tolerance of Spin Thermoelectric Devices for Radiation – Satoru Okayasu	45
------------	---	----

3-5	Elucidation of Low-Energy Vibrational Modes of Deuterated Water Clusters – Utilization of Terahertz-Infrared Absorption Spectroscopy and Ab Initio Calculation – Koichiro Yamakawa	46
------------	---	----

3-6	Exploration of the Exotic Structure of P_c – Hybrid State with a Mixture of Compact State and Hadron Molecule – Yasuhiro Yamaguchi	47
------------	--	----

4 Nuclear Science and Engineering Research

Highlight	Fundamental Technologies for Nuclear Energy Innovation	48
------------------	--	----

4-1	Toward High-Energy Neutron Applications – Development of Nuclear Reaction Database for Basic Sciences and Medicine – Shinsuke Nakayama	49
------------	---	----

4-2	Estimating Nuclear Data Using a Machine Learning Technique – Toward the Development of a High-Quality Nuclear Reaction Database – Hiroki Iwamoto	50
4-3	Toward Clarifying the Chemical States of Nuclear Fuel Debris – Applicability of Micro-Raman Spectroscopy – Ryoji Kusaka	51
4-4	Reassessment of Atomic Bomb Survivor Doses – Joint Japan-U.S. Study to Improve Epidemiological Research Accuracy – Tatsuhiko Sato	52
4-5	Quicker calculation of Atmospheric Dispersion of Radioactive Materials under Various Conditions – Development of the Atmospheric Dispersion Database System WSPEEDI-DB – Hiroaki Terada	53
4-6	Clarification of the Spontaneous Microcracking of Aluminum Alloys – Toward the Realization of High-Strength Alloys through Computational Science – Tomohito Tsuru	54
4-7	Extent of Damage to Material when Exposed to Proton Beam – Contribution to the Safety of Accelerator-Driven Systems – Shin-ichiro Meigo	55

5 Neutron and Synchrotron Radiation Research

Highlight	Contributions to Innovative Achievement in Science and Technology	56
5-1	Toward Stable Operation of a High-Intensity Proton Beam – Development of an Online Monitoring System for the Injection Stripper Foil – Pranab Kumar Saha	57
5-2	Strengthening Mechanism of Cast Iron Elucidated by a High-Intensity Pulsed Neutron Beam – Deformation Response of Each Constituent Phase Monitored by Neutron Diffraction – Stefanus Harjo	58
5-3	Realization of a Highly Polarized Neutron Beam across a Wide Energy Range – Development and Application of a Neutron Polarization Device Using Highly Polarized ^3He – Takuya Okudaira	59
5-4	Strange Short-Range Order of Conduction Electron Spins Realized at High Temperatures – Unexpected State Found in the Newly Synthesized Magnet, Mn_3RhSi – Hiroki Yamauchi	60
5-5	Development of a Metal Adsorbent Using Bone Waste – A Low-Cost and High-Performance Metal Adsorbent Prepared from Food Waste – Yurina Sekine	61
5-6	Fast Molecules Passing through Carbon-Atom Net – Discovery of Oxygen Molecules Slipping through Graphene – Akitaka Yoshigoe	62

5-7	Atomic-Level Observation of Magnetic Ordering Process in Ferromagnetic Semiconductors – Exploring the Mechanism of Ferromagnetism for Its Practical Use in Spintronics Devices – Yukiharu Takeda	63
------------	---	----

6 HTGR Hydrogen and Heat Application Research

Highlight	Research and Development on HTGR, Hydrogen Production, and Heat Application Technologies	64
6-1	Prediction of Thermal-Hydraulic Behavior in HTGR Accidents – Development of Evaluation Methodology of Air-Ingress Behavior in HTGR – Takeshi Aoki	65
6-2	Nuclear Design Policy to Maintain the Integrity of Coated Fuel Particles – Derivation of the Ideal Power Distribution to Minimize the Kernel Migration Rate – Shoichiro Okita	66
6-3	Toward the Realization of High Temperature Gas-Cooled Reactor for Safe Reduction of Plutonium Inventory – Microstructure Observation of a Simulated Fuel Kernel – Jun Aihara	67
6-4	Toward Metallic Sulfuric Acid Decomposers in the IS Process – Discovery of Steel Materials with Corrosion Resistance Equivalent to Ceramics in a Sulfated Gas Environment – Noriaki Hirota	68
6-5	Membrane Technique Advancing the IS Process – Enhancement of the HI Conversion by Silica-Based Membrane Reactor – Odtsetseg Myagmarjav	69
6-6	Energy Saving of the Main Reaction in the IS Process – Membrane and Electrode Development for the Bunsen Reaction Overvoltage Reduction – Nobuyuki Tanaka	70
6-7	Shortening the Calculation Working Time for the Criticality Control Rod Position – Development of a Utility Tool for Auto Seeking the Critical Control Rod Position – Hai Quan Ho	71

7 Research and Development of Fast Reactors

Highlight	Development of Technology Base and Infrastructure toward Improving the Fast Reactor Cycle	72
7-1	Observation of Nuclides Adsorbed inside the Column Using Neutrons – Non-Destructive Visualization of Nuclides by Resonance Neutron Imaging – Yasunori Miyazaki	73

7-2	Improvement of the Calculation Accuracy of Power Distribution for Large Fast Reactors – Refinement of Control-Rod Calculation Method – Kazuo Takino	74
7-3	Clarification of the Relocation Behavior of Degraded Fast Reactor Core Materials under Severe Accident – Development of Thermophysical Properties Database for Stainless Steel Containing Boron Carbide – Toshihide Takai	75
7-4	Optimization of Alloying Components of Nuclear Core Materials – Development of an Estimation Method for Irradiation-Induced Point Defect Behavior – Yoshihiro Sekio	76
7-5	Improvement and Demonstration of an Extraction Chromatography Flow-Sheet to Recover Trivalent Minor Actinides – Efficient MA(III)/Ln(III) Separation Process – Sou Watanabe	77

8 Research and Development on Fuel Reprocessing, Decommissioning, and Radioactive Waste Management

Highlight	Toward Decommissioning Nuclear Facilities and Managing Radioactive Waste	78
8-1	Implementation of Disposal Project of LLW Generated in Research, Medical, and Industrial Facilities – Preparation of “Concentration Equivalent Dose Criteria” as the Standard for the Selection of Important Nuclides – Toshikatsu Sugaya	80
8-2	Recovery of Nuclear Materials from Spent Extraction Solvent Using Solid Adsorbent – Investigation of Complex Formation Reaction of Iminodiacetic Acid Group in Solvent – Yoichi Arai	81
8-3	Turning Difficult-to-Treat Wastes into Stable Waste Packages – Investigation of Radioactive Aluminum Waste Treatment Technology Using the Bayer Process – Misaki Seki	82
8-4	Safety Improvements for Plutonium-Handling Facilities – Development of Fireproof Sheet on Glove Box Panels – Kohei Kawasaki	83
8-5	Direct Observation of the Fracture Induced by Gallery Excavation – Visualization Technology Using a Resin Injection Method – Akitaka Sakurai	84
8-6	Factors Affecting Rock Desaturation in Tunnel Excavation – Numerical Simulation on the Effects of Dissolved Gas and Rock Permeability – Kazuya Miyakawa	85
8-7	From Micro to Macro: Approaching Mountain Formation Processes Based on Age Determinations of Minerals – Insights to the Ou Backbone Range Obtained from Low-Temperature Thermochronology – Shoma Fukuda, Shigeru Sueoka	86
8-8	Reduced Geological Sample Size for Radiocarbon Dating at JAEA-AMS-TONO – Preparation Techniques Using One-Twentieth the Sample Size of the Conventional Method – Takahiro Watanabe	87

8-9	Safety Assessment Considering the Evolution of Topography and the Depth of the Disposal Facility – Development of an Analysis Tool to Evaluate the Topography and Depth of a Disposal Facility – Masaaki Yamaguchi	88
8-10	Electrochemical Methods to Evaluate Overpack Corrosion – Search for Passivation Conditions of Carbon Steel Surrounded by Buffer Material – Ayami Kitayama	89

9

Computational Science and E-Systems Research

Highlight	Computational Science for Nuclear Research and Development	90
9-1	Plume Dispersion Simulations Satisfying Accuracy Criteria for Environmental Assessments – Real-time Ensemble Calculations with Meter-Order Resolution – Naoyuki Onodera	91
9-2	Exascale CFD Simulations on Fugaku and Summit – Development of Mixed-Precision Matrix Solvers for Many-Core CPUs and GPUs – Yasuhiro Idomura	92
9-3	Theoretical Prediction of “Fermi Arc” – Development of Novel Method for Analyzing Strongly Correlated Electrons in Heavy-Element Compounds – Yuki Nagai	93
9-4	Prevention of Hydrogen Embrittlement in Aluminum Alloys – Identification of the Intermetallic Compounds that Take Away Hydrogen from Aluminum Lattice – Masatake Yamaguchi	94

10

Development of Science & Technology for Nuclear Nonproliferation

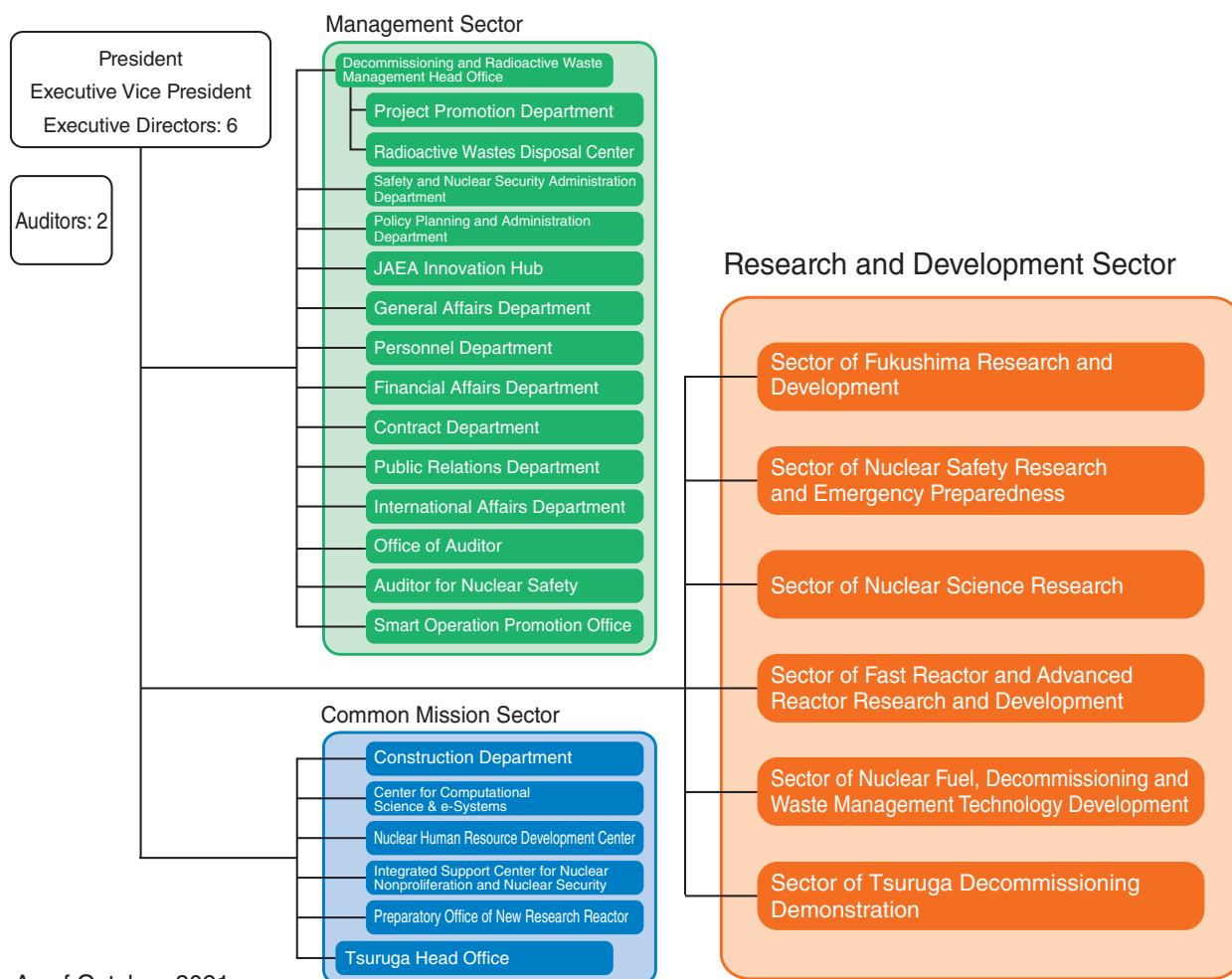
Highlight	Development of Technology and Human Capacity Building in the Nuclear Nonproliferation and Nuclear Security Fields to Support the Peaceful Use of Nuclear Energy	95
10-1	Toward a World without Nuclear Weapons and Nuclear Terrorism – Case Study and Factor Analysis of Denuclearization – Makiko Tazaki	96

About this Publication and the JAEA Organizational Outline

This publication introduces the latest research and development (R&D) in the various fields of the Japan Atomic Energy Agency (JAEA). Each chapter presents the activities of a single sector. The R&D sectors perform their activities through R&D centers or institutes, the bases of which span one to several locations. These centers and institutes are located throughout Japan, as highlighted on the map below. The following introduction outlines the research undertaken within each sector.

1. **The Sector of Fukushima Research and Development** promotes R&D on the decommissioning and environmental restoration corresponding to the accident at the Fukushima Daiichi Nuclear Power Station (1F) of the Tokyo Electric Power Company Holdings, Inc. (TEPCO). This sector promotes the development of the essential R&D infrastructure of the 1F decommissioning efforts.
2. **The Nuclear Safety Research Center and Nuclear Emergency Assistance and Training Center in the Sector of Nuclear Safety Research and Emergency Preparedness** perform research into safety measures that support the national nuclear safety bodies that regulate nuclear facilities (e.g., nuclear power plants) at the Nuclear Science Research Institute. Further, they perform R&D for nuclear emergency monitoring and protective measures in Hitachinaka City, Ibaraki Prefecture.
3. **The Advanced Science Research Center in the Sector of Nuclear Science Research** explores novel disciplines in advanced atomic energy sciences to develop theories and investigate novel phenomena, materials, and technologies. In particular, seven research themes have been organized under two divisions: advanced actinides science and advanced nuclear materials science.
4. **The Nuclear Science and Engineering Center in the Sector of Nuclear Science Research** undertakes fundamental research into vital technologies that are required for nuclear energy use at the Nuclear Science Research Institute.
5. **The Materials Sciences Research Center and J-PARC Center in the Sector of Nuclear Science Research** are engaged in research using neutrons at the Nuclear Science Research Institute and the Japan Proton Accelerator Research Complex (J-PARC). Research using synchrotron radiation is performed at the Harima SR Radioisotope Laboratory.
6. **The headquarters and the HTGR Research and Development Center in the Sector of Fast Reactor and Advanced Reactor Research and Development at the Oarai Research and Development Institute** further the development of high-temperature gas-cooled reactor (HTGR) technology, technology for hydrogen production through high-temperature water splitting, and technology for helium gas turbines.

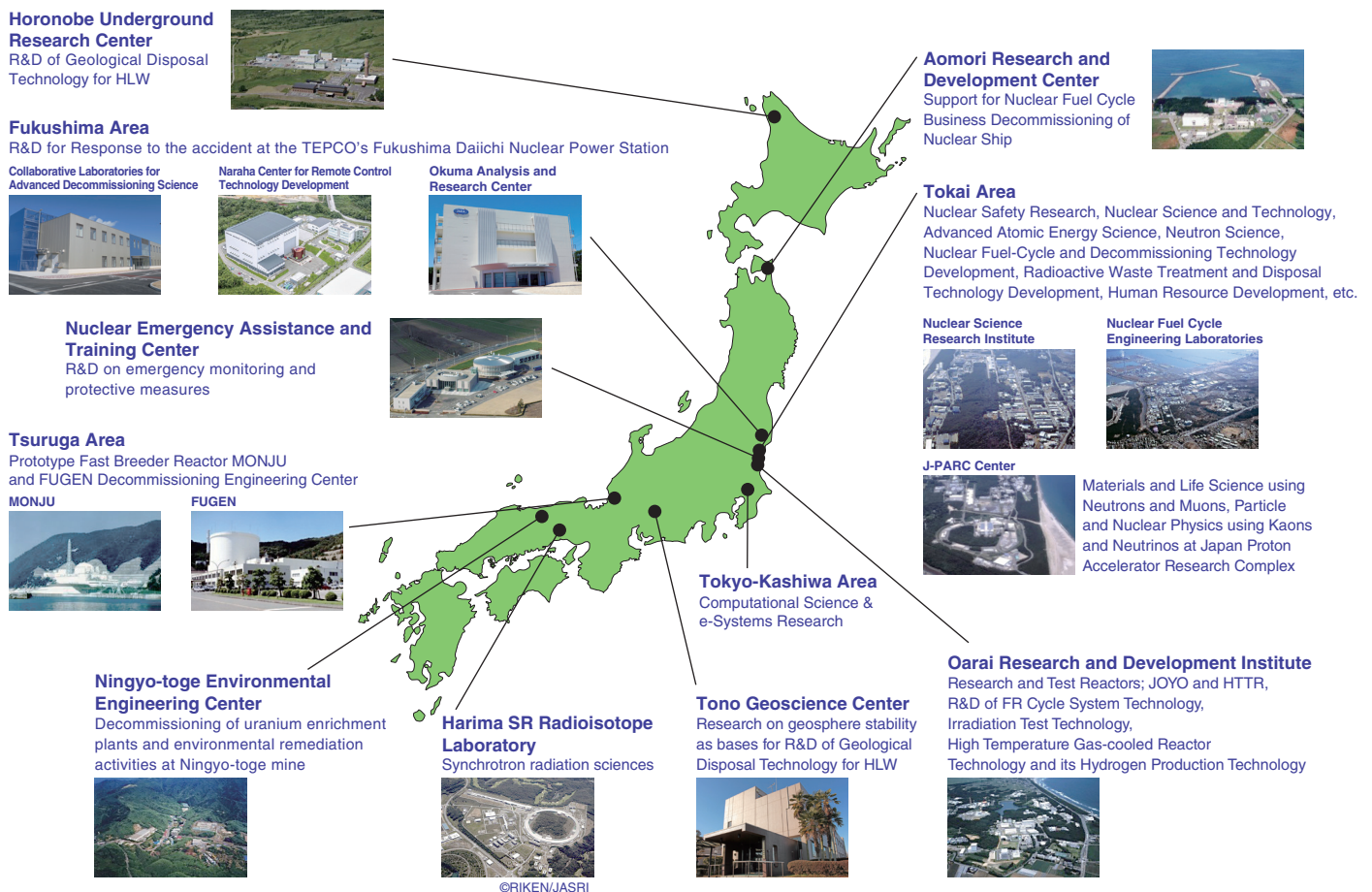
JAEA -Organizational Outline-



As of October, 2021

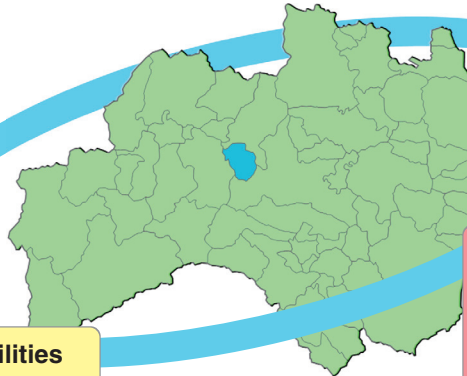
7. **The headquarters, the Fast Reactor Cycle System Research and Development Center, and the Tsuruga Comprehensive Research and Development Center in the Sector of Fast Reactor and Advanced Reactor Research and Development** aim to establish fast reactor (FR) cycles to address long-term energy security and global environmental issues. This work includes enhancing the safety of the FR system at the Oarai Research and Development Institute, compiling the results on the prototype fast breeder reactor Monju (MONJU), attaining inspection and repair technologies for the FR system at the Tsuruga Comprehensive Research and Development Center, manufacturing plutonium fuel and reprocessing spent FR fuel at the Nuclear Fuel Cycle Engineering Laboratories in cooperation with the Sector of Nuclear Fuel, Decommissioning and Waste Management Technology Development.
8. **The Sector of Nuclear Fuel, Decommissioning and Waste Management Technology Development** advances technologies for the safety and rational decommissioning of nuclear power facilities and measures for the processing and disposing of radioactive waste. It operates at the Aomori Research and Development Center, the Nuclear Fuel Cycle Engineering Laboratories, and the Ningyo-toge Environmental Engineering Center. The sector also performs multidisciplinary R&D that intends to improve the reliability of the geological disposal of high-level radioactive waste in Japan. One vital field is the establishment of techniques for the evaluation of the long-term stability of the geological environment. This is performed at the Tono Geoscience Center. The primary focus at the Horonobe Underground Research Center and the Nuclear Fuel Cycle Engineering Laboratories is safety assessment and improving technologies for the design of geological disposal facilities. The Nuclear Fuel Cycle Engineering Laboratories also focus on developing nuclear fuel cycle technology.
9. **The Center for Computational Science & e-Systems** aims to advance simulation technologies and fundamental technologies in computational science. Further, it aims to improve the operation and maintenance of computer systems and networks. These activities are primarily conducted at the Nuclear Science Research Institute and the Kashiwa Office.
10. **The Integrated Support Center for Nuclear Nonproliferation and Nuclear Security (ISCN)** is involved in strengthening nuclear nonproliferation and nuclear security both domestically and internationally. This is achieved through the development of technologies for IAEA safeguards and nuclear detection and forensics, policy research and analysis, capacity-building support activities targeting Asian countries, operation of CTBT international monitoring facilities (located in Japan), and coordination and support for nuclear fuel transportation undertaken by the JAEA. These efforts are primarily undertaken at Head Office and the Nuclear Science Research Institute.

R&D Institutes/Centers of JAEA



Assistance in Environmental Restoration and Decommissioning

As Japan's sole comprehensive institute in the field of nuclear energy, JAEA is progressing the R&D into Fukushima Daiichi NPS Decommissioning and the environment restoration as well as sustainable human resource development.



Constructing the R&D facilities

- Operating of the R&D facilities
- Progressing the R&D and human resource development by collaboration between industry, academia, and the government
 - Operating NARREC
 - Operating Tomioka Collaborative Laboratories of Collaborative Laboratories of CLADS
 - Operating Okuma Analysis and Research Center
 - Building a network that allows interactions between human resources from domestic and overseas universities, research institutions, and industry to delete.

R&D for environmental restoration

- Conducting R&D based on policies, such as the "Basic Guidelines for the Reconstruction and Revitalization of Fukushima" and social needs, such as the basic policy for Fukushima recovery and Revitalization
 - R&D on environmental monitoring and mapping (Topics 1-10, 1-11, and 1-12)
 - Research on environmental dynamics (Topics 1-13, 1-14, 1-15, 1-16, 1-17, and 1-18)

R&D for decommissioning of Fukushima Daiichi NPS

- Conducting R&D based on the "Mid-and-Long-Term Roadmap towards the Decommissioning of TEPCO's Fukushima Daiichi NPS" and NDF's "Technical Strategic Plan"
- Reflecting the needs of the Fukushima Daiichi NPS decommissioning site in R&D
 - Handling the fuel debris (Topics 1-1, 1-2, 1-3, and 1-4)
 - Treatment and disposal of radioactive wastes (Topic 1-5)
 - Clarify Fukushima Daiichi NPS accident progression scenario (Topic 1-6)
 - Remote handling technics (Topic 1-7)
 - Nuclear reactor integrity assessment (Topic 1-8)
 - Improving the safety of the work environment at 1F decommissioning site (Topic 1-9)

Fig.1-1 Overview of activities regarding the decommissioning of Fukushima Daiichi NPS based on the Mid-and-Long-Term Road Map

As Japan's only comprehensive institute in the field of nuclear energy, the Japan Atomic Energy Agency (JAEA) began restoration efforts in Fukushima Prefecture immediately after the accident at TEPCO's Fukushima Daiichi NPS (1F). JAEA has been engaged in research and development (R&D) into decommissioning 1F and the environmental restoration of Fukushima and has aimed to improve JAEA's R&D facilities with the Sector of Fukushima Research and Development at the core. Currently, JAEA is conducting R&D related to the 1F accident, mainly in the fields shown in Fig.1-1.

Three facilities in the Sector of Fukushima Research and Development are part of the Fukushima Innovation Coast Framework (field of decommissioning) and contribute to the decommissioning of 1F through R&D: Tomioka Collaborative Laboratories of the Collaborative Laboratories for Advanced Decommissioning Science (CLADS), Naraha Center for Remote Control Technology Development (NARREC), and Okuma Analysis and Research Center. CLADS has also set up a laboratory in the Fukushima Prefectural Centre for Environment Creation (Miharu Town and Minamisoma City), where researchers are performing R&D related to environmental restoration in Fukushima through collaboration with Fukushima Prefecture and The National Institute for Environmental Studies. Furthermore, JAEA has increased collaboration with the Sector of Fukushima Research and Development and other sectors to work on decommissioning 1F and the environmental restoration across all sectors of JAEA. We at JAEA are focused on improving collaboration between industry, academia, and the government and cooperating with research institutes abroad. Human resource development for mid-and-long-term R&D activities is also underway.

According to the "Mid-and-Long-Term Roadmap toward

the Decommissioning of 1F" formulated by the Japanese government and the "Technical Strategic Plan" detailed by the Nuclear Damage Compensation and Decommissioning Facilitation Corporation (NDF), TEPCO and companies related to 1F decommissioning are expected to conduct applied research and practical application research, whereas JAEA is responsible for basic and fundamental research. Thus, collaboration among these R&D projects must be promoted to ensure 1F decommissioning. To ensure that the R&D activities are truly based on the needs of the 1F decommissioning site, the Sector of Fukushima Research and Development has formulated the Overall Map of Basic and Fundamental Research, which is updated every year in collaboration with various stakeholders, including TEPCO, governmental organizations, and companies related to 1F decommissioning. In the field of environmental restoration, JAEA conducts R&D based on social needs and policies, such as the Basic Guidelines for the Reconstruction and Revitalization of Fukushima, and contributes to helping evacuated residents return, industry restoration, reconstruction, and residents' safety by publishing the results and providing technology to local governments.

The Sector of Fukushima Research and Development will continue to progress R&D for 1F decommissioning and environmental restoration by integrating international insights and actively disseminating the results obtained domestically and internationally. Additionally, the Sector of Fukushima Research and Development will contribute to the reconstruction of Fukushima by continuing to promote the revitalization of local industries and human resource development as a platform for collaboration by building a network of local companies and research/educational institutions in Fukushima.

1-1 Revealing the Characteristics of Fuel Debris

— Formation Mechanisms of Metallic Fuel Debris Originating from Control Rods —

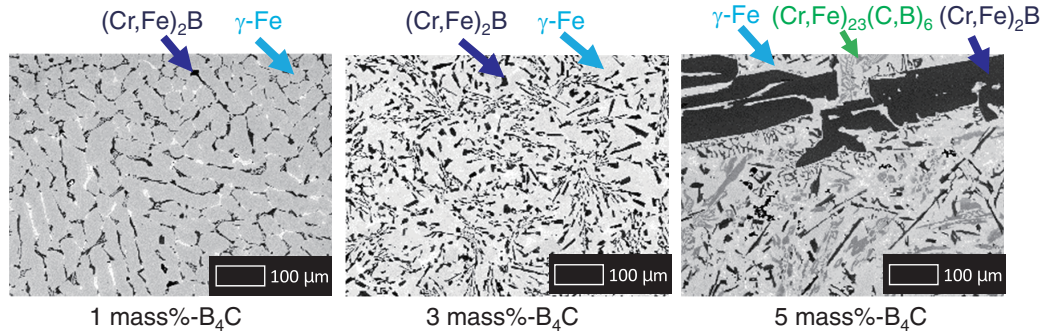


Fig.1-2 Backscattered electron images collected on cross sections of the prepared metallic fuel debris samples
 Samples are shown under three boron carbide (B_4C) mass concentrations. The $(Cr,Fe)_2B$ (dark phase), γ -Fe (bright phase), and $(Cr,Fe)_{23}(C,B)_6$ (mid-dark phase) phases are indicated with blue, light blue, and green arrows, respectively.

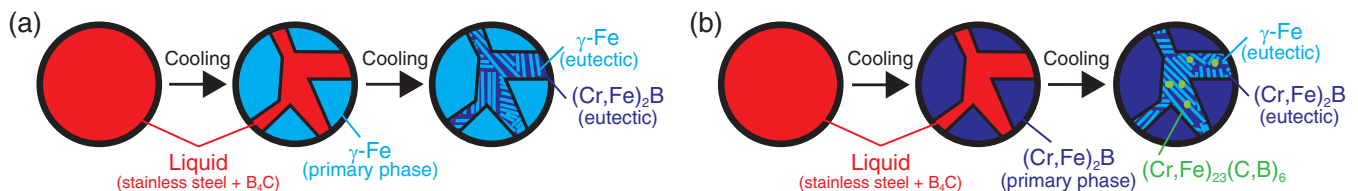


Fig.1-3 Solidification mechanism of metallic fuel debris
 Proposed mechanism for systems containing a B_4C mass concentration (a) below 3% and (b) above 3%; the primary phase differs depending on the initial B_4C concentration.

We at nuclear fuel debris science group aim to reveal the physical and chemical characteristics of the remaining fuel debris at TEPCO's Fukushima Daiichi NPS (1F), which is essential to develop secure and safe 1F fuel debris retrieval and decommissioning strategies. Although the fuel debris remaining in 1F is still unidentified at this time, it can be generally classified into three as follows:

- **Metallic fuel debris** composed mainly of stainless steel, boron carbide, and metallic zirconium,
- **Oxide fuel debris** consisting mainly of uranium and zirconium oxides, and
- **Concrete-based fuel debris** with a silicate matrix.

Boron carbide (B_4C) used in the control rods of 1F causes eutectic melting reaction with metals to form metallic fuel debris. Therefore, it is presumed that a large amount of metallic fuel debris remains in 1F. Metallic fuel debris was, however, not generated in the past severe accidents (i.e., at Three Mile Island or Chernobyl) because of the difference in reactor type. Hence, the characteristics of the metallic fuel debris are mostly veiled even to date. In order to reveal the formation mechanisms of metallic fuel debris, this study performed high temperature reaction experiments by melting stainless steel and boron carbide, and prepared metallic fuel debris samples under

various conditions.

Example backscattered electron images collected on cross sections of the prepared metallic fuel debris samples are shown in Fig.1-2. The $(Cr,Fe)_2B$ phase (i.e., a chromium–iron–boron intermetallic compound) was found to crystallize and grow with increasing B_4C content. A summary of the solidification mechanism of the metallic fuel debris based on the results from our detailed analysis is shown in Fig.1-3. Here, γ -Fe (i.e., a metallic phase of iron) was the primary phase when the initial mass concentration of B_4C was below 3 mass%, as shown in Fig.1-3(a). When the B_4C mass concentration exceeded 3 mass%, however, $(Cr,Fe)_2B$ became the primary phase, and a third phase, $(Cr,Fe)_{23}(C,B)_6$, was also formed, as shown in Fig.1-3(b). This solidification mechanism can vary with the carbon, boron, and chromium concentration.

This research demonstrates how our research group is tackling the problems posed by fuel debris from the viewpoint of basic research.

This work was supported financially in part by the Japan Society for the Promotion of Science (JSPS) KAKENHI Grant-in-Aid for Early-Career Scientists (No.JP20K15209).

(Takehiro Sumita)

Reference

Sumita, T. et al., Solidification and Re-Melting Mechanisms of SUS- B_4C Eutectic Mixture, Journal of Nuclear Materials, vol.543, 2021, 152527, 15p.

1-2 Development of Radiation Detector for Non-Destructive Assay of Nuclear Fuel Debris

— γ -ray Spectrometry System Specific to High Dose-Rate Measurements Using CeBr_3 —

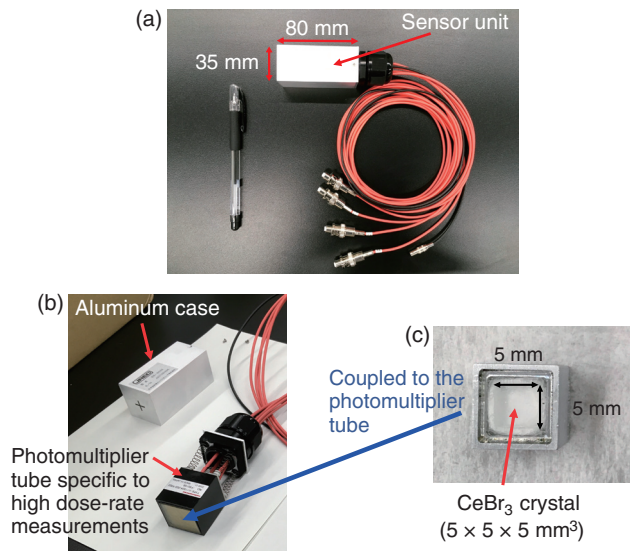


Fig.1-4 γ -ray spectrometry system specifically for high dose-rate measurements

(a) The developed compact γ -ray measurement system. (b) A scintillator can be coupled with a photomultiplier tube for high dose-rate measurements. (c) Fabricated small-volume CeBr_3 scintillator ($5 \times 5 \times 5 \text{ mm}^3$).

In TEPCO's Fukushima Daiichi NPS (1F), the preparation for the retrieval of nuclear fuel debris from the reactor pressure vessels, which is considered to be the most difficult process, is underway. The debris comprises mixed nuclear fuel and structural materials that melted at a high temperature and have since been solidified. Semiconductor detectors with radiation shielding are often used to measure high dose-rate nuclear fuels, including nuclear fuel debris. However, these instruments are large and cannot easily be used at 1F, where many buildings are damaged or under decommissioning. Further, high dose-rate operations require remote devices. Therefore, we developed a small, lightweight γ -ray spectral measurement system for high dose rates, as shown in Fig.1-4(a).

Scintillation detectors offer several advantages over semiconductor detectors at high dose rates; in particular, the CeBr_3 scintillator provides a fast decay time ($<20 \text{ ns}$) and good energy resolution (4% at 662 keV). A small volume ($5 \times 5 \times 5 \text{ mm}^3$) of CeBr_3 was fabricated and encapsulated to prevent hygroscopicity, as shown in Fig.1-4(c). The developed scintillation package was coupled with a photomultiplier tube (or sensor unit, see Fig.1-4(b)) specifically for high dose rates,

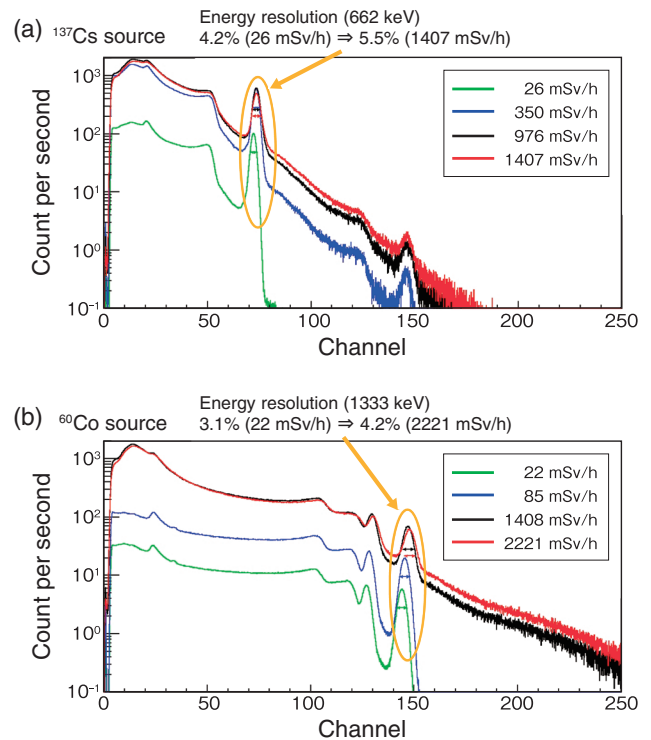


Fig.1-5 γ -ray spectra

γ -ray spectra under (a) a ^{137}Cs radiation field at dose rates up to 1407 mSv/h, and (b) under a ^{60}Co radiation field at dose rates up to 2221 mSv/h. The energy resolutions at 662 and 1333 keV were evaluated under these radiation fields.

and a fast digital circuit was used to realize a high count rate and flexible pulse signal processing.

Next, γ -ray spectra were obtained at several dose rates under ^{137}Cs and ^{60}Co radiation fields to investigate the performance at high dose rates; the results are shown in Fig.1-5. (a) Under the ^{137}Cs radiation field, when the exposure dose rate was ranged from 26 to 1407 mSv/h, the relative energy resolution at 662 keV was 4.2% at 26 mSv/h and 5.5% at the highest dose rate of 1407 mSv/h. (b) Under the ^{60}Co radiation field, when the exposure dose rate ranged from 22 to 2221 mSv/h, the relative energy resolution at 1333 keV was 3.1% at 22 mSv/h and 4.2% at the highest dose rate of 2221 mSv/h. The energy resolution was high enough to identify the principle γ -ray spectral lines of ^{134}Cs , ^{137}Cs , ^{60}Co , and ^{154}Eu .

This research was done in collaboration with the University of Tokyo and the National Institute of Advanced Industrial Science and Technology. Our contributions will help realize the non-destructive assay of nuclear fuel debris, which will contribute to the safe and rapid decommissioning of 1F.

(Masaaki Kaburagi)

Reference

Kaburagi, M. et al., Gamma-ray Spectroscopy with a CeBr_3 Scintillator under Intense γ -ray Fields for Nuclear Decommissioning, Nuclear Instruments and Methods in Physics Research Section A, vol.988, 2021, 164900, 8p.

1-3 Chemical Forms of Radionuclides in Fuel Debris

— Structure of Concrete Interaction Products and Distribution of Sr and Ba —

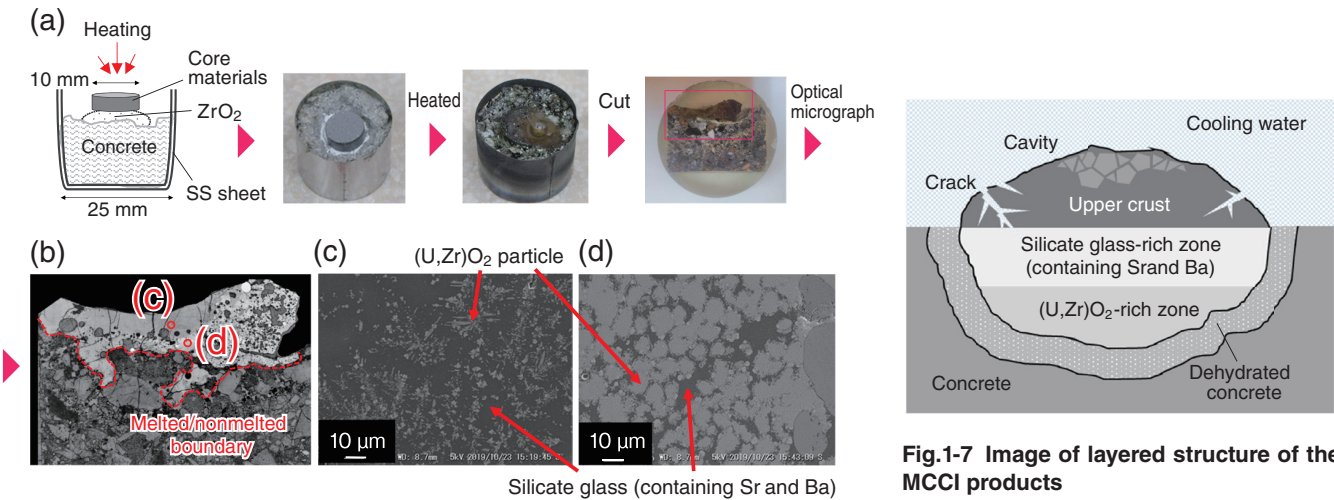


Fig.1-6 (a) Schematic image and appearance of simulated MCCI product, (b) optical micrograph of a cross section of the simulated MCCI product, (c) SEM image of the upper region in the once-melted zone, and (d) SEM image of the bottom region in the once-melted zone

Core materials mixture was placed on a piece of concrete and MCCI was simulated using a light-concentrated heating technique. The cross-sectional images of the once-melted zone show that dark silicate glass (containing Sr and Ba) is dominant in the upper region, while (U,Zr)O₂ is rich in the bottom region.

Fig.1-7 Image of layered structure of the MCCI products

(U,Zr)O₂ particles tend to sink in the bottom region, whereas silicate glass is likely to solidify in the upper region. The surface crust may have cracks and cavities, and therefore water may contact the upper silicate glass.

In the severe accident at TEPCO's Fukushima Daiichi NPS (1F), the molten corium consisting of nuclear fuels and structural materials was predicted to spread over the concrete floor of the primary container vessel, resulting in molten core-concrete interaction (MCCI). The MCCI products continue to be exposed to cooling water. Under such conditions, the water-soluble radionuclides may be gradually dissolved from the MCCI products, and then, some of these radionuclides will likely migrate via water. Knowing the structure of MCCI products and the distribution of such radionuclides in MCCI products is important to understanding the diffusion behavior within 1F. In this study, we focused on Sr and Ba, which have high radioactivity. A reaction test between simulated corium (containing nonradioactive Sr and Ba) and concrete was performed and information on the structure of MCCI products and the distribution of Sr and Ba was experimentally obtained.

Fig.1-6 (a) shows a schematic illustration and appearance of the simulated MCCI product. The powder mixture of simulated core materials (U_{0.5}Zr_{0.5}O₂, ZrH₂, stainless steel (SS), B₄C, Mo-Ru-Rh-Pd, BaCO₃, and SrCO₃) was pressed into a tablet and placed on a basaltic concrete piece. Light from a Xe lamp (3 kW maximum) was directed onto the tablet surface using a light-concentrating heating device to form a simulated MCCI product under a vertical temperature gradient.

The solidified sample was cut in a vertical direction and Fig.1-6 (b) shows the optical micrograph of the cross section.

The corium and concrete were interacted as liquid phases and solidified in the upper gray region (once-melted zone). Below the once-melted zone, concrete did not melt but thermally dehydrated. Figs.1-6 (c) and (d) show SEM (scanning electron microscope) images of the upper region and bottom region of the once-melted zone, respectively. The main phases are dark silicate glass and bright (U,Zr)O₂ particles. Sr and Ba were detected in the silicate glass (approximately 3at%-Sr and 2at%-Ba), whereas they were not detected in (U,Zr)O₂. Thermodynamic analysis reveals that Sr and Ba tend to dissolve in silicate glass, rather than in (U,Zr)O₂.

(U,Zr)O₂ precipitated as fine particles (2–3 μm) in the upper region, while it precipitated as bigger particles (10–20 μm) in the bottom region. In addition, the content of (U,Zr)O₂ is much higher in the bottom region. During the heating tests, sedimentation of (U,Zr)O₂ particles may have occurred in the liquid silicate glass because of its higher density.

An image of the MCCI product layered structure is drawn in Fig.1-7. According to the 1F accident scenario, the crust might have formed on the top surface with cracks and cavities. The water possibly contacted the silicate glass-rich zone, where Sr and Ba are likely to be concentrated. Future research will include the leaching behavior of Sr and Ba from silicate glass. These data will contribute to the diffusion behavior of radionuclides within 1F.

(Ayako Sudo)

Reference

Sudo, A. et al., Experimental Evaluation of Sr and Ba Distribution in Ex-Vessel Debris under a Temperature Gradient, Journal of Nuclear Science and Technology, vol.58, issue 4, 2021, p.473–481.

1-4 To Establish Safer Criticality Management of Fuel Debris

— Optimization of the Core Configuration of the New STACY for Debris Simulation —

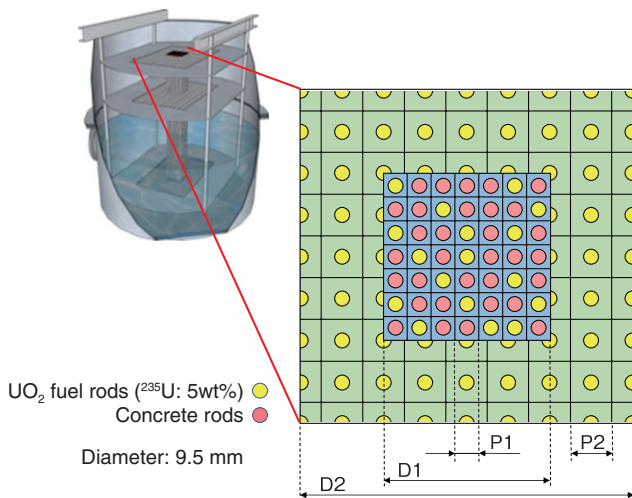


Fig.1-8 Overview of the new STACY and optimization parameters

UO₂ fuel rods in the new STACY are supported by lattice plates. The center lattice is loaded with UO₂ fuel rods and concrete rods, and the outer lattice is loaded only with UO₂ fuel rods to achieve criticality. The interval of the center lattice is arbitrarily adjusted to simulate the neutron-moderation conditions in which the fuel debris is located.

In the accident at TEPCO's Fukushima Daiichi NPS, nuclear fuel melted down, resulting in the formation of fuel debris containing structural materials such as steel and concrete. For the retrieval and management of the fuel debris, criticality safety is essential, therefore computations are under way to evaluate criticality characteristics of fuel debris. However, there are no experimental data on the criticality of fuel debris to validate the analytical evaluation. Hence, we started a project to obtain experimentally the data of fuel debris using the new STACY critical assembly, in which pseudo fuel debris rods with well-known composition will be loaded.

In the case of fuel debris including concrete, the concrete itself contains water, which contributes to neutron moderation along with the surrounding water. It is also necessary to evaluate the effects of other concrete components such as Mg, Si, Al, and Ca on criticality characteristics. The preliminary perturbation calculation revealed that the neutron capture reaction of Si had a significant effect. To examine the Si effect efficiently, the core configuration should be optimized. Because of the technical constraints in preparation of the pseudo fuel debris rods with various compositions, and reduction of radioactive waste throughout the experiments, it was decided to use, instead of pseudo fuel debris rods, a combination of UO₂ fuel rods and concrete sample rods to simulate environments of the fuel debris. At the same time, the goal of core configuration was set to obtain maximum Si sensitivity with a small number of concrete sample rods.

As shown in Fig.1-8, the fuel rods are arranged at

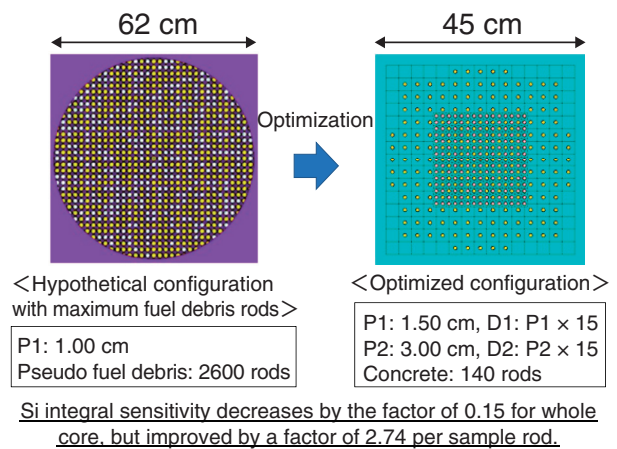


Fig.1-9 Pressure variation of metal lattices of YH₃

In the optimized core configuration, the integral Si sensitivity is lower than that of the hypothetical case with a large amount of pseudo fuel debris, but the sensitivity per sample rod is higher. Note that this core can be realistically constructed. Other optimizations were performed for the cases of P1 = 1.00 cm and 1.50 cm.

predetermined intervals by lattice plates in the core tank. By changing the lattice plates, it is possible to simulate various neutron-moderation conditions in which the fuel debris is located. In the optimization, a two-region core configuration was devised to reduce the total number of fuel rods, with UO₂ fuel rods and concrete sample rods in the central region and only UO₂ fuel rods in the outer region. The optimization parameters are the lattice interval (P1, P2), the size of the region (D1, D2), and the ratio of concrete sample rods (w). First, P1 was set to obtain a targeted condition of neutron moderation for fuel debris, P2, D1, D2, and w were optimized to maximize the sensitivity of the Si neutron capture reaction. Fig.1-9 shows one of the results of the core configuration optimization. Although the integral Si sensitivity of the optimized core configuration is lower than the hypothetical case in which a large amount of simulated fuel debris is prepared and loaded, the sensitivity obtained per concrete sample rod is 2.74 times higher than that of the hypothetical case. In addition, a realistically constructible core configuration is obtained. These experimental data will greatly contribute to obtaining the effect of concrete components including Si on criticality characteristics and is expected to be useful for the development of criticality evaluation methods for the handling of fuel debris during decommissioning.

The work reported in this article was performed under the auspices of the Secretariat of Nuclear Regulation Authority (NRA), Japan.

(Satoshi Gunji)

Reference

Gunji, S. et al., Criticality Configuration Design Methodology Applied to the Design of Fuel Debris Experiment in the New STACY, Journal of Nuclear Science and Technology, vol.58, issue 1, 2021, p.51–61.

1-5 Methodology to Remove Cs from Soil

—Preparation for the Treatment of Contaminated Soil—

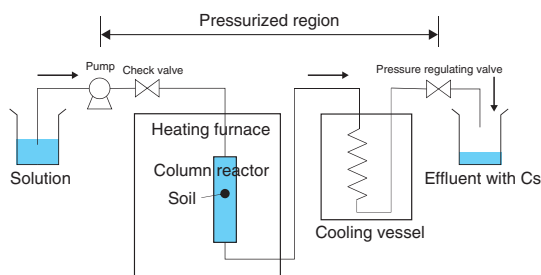


Fig.1-10 Hydrothermal treatment device to remove Cs from soil

The soil particles were loaded into the reactor, heated to a constant temperature, and then leached with a solution for Cs desorption. Cs was recovered from the effluent of the column reactor.

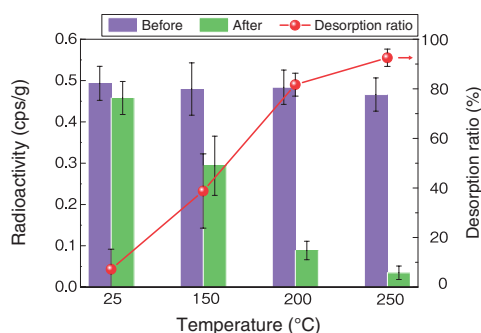


Fig.1-11 Removal of radioactive Cs from actual contaminated soil

The radioactivity of the soil was greatly reduced after treatment with Mg-solution at temperatures ≥ 200 °C; more than 80% of the Cs was removed.

The soil surrounding TEPCO's Fukushima Daiichi NPS had been contaminated with radionuclides that were released during the accident, including ^{137}Cs . Volume reduction techniques of contaminated soil are needed for its storage and management until it can be feasibly disposed of in the future. As radioactive Cs in the soil might be selectively and strongly adsorbed onto the clay minerals of the local soil, sieving can be used to roughly separate the minerals from the soil and thus provide Cs enrichment. Nevertheless, novel chemical treatment techniques capable of removing Cs from clay are indispensable for effective soil decontamination.

Generally, Cs trapped by soil particles is fixed in the clay interlayer. Cation-exchange methods using highly concentrated salt solutions at temperatures above the boiling point of water can be used to remove this strongly bound Cs. However, Cs can be resorbed during cooling, making decontamination difficult and requiring that the soil particles are treated with leaching solutions and then separate them in subcritical and pressurized conditions (i.e., hydrothermal conditions). Removing Cs from soil requires the primary contact of soil particles with an aqueous solution under pressure and their fast separation from solution containing Cs.

Therefore, we conducted Cs removal tests via the continuous reaction of solid and liquid under high temperature and pressure.

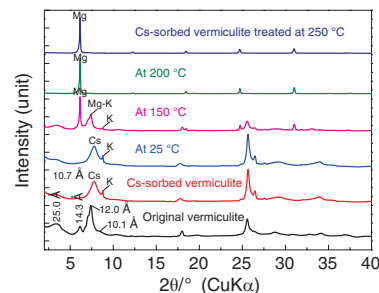


Fig.1-12 Ion exchange between Mg and Cs on vermiculite in subcritical conditions

Cs-sorbed vermiculite has two peaks representing the Cs-interlayer with a basal spacing of 10.7 Å ($=10^{-10}$ m) and the K-interlayer in 10.1 Å. The Cs-interlayer peak disappeared after treatment with 0.01 M solution of Mg at temperatures > 150 °C.

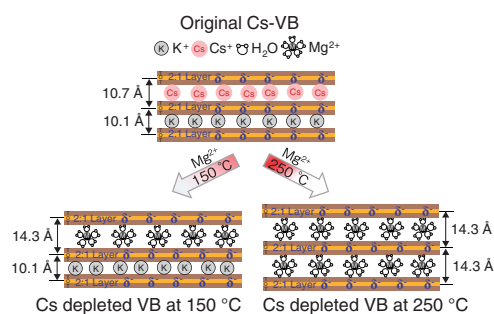


Fig.1-13 Reaction model of Mg exchange with fixed Cs in soil particles of vermiculitized biotite (VB)

The ion-exchange reaction, in which the trapped monovalent Cs⁺ ion are replaced by divalent Mg²⁺, was highly temperature dependent; increasing the temperature also increased the efficiency.

A column system was designed for Cs desorption in which a reactor was loaded with soil particles that were then leached at a constant temperature by continuous circulation of an aqueous solution, as shown in Fig.1-10. An Mg solution shown to be effective for Cs leaching in previous studies was used to remove Cs from contaminated soil. After treatment at ≥ 200 °C, the soil radioactivity was greatly decreased, and the Cs removal ratio was $> 80\%$, as summarized in Fig.1-11. This Cs removal process by Mg exchange in Cs-sorbed vermiculite was then explored by XRD. As shown in Fig.1-12, no Mg-interlayer peak was present in the samples at 25 °C; however, above 150 °C, peaks representing the Mg- and K-interlayers were present in the treated samples, whereas the peak representing the Cs-interlayer (10.7 Å ($=10^{-10}$ m)) was not observed. Further, the proposed method using Mg effectively removed Cs trapped in the layered vermiculite (i.e., achieved a higher removal ratio) at treatment temperatures ≥ 200 °C (Fig.1-13).

Overall, the proposed method presents an effective and feasible Cs removal chemical treatment for soil decontamination.

This work includes partial results from joint research with the Tokyo Institute of Technology titled “Research on radioactive material recovery from radioactive waste by subcritical water washing and solid-phase extraction”.

(Xiangbiao Yin, Yoshikazu Koma)

Reference

Yin, X., Koma, Y. et al., Selective Removal of Radiocesium from Micaceous Clay for Post-Accident Soil Decontamination by Temperature-Controlled Mg-Leaching in a Column, Journal of Hazardous Materials, vol.387, 2020, 121677, 10p.

1-6 Toward Understanding Core Melting Behavior in RPVs

— Evaluation of RPV Failure Mechanism —

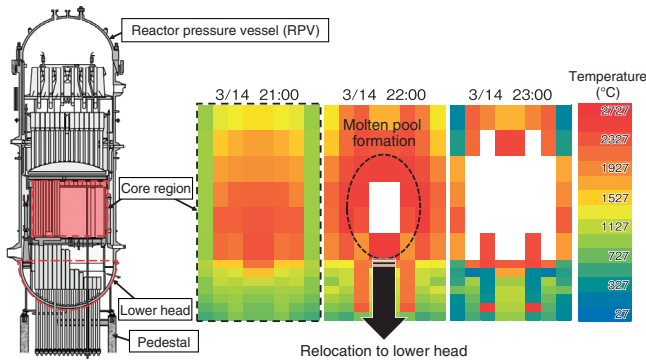


Fig.1-14 Estimated core temperature profile of Unit 2

Accident analysis was numerically conducted using RELAP/SCDAPSIM, a severe accident analysis code. The relocation of core material to the lower plenum (timing of relocation and amount relocated) were estimated by comparing the measured pressures of RPV and PCV during the accident with the numerical results.

The state of fuel debris and fission products deposited in the reactor pressure vessel (RPV) and primary containment vessel (PCV) must be understood for TEPCO's Fukushima Daiichi NPS (1F) decommissioning. As a result of internal investigations of the PCV of Unit 2, the state inside the pedestal, i.e., the cylindrical structure supporting the RPV, has become well understood. Since the structures inside the pedestal remain mostly intact, the temperature of the fuel debris relocated from the RPV to the pedestal inside is estimated to be lower than the melting temperature of oxidic nuclear fuel. According to conventional understanding, a high-temperature oxidic molten pool will be developed in the RPV lower head before the vessel failure (VF). However, recent investigations and numerical analyses have demonstrated that a mixed solid-liquid pool (i.e., where the oxidic components remain solid and only the metallic components are molten) was formed, and the local thermal load caused the VF.

Therefore, a severe accident (SA) analysis of Unit 2 of 1F was conducted, and the core materials relocated into the lower head were estimated to understand the 1F-specific VF mechanism. The calculated core temperature profile demonstrates that the core temperature reached a maximum of 2500 °C at 22:00, indicating the formation of a molten pool, as shown in Fig.1-14. The calculation results estimate that approximately 60% of the core inventory relocated to the lower head within the next several hours. Although the core debris must have moved to the pedestal inside due to VF, the location and mechanism of VF have not yet been identified.

Given that VF is caused by heat-up of the vessel walls,

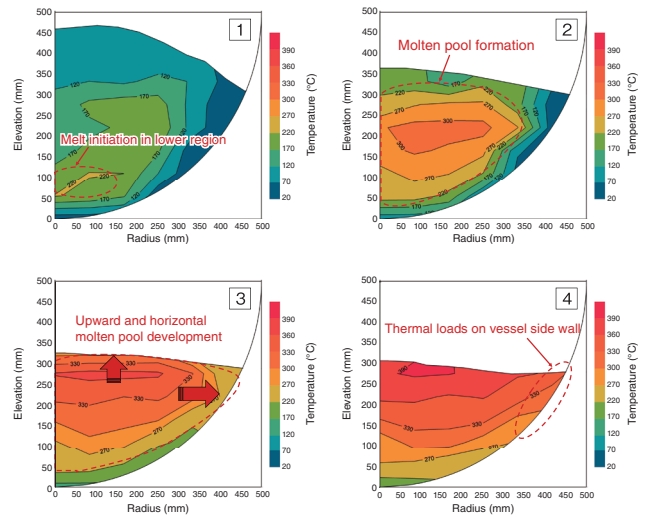


Fig.1-15 Temperature profile in LIVE-J1 experiment*

The temperature profile of LIVE facility used to simulate the lower head of an RPV is shown. The preloaded solid simulant materials began melting in the lower region of the debris bed to form a molten pool, which developed both upwards and horizontally.

their temperature profiles are necessary to evaluate the failure modes. In collaboration with the LIVE facility at Karlsruhe Institute of Technology (KIT), we conducted an experiment to understand the heat transfer of debris comprising materials with various melting temperatures. Ceramics and nitrate salts were used to represent oxidic and metallic components of fuel debris, respectively. When compared with the 1F reactor, the test facility had a scale of 1:5.5. The simulated debris particles, comprising 245.4 kg of ceramics and 79.6 kg of nitrate salts, were preloaded in the test vessel. The decay heat was then simulated by the heating planes, where the boundary conditions of the top surface and sidewall were adiabatic and natural air convection, respectively. The resulting temperature evolution during the test is shown in Fig.1-15. Debris melting began from the lower region, and the molten pool developed both upwards and horizontally. This experiment showed that horizontal heat transfer occurs due to convection, even in a pool comprising a mixture of solid and liquid, and that the thermal loads on the vessel sidewall became large. Combining these results with numerical analysis will allow the failure mechanism of Unit 2 to be identified.

These results were obtained in part thanks to the cooperative research between JAEA and KIT.

(Hiroshi Madokoro)

* Madokoro, H. et al., LIVE Experiment on Thermal Behavior of Solid-Liquid Mixture Pool in RPV Lower Head, Atomic Energy Society of Japan 2021 Fall Meeting, online, 2021, 2J08 (in Japanese).

Reference

Madokoro, H. et al., Estimation of the Core Degradation and Relocation at the Fukushima Daiichi Nuclear Power Station Unit 2 Based on RELAP/SCDAPSIM Analysis, Nuclear Engineering and Design, vol.376, 2021, 111123, 15p.

1-7 Laser Ultrasonic Approach to Detect Corrosion of Reinforced Concrete

— Toward Nondestructive Testing Technology for Decommissioning —

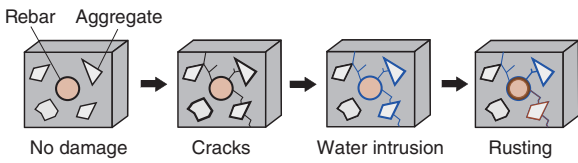


Fig.1-16 Corrosion process of RC

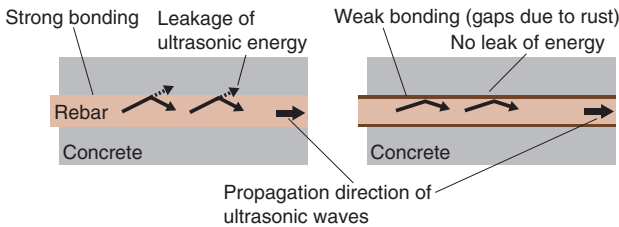


Fig.1-17 Differences in the propagation of ultrasonic waves through rebar due to the degree of bonding to the surrounding concrete

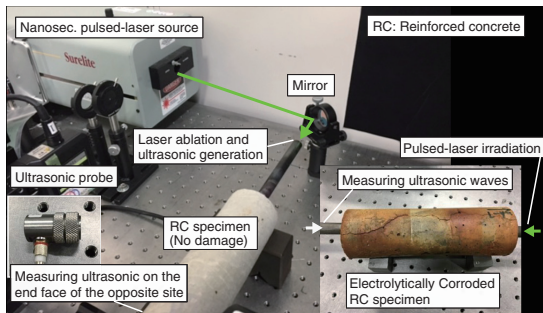


Fig.1-18 Experimental setup and specimen used for measuring ultrasonic waves propagating through the RC rebar

The structural integrity of the buildings damaged by earthquakes and hydrogen explosions must be maintained to complete the long-term decommissioning of TEPCO's Fukushima Daiichi NPS safely and smoothly. Additionally, technology capable of detecting and evaluating the deterioration of the buildings is needed to prevent further damages caused by future earthquakes. During the accident, seawater penetrated the reactor; further, the buildings are still exposed to rain. Therefore, we developed a non-destructive method to evaluate the corrosion of reinforced concrete (RC).

The deterioration process of RC by corrosion is summarized in Fig.1-16. Rebar and the surrounding concrete are tightly bonded when healthy; as deterioration progresses, however, the degree of bonding decreases. Due to this change in bonding, the waveforms of the ultrasonic waves propagating through the rebar vary, suggesting that the level of deterioration might be detectable from the changing waveforms (Fig.1-17).

Therefore, we investigated the correlation between the degree of the bonding and waveform of the ultrasonic wave using the experimental setup and specimen shown in Fig.1-18. Here, bonding degradation was simulated by electrolytic corrosion. The ultrasonic wave was excited by irradiating the cut surface of the rebar with a nanosecond pulsed laser. The waveforms

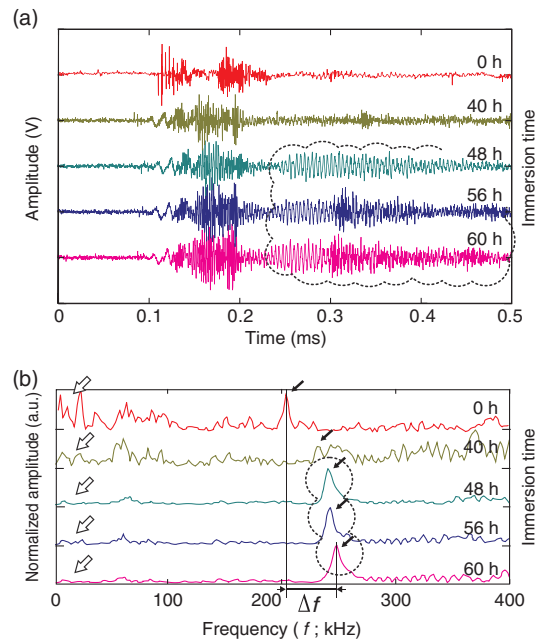


Fig.1-19 A collection of ultrasonic signals in the (a) time and (b) frequency domain at the same immersion time interval

The signals enclosed by the dotted line in (a) correspond to the peaks noted in (b). The white arrows in (b) show that the low-frequency component of the signals decreased as the corrosion progressed. The black arrows in (b) show that the peaks became apparent as the low-frequency component decreased. Δf in (b) shows the amount by which the peak moves to the high-frequency side due to the decrease of the rebar diameter caused by electrolytic corrosion.

were measured using an ultrasonic probe on the opposite cut surface of the rebar. After measuring the ultrasonic waveforms, the specimen was subjected to electrolytic corrosion. The obtained ultrasonic waveforms after varying immersion times are shown in the time and frequency domains in Figs.1-19(a) and (b), respectively.

Characteristic resonance waveforms were present after 48 hours of immersion (as indicated by the dotted line). In the frequency domain, these waveforms were noticeable as a decrease in the low-frequency component. These waveforms were caused by the change in wave propagation owing to the weakening of the bonding. The resonance of the ultrasonic wave at the cut surface of the rebar causes these signals. Δf indicates that the peak of these signals shifted toward the high-frequency side as the rebar diameter decreased due to electrolytic corrosion (Fig.1-19(b)).

These resonant signals are correlated with the diameter of the rebar; deterioration via corrosion thus progressed as the intensity of the low-frequency component decreased and the signal peaks shifted to the high-frequency region. Our findings indicate that ultrasonic waves propagating through rebar can be used to detect and evaluate the corrosion of RC.

(Akinori Furusawa)

Reference

Furusawa, A. et al., Proposal of Laser-Induced Ultrasonic Guided Wave for Corrosion Detection of Reinforced Concrete Structures in Fukushima Daiichi Nuclear Power Plant Decommissioning Site, Applied Sciences, vol.9, issue 17, 2019, 3544, 12p.

1-8 Aiming to Predict PCV Corrosion

— Development of Corrosion Database under Varying Irradiation Conditions —

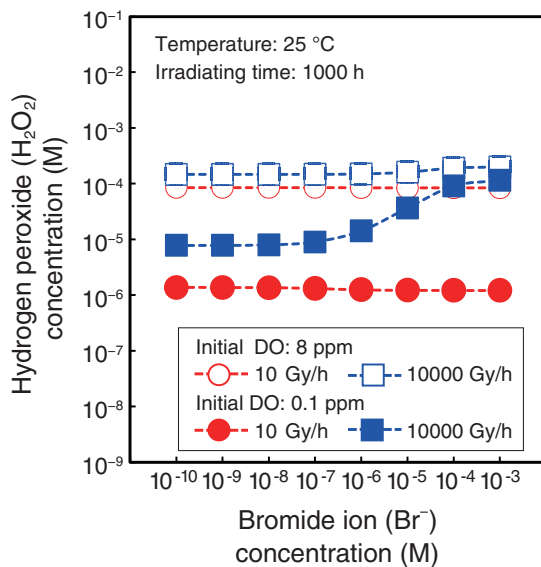


Fig.1-20 Example calculation of water quality under irradiation using the developed radiolysis database

Br^- ions are present in seawater. More H_2O_2 , which causes corrosion of metals, was generated when the concentration of Br^- ions and dose rate were high. (1 M = 10^3 mol/m³)

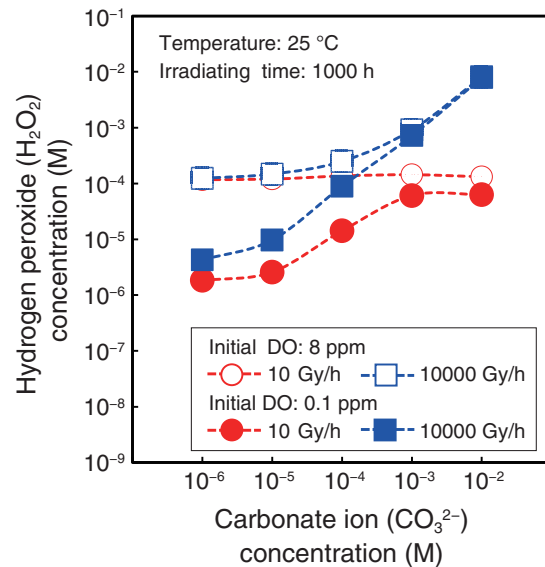


Fig.1-21 Example calculation of water quality under irradiation using the developed radiolysis database

CO_3^{2-} ions are present in air and groundwater. More H_2O_2 was generated when the concentration of CO_3^{2-} ions and dose rate were high. (1 M = 10^3 mol/m³)

Stagnant water and cooling water inside the Primary Containment Vessel (PCV) are exposed to radioactive materials, including fuel debris and released cesium. Further, these materials may contain many impurities, such as ions from seawater and metal ions released from steel. The PCV is currently filled with nitrogen gas. However, the PCV will likely be opened during decommissioning, allowing an inflow of oxygen (O_2) gas, which will lead to variation of dissolved oxygen (DO; 0–8 ppm). Hydrogen peroxide (H_2O_2) accelerates the corrosion of metals and is generated by water radiolysis under irradiation. Thus, generated H_2O_2 may accelerate the corrosion of PCV structural materials and hinder decommissioning.

Therefore, we are developing a database that can be used to estimate the radiolysis and corrosion of structural materials due to the presence of water containing various impurities under a wide DO concentration range under irradiation. This work has involved collaborations between JAEA and the National Institutes for Quantum Science and Technology, Osaka Prefecture University, Tokyo Institute of Technology, Tohoku University, and the University of Tokyo. This database comprises three parts: a radiolysis database, a corrosion database on corrosion under irradiation, and investigation sheets on corrosion risks present during decommissioning. We at JAEA have mainly focused on building the radiolysis database.

The rate constants for 215 reactions of radiolytic species,

including pure water radiolysis and chloride (Cl^-), bromide (Br^-), sulfate (SO_4^{2-}), carbonate (CO_3^{2-}), bicarbonate (HCO_3^-), and ferrous (Fe^{2+}) ions, have been collected to build this radiolysis database.

The calculated H_2O_2 concentrations for Br^- and CO_3^{2-} are shown in Figs.1-20 and 1-21, respectively. Here, the corrosion rate of carbon steel (i.e., a material used in the PCV) increased with increasing H_2O_2 concentration. Overall, the results demonstrated that the DO, Br^- ion, and CO_3^{2-} ion concentrations must be reduced to reduce the generation of H_2O_2 under higher dose rates. The amount of radiolytic products varied by the effects of anions contained in seawater and ferrous ion released from steel on radiolysis. The developed database is expected to be applied to evaluate corrosive environments and hydrogen generation by radiolysis in containers storing contaminated water. Future efforts will include expanding the developed database to encompass a wider range of conditions and using it to analyze corrosion-prevention countermeasures.

This work was conducted as a part of the Nuclear Energy Science & Technology and Human Resource Development Project “Analysis of Corrosion Mechanism in Specific Environment” funded by the Ministry of Education, Culture, Sports, Science and Technology (MEXT), Japan.

(Tomonori Sato)

Reference

Sato, T. et al., Database for Corrosion under Irradiation Conditions (Contract Research), JAEA-Review 2021-001, 2021, 123p. (in Japanese).

1-9 Radiation Position Detection under High Dose Rate Using Optical Fibers

— An Approach to Detect the Position of Radiation Focusing on the Wavelength Information of Light —

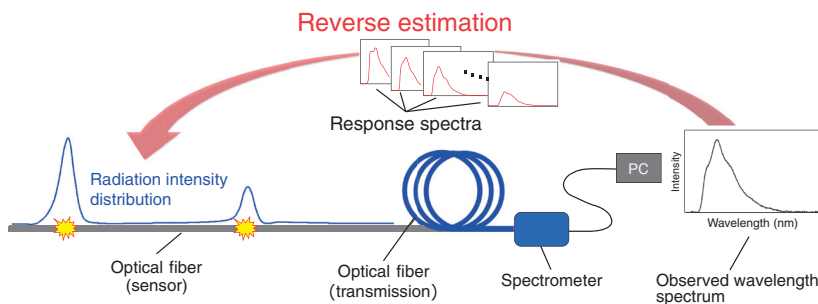


Fig.1-22 Schematic of the proposed method

By detecting the wavelength spectrum at one side of the fiber, the incident position of radiation can be estimated using the wavelength dependency of light attenuation inside the fiber.

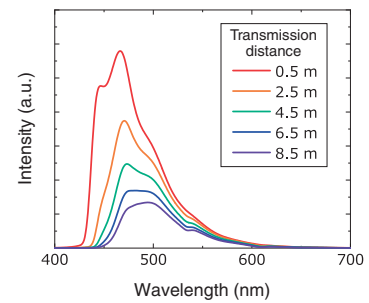


Fig.1-23 Light attenuation inside the optical fiber

The shape of the wavelength spectrum changes with changes in the light transmission distance.

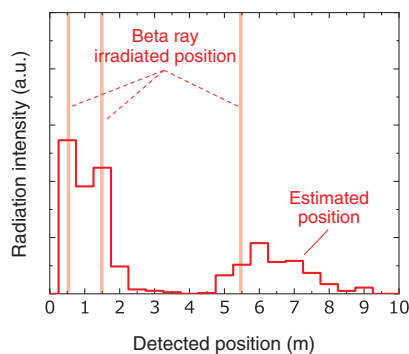


Fig.1-24 Position detection of the beta ray using a $^{90}\text{Sr}/^{90}\text{Y}$ source

The incident position of the beta ray was reasonably estimated.

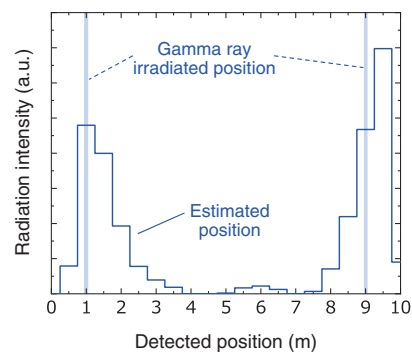


Fig.1-25 Position detection of the gamma ray using a ^{60}Co source

The incident position of the gamma ray (3 Gy/h) was reasonably estimated.

The distribution of radioactive substances at TEPCO's Fukushima Daiichi NPS (1F) decommissioning site must be measured to reduce the external dose of workers and to ensure efficient decontamination. Fiber-optic radiation sensors can be used to measure the distribution of radioactive substances. Among methods employing these sensors, the time-of-flight method, which determines the incident position of radiation to the fiber from the time difference of the light reaching both ends of the fiber, has been applied in the 1F decommissioning site. However, because the time-of-flight method must detect light at both ends of the fiber, it cannot easily be applied in high dose-rate environments, such as inside the 1F reactor building due, to the increase in separation error of the signal position.

Therefore, in collaboration with Nagoya University, we developed a method to measure the radiation intensity distribution along the fiber under a high dose-rate environment that requires light readouts from only one side of the optical fiber; a schematic of the developed method is shown in Fig.1-22. In this method, the light emitted from the interaction between the fiber and the radiation is detected by a spectrometer placed at one side of the fiber. The spectrometer captures the wavelength spectrum, which shows the relative intensity of each color of light. The emitted light is gradually attenuated inside the fiber due to the

absorbance and scattering of light. The degree of attenuation depends on the color of the light; thus, the captured wavelength spectrum varies with the light transmission distance, as shown in Fig.1-23. Therefore, the radiation intensity distribution along the fiber can be estimated by analyzing the wavelength spectrum from only one side of the fiber. Additionally, since the wavelength spectrum measured by the spectrometer is an integrated intensity of each color of light, the saturation of the signal under the high dose-rate environment can be avoided.

Example of position detection using a beta ray from $^{90}\text{Sr}/^{90}\text{Y}$ (source intensity: 1-MBq) and a gamma ray from ^{60}Co (irradiated dose rate: 3 Gy/h) are shown in Figs.1-24 and 1-25, respectively. Both estimated positions show good agreement with the actual radiation incident position. Therefore, the proposed method can effectively detect the position of gamma and beta rays at the 1F decommissioning site.

This work was partially supported by JAEA Nuclear Energy S&T and Human Resource Development Project "Measurement Methods for the Radioactive Source Distribution Inside Reactor Buildings using a One-dimensional Optical Fiber Radiation Sensor" (No.JPJA19B19206529).

(Yuta Terasaka)

References

- Terasaka, Y. et al., Feasibility Study of the One-Dimensional Radiation Distribution Sensing Method Using an Optical Fiber Sensor Based on Wavelength Spectrum Unfolding, *Journal of Nuclear Engineering and Radiation Science*, vol.7, issue 4, 2021, 042002, 7p.
- Collaborative Laboratories for Advanced Decommissioning Science, et al., Measurement Methods for the Radioactive Source Distribution Inside Reactor Buildings Using a One-Dimensional Optical Fiber Radiation Sensor (Contract Research) -FY2019 Nuclear Energy Science & Technology and Human Resource Development Project-, JAEA-Review 2020-063, 2021, 44p. (in Japanese).

1-10 Impact of Large Typhoons on the Estuary Mass Flux

— Observation of Radioactive Cesium in the Estuary in 2019 —

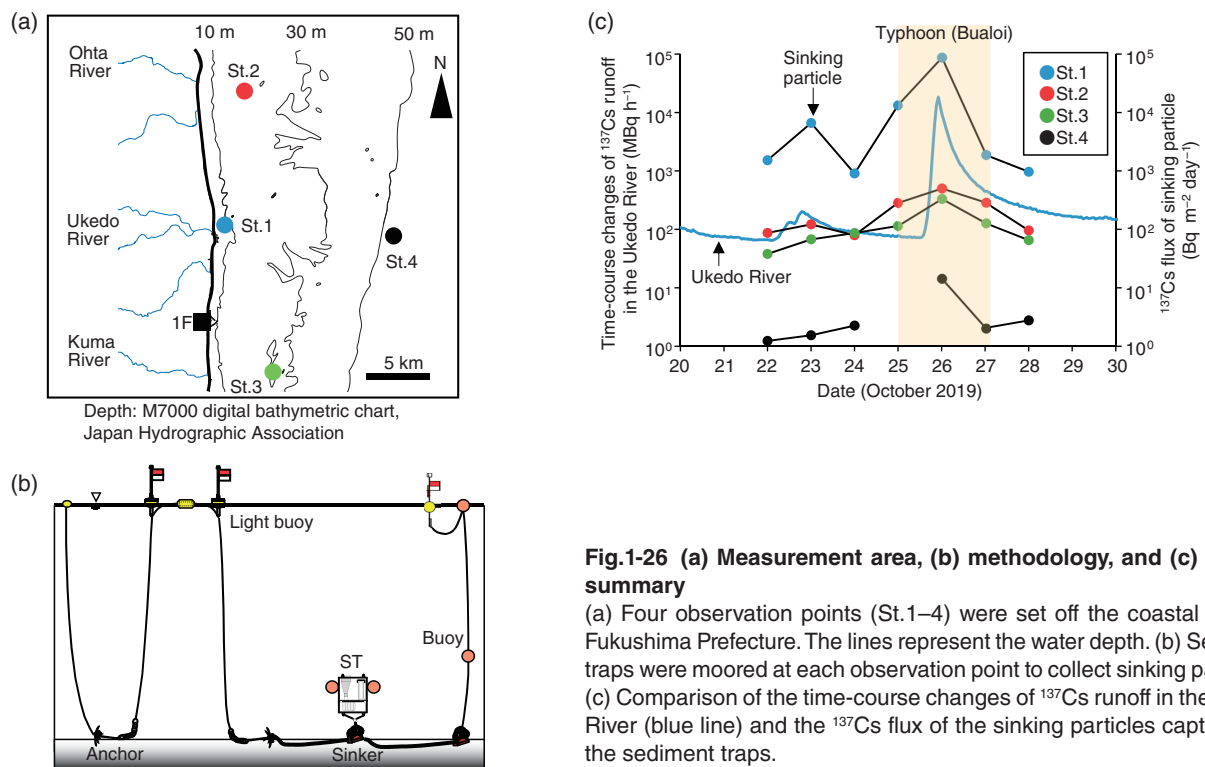


Fig.1-26 (a) Measurement area, (b) methodology, and (c) results summary

(a) Four observation points (St.1–4) were set off the coastal area of Fukushima Prefecture. The lines represent the water depth. (b) Sediment traps were moored at each observation point to collect sinking particles. (c) Comparison of the time-course changes of ^{137}Cs runoff in the Ukedo River (blue line) and the ^{137}Cs flux of the sinking particles captured by the sediment traps.

Dynamic radioactive cesium studies have been conducted since the accident at TEPCO's Fukushima Daiichi NPS (1F) that occurred 10 years ago. Radioactive cesium is likely transported from land to sea, mainly through rivers, although the release of radioactive cesium from 1F into the ocean is limited. Therefore, we have been conducting continuous surveys in the Ukedo River estuary to clarify the radioactive cesium transport mechanisms. Radioactive cesium is transported from rivers to the ocean only during floods (e.g., during typhoons) rather than via continuous outflows. Fine particles that are easily absorbed by radioactive cesium (i.e., the cesium absorbs the fine particles) washed away by the river during flooding and transported to the sea.

To evaluate the transfer mechanism of radioactive cesium to the ocean during floods, we installed sediment traps (STs) at four locations along the coastal area of the estuary targeting the Ukedo River, which has a large basin around the 1F, during the Bualoi Typhoon in 2019. The location of the STs and the methodology used for sediment capture of particles settling toward the seafloor (i.e., sinking particles) are summarized in Figs.1-26(a) and (b), respectively. The radioactive cesium (^{137}Cs) concentration and mass flux (i.e., the mass flow rate of the sinking particles) of the collected particles were measured. The particle samples were collected from October 22nd to October 28th; the typhoon passed through this area on the 25th–26th.

We determined that the concentration of ^{137}Cs in the sinking particles was highest during the typhoon additionally, the highest

concentration of ^{137}Cs was present at St.1; this concentration was approximately 100 times that present at St.4, which is 14 km away from the coast and had the lowest concentration of ^{137}Cs .

The movement of ^{137}Cs can be evaluated by the ^{137}Cs flux, which is obtained by multiplying the ^{137}Cs mass flux by the concentration of ^{137}Cs . The ^{137}Cs flux increased significantly as the typhoon approached. In particular, the ^{137}Cs flux at St.1 was approximately two orders of magnitude higher during the typhoon than before or after it. These results correspond well with the observed time course of ^{137}Cs runoff (i.e., flow rate \times ^{137}Cs concentration) of the Ukedo River, which was estimated from the water level (i.e., flow rate index) and turbidity (i.e., ^{137}Cs index in river water) at the Ukedo River observation point approximately 3.5 km upstream from the estuary, as shown in Fig.1-26(c). This increase in the ^{137}Cs flux of the sinking particles only occurred during the typhoon; by the end of the observation period, two days after the typhoon had passed, the ^{137}Cs flux had returned to normal.

Overall, we determined that the concentration of ^{137}Cs in runoff from the river to the ocean in the mouth of the Ukedo River during a typhoon was remarkable. However, this effect occurred only within 14 km of the coast and only lasted for two days.

This study was partly supported by the Secretariat of the Nuclear Regulation Authority (NRA), Japan.

(Toshiharu Misonou)

Reference

Misonou, T. et al., Survey on the Radioactive Substance in the Coastal Areas near Fukushima Prefecture in FY2019 (Contract Research), JAEA-Research 2020-008, 2020, 166p. (in Japanese).

1-11 Visualization of Radiological Map Using Machine Learning

— Analytical Method Using Big Data of Radiation Measurements in Fukushima —

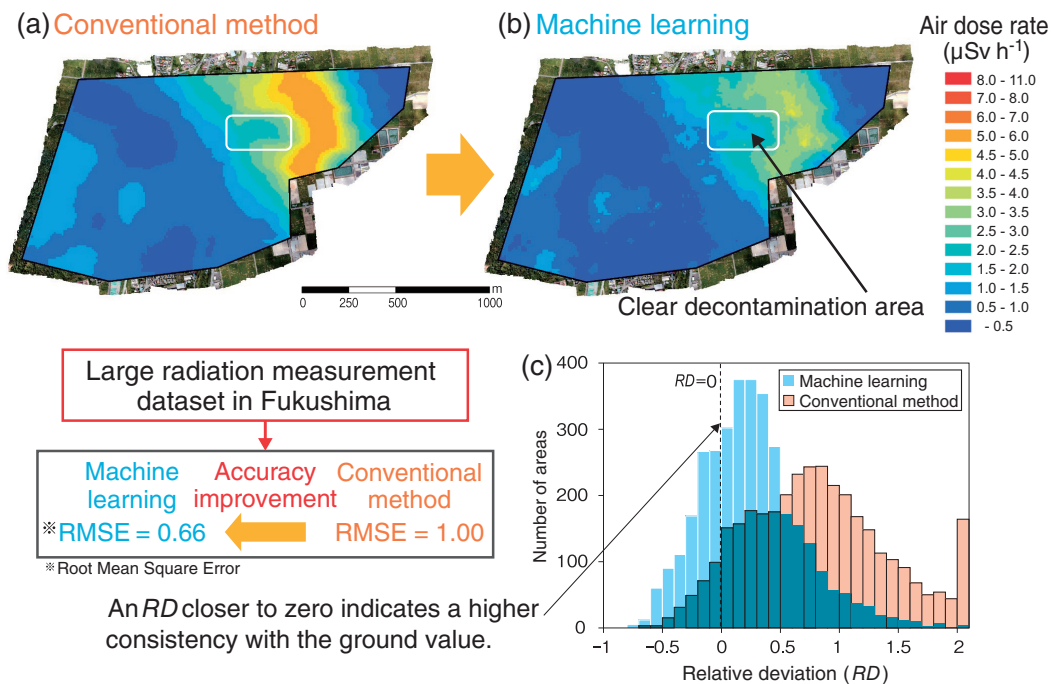


Fig.1-27 Air dose rate map converted by machine learning

Air dose rate map converted by (a) the conventional method and (b) the proposed machine-learning method using an ANN. (c) A histogram of the relative deviation (RD) between the simulated and measured value.

We have been performing airborne radiation surveys (ARs) using unmanned aerial vehicles (UAVs) for environmental radiation monitoring and nuclear disaster prevention since TEPCO's Fukushima Daiichi NPS (1F) accident in 2011. ARs allow measurements to be taken quickly across a wide area where people cannot walk. However, the analyzed data has unavoidable uncertainty when converting ARS data to the ambient dose equivalent rate (i.e., air dose rate) at 1 m above ground level (AGL). In the conventional conversion method, the ground topography is assumed flat, and the air dose rate distribution is assumed uniform. When conditions deviate from these hypothetical conditions, the calculated air dose rates can be highly inaccurate. Although inverse analysis has been demonstrated to be effective, this method requires extensive calculation times. Therefore, we developed an analysis method for real-time and exact analysis using an artificial neural network (ANN), which is a machine-learning system.

The large amount of radiation data that has been obtained around 1F (big data) was applied as training data while constructing the ANN. This training data, containing 37936 data sets, comprised ARS data from an unmanned helicopter and ground-based survey data measured using a backpack survey meter. The ANN was constructed using NeuralWorks Predict (NeuralWare, Carnegie, U.S.A.). The data sets not contained in the training data were

converted to ground air dose rates at 1 m AGL to use as test data; the error (RMSE and RD) between the converted data and the ground-based survey data was then calculated. The RMSE and RD were used as an index of reenactment improvement. Comparing the dose rate distribution maps converted by the conventional method (Fig.1-27(a)) and the machine-learning method (Fig.1-27(b)), the dose-rate distribution of the proposed method was sharper in the decontaminated areas. The RMSEs of the conventional and proposed methods were 1.00 and 0.66, respectively. Additionally, the RD of the proposed method approached zero, as shown in Fig.1-27(c). Therefore, the proposed machine-learning method was more accurate than the conventional method. Further, the optimum parameters were successfully from the big data. In the example shown in Fig.1-27, the inverse problem analysis method required several hours, whereas the proposed method reproduced the dose rate map better than conventional methods in only a few minutes.

Future efforts will aim to improve the quality of conversion by additional measured and simulated data in difficult-to-approach areas, such as the forest and farmland.

This research was part of the joint research with Nagoya University.

(Miyuki Sasaki)

Reference

Sasaki, M. et al., New Method for Visualizing the Dose Rate Distribution around the Fukushima Daiichi Nuclear Power Plant Using Artificial Neural Networks, Scientific Reports, vol.11, 2021, 1857, 11p.

1-12 Improving the Accuracy in Estimation of Air Dose Rate Decrease

— A New Model for Simulation of Temporal Changes Due to an Environmental Effect —

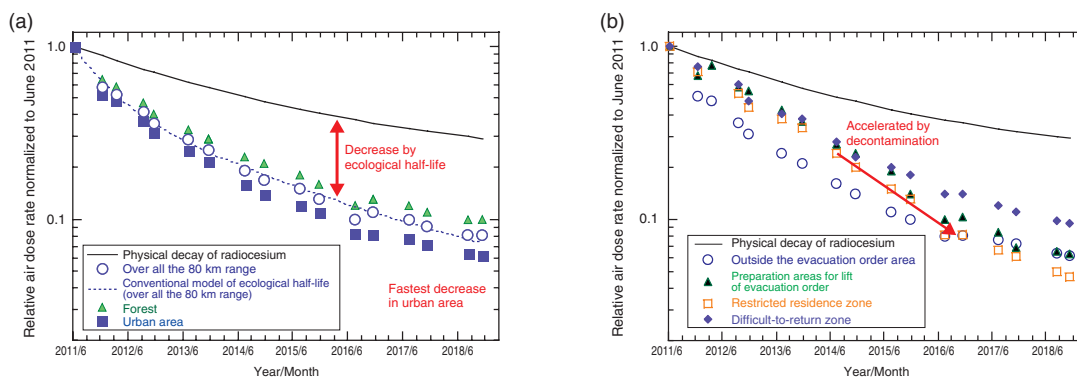


Fig.1-28 Decreasing trend in air dose rates by the car-borne surveys within 80 km of 1F

Relative air dose rates normalized to June 2011 are shown as for (a) over all regions within 80 km of 1F and land-use category, (b) dependence on the evacuation order areas (as for the urban area land-use category).

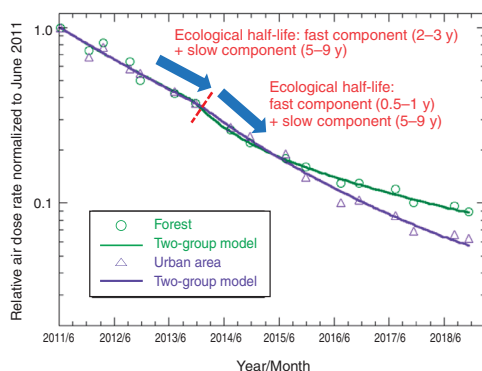


Fig.1-29 Comparison of air dose rates between the measured values and those of the two-group model

The curves evaluated from the ecological half-lives analyzed with the two-group model are in good agreement with the measured data with respect to the forest and urban area land-use categories in the preparation areas for lift of evacuation order.

After TEPCO's Fukushima Daiichi NPS (1F) accident, we performed a series of measurements of the air dose rates using car-borne surveys to evaluate the air dose rate distribution and to obtain basic data for decisions on lifting the evacuation orders. The measurements were carried out using the Kyoto University Radiation Mapping (KURAMA) system developed by the Kyoto University Research Reactor Institute. The KURAMA system consists of radiation measuring equipment installed in ordinary cars, which survey air dose rates continuously along the road.

We have analyzed a huge amount of air dose rate data to precisely evaluate its temporal change. Air dose rates decrease due to physical decay of radiocesium and environmental effects such as weathering and decontamination. Ecological half-lives are parameters that model the decreases in the air dose rate due to environmental effects other than the physical decay of radionuclides. A conventional bi-exponential model of ecological half-life describes the decrease in the air dose rates with fast and slow decreasing components (short and long half-lives, respectively).

The ratio of the air dose rate in November 2018 to that in June 2011 measured over all the regions within 80 km of 1F, where the influence of radiocesium emitted by the accident was relatively significant, was evaluated as 0.08 (see circles in Fig.1-28(a)). This ratio is very small compared with that predicted from the physical decay of radiocesium (0.29; see the solid line in Fig.1-28(a)). This difference is due to the ecological half-lives, and the conventional bi-exponential model describes the decrease in air dose rates as the dashed line in Fig.1-28(a). This figure also shows that the decreasing rate is lowest in the forest and highest

in the urban area, which is a result of human activities.

The decreasing trend of the air dose rates depends on the types of the areas as shown in Fig.1-28(b). Decontamination works have been actively carried out in the preparation areas for lift of evacuation order and in the restricted residence zone, where the decrease in the air dose rates accelerated after 2013. As a result, there is a significant difference from the decreasing trend of the difficult-to-return zone. In such a case, the conventional bi-exponential model could not represent the temporal changes in air dose rates well. Therefore, we newly introduced the two-group model where the fast component of the ecological half-life is shortened by the effect of the decontamination works. We applied this model to the preparation areas for lift of evacuation order and obtained the values of 0.5–1 y for the ecological half-life of the fast-decreasing components after the year 2013, which was significantly shorter than the values of 2–3 y obtained before 2013. The two-group model improved the evaluation of the fast component, and the curves of the decrease in the air dose rate obtained from the model are in good agreement with the measured data as shown in Fig.1-29. These results visualize the effect of decontamination and are expected to be used in future studies such as decontamination planning or cancellation of evacuation orders.

This study was a part of the results of the consignment project conducted on “Aggregation of radioactive material distribution data associated with TEPCO Fukushima Daiichi Nuclear Power Station accident in FY2018”, supported by the Nuclear Regulation Authority (NRA), Japan.

(Masaki Andoh)

Reference

Andoh, M. et al., Evaluation of Decreasing Trend in Air Dose Rate and Ecological Half-Life within an 80 km Range from Fukushima Dai-ichi Nuclear Power Plant, Using Car-Borne Survey Data Measured by KURAMA Systems up to 2018, *Journal of Nuclear Science and Technology*, vol.57, issue 12, 2020, p.1319–1330.

1-13 Sediment Characteristics Determine the Behavior of Cesium in Rivers

— Adsorption/Desorption Mechanism of Radioactive Cesium onto River Sediments —

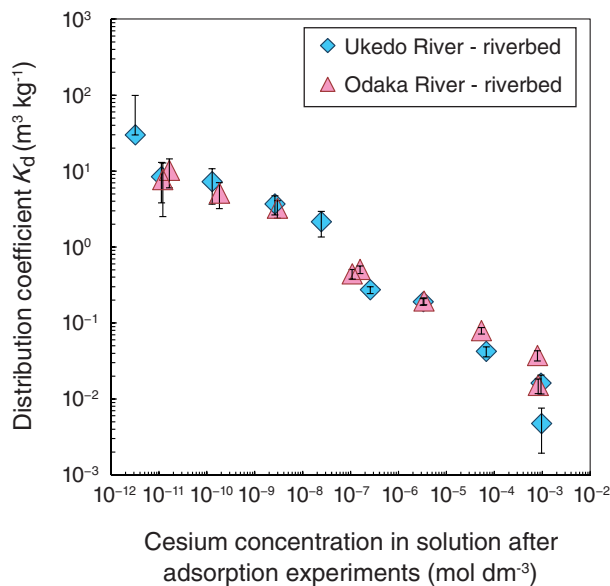


Fig.1-30 Distribution coefficient of cesium to sediments
As the distribution coefficient (K_d) increased as the concentration of cesium in the solution decreased, the distribution coefficient, K_d , increased.

Radioactive cesium discharged by the accident at TEPCO's Fukushima Daiichi NPS remains in forest soil and is gradually flowing into the river system. The adsorption mechanism of cesium by sediments must be clarified to estimate the changing concentration of dissolved cesium in river water. Therefore, we collected sediments from the riverbed in the lower reaches of the Odaka and Ukedo Rivers and evaluated their cesium adsorption and desorption characteristics.

Adsorption experiments were conducted on sediments in a 0.01 mol dm⁻³ (M) sodium chloride (NaCl) solution with various initial cesium concentrations. The sediment samples were sieved using a pore size of 2 mm. After 68 days, when the adsorption equilibrium was attained by time dependence, the ratio of adsorbed cesium to cesium in solution (i.e., the distribution coefficient, K_d) increased in all collected river sediments as the concentration of cesium in the solution decreased (see Fig.1-30). A portion of the minerals residing in the sediment thus likely easily adsorb cesium; however, due to low site to absorb, the adsorbed rate of cesium is relatively high when the concentration is low.

Next, the sediments after the adsorption experiments were added stepwise into the solution with different desorption

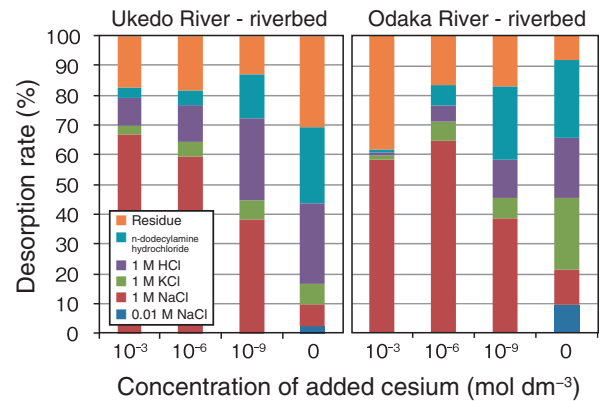


Fig.1-31 Desorption rate of cesium by sequential extraction
The sediment samples before and after adsorption experiments, in which 10⁻³ to 10⁻⁹ mol dm⁻³ of cesium were added, were immersed stepwise into the solution with different desorption effect. It was found that there was strong effects. Strong adsorption sites were found from which cesium was difficult to be desorbed even by the solution capable of dissolving mineral surfaces.

effects. As the concentration of initially added cesium decreased, the proportion of components adsorbed via ion exchange and then desorbed by NaCl and potassium chloride (KCl) decreased. On the other hand, the proportion of components desorbed by hydrochloric acid (HCl), which dissolves the mineral surface, and dodecylamine hydrochloride, which spreads the interlayer spacing of clay minerals, increased (Fig.1-31). We determined that the mineral in the sediment has a mixture of adsorption sites which easy to desorbed and difficult to desorbed. The Odaka River had a higher proportion of components adsorbed via ion exchange in the sediment than in the Ukedo River, indicating a higher content of smectite than mica minerals; cesium adsorption onto smectite was dominated by ion exchange.

The concentration of dissolved radioactive cesium in river water is very low (i.e., approximately 0.1 Bq/L in the Ukedo River) due to the strong adsorption of cesium onto the part of the minerals from which cesium cannot easily be desorbed. The adsorption and desorption characteristics of cesium from these minerals will aid efforts to estimate the concentration of radioactive cesium in river water.

(Kenso Fujiwara)

References

- Tachi, Y., Fujiwara, K. et al., Key Factors Controlling Radiocesium Sorption and Fixation in River Sediments around the Fukushima Daiichi Nuclear Power Plant. Part 1: Insights from Sediment Properties and Radiocesium Distributions, Science of The Total Environment, vol.724, 2020, 138098, 11p.
Tachi, Y., Fujiwara, K. et al., Key Factors Controlling Radiocesium Sorption and Fixation in River Sediments around the Fukushima Daiichi Nuclear Power Plant. Part 2: Sorption and Fixation Behaviors and Their Relationship to Sediment Properties, Science of The Total Environment, vol.724, 2020, 138097, 10p.

1-14 Remobilization of Radiocesium from Sediments

— Mass Balance of Dissolved ^{137}Cs in an Artificial Reservoir in Fukushima —

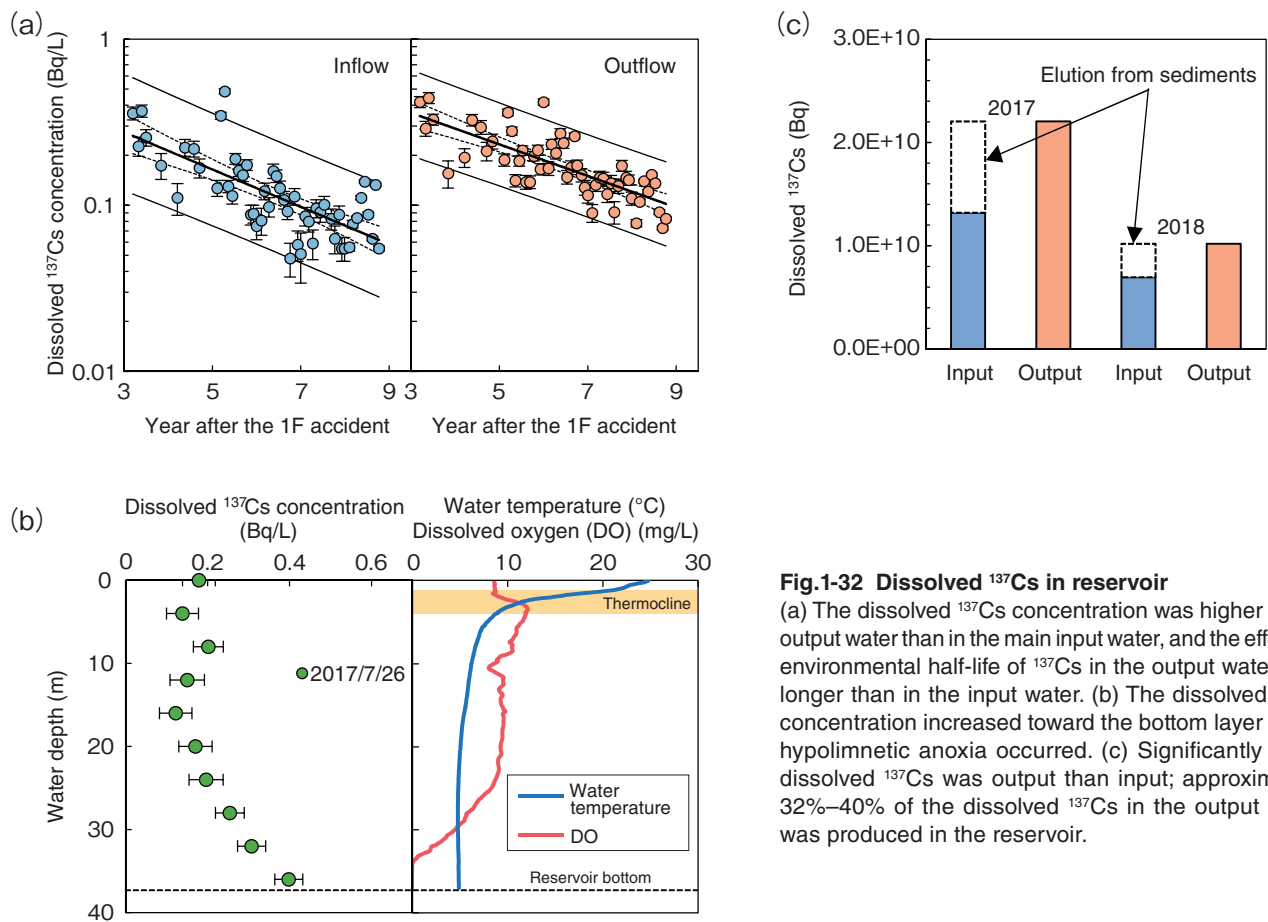


Fig.1-32 Dissolved ^{137}Cs in reservoir

(a) The dissolved ^{137}Cs concentration was higher in the output water than in the main input water, and the effective environmental half-life of ^{137}Cs in the output water was longer than in the input water. (b) The dissolved ^{137}Cs concentration increased toward the bottom layer when hypolimnetic anoxia occurred. (c) Significantly more dissolved ^{137}Cs was output than input; approximately 32%–40% of the dissolved ^{137}Cs in the output water was produced in the reservoir.

The origins and dynamics of dissolved radionuclides with high mobility and bioavailability in freshwater systems must be clarified to assess their transfer from water to crops and aquatic organisms. To quantitatively evaluate the long-term temporal changes and detail the mass balance of dissolved ^{137}Cs in the Ogaki Dam Reservoir, which has a catchment with a high ^{137}Cs inventory due to the accident at TEPCO's Fukushima Daiichi NPS (1F), we investigated ^{137}Cs concentrations using time series of water input and output samples.

Our results showed that the dissolved ^{137}Cs concentration was significantly higher in the output water than in the main input water, as shown in Fig.1-32(a). Additionally, the effective environmental half-life of ^{137}Cs was longer in the output water (3.6 y) than in the input water (2.9 y). Thus, the concentration of dissolved ^{137}Cs was influenced by the supply from the river input and production within the reservoir (e.g., elution from sediments). The vertical temperature profile showed a stratification with a clear thermocline; hypolimnetic anoxia occurred below a depth of 33 m, as shown in Fig.1-32(b). The dissolved ^{137}Cs concentration was relatively constant under oxic conditions but increased with depth under anoxic conditions.

These results support the assertion that the ^{137}Cs concentration gradients in the reservoir water column were caused by the release of ^{137}Cs from sediment to the overlying water. This mobilization of ^{137}Cs from the sediment likely results from the ion-exchange displacement of ^{137}Cs from sediments by cations (e.g., NH_4^+) released during the anaerobic decomposition of organic matter. We also performed a mass balance of dissolved ^{137}Cs in the reservoir to elucidate the contribution of dissolved ^{137}Cs from the river and reservoir sediments to ^{137}Cs in the reservoir output. The annual output of dissolved ^{137}Cs was significantly higher than the total dissolved ^{137}Cs input; approximately 32%–40% of the dissolved ^{137}Cs output was not input by the river and, thus, likely produced from sediments, as summarized in Fig.1-32(c).

Our results regarding the long-term dynamics and mass balance of dissolved ^{137}Cs in the reservoir provide important quantitative information for evaluating the catchment's environmental recovery rate and the presence of reservoir sediments containing high ^{137}Cs levels.

(Hironori Funaki)

Reference

Funaki, H. et al., Reservoir Sediments as a Long-Term Source of Dissolved Radiocaesium in Water System; a Mass Balance Case Study of an Artificial Reservoir in Fukushima, Japan, *Science of The Total Environment*, vol.743, 2020, 140668, 9p.

1-15 Rapid Analysis of ^{90}Sr in Small Bone Samples

— Applicability of Sr Resin for ICP-MS of ^{90}Sr in Hard Tissues —

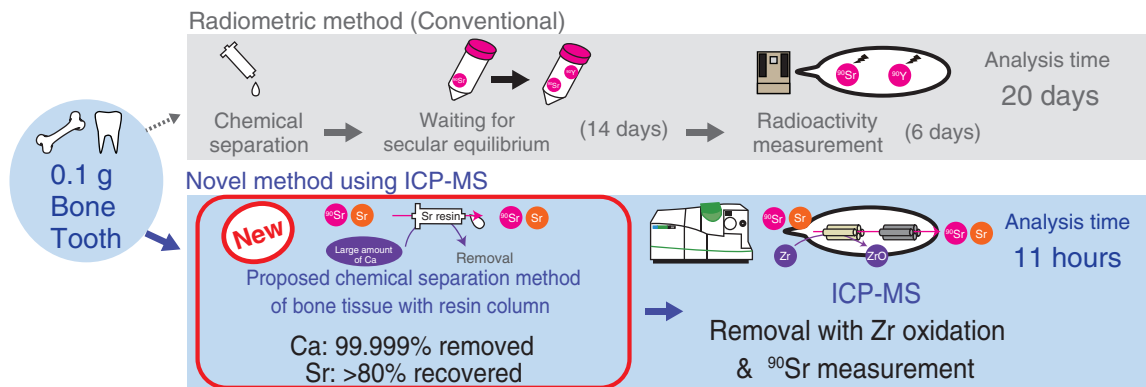


Fig.1-33 Conventional radiometric method and proposed ICP-MS method to determine ^{90}Sr concentration in bone and tooth samples

The developed chemical separation method removes interfering substances, such as Ca, in bones by repeated column separation. Rapid analysis of the ^{90}Sr concentration of bone and tooth samples was achieved by ICP-MS coupled with the developed separation techniques.

Table 1-1 Measured ^{90}Sr concentration in 0.1 g of cattle bone and tooth using the proposed ICP-MS and radiometric methods

Comparable radioactivity concentrations of ^{90}Sr in 0.1 g of hard tissues were found using the proposed and conventional radiometric methods. Further, the proposed method using ICP-MS had a lower detection limit than did the radiometric method.

Sample	Cattle bone		Cattle tooth	
	ICP-MS	Radiometric	ICP-MS	Radiometric
^{90}Sr concentration \pm SD (Bq/kg)	700 \pm 250	750 \pm 65	210 \pm 94	240 \pm 24
Limit of detection (Bq/kg)	36	91	36	87

SD: Standard deviation of ^{90}Sr concentration

Strontium-90 (^{90}Sr) is a typical fission product, has a half-life of 28.8 y, and has bone-seeking properties. The radioactivity concentration of ^{90}Sr in hard tissues of mammals (e.g., bones, teeth) is positively correlated with that of plants or soils obtained from the fields where the mammals have grown. Thus, the ^{90}Sr concentration in hard tissues can be used to clarify the ^{90}Sr distribution in the local environment. However, the conventional ^{90}Sr analysis method (i.e., the radiometric method) needs samples of at least 1 g and thus cannot be used to determine ^{90}Sr in small bone, tooth, or fish otolith samples.

Recently, a ^{90}Sr analysis method in soil and plants using inductively coupled plasma mass spectrometry (ICP-MS) has been developed that has a comparable detection limit. Although this method can be used to analyze small samples with low Ca content, such as soils and plants, the high concentration of Ca and isobar (e.g., zirconium-90; ^{90}Zr) in hard tissues interferes with ^{90}Sr measurements. To measure the radioactivity concentration of ^{90}Sr in hard tissues using ICP-MS, therefore, we investigated using a resin column to remove these interfering elements.

After acid digestion of 0.1-g samples of bones and teeth, the interfering elements were removed by chemical separation using a Sr resin to selectively uptake Sr into crown ether sites. ICP-MS was then performed on the solution eluted from the resin to determine the ^{90}Sr concentration. The recovery

rate of Sr was calculated using the degree of the decrease in 11 μg of stable strontium-88 (^{88}Sr) in the 0.1 g samples before and after separation.

By performing column separation twice, our developed method recovered more than 80% of the Sr and removed 99.999% of the Ca. Furthermore, the proposed method provided results more rapidly than the conventional radiometric method (11 hours versus 20 days, respectively). Thus, coupling ICP-MS and our proposed separation technique allowed for the rapid analysis of ^{90}Sr in cattle bone and tooth samples, as shown in Fig.1-33. The activity concentrations determined by ICP-MS after separation were in good agreement with those by the conventional radiometric method, as shown in Table 1-1. Further, the ^{90}Sr detection limit using ICP-MS of 0.1 g samples was lower than that of the radioactivity measurement. Therefore, coupling the proposed separation technique with ICP-MS can be used to quantify the ^{90}Sr concentration in small bone and tooth samples of terrestrial animals, thereby allowing researchers to track the distribution of ^{90}Sr in animal habitats.

This work was performed in collaboration with Tohoku University as part of a project entitled, “Investigation of Sr incorporation recorded in teeth of animals related to environmental transfer”.

(Kazuma Koarai)

Reference

Koarai, K. et al., Rapid Analysis of ^{90}Sr in Cattle Bone and Tooth Samples by Inductively Coupled Plasma Mass Spectrometry, Journal of Analytical Atomic Spectrometry, vol.36, issue 8, 2021, p.1678–1682.

1-16 Speciation of Cs in Tree Tissues

— Elucidation of the Mobility of Cs inside Trees Using Synchrotron Radiation —

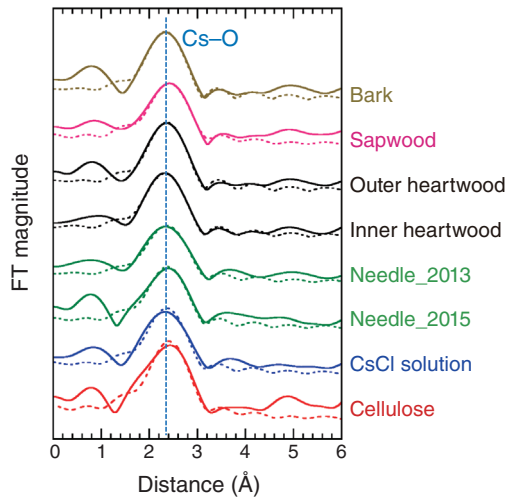


Fig.1-34 Analytical results of EXAFS spectra for *C. japonica*
EXAFS oscillations were extracted from spectra; the Fourier transform (FT) was then performed to obtain the radial structural functions. The solid and dotted lines indicate measured and fitted data, respectively. 1 Å is equivalent to 0.1 nm (i.e., 10^{-10} m).

Large amounts of radiocesium emitted by the accident at TEPCO's Fukushima Daiichi NPS (1F) were deposited across a wide land surface, including most of Fukushima Prefecture. Researchers have aimed to understand the behavior of 1F-derived radiocesium in forest systems because approximately 70% of Fukushima Prefecture is occupied by forests. It has been suggested that mobile 1F-derived radiocesium is translocated inside tree bodies over time. However, the chemical speciation of Cs in trees has not been well documented.

Therefore, we applied extended X-ray absorption fine structure (EXAFS) spectroscopy to speciate Cs in tree samples. Bark, sapwood, heartwood, and needle samples were collected from four tree species in Fukushima: *Cryptomeria japonica* (*C. japonica*), *Pinus densiflora* (*P. densiflora*), *Quercus serrata* (*Q. serrata*), and *Eleutherococcus sciadophylloides* (*E. sciadophylloides*). *C. japonica* and *P. densiflora* are representative evergreen conifers, whereas *Q. serrata* and *E. sciadophylloides* are broad-leaved deciduous trees. Each sample was ground into a powder and then mixed with an aqueous $^{133}\text{CsCl}$ solution. The EXAFS spectra of the Cs-adsorbed samples were then obtained at a synchrotron facility.

The obtained Cs L_{III} -edge EXAFS spectra of Cs-adsorbed samples of *C. japonica* are shown in Fig.1-34. Similar spectra were obtained for the hydrated Cs^+ ion (i.e., the aqueous CsCl

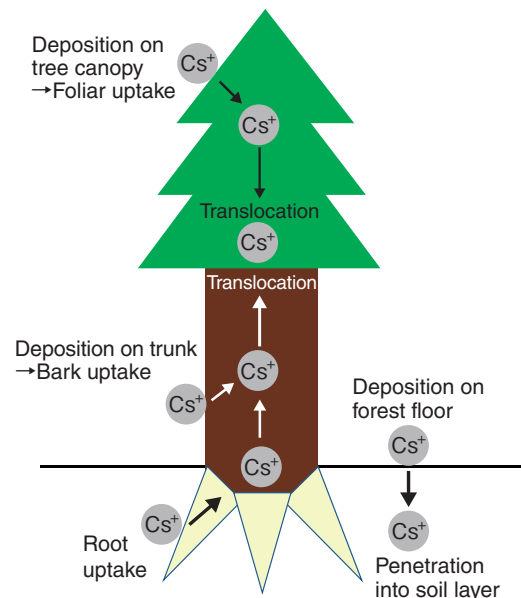


Fig.1-35 Uptake and translocation of Cs inside tree body
Radiocesium is absorbed into a tree body through foliar and bark uptake and then translocated inside the tree body in a mobile form. Root uptake can be an important route in the long-term radiocesium cycle.

solution) and each tree sample. The Cs-adsorbed tree and cellulose samples showed only the Cs–O shell, suggesting that hydrated Cs^+ ions were electrostatically bound to negatively charged functional groups, such as carboxyl and phenolic hydroxyl groups, in components of tree tissues. Cs adsorption due to this so-called outer-sphere complex could decrease in the presence of competing cations. Considering the competing cations (e.g., K^+ , Ca^{2+}) in sap and stemflow, Cs is not expected to strongly fix to tree tissues. The results of EXAFS analysis support the consensus among researchers that radiocesium is translocated inside tree bodies in a mobile form, as summarized in Fig.1-35.

Similar results were found for *P. densiflora*, *Q. serrata*, and *E. sciadophylloides*. It is assumed that the distribution of radiocesium is governed mainly by chemical and physiological properties. Overall, our work helped clarify the speciation of Cs in tree tissues. Further studies regarding the behavior of radiocesium in individual tree species and the resulting plant physiology would improve our understanding of the long-term radiocesium cycle in forest systems.

This work was supported by the Japan Society for the Promotion of Science (JSPS) KAKENHI Grant-in-Aid for Challenging Exploratory Research (No.JP15K12206).

(Kazuya Tanaka)

Reference

Tanaka, K. et al., Speciation of Cesium in Tree Tissues and Its Implication for Uptake and Translocation of Radiocesium in Tree Bodies, Science of The Total Environment, vol.755, part 2, 2021, 142598, 8p.

1-17 Where Does the Radiation Determining Air Dose Rates in Forests Originate?

— Simulations Reveal the Connection between the Movement of Radioactive Cesium and Air Dose Rate Trends —

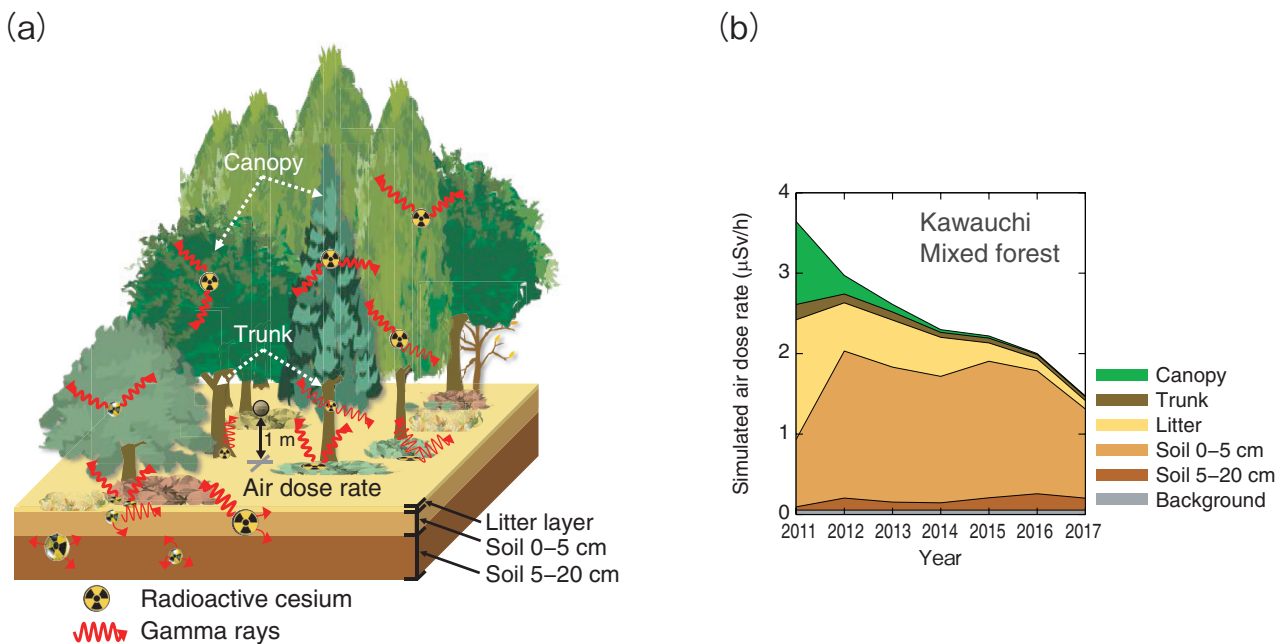


Fig.1-36 Modeling the contributions of radiation originating in different locations in forests to air dose rates

(a) Schematic showing how radioactive cesium (^{134}Cs and ^{137}Cs) exists in different parts of forests (in trees, the litter layer, and soil layers). The gamma rays emitted from ^{134}Cs and ^{137}Cs in the different locations in forests all make separate contributions to the air dose rate. (b) Simulation results showing a breakdown of the contributions to the air dose rate in a mixed forest in Kawauchi, Fukushima Prefecture, for 2011 to 2017. The trend of the total air dose rate is a consequence of the physical decay of ^{134}Cs and ^{137}Cs and the movement of these radioisotopes between different parts of the forest.

Around 70% of the atmospheric fallout in Japan from the 2011 TEPCO's Fukushima Daiichi NPS landed on forests. Forestry workers and residents living near forests are interested in air dose rate trends inside forests. The physical decay of radioactive cesium (^{134}Cs and ^{137}Cs), the radiation attenuation properties of forest matter, and the movement of ^{134}Cs and ^{137}Cs internally between different locations within forests need to be considered to explain the air dose rate trends (Fig.1-36(a)).

It is not clear a priori where the main radiation determining air dose rates in forests originates from because this cannot be measured easily. JAEA collaborated with the Forestry and Forest Products Research Institute and the University of Tsukuba to create simulation models that can explain air dose rate trends in forests. The models used particle and heavy Ion transport code system (PHITS) to simulate the gamma rays emitted by radioactive cesium and their interactions with matter to calculate air dose rates. By simulating the gamma rays originating in different locations in forests in turn, it was possible to calculate their separate contributions to the air dose rate. The models were initialized using measurements of densities, dimensions, and ^{134}Cs and ^{137}Cs radioactivity concentrations of forest matter sampled in eastern Japan between 2011 and 2017.

The results showed that the radioactive cesium making the main contribution to the elevated air dose rate in all forests was located either in the litter layer, the top 5 cm of forest soil, or the forest canopy.

Radioactive cesium within the forest canopy was a significant contributor to air dose rates in 2011 and 2012 in forests containing mainly evergreen trees (e.g., the mixed forest in Kawauchi, Fukushima Prefecture, Fig.1-36(b)), due to interception of the radioactive fallout in March 2011 by the canopy. By 2017, radioactive cesium located in the top 5 cm of forest soil was the main contributor to elevated air dose rates at this site and others, due to the breakdown of previous years' litter layers.

In the future, the created models will be used to make predictions for how different forest management options will affect air dose rates. The goal of this research will be to find effective and practicable proposals for reducing air dose rates in forests.

This research was conducted as part of a collaboration with the Forestry and Forest Products Research Institute and the University of Tsukuba.

(Minsik Kim)

Reference

Malins, A., Kim, M. et al., Calculations for Ambient Dose Equivalent Rates in Nine Forests in Eastern Japan from ^{134}Cs and ^{137}Cs Radioactivity Measurements, *Journal of Environmental Radioactivity*, vol.226, 2021, 106456, 12p.

1-18 Understanding the Cesium Adsorption Behavior in Concrete

— Accurate Simulation of Cement Hydrate Using Machine Learning Molecular Dynamics —

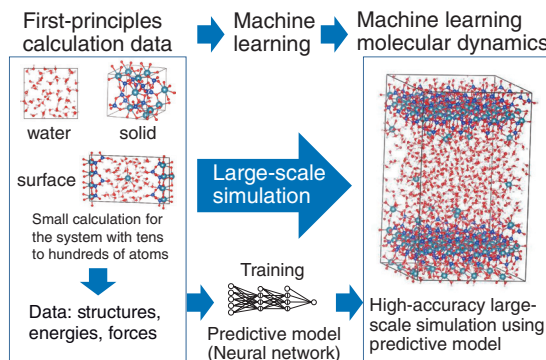


Fig.1-37 Schematic representation of machine learning molecular dynamics

By performing a large number of FP calculations for various structures (solid, water, surface, etc.) with small system size, the FP data set (about 70000 structures) is created, and a predictive model reproducing the energy and forces of the FP data is constructed using machine learning. Molecular dynamics based on this predictive model enables us to conduct a high accuracy large-scale simulation.

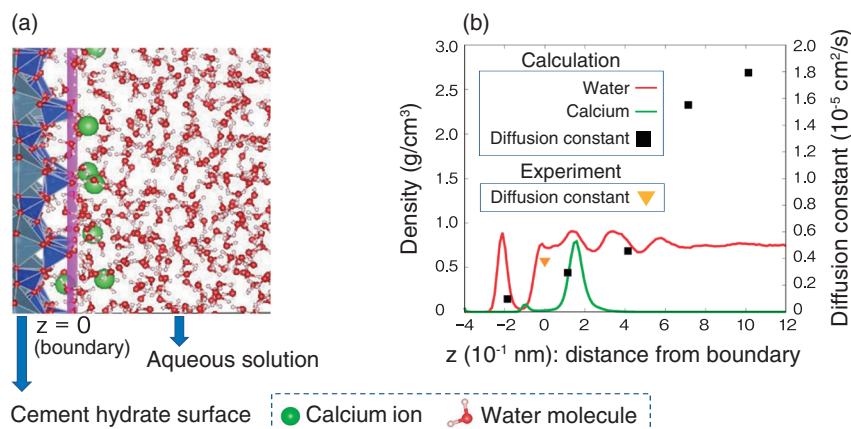


Fig.1-38 Distribution and transport properties of water and ions at the water-surface interface of cement hydrate
 (a) Structure of CH surface and water interface obtained by MLMD. The boundary between the CH surface and aqueous solution is set at $z=0$. (b) Computed density distribution of water and calcium ions near the interface, and the diffusion constants of water. It can be found that the diffusion constants of water become significantly lower than that of bulk water, and the ions are localized near the CH surface.

At TEPCO's Fukushima Daiichi NPS, due to damage to the reactor pressure vessel, a huge amount of radioactive cesium has been adsorbed into the concrete of the reactor containment vessel. For the disposal and volume reduction of large amounts of contaminated concrete obtained by decommissioning the nuclear power plants, understanding the adsorption behavior of cesium in concrete becomes important.

It is known that cesium ions are strongly adsorbed into cement hydrate (CH) in concrete, a very porous substance. Cesium ions are presumed to diffuse with water in the porous CH and adsorb onto the surface of CH. Atomic simulation is an essential tool to obtain detailed information about the form and intensity of cesium adsorption on CH. However, large-scale simulation taking into account the chemical reaction and water transport in the pores of CH is required, which is difficult to achieve with high accuracy first principles (FP) calculations due to its high computational effort.

In this study, we used machine learning molecular dynamics (MLMD) to overcome the computational cost of FP calculation. In this method, using a large amount of FP calculation data for various CH structures with tens to hundreds of atoms, a predictive model (machine learning force field: MLFF)

reproducing the results of the FP calculation is created using a machine learning technique (see Fig.1-37). Molecular dynamics simulation using MLFF is called MLMD, which enables us to conduct simulation with almost FP accuracy and much lower computational effort than an FP calculation.

As a first step toward elucidating the adsorption behavior of cesium on CH, we constructed the MLFF for the basic constituent elements of CH: silicon, calcium, hydrogen, and oxygen atoms. Using the constructed MLFF, we conducted a large-scale MLMD simulation for the CH-water interface, including thousands of atoms, to investigate the transport and adsorption properties of water and calcium ions. Our simulation successfully reproduced the experimental values of the diffusion constant of water near the CH surface as shown in Fig.1-38.

In the past, accurate simulations using FP calculations have been difficult for complex systems such as CH. We have shown that MLMD enables us to perform the simulation of CH with almost FP accuracy. Future work will aim to extend the MLFF of cesium to clarify the adsorption behavior of radioactive cesium in concrete.

(Keita Kobayashi)

Reference

Kobayashi, K. et al., Machine Learning Potentials for Tobermorite Minerals, Computational Materials Science, vol.188, 2021, 110173, 14p.

Implementing Continuous Improvements in Safety and Emergency Preparedness

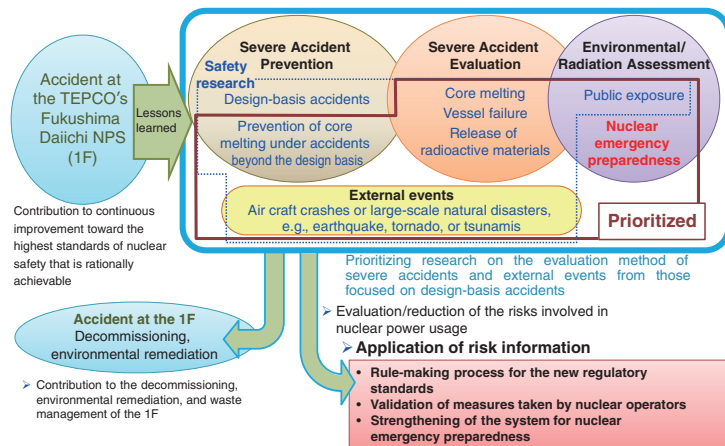


Fig.2-1 Directions of activities at the Sector of Nuclear Safety Research and Emergency Preparedness

In accordance with the lessons learned from the accident at 1F, we have promoted studies on the prevention and evaluation of severe accidents, assessments of external events and environmental-impact, and nuclear emergency preparedness.

The Sector of Nuclear Safety Research and Emergency Preparedness aims to perform advanced safety research from a long-term viewpoint to provide a technical basis for nuclear safety assessments through calculations, experiments, and measurement techniques, as well as technical support for nuclear regulatory administration. These efforts contribute to the development of safety criteria and/or guidance, and can support efforts to update safety regulations for continuous improvement of safety.

Prior to the accident at the TEPCO's Fukushima Daiichi NPS (1F), research efforts were focused on design basis events to assess the safety of a nuclear reactor; after the 1F accident occurred and was carefully reviewed, the research efforts were modified in accordance with the lessons learned from the accident, as shown in Fig.2-1. Various research activities to reduce the risks associated with operating nuclear facilities and their uncertainties have been expanded and prioritized, such as prevention and mitigation during the progression of severe accidents, external event assessment, preparation for and in response to emergency situations, and environmental impact assessments and waste management strategies related to the 1F accident.

This research is featured by large-scale facilities where various accident conditions can be simulated. For example, the high-pressure thermal-hydraulic loop (HIDRA) shown in Fig.2-2 has been constructed and used to develop sophisticated techniques to evaluate core heat transfer. The Nuclear Safety Research Reactor, shown in Fig.2-3, has been used to investigate the fuel failure limit and the effect of fuel failure on the nuclear reactor during a reactivity-initiated accident, which is a design-basis event. Several studies regarding material degradation, the structural integrity of components important for safety, and ultra-trace analysis of nuclear materials for

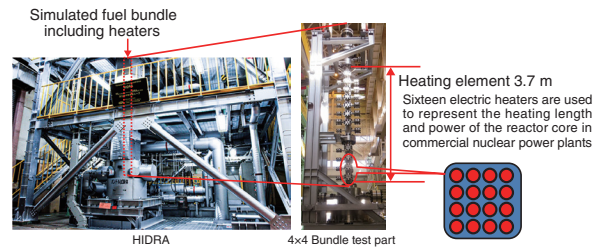


Fig.2-2 High-pressure thermal-hydraulic loop (HIDRA)
Experiments performed using HIDRA help clarify reactor core cooling performance under severe thermal and hydraulic conditions beyond the design basis.

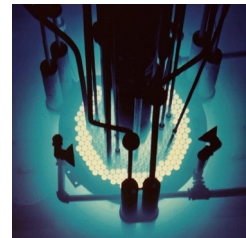


Fig.2-3 Nuclear Safety Research Reactor (NSRR)
The NSRR allows experiments simulating a rapid power increase during a reactivity-initiated accident and under high-temperature conditions beyond the design basis to be safely performed.

nuclear safeguards, among others, have also been performed. Further, we have acted as the operating agent in the OECD/NEA project "Analysis of Information from Reactor Buildings and Containment Vessels of Fukushima Daiichi NPS (ARC-F)".

To investigate emergency preparedness, the effectiveness of shelters' radiation protection countermeasures has been evaluated, as has the performance level required for nuclear emergency response materials/equipment. Moreover, techniques to integrate data obtained by different monitoring methods and investigate radioactivity distributions in coastal regions around 1F are under development. Domestic nuclear power plants are now monitored for background radioactivity in preparation for nuclear emergencies.

This chapter presents the results of the following recent research activities: the development of a portable thyroid dose monitoring system for emergency situations (Topic 2-1), the influence of monitoring post contamination on its response (Topic 2-2), a simulation of projectile impact on a reactor building (Topic 2-3), the suppression of volatile ruthenium release from high-level liquid waste under severe accident conditions at reprocessing plants (Topic 2-4), the prediction of reactor pressure vessel embrittlement via machine learning (Topic 2-5), the advanced modeling of radionuclide migration in the geosphere (Topic 2-6), the determination of the uranium purification period for nuclear safeguards (Topic 2-7), and the developed training programs of emergency response robots (Topic 2-8).

Two other topics related to 1F-accident, the design optimization for criticality experiments on simulated fuel debris (Topic 1-4) and the decreasing trend of air dose rates in Fukushima prefecture after the 1F accident (Topic 1-12), were also detailed in Chapter 1.

2-1 Reliable Thyroid Dose Measurement after a Severe Nuclear Accident — Developing a Portable Thyroid Dose Monitor —

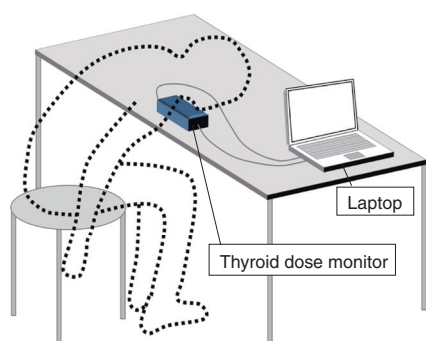
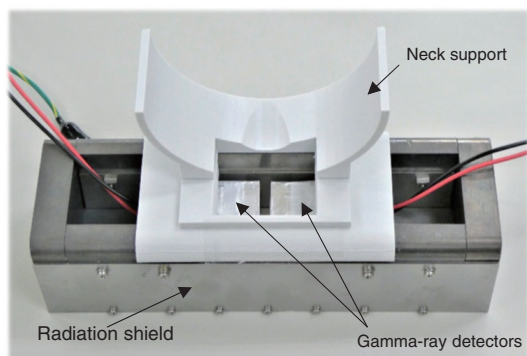


Fig.2-5 Subject's position during measurement
The subjects put their throat on the thyroid monitor.

After a severe nuclear accident, the radioiodine monitoring in thyroids should be carried out for residents and emergency workers in the radiologically affected area. In-vivo measurement methods using thyroid dose monitors have typically been employed to determine the radioiodine activity in the thyroid. Individual monitoring should be conducted as early as possible after exposure to assess the equivalent dose to the thyroid; for example, the ^{131}I remaining activity in a human's thyroid decreases according to its short half-life of 8.02 days. However, most thyroid monitors currently used in medical facilities are large and heavy and thus not easily transportable to evacuation centers, where many people can be measured immediately following an accident. After the accident at TEPCO's Fukushima Daiichi nuclear NPS, NaI(Tl) scintillation survey meters, which are widely employed to measure the ambient dose equivalent rate, were used to screen the ^{131}I exposure in children's thyroids. Under high dose rate background conditions, however, this method cannot always provide reliable data.

We therefore developed a desktop-type thyroid dose monitor that can be easily installed in evacuation centers and works well under high background dose rates. The monitor comprises two gamma-ray spectrometers embedded into a box-shaped radiation shield made of lead and tungsten heavy alloy, as shown in Fig.2-4. The radiation shield effectively reduces the background radiation from the environment and the rest of the body; thus, the gamma-rays originating from the subject's

Fig.2-4 Developed thyroid dose monitor

Two gamma-ray spectrometers are underneath the box-shaped radiation shield. Gamma rays originating from the subject's thyroid are selectively detected while background radiation is reduced. This desktop-type monitor can be installed easily in evacuation centers.

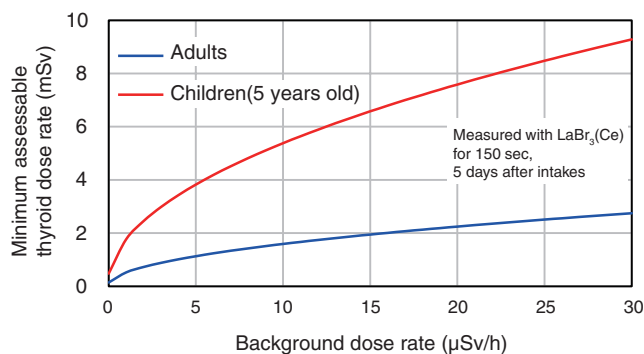


Fig.2-6 Minimum assessable thyroid equivalent dose

The monitor can accurately measure the thyroid dose even under high background doses. Children have a higher minimum detection limit owing to their higher dose conversion factor under the same ^{131}I activity.

thyroid can be selectively detected. Depending on the expected measurement situation, two kinds of gamma-ray spectrometers can be used: CdZnTe detectors for a high-energy resolution model or LaBr₃(Ce) detectors for a high-efficiency model. As subjects are measured in the posture illustrated in Fig.2-5, the required table and chair could be easily prepared at an evacuation center.

A prototype of the proposed thyroid dose monitor was validated in the photon reference field established at the Facility of Radiation Standards at the JAEA. The resulting minimum assessable thyroid equivalent dose under varying background dose rates produced by a ^{137}Cs source is shown in Fig.2-6. These results confirmed that for both children and adults, even under high background dose conditions, the monitor can assess thyroid equivalent doses of <10 mSv, which is sufficiently lower than the level at which health effects study is required. Further, calibration and background correction procedures were established to ensure accurate measurements.

After commercialization, the developed monitors will be deployed to nuclear facilities and off-site centers in prefectures where such facilities are located. Such monitors may also be useful in the field of nuclear medicine, such as in radioiodine therapy.

This work was supported by the Nuclear Regulation Authority (NRA) of Japan under Radiation Safety Research Promotion Fund (No.JPJ007057).

(Sho Nishino)

Reference

Nishino, S. et al., Prototype Test of a Portable Thyroid Dose Monitoring System Using Gamma-Ray Spectrometers, Radiation Measurements, vol.134, 2020, 106292, 5p.

2-2 Can Contaminated Monitoring Posts Measure Accurately in a Nuclear Accident?

— Influence of Contamination on Measured Dose Rates at Monitoring Posts —

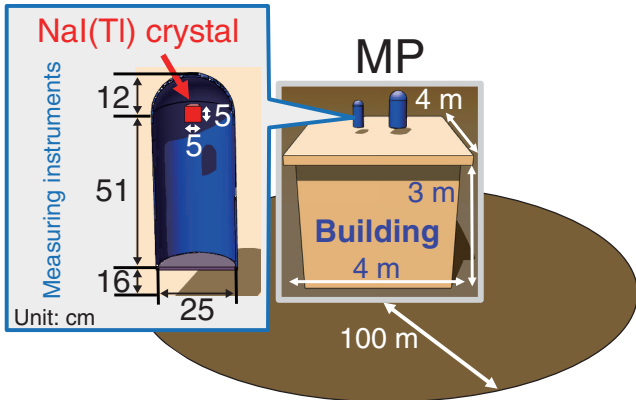


Fig.2-7 Geometry simulated by the particle and heavy ion transport code system (PHITS)

A full-scale monitoring post (MP; containing instruments with a NaI(Tl) crystal) and concrete building were simulated on the ground with a radius of 100 m. All empty spaces were filled with air.

If a nuclear accident occurred and radioactive material was released, protective measures, such as evacuations, will be taken for inhabitants based on the ambient dose rate of the surrounding environment, which is measured using measuring instruments on monitoring posts (MPs). However, if an MP was as contaminated as the surrounding environment, the measured dose rate may be higher than that of the surrounding environment owing to the contamination near the instruments. Inaccurately high readings may lead to excessively protective measures, such as an unnecessary evacuation with many evacuees, leading to a difficult situation for decision makers. To avoid such a situation, the influences of MP contamination on the measured dose rate were estimated.

The Particle and Heavy Ion Transport code System (PHITS) was used to estimate the influence. Under the assumption that the building and ground surface of the MP are contaminated, a simple simulation geometry was first modeled, as shown in Fig.2-7. The contamination of the surface of measuring instruments was assumed negligible owing to their small surface area and material (reinforced plastic), which is less likely to be contaminated. A full-size MP comprising a concrete building and measuring instruments was modeled. The measuring instrument has a NaI(Tl) scintillation detector; radiation is detected by the cylindrical crystal of the detector. The ground surface was assumed to be soil with a radius of 100 m considering the mean free path of γ -rays in air. In the PHITS calculation, the

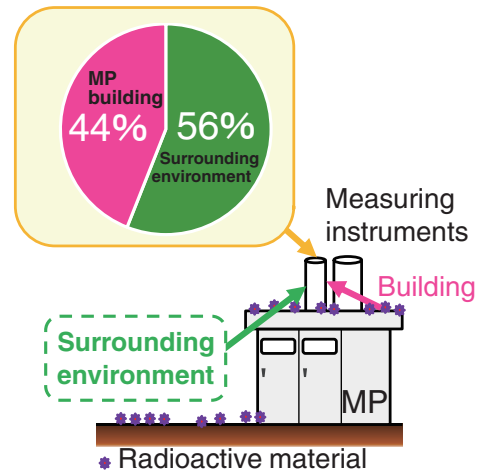


Fig.2-8 Influence of MP contamination on the measured dose

The PHITS calculations show that the dose rate from a contaminated MP accounts for about 44% of the measured value when the roof and ground surface of the MP are uniformly contaminated under the geometry shown in Fig.2-7.

surface of the building and ground of the MP was assumed to be uniformly contaminated with the same surface density. Using the PHITS, the amount of γ -ray radiation generated by ^{134}Cs , ^{137}Cs , and ^{131}I and the associated radiation energy detected by the NaI(Tl) crystal and the dose rate were estimated given the radionuclide ratios from the accident at TEPCO's Fukushima Daiichi NPS. The influence of radiation from the ground surface was classified as influence from the surrounding environment, and radiation influence from the MP roof was classified as influence from the MP building.

The simulation results under these conditions demonstrated that 44% of the measured radiation was caused by contamination of the MP; only 56% was from the surrounding environment (Fig.2-8), thus suggesting that the dose rate measured by MPs can be an overestimation. However, the simple MP geometry assumed in this simulation may have caused the overestimation, i.e., accounting for the actual, more-complex geometry and instrument contamination would decrease the contamination ratio of the MP and reduce the overestimation.

Future work will therefore include clarifying the estimation of the dose rate, which can then be used to calibrate MPs and update future nuclear accident response procedures.

This study was conducted using the supercomputer SGI ICE X at the JAEA.

(Hirokazu Hiraoka)

Reference

Hiraoka, H. et al., Influence of Artificial Radionuclide Deposited on a Monitoring Post on Measured Value of Ambient Dose Rate, Proceedings of 27th International Conference on Nuclear Engineering (ICONE-27), Tsukuba, Japan, 2019, 5p.

2-3 Prediction of Structural Damage from Projectile Impacts

— Numerical Evaluation of Penetration Damage under Realistic Conditions —

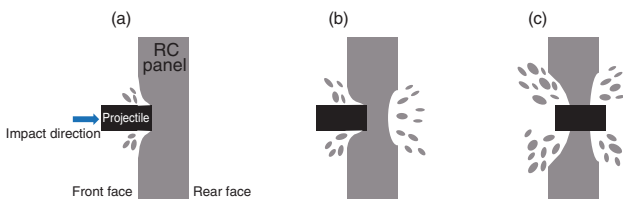


Fig.2-9 Local damage mode of RC panel
The local damage to the reinforced concrete (RC) panel includes (a) penetration, (b) scabbing, and (c) perforation.

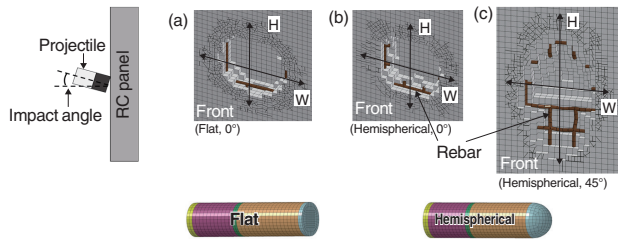


Fig.2-10 Numerical results for penetration damage to RC panel for cases (a) 1, (b) 2, and (c) 4
Under normal impact (i.e., 0°), the damage area on the front face of the RC panel damaged by the (b) hemispherical projectile was slightly smaller than that produced by the (a) flat projectile. (c) Oblique impact conditions (i.e., 45°) led to a greater maximum penetration depth and width.

As stipulated by the Nuclear Regulation Authority of Japan, nuclear facilities must be evaluated for their ability to withstand projectile impacts induced by tornadoes or aircraft. These evaluations must comprise the resulting local damage to the area of collision (Fig.2-9), the overall response of nuclear facility buildings, and the influence of vibrations propagating along the wall or floor on any internal equipment. As part of this ongoing effort, the work summarized here focused on evaluating the local damage to a building’s outer wall made of reinforced concrete (RC) under various impact conditions.

Local damage to an RC plate-shaped structure, or RC panel, can be categorized as penetration, scabbing, or perforation. Various empirical formulas depending on the damage mode have been developed to evaluate the local damage suffered by RC panels subjected to normal impact by rigid projectiles, i.e., projectiles impacting at an angle of 0° and assumed to not undergo any deformation during impact. However, this assumption is not valid for many possible projectiles; an evaluation method taking into account realistic impact conditions relevant to projectiles capable of deforming and absorbing energy at the time of collision, such as airplanes, was thus developed.

First, the finite element method was used to simulate the local damage of an RC panel representing the outer wall of a nuclear facility building, where a flat projectile that is regarded as a scaled engine model was used to impact the RC panel at a normal angle. The proposed numerical method was validated with experimental results. This validated

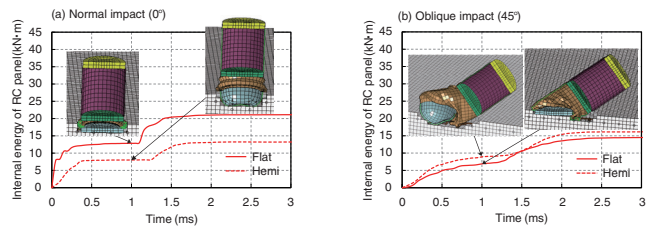


Fig.2-11 Time history of internal energy of RC panel
Varying the shape and impact angle of a projectile changed the local damage to the RC panel. Under normal impact, a hemispherical projectile caused less damage than did a flat projectile; this difference was not present under oblique impact.

Table 2-1 Calculated height (H), width (W), and penetration depth (D) of damage in each case, in mm

Case No.	Impact conditions	Damage dimension* (H × W × D)
Case 1	Flat, 0°	140 × 129 × 50
Case 2	Hemispherical, 0°	130 × 120 × 50
Case 3	Flat, 45°	240 × 140 × 50
Case 4	Hemispherical, 45°	240 × 130 × 70

*including crack distribution

model was then used to examine the penetration damage under various impact conditions, including different nose shapes (i.e., flat or hemispherical) and impact angles (i.e., normal, 0°, or oblique, 45°), as detailed in Table 2-1. The results, summarized in Table 2-1 and Fig.2-10, show that under oblique impact, the damage area of the RC panel tends to be longer and broader. However, different nose shapes did not significantly vary the damage dimensions.

Because damage had occurred inside the RC panel as well, the internal energy was analyzed. Under normal impact, the internal energy of the RC panel after impact with a hemispherical projectile was 40% lower than after impact with a flat projectile. The buckling of the hemispherical nose may have led to a part of the impact energy being absorbed, thus reducing the internal energy of the RC panel. Under oblique impact, the internal energy of the RC panel was similar using either nose shape. After impact with the flat projectile, the internal energy of the RC panel under oblique impact was about 30% lower than that under normal impact, whereas the impact angle of the hemispherical projectile had only a minor effect on the internal energy of the RC panel (Fig.2-11).

These results provide a technical background for evaluating local damage to RC panels subjected to projectile impact under realistic conditions. Future efforts will include expanding the model to analyze the overall response of the building and evaluate the effects of impact vibrations on internal equipment.

(Zuoyi Kang)

Reference

Kang, Z. et al., Impact Simulations on Local Damage of Reinforced Concrete Panel Influenced by Projectile Nose Shape, Mechanical Engineering Journal, vol.7, issue 3, 2020, 19-00566, 20p.

2-4 Accident Simulation: HLLW Evaporation to Dryness

— Evaluating the Restraint Effect on the Release of Volatile Ruthenium —

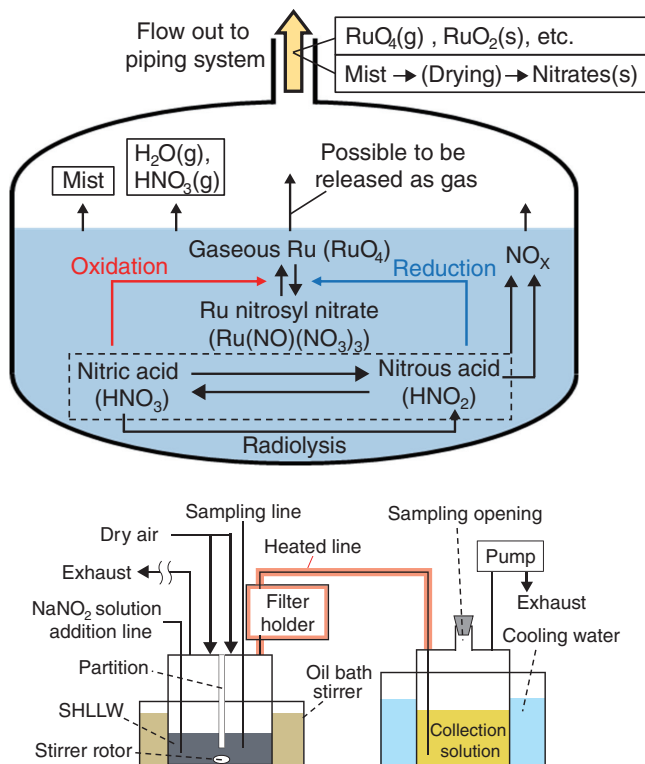


Fig.2-13 Experiment device for boiling SHLLW and collecting RuO₄
 The simulated HLLW (SHLLW) was heated to keep a constant release rate of vapor and maintained at a temperature of approximately 103 °C. Generated gases were carried to the collection solution by the input dry air ventilation. The filter on the heated line catches mist, thus allowing only gaseous compounds to be passed to the collection solution. By adding sodium nitrite (NaNO₂) solution in the SHLLW, NO_x are generated and they cause additional mist. The partition minimized the effect of releasing mist caused by adding NaNO₂ solution.

High-level liquid waste (HLLW) containing radioactive elements is temporarily stored in reprocessing plants, where uranium and plutonium are extracted from the spent nuclear fuels and the HLLW must be cooled continuously to remove decay heat. If the cooling functions are lost and countermeasures do not work sufficiently, the temperature of the HLLW may increase above the boiling point, the water will evaporate and the HLLW will dry up. This evaporation to dryness due to the loss of cooling functions has been defined as a severe accident (i.e., beyond the design basis) of the reprocessing plant; sufficient countermeasures to suppress the release of radioactive materials must be developed.

Since ruthenium (Ru) forms volatile compounds, such as ruthenium tetroxide (RuO₄), more Ru would be released from the HLLW to out of the reprocessing plant than other elements in such an accident because RuO₄ cannot be trapped in filters. Therefore, properly assessing the safety of a reprocessing plant requires an understanding of the release behavior of Ru.

RuO₄ is generated by the oxidation of ruthenium nitrosyl nitrate by nitric acid in the HLLW. On the other hand, RuO₄ can be reduced by nitrous acid, which is generated by the radiolysis

Fig.2-12 HLLW tank during an evaporation and dryness accident

The flow of gases and mists from high-level liquid waste (HLLW) is summarized here. During this type of accident, water vapor (H₂O(g)), nitric acid vapor (HNO₃(g)), NO_x, HLLW mist, and volatile compounds comprising mainly RuO₄ could be released.

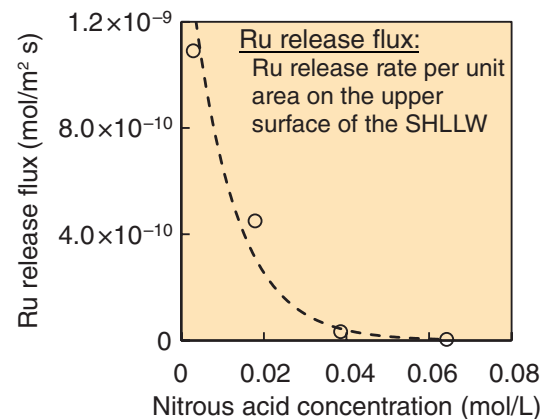


Fig.2-14 Relationship between nitrous acid concentration and Ru release flux

The circles show experimental data and the dotted line shows exponential fitting line. The Ru release flux decreased exponentially as the concentration of nitrous acid in the SHLLW increased.

of nitric acid in the HLLW, thereby reducing the release of RuO₄ (Fig.2-12).

To clarify the relationship between the nitrous acid concentration and the amount of RuO₄ released from boiling HLLW, simulated HLLW (SHLLW) prepared with non-radioactive compounds was heated under fixed conditions; the experimental design is summarized in Fig.2-13. For the nitrous acid concentration in the SHLLW keeping constant, sodium nitrite solution was continuously added. The amount of RuO₄ released from the boiling SHLLW was trapped in the collection solution and measured.

As shown in Fig.2-14, increasing the nitrous acid concentration caused less RuO₄ to be released. More specifically, increasing the nitrous acid concentration led to an exponential decrease in the Ru release flux. This result contributes to the quantitative analysis of released radioactive isotopes during reprocessing plant accidents.

This work was supported by the Nuclear Regulation Authority (NRA), Japan.

(Ryoichiro Yoshida)

Reference

Yoshida, R. et al., Restraint Effect of Coexisting Nitrite Ion in Simulated High Level Liquid Waste on Releasing Volatile Ruthenium under Boiling Condition, Journal of Nuclear Science and Technology, vol.58, issue 2, 2021, p.145–150.

2-5 A Nonparametric Bayesian Method for Predicting the Embrittlement of Reactor Pressure Vessels — Toward Further Reliability of Integrity Assessment in Long-Term Operation —

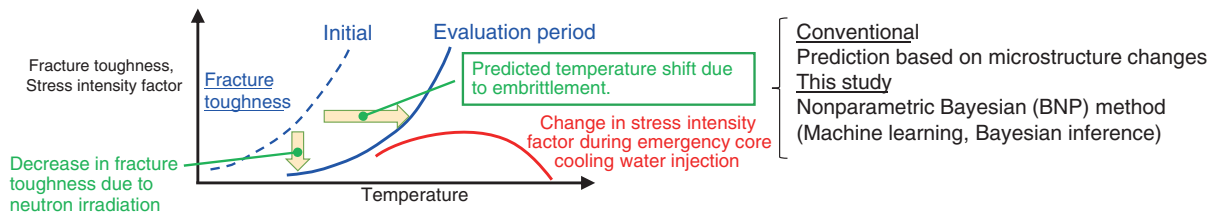


Fig.2-15 Overview of the structural integrity assessment of a reactor pressure vessel (RPV)

Neutron irradiation embrittlement of the steel used in RPVs increase with operating time in light-water reactors. Based on the predicted transition temperature shift (i.e., embrittlement), the fracture toughness should exceed the stress intensity factor caused by the rapid cooling of coolant water.

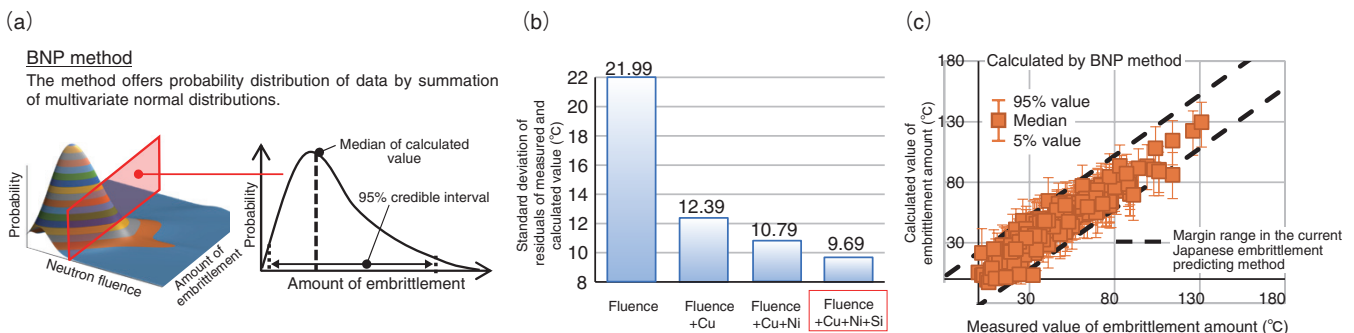


Fig.2-16 Analyses by nonparametric Bayesian (BNP) method

(a) Schematic of the obtained probability distribution. Here, the probability distribution of embrittlement under varying neutron fluence is provided as an example; the corresponding probability distribution of the embrittlement with other variables can be obtained by specifying the arbitrary values for the other factors. (b) The lower standard deviation of the residuals of the calculated and measured values corresponds to better predictability; thus, the accuracy of embrittlement prediction was improved. (c) Using the proposed method confirmed the accuracy of the embrittlement prediction margin established by the current Japanese code.

As the reactor pressure vessel (RPV) is the most important safety-related structural component, its failure should be prevented during operation. As shown in the structural integrity assessment of RPV in Fig.2-15, the fracture toughness of the steel comprising the RPV must exceed the stress intensity factor in the event of rapid cooling caused by the operation of the emergency core cooling system. Neutron irradiation decreases the fracture toughness, which is expressed by a shift in the reference temperature of the nil-ductility transition (ΔRT_{NDT}). It is therefore essential to accurately predict ΔRT_{NDT} during long-term operation. ΔRT_{NDT} is highly dependent on the irradiation conditions and chemical composition of the steel used in the RPV; however, the factors affecting ΔRT_{NDT} need to be understood more precisely to improve the accuracy of ΔRT_{NDT} prediction. It is also important to ensure that the embrittlement prediction margin in the current structural integrity assessment is set appropriately.

Machine learning and Bayesian statistics (i.e., the nonparametric Bayesian (BNP) method) were therefore applied to analyze the factors affecting ΔRT_{NDT} and to evaluate the uncertainties of ΔRT_{NDT} prediction under various irradiation conditions and chemical compositions. Using the BNP method provides the probability distribution of the data by summing the multivariate

normal distribution and can quantitatively evaluate the uncertainties of the calculated ΔRT_{NDT} in response to a limited amount of data or scattered data, as shown in Fig.2-16(a).

The developed method was then used to analyze data from pressurized water reactors collected over several decades. Our analysis revealed that the prediction accuracy could be improved by considering the Si content in addition to the Cu and Ni content, which have been documented to significantly affect the ΔRT_{NDT} (Fig.2-16(b)). Furthermore, as shown in Fig.2-16(c), the values including uncertainties obtained by the proposed BNP method were mostly within the currently established margins, thereby confirming the appropriateness of the current Japanese embrittlement prediction method.

Efforts to apply this developed BNP uncertainty evaluation method to the probabilistic structural integrity assessment method are ongoing to quantitatively evaluate the safety margin in the structural integrity assessment that is under development for implementation in Japan.

This work was performed under the contract research entrusted from the Regulatory Standard and Research Department, Secretariat of Nuclear Regulation Authority (NRA), Japan.

(Hisashi Takamizawa)

Reference

Takamizawa, H. et al., Bayesian Analysis of Japanese Pressurized Water Reactor Surveillance Data for Irradiation Embrittlement Prediction, Journal of Pressure Vessel Technology, vol.143, issue 5, 2021, 051502, 8p.

2-6 Migration of Radionuclides from Radioactive Wastes of Reactor Core Structures in Underground Environments

— Modeling Niobium Sorption onto Clay Minerals in the Presence of Calcium —

- Nb sorption was described by complexation of aqueous species and surface hydroxyl groups (surf_OH) of clay minerals.
- Only Nb-OH complexes were considered by Ervanne et al.
- ➔ Our model deals with Ca-Nb-OH complexes.

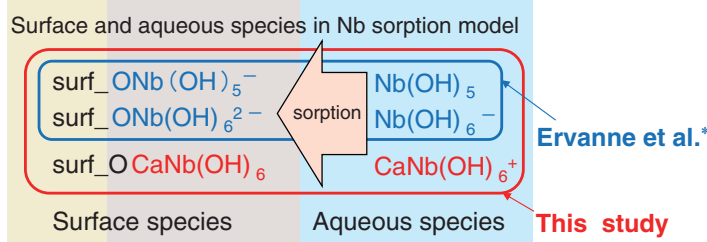


Fig.2-17 Conceptual drawing of Nb sorption model

The proposed sorption model includes the aqueous species (CaNb(OH)₆⁺), which was confirmed to form in the solubility experiments in addition to aqueous Nb(OH)₅, aqueous Nb(OH)₆⁻, and surface_OCaNb(OH)₆ (surf_OCaNb(OH)₆).

Radioactive waste from activated reactor core internals is classified as relatively higher radioactive waste, which is a category of low-level waste. As these wastes contain long-lived radionuclides and must be kept away from the biosphere long-term, it is planned to be disposed of underground in Japan. Safety assessments of radioactive waste disposal must analyze the capacity of radionuclides leached from waste forms to migrate through the bedrock to the biosphere, where humans can be exposed to the waste. The migration of radionuclides is expected to be slowed by sorption onto rock-forming minerals. This process is affected by coexisting ions in groundwater, the compositions which may change according to the long-term disposal environment. Therefore, a reliable model must be developed to estimate the sorption properties of radionuclides onto rock-forming minerals.

Niobium-94 (⁹⁴Nb) is a long-lived radionuclide (half-life: 20300 y) contained in the wastes of reactor core internals and important in the safety assessment of waste disposal because of its contribution to radiation doses. However, few researchers have examined the sorption of Nb onto minerals. Ervanne et al.* examined the effect of sodium (Na) and calcium (Ca) on Nb sorption onto illite, which is a type of rock-forming clay mineral with a high specific surface area (i.e., high sorption capacity). In the presence of Na, the experimental sorption data were reproduced by their proposed model, which assumed aqueous and surface species of Nb hydroxide complexes (Nb_x(OH)_y^{5x-y}). However, their model did not agree with the data obtained in the presence of Ca.

Therefore, we developed a Nb sorption model to resolve

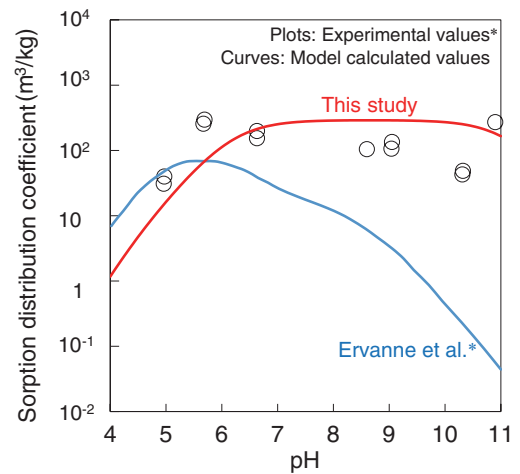


Fig.2-18 Model results for Nb sorption onto illite in 0.1 M Ca(ClO₄)₂ solution

The proposed model can explain the tendency of the experimental data provided by Ervanne et al.* in the presence of Ca. The sorption distribution coefficient is the ratio of the concentration of Nb adsorbed on the solid phase to that in solution; the higher the value, the higher the sorption property.

this divergence by assuming the existence of Nb complexes with OH⁻ and Ca²⁺ (Ca-Nb-OH complex), which had not been considered before. In order to confirm the formation of aqueous Ca-Nb-OH complexes, solubility experiments of Nb were performed under various Ca concentrations and pH. The experimental results showed that CaNb(OH)₆⁺ was formed as the dominant aqueous species, in addition to Nb(OH)₆⁻ and Nb(OH)₇²⁻. Additionally, Ca-Nb-OH complexes containing surface OH⁻ groups (surf_OH) were assumed to be formed and follow the sorption reaction: surf_O⁻ + CaNb(OH)₆⁺ = surf_OCaNb(OH)₆. In this reaction, we excluded H⁺ because no pH dependence was observed in the sorption data. Therefore, CaNb(OH)₆⁺ and surf_OCaNb(OH)₆ were added to each species in the developed model (Fig.2-17). The Nb sorption onto illite in a 0.1 M Ca(ClO₄)₂ solution was then calculated using the geochemical calculation code (PHREEQC) with thermodynamic CaNb(OH)₆⁺ data determined from the solubility experiments. The model results represented trends in the experimental data obtained by Ervanne et al.* that could not be explained by the previous model, as shown in Fig.2-18.

The results of this study will be used as a scientific basis for highly reliable evaluation of the sorption property of ⁹⁴Nb to rock in the future disposal of the wastes from reactor core internals.

(Saki Ohira)

* Ervanne, H. et al., Modelling of Niobium Sorption on Clay Minerals in Sodium and Calcium Perchlorate Solutions, Radiochimica Acta, vol.102, issue 9, 2014, p.839–847.

Reference

Yamaguchi, T., Ohira, S. et al., Consideration on Modeling of Nb Sorption onto Clay Minerals, Radiochimica Acta, vol.108, issue 11, 2020, p.873–877.

2-7 Detection of Undeclared Uranium Purification Activities

— $^{230}\text{Th}/^{234}\text{U}$ Radio-Chronometry with a Single Uranium Particle —

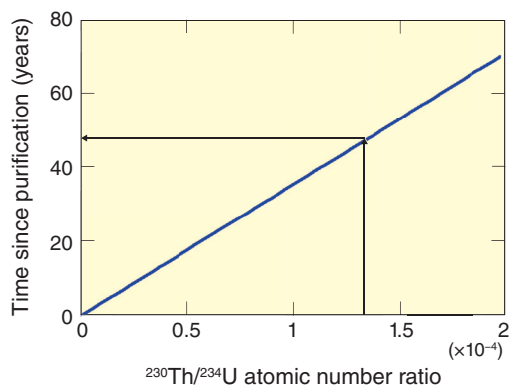


Fig.2-19 Relationship between the number of years since the purification period and the $^{230}\text{Th}/^{234}\text{U}$ atomic number ratio

Immediately after uranium is purified, ^{230}Th begins accumulating due to radioactive decay of ^{234}U . Therefore, the number of years elapsed from the date of purification can be clarified by analyzing the atomic number ratios of both nuclides.

The International Atomic Energy Agency (IAEA) conducts safeguards to ensure that nuclear materials, such as uranium, are only used for peaceful (*i.e.*, energy-related) purposes. One such activity comprises environmental sample analysis to detect undeclared nuclear activities by analyzing the composition and quantity of ultra-trace amounts of nuclear materials adhering to the special cloths that IAEA inspectors use to wipe down walls and other surfaces inside and outside nuclear facilities. The samples collected are analyzed by the IAEA Network Analytical Laboratories, of which JAEA is a part. The year of uranium purification can provide evidence of the existence of an undeclared nuclear development program; thus, researchers have aimed to develop analytical methods to estimate the year of uranium purification.

The uranium isotope ^{234}U undergoes radioactive decay to thorium-230 (^{230}Th) with a half-life of approximately 250000 years. As shown in Fig.2-19, the ratio of $^{230}\text{Th}/^{234}\text{U}$ atoms increases with time from purification; by analyzing this ratio, the time elapsed since uranium purification can be estimated.

However, the uranium particles captured on samples collected by IAEA inspectors are very small, weighing only nano-grams (10^{-9} g). In ordinary laboratories, accurate results cannot be obtained with such a small sample due to the influence of natural uranium in environmental dust. Therefore, a $^{230}\text{Th}/^{234}\text{U}$ atomic number ratio analysis technique using chemical separation was developed for use on a single uranium particle at the Clean Laboratory for Environmental Analysis and Research. The isotope dilution method was applied by adding a standard to

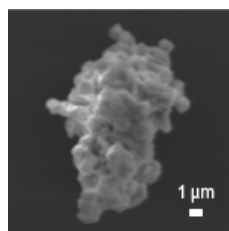


Fig.2-20 Scanning electron microscope image of a single uranium particle

By analyzing the $^{230}\text{Th}/^{234}\text{U}$ atomic number ratio of a single uranium particle (about $1/100$ mm in size), it is possible to estimate when uranium purification took place.

Table 2-2 Calculated time since purification using a single uranium particle

Despite the high uncertainty of the atomic number ratio, the number of years since purification was accurately estimated.

ID	size (μm)	$^{230}\text{Th}/^{234}\text{U}$ Atomic ratio ($\times 10^{-4}$)	Analytical results (years)	Difference between predicted and actual purification (years)
1	9	1.60 ± 0.37	57 ± 33	3.6
2	8	1.72 ± 0.43	60 ± 36	2.0
3	9	1.94 ± 0.75	68 ± 63	-6.2

the sample to obtain accurate atomic number ratios. A single standard with a known $^{229}\text{Th}/^{233}\text{U}$ atomic number ratio was prepared to ensure accurate values could be obtained without strictly controlling the amount added to the sample or the weight of the standard material. An image of a sample particle analyzed is shown in Fig.2-20. This particle was prepared from a reference material with a known date of purification. After the uranium particles were dissolved, standards were added, and chemical separation pretreatment was performed. The $^{230}\text{Th}/^{229}\text{Th}$ and $^{234}\text{U}/^{233}\text{U}$ ratios were then analyzed by inductively coupled plasma mass spectrometry (ICP-MS), and the $^{230}\text{Th}/^{234}\text{U}$ atomic number ratio was calculated to estimate the years since purification.

The obtained results are shown in Table 2-2. For particles with a diameter of 8 to 9 μm, the actual period of purification (61 years) was estimated with an error of between -6.2 and 3.6 years. Therefore, the proposed technique can accurately estimate the year of uranium purification from a single uranium particle, as required by the IAEA. Future efforts will include the use of ICP-MS equipped with high-sensitivity multiple detectors. The ultra-trace amounts of ^{230}Th in uranium particles in the range of femto-grams (10^{-15} g) can be then determined with more accurately to estimate the year of purification. By applying this technology to the analysis requested by the IAEA, we hope to contribute to international safety and cooperation.

A part of this study was conducted in FY2020, sponsored by the Nuclear Regulation Authority (NRA), Japan.

(Daisuke Suzuki)

Reference

Suzuki, D. et al., Age Determination Analysis of a Single Uranium Particle for Safeguards, Journal of Radioanalytical and Nuclear Chemistry, vol.328, issue 1, 2021, p.103-111.

2-8 Operating Robots Entering the Accident Site on Behalf of a Person — Training of Robot Operators for Nuclear Disaster Response —

Table 2-3 Remote control equipment in JAEA emergency support organization

In the event of an accident at a nuclear facility, such as the research reactor of Japan Atomic Energy Agency (JAEA) that cannot be accessed by workers due to contamination by radioactive materials, we have the following remote equipment and trained operators. We are also improving the functionality of these machines and replacing old ones.

Classification	Reconnaissance robot	Robot with arm	UAV
			
Feature	<ul style="list-style-type: none"> • Measurement instruments such as dose rate meters. 	<ul style="list-style-type: none"> • The payload of the 6-axis arm is 100 kg. • The gripping force of the hand at the end of the arm is 1960 N. 	<ul style="list-style-type: none"> • Programming flight



Fig.2-21 Non-visual operation training via a robot camera in intermediate level training

In the event of an accident, the robot must be accurately operated using only the camera images attached to it. However, the camera image is two-dimensional, making the distance difficult to grasp. Then, unlike visual operation, non-visual operation via a robot’s camera is much more difficult.

Japan Atomic Energy Agency (JAEA) has established an emergency support organization at Naraha Centre for Remote Control Technology Development (NARREC) in case of an accident at one of its nuclear facilities. The JAEA’s specific nuclear facilities are subject to emergency support. In case of an accident at these facilities that cannot be accessed by workers due to contamination by radioactive materials, the support organization has robots that can enter the accident site to survey and measure the internal situation, as well as unmanned aerial vehicles (UAVs) that can take pictures and make measurements from the air. In addition, since 2017, we have been continuously educating and training the operators for the remote control equipment at the accident site. The operators consist of the above-mentioned nuclear facilities, and they are trained to improve their operation skills using the training facilities in NARREC. This is known as operation training for remote control equipment operators.

There are three types of remote control equipment used in the training; reconnaissance: robots, robots with arms, and UAVs (Table 2-3). The reconnaissance robot is a small device that can take pictures of the accident site and measure radiation levels. The UAV flies over the accident site to check the exterior of the facility.

The operation training commences at the beginner level and progresses to the intermediate and advanced levels. Additional training is provided based on each trainee’s progress, and the program is designed to ensure that even trainees with no prior knowledge of remote control equipment can acquire operating skills within a certain period. The programs for the beginner

and intermediate levels of training are described below.

In the beginner training, after learning the relevant laws and regulations as well as the specifications of the robot as introductory education, the trainees learn the basic operation procedures on the actual robot for training. In the training of robots that run on the ground, such as reconnaissance robots and robots with arms, trainees will learn basic running by visual operation, overcoming obstacles, running in narrow areas, and grabbing objects with their arms.

In the intermediate level training, based on the basic knowledge and basic operation skills acquired in the beginner level training, the objective is to acquire applied operation skills more suited to the situation at the time of an accident. For reconnaissance robots and robots with arms, trainees learn to perform non-visual operations via the robot’s camera (Fig.2-21), and for UAVs, trainees learn to fly the designated points using a wireless drone. Since there are only a few opportunities for the trainees to conduct operation training once or twice a year, a review of the previous training session is conducted at the beginning of each training session to ensure that knowledge is retained.

As of April 2021, JAEA has a total of 24 trainees who have undergone the above-mentioned education and training, and to maintain their operational skills, regular operation training is conducted to prepare for any accidents that may occur. The training materials and facilities are also improved as needed to meet the on-site conditions of each facility.

(Yusuke Chiba)

Reference

Chiba, Y. et al., Training Programs of Emergency Response Robots Operation for Operators in Each Site of JAEA Beginner Class / Intermediate Class, JAEA-Technology 2019-002, 2019, 29p. (in Japanese).

Advanced Science Explores the Future

To discover new principles and phenomena, the Advanced Science Research Center is conducting frontier research related to atomic energy sciences. Toward the International COE by using the advantage of JAEA.

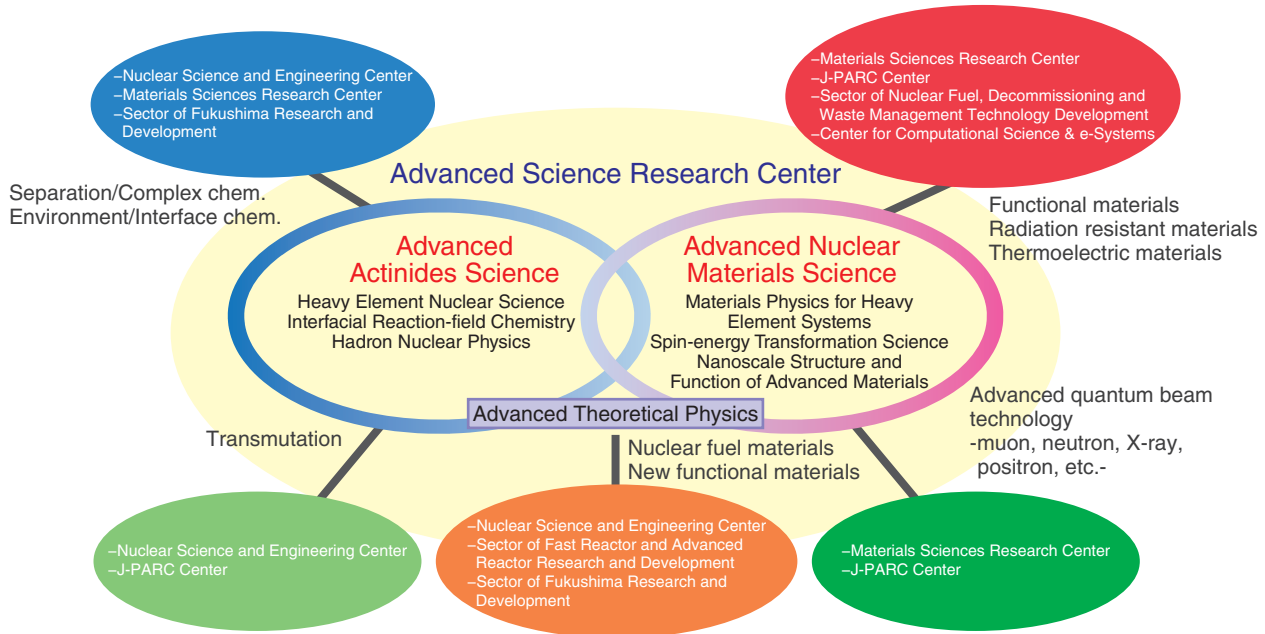


Fig.3-1 Role of advanced nuclear scientific research

We aim to perform high-impact scientific and technical studies related to state-of-the-art nuclear and material science.

Most nuclear-energy-related technology is based on basic science. Besides seeking solutions to today's energy problems, future research must respond to the new developments in the field that are expected in the next few decades.

The Advanced Science Research Center (ASRC) explores new possibilities of nuclear energy from the perspective of basic science. During this process, we aim to establish new research fields and further develop the existing science and technology.

Our mid-term plan began in FY2015 and has focused on two main areas: advanced actinides science and advanced nuclear materials science. In the former, we aim to conceptualize nuclear and heavy-element-based actinide science in a new way; in the latter, we are investigating and developing new materials for nuclear-energy purposes. In FY2019, a theoretical physics group was established to connect these aims to develop and enhance new research ideas across the various fields of sciences of the existing research areas. Through interactions between the two areas and collaboration with research institutes within and outside of the Japan Atomic Energy Agency, JAEA, we are cultivating new fields of nuclear-energy science (Fig.3-1).

Numerous achievements have been made throughout FY2020 and are thus highlighted in this chapter. Through our advanced actinides science, a new method to investigate as-yet-unknown fission reactions was developed (Topic 3-1). This achievement will help elucidate the fission mechanism and the nucleus structure. Additionally, our chemical research contributed to the determination of the chemical state of cesium inside trees, which

was detailed in Chapter 1 (Topic 1-16) and will help elucidate the migration behavior of cesium in the forest in Fukushima. Research into hadron nuclear physics allowed us to analyze the event in which a special nucleus, the Ξ hypernucleus, is produced (Topic 3-2). This analysis contributes to the understanding of the interior of neutron stars.

Substantial results have also been achieved in the field of advanced nuclear materials science. A prototype cooling device using $\text{KBaYb}(\text{BO}_3)_2$ was developed that can reach 0.04 K and is expected to replace conventional Helium-3 refrigerators (Topic 3-3). In spin-energy transformation science, we revealed that spin thermoelectric devices have a high tolerance to radiation and keep their performance for a few hundred years (Topic 3-4). The devices are expected to be used as nuclear batteries in spacecraft. In the nanomaterials research, terahertz-infrared absorption spectra of deuterated water clusters were measured (Topic 3-5), which will help provide an accurate evaluation of the greenhouse effect of water.

The mass and lifetime of the pentaquark P_c comprising five quarks were predicted as part of our theoretical physics research (Topic 3-6). Understanding the P_c structure is expected to lead to a better understanding of the exotic nature of hadrons.

The ASRC considers that developing human nuclear resources with expertise and demonstrating their total abilities via basic nuclear research is vital.

3-1 Nuclear Fission Unveiled via Multinucleon Transfer Reaction

— Opening Fission Research in Unexplored Region of the Chart of Nuclei —

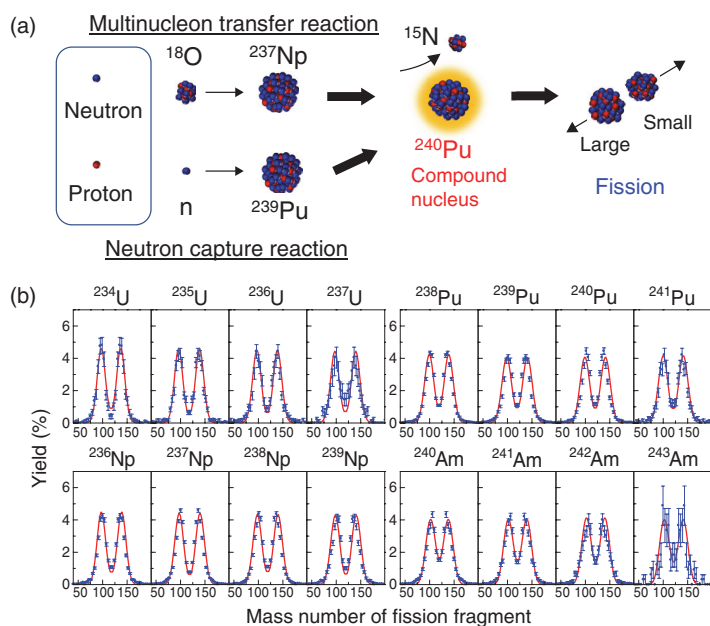


Fig.3-2 Multinucleon transfer reaction and fission-fragment mass distribution

(a) The compound nucleus ^{240}Pu can be produced using the multinucleon transfer reaction, $^{18}\text{O} + ^{237}\text{Np}$. (b) Fission-fragment mass distribution of several nuclei produced in the $^{18}\text{O} + ^{237}\text{Np}$ reaction. The solid curves show the model calculation.

Nuclear fission is a phenomenon observed in heavy nuclei and is widely used to generate electric power in power plants. In the scientific field, fission is expected to occur at the end of the rapid process of nucleosynthesis in stars, which would change the abundance of elements in nature. Better understanding the fission process will largely impact science and industry.

Neutron capture reactions, an example illustrated in Fig.3-2(a) for neutron capture by plutonium-239 (^{239}Pu) to form the compound nucleus ^{240}Pu , have mainly been used to study fission. However, this method is applicable only to limited nuclei, as the available target material are scarce in terms of purity and half-life enough to make a target sample. To overcome this restriction and expand the region of nuclei that can be studied, we developed a method based on multinucleon transfer reaction using a heavy-ion beam. This approach can generate fission data for many nuclei in one reaction, including neutron-rich nuclei that have not yet been investigated, such as those produced in stars.

The idea of this method is shown in Fig.3-2(a); for example a neptunium (^{237}Np) target is bombarded with an oxygen (^{18}O) beam to produce ^{240}Pu by exchanging neutrons and protons, and emitting nitrogen nucleus (^{15}N). The method was developed at the JAEA tandem accelerator facility in Tokai. The obtained

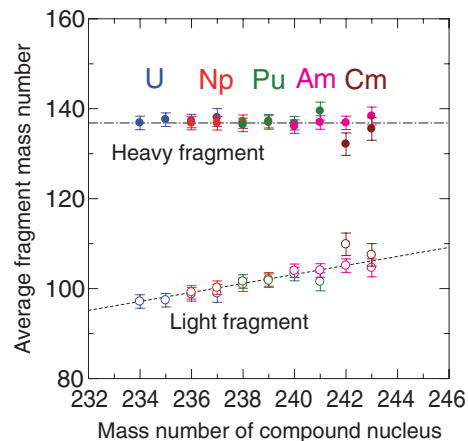


Fig.3-3 Average mass of heavy and light fragments

These values were obtained from the fission data shown in Fig.3-2. The heavy fragments have almost the same mass number, indicating that nuclear structure of the heavy nucleus regulates the fission process.

fission-fragment mass distribution of ^{240}Pu is shown in Fig.3-2(b). The data agreed well with those obtained by neutron-induced fission of ^{239}Pu , confirming that the proposed approach can provide a surrogate for neutron-induced reaction. In accordance with the different numbers of transferring neutrons and/or protons, fission data for many compound nuclei can be obtained in a single experiment. Among the obtained fission-fragment mass distributions, data for $^{236,239}\text{Np}$, $^{238,239}\text{Pu}$, and $^{240,241}\text{Am}$ cannot be obtained from neutron-capture reactions.

The average fragment-mass numbers of heavy and light fragments from this experiment are given in Fig.3-3. Interestingly, the heavy fragments have an average mass of 136–138, whereas that of light fragments increases with the mass of the compound nucleus. These results indicate that the nuclear structure of the heavy fragment has an essential role in fission and that fission proceeds so as to evolve an internal structure of heavy nucleus.

This work was supported by MEXT (Ministry of Education, Culture, Sports, Science and Technology, Japan) program, “Comprehensive study of delayed-neutron yields for accurate evaluation of kinetics of high burn-up reactor”.

(Katsuhisa Nishio)

Reference

Vermeulen, M. J., Nishio, K. et al., Measurement of Fission-Fragment Mass Distributions in the Multinucleon Transfer Channels of the $^{18}\text{O} + ^{237}\text{Np}$ Reaction, *Physical Review C*, vol.102, issue 5, 2020, 054610, 11p.

3-2 Determination of the Mass of a Ξ Hypernucleus

— New Information to Understand the Structure of Neutron Stars —

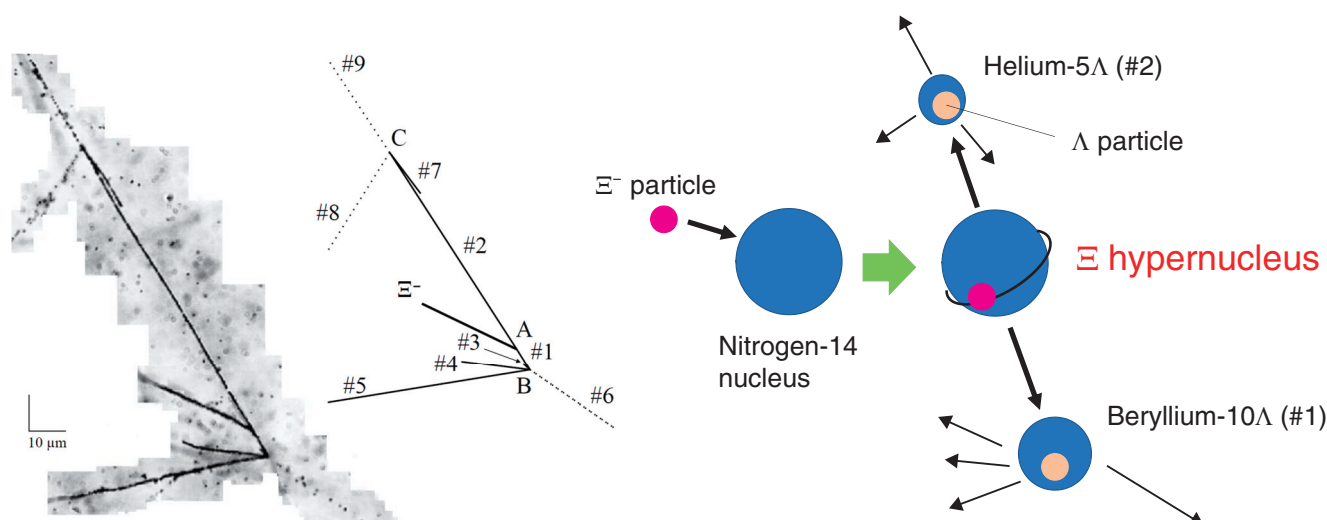


Fig.3-4 Picture (left) and schematic drawing (right) of the new Ξ hypernucleus event

A Ξ^- particle is captured by a nitrogen-14 nucleus at point A, forming a Ξ hypernucleus, which then decays into a beryllium-10 Λ hypernucleus (#1) and a helium-5 Λ hypernucleus (#2). The beryllium-10 Λ nucleus decays into several nuclei (#3–#6) and a few neutrons (not seen) at point B, whereas the helium-5 Λ nucleus decays into a helium-4 nucleus (#7), a pion (#8), and a proton (#9) at point C.

Although normal nuclei comprise protons and neutrons, special nuclei called hypernuclei containing baryons with strange quarks are known to exist; two such hypernuclei are Lambda (Λ) and Xi (Ξ) baryons. Λ hypernuclei, which contain one strange quark, have been extensively studied, whereas hypernuclei with a Ξ particle, which contains two strange quarks, have been rarely studied.

There are several motivations to study Ξ hypernuclei, one of which is neutron stars. Ξ is one of the particles that could appear in neutron stars, and whether or not it appears depends on the interaction with protons and neutrons. Therefore, it is important to determine the strength of the interaction using ground experiments; high-quality experimental data on Ξ hypernuclei have been long-awaited.

Therefore, we performed an experiment to produce Ξ^- (Ξ with a negative charge) particles in abundance using a high-intensity K beam at the J-PARC Hadron Experimental Facility. The produced Ξ^- particles were then injected into special picture films, called nuclear emulsions, to record Ξ hypernuclear events. After developing the films, we then used our optical microscope system to search for the Ξ hypernuclear events. We found an event during which a Ξ^- particle was absorbed by a nucleus in the emulsion film to form a Ξ hypernucleus, which then broke

up into two Λ hypernuclei (Fig.3-4). An extensive analysis demonstrated that the Ξ^- was absorbed by a nitrogen-14 nucleus, and the two Λ hypernuclei were beryllium-10 Λ and helium-5 Λ .

The binding energy of the Ξ^- particle was determined as 1.27 ± 0.21 MeV. Assuming only Coulomb interaction between the Ξ^- particle and the nitrogen-14 nucleus, the binding energy would be 0.39 MeV; the large difference is due to the strong interaction. Hence, these results allow the strength of this strong interaction to be estimated, thereby helping to clarify the interior workings of neutron stars, which can be considered astronomical-sized nuclei.

Only a part of the data obtained in the experiment has been analyzed; as we continue, we expect to discover more such interesting events. Additionally, we are developing a new analysis method that will enable us to find 10 times as many Ξ hypernuclei. By observing many Ξ hypernuclei events, we will obtain detailed information on the strong interactions involving Ξ particles to clarify how Ξ particle affects the properties of neutron stars.

This work was supported by the Japan Society for the Promotion of Science (JSPS) KAKENHI Grant-in-Aid for Scientific Research (S) (No.JP23224006).

(Kiyoshi Tanida)

Reference

Hayakawa, S. H., Tanida, K. et al., Observation of Coulomb-Assisted Nuclear Bound State of Ξ^- - ^{14}N System, Physical Review Letters, vol.126, issue 6, 2021, 062501, 6p.

3-3 Magnetic Cooling to Near Absolute Zero Temperatures

— Cooling to Extremely Low Temperature Realized by Quantum Fluctuations in "Ytterbium Magnet" —

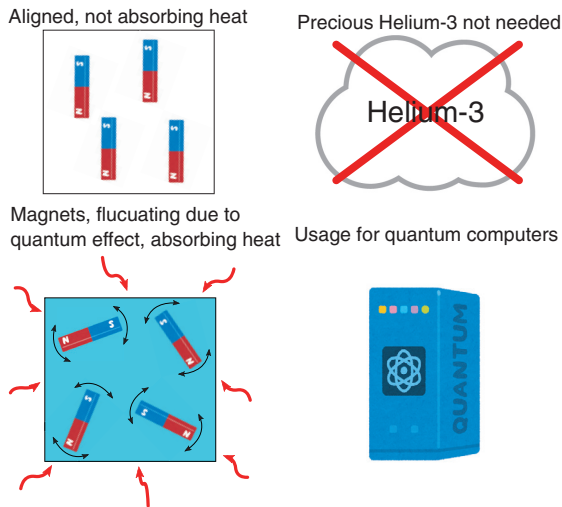


Fig.3-5 Features and utilization of magnetic cooling using quantum fluctuations

In normal magnetic materials, the magnetic moments (shown as magnets) align at low temperatures and do not absorb heat (top left). In a magnetic material with a strong quantum effect, the magnetic moments do not align as the temperature nears absolute zero due to quantum fluctuations, and heat can be absorbed without precious helium-3 (bottom left). Ultra-low temperature refrigeration is necessary for quantum computers.

Ultra-low temperature refrigeration is needed for fundamental research and in some applications, such as superconductivity and quantum computers; these needs have increased the demand for high-performance refrigerators.

Most ultra-low temperature refrigerators use helium-3 for cooling. However, after the 9/11 terrorist attacks in the United States, the demand for helium-3 used for nuclear material detectors increased sharply, causing a supply crisis. This shortage led to increased interest in magnetic cooling, summarized in Fig.3-5, which does not require helium-3.

In traditional magnetic cooling, heat is absorbed by the fluctuations of the magnetic moments, which are minute magnet in a magnetic material. At low temperatures, however, the magnetic moments align and can no longer absorb heat, thereby limiting the achievable temperature to critical temperature below which magnetic moments align.

The key to overcoming this limit is the quantum effect. In Newtonian classical mechanics, both atoms and magnetic moments should be completely stationary at absolute zero due to the disappearance of thermal fluctuations. Quantum mechanics, however, which describes microscopic phenomena more accurately, shows that atoms and magnetic moments continue to fluctuate even at absolute zero. These fluctuations are called quantum fluctuations. Most substances solidify at absolute zero as the thermal fluctuations disappear, but helium, for example, does not solidify and remains a liquid because of quantum fluctuations. Among magnetic materials, an effect called "magnetic frustration" suppresses the alignment of the magnetic moments; these "frustrated magnets" contain magnetic moments that maintain quantum fluctuations even at extremely

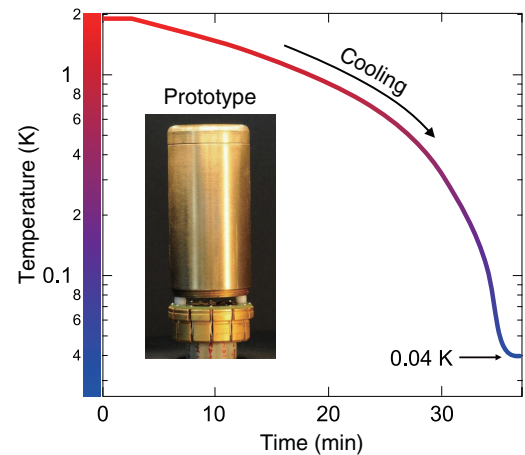


Fig.3-6 Actual cooling using the prototype device
Using the prototype shown in the inset photo, a temperature of 0.04 K was achieved.

low temperatures. Such magnetic materials may be cooled to ultra-low temperatures because of the manifestation of quantum effects.

A prototype cooling device containing $\text{KBaYb}(\text{BO}_3)_2$, which has a strong magnetic frustration, was thus developed. We then compared the cooling performance of the developed device with a commercially available magnetic cooling device that uses a conventional refrigerant; the results are summarized in Fig.3-6. The developed prototype reached 0.04 K, significantly closer to absolute zero than the commercial device, which reached 0.08 K.

In addition, conventional refrigerants contain many water molecules, which causes their deterioration, such as dehydration and deliquescent. As $\text{KBaYb}(\text{BO}_3)_2$ does not contain water molecules, it is stable in air.

State-of-the-art helium refrigerators can maintain their low temperature for a long time, although they require helium-3 and have extremely complicated structures. On the other hand, magnetic cooling devices have a much simpler structure and do not require helium. Therefore, its use at the international space station is considered for future. The major drawback was that continuous cooling was not possible, but recent research and development has eliminated this drawback. Magnetic cooling may replace helium-3 refrigerators in the future, and the proposed $\text{KBaYb}(\text{BO}_3)_2$ cooling device may be used widely for magnetic refrigeration.

This research was supported by the Japan Society for the Promotion of Science (JSPS) KAKENHI (No.JP20K22338, JP20KK0061).

(Yoshifumi Tokiwa)

Reference

Tokiwa, Y. et al., Frustrated Magnet for Adiabatic Demagnetization Cooling to Milli-Kelvin Temperatures, Communications Materials, vol.2, issue 1, 2021, 42, 6p.

3-4 For a Radio-Resistant Thermoelectric Generation System — Tolerance of Spin Thermoelectric Devices for Radiation —

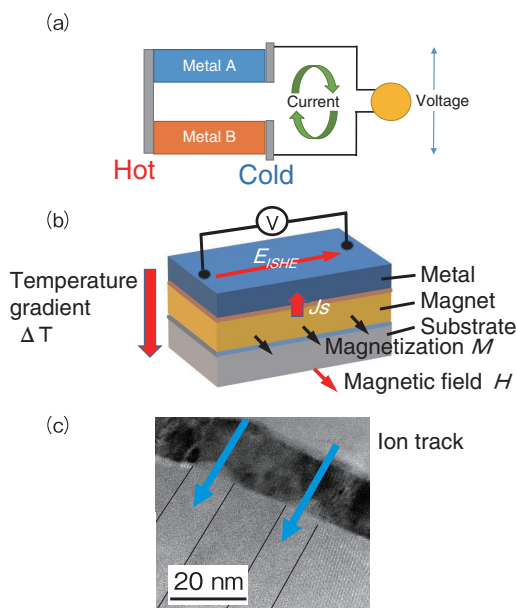


Fig.3-7 Conceptualization of (a) thermoelectricity and (b) a device based on the spin Seebeck effect (SSE), (c) photo of the proposed device irradiated with 320 MeV of Au ions

(a) A temperature gradient on a dissimilar metal junction induces a voltage; this is well known as the Seebeck effect.

(b) Due to its in-plane magnetization and perpendicular temperature gradient, a spin current J_s is injected into a metal layer. And the J_s is converted to the voltage E_{ISHE} in the metal layer.

Thermoelectric (TE) devices convert heat to electricity and are important for recycling and reusing waste heat in cars or factories. Nuclear batteries, which combine a TE device and a radioisotope, can be used as an electric sources for spacecraft in deep space. A TE device is similar to a thermocouple, which comprises a junction between two dissimilar metals or semiconductors. Applying a thermal gradient across this junction generates an electric voltage, causing a current to flow through the circuit, as shown in Fig.3-7(a). However, such junctions in classical TE devices are sensitive to radiation and must be shielded from the radioisotopes of the nuclear battery.

Spintronics refers to a developing subset of microfabrication techniques at the atomic level that considers the spin of electrons, one of the inherent magnetic properties of electrons. Recently, TE devices based on spintronics (i.e., spin TE devices) have been developed and demonstrated to provide excellent results. Furthermore, spin TE devices are expected to tolerate radiation well, although this has yet to be demonstrated experimentally. Embedding spin TE devices in nuclear batteries may lead to the development of a TE system resistant to radiation; however it is unclear how long the spin TE devices can work with radioisotopes. Therefore, we developed a spin TE device based on the spin Seebeck effect (SSE) and aimed to confirm its resistance to radioisotope. The proposed device has a metal/magnet bilayer structure deposited on a substrate. The interface between the layers is important to the ability of the TE to generate electricity

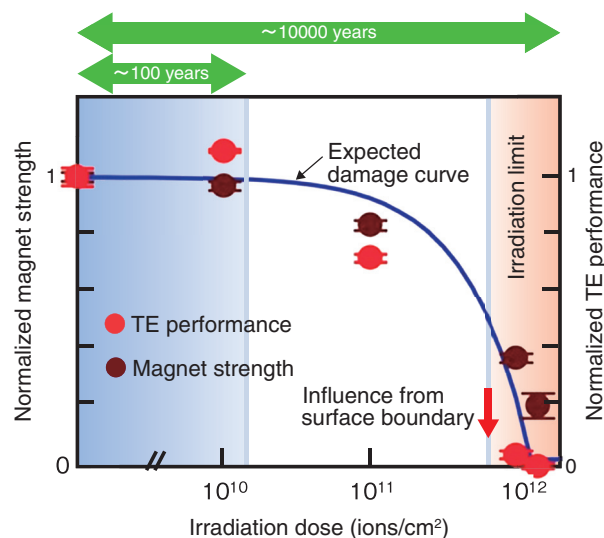


Fig.3-8 Performance of the proposed devices under ion irradiation

As the ion dose increased, the SSE voltage (●) of the device decreased to zero above a threshold. The electric performance of the device depends on the magnetic strength of the sample. The sudden drop near the threshold is caused by the boundary condition. Here, we evaluated the limit of the device near spent nuclear fuel.

(Fig.3-7(b)).

The fabricated sample devices were irradiated with swift heavy ions (320 MeV of Au ions) to ensure the existence of severe boundary conditions and simulate near spent nuclear fuel. The resulting ion tracks are shown by the blue arrows in Fig.3-7(c). Here, the zone within the black lines is a nano-scale amorphous defect caused by an ion. This region is no longer magnetized and thus cannot contribute to the electricity generation by the device. The measured magnet strength and electricity generated under varying irradiation doses are summarized in Fig.3-8. The measured device voltage (●) decreased as the irradiation dose increased, and diminished to zero after a dosage threshold. These results demonstrate clear usage limits of the proposed device under heavy ion irradiation and could be used to determine a cumulative upper limit of irradiation by fission fragments near spent fuel. In general, a dose rate of approximately 100 MeV of fragments emitted from the fuel surface can be estimated from the actual neutron dose on the fuel cask surface. Converting the experimental usage limit to the actual TE device running time using this fragment rate, we estimate that the proposed TE device based on the SSE can maintain its performance for a few hundred years.

This study was partially supported by the Japan Society for the Promotion of Science (JSPS) KAKENHI Grant-in-Aid for Scientific Research (C) (No.JP17K05126).

(Satoru Okayasu)

Reference

Okayasu, S. et al., Tolerance of Spin-Seebeck Thermoelectricity against Irradiation by Swift Heavy Ions, Journal of Applied Physics, vol.128, issue 8, 2020, 083902, 7p.

3-5 Elucidation of Low-Energy Vibrational Modes of Deuterated Water Clusters — Utilization of Terahertz-Infrared Absorption Spectroscopy and Ab Initio Calculation —

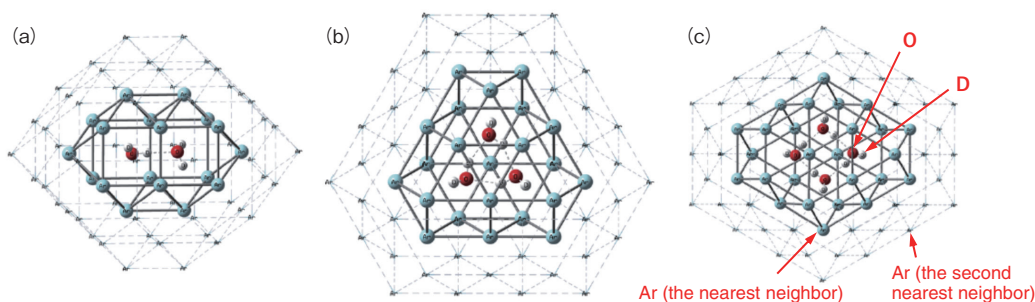


Fig.3-9 The most stable structures of deuterated water clusters trapped in solid Ar

By using ab initio calculation, we determined the most stable structures of the (a) dimer, (b) trimer, and (c) tetramer formed in solid Ar. The nearest-neighbor Ar atoms are connected with each other through solid lines, whereas the second-nearest-neighbor ones through dashed lines.

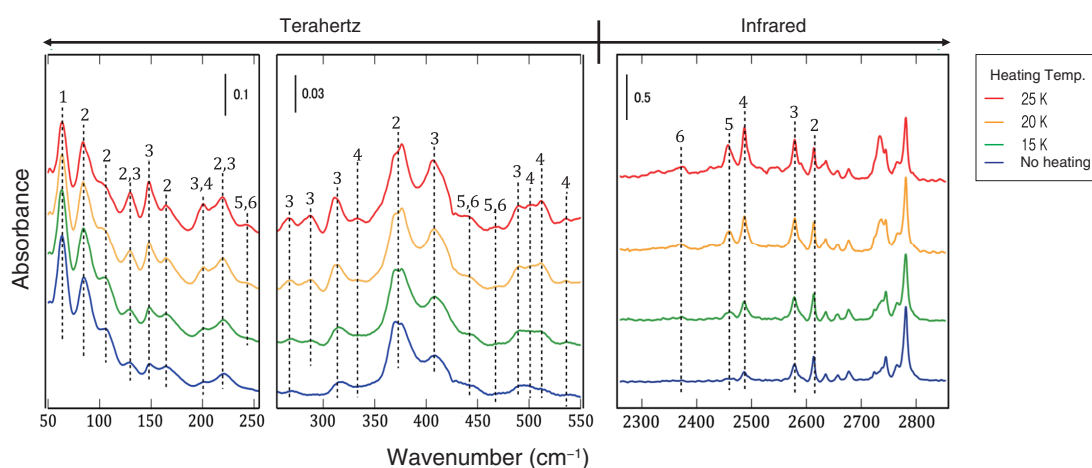


Fig.3-10 Heating-temperature dependence of the terahertz-infrared spectrum of deuterated water clusters

We measured spectra at 8 K before heating and after heating at 15, 20, and 25 K. The numbers of 1–6 indicate the sizes of deuterated water clusters while the vertical bars show the scales of absorbance. The wavenumber of the horizontal axis is proportional to the frequency of light, i.e. $33 \text{ cm}^{-1} \approx 1 \text{ THz}$. The increase in absorbance means that the amount of the corresponding cluster got larger.

Nano-sized water clusters have been intensively investigated in a spectroscopic way to reveal the nature of hydrogen bond interaction. Compared with the infrared (IR) range, only a few spectral measurements in the terahertz (THz) range have been reported, so that the assignment of the vibrational mode to THz absorption was not established even for the dimer. In the present study, we measured THz-IR absorption spectra of deuterated-water (D_2O) cluster formed in solid Ar and conducted ab initio vibrational calculation to identify the THz absorption peaks of the dimer, trimer, and tetramer.

A gaseous mixture of Ar and D_2O was condensed on the gold plate cooled down to 8 K by liquid helium. The most stable structures (Fig.3-9) and vibrational frequencies of the dimer, trimer, and tetramer trapped in solid Ar was determined by ab initio calculation.

In Fig.3-10, THz-IR spectra before and after heating the sample are displayed. The IR-absorption peaks due to clusters larger than the dimer were found to increase in absorbance with raising the heating temperature. This means the cluster-size

growth due to the thermal diffusion of D_2O . By comparing the heating-temperature dependence of the peak intensities in the THz range with the IR range and using the results of ab initio calculation, we determined the assignments of the THz peaks to the vibrational modes of the dimer, trimer, and tetramer.

The above accomplishment leads to the precise description of hydrogen-bond potentials, which characterize the physicochemical properties of ice and water. In addition, the fact that the greenhouse effect of water vapor is enhanced by clustering in atmosphere has been revealed recently. The cluster-size dependence of the THz-absorption intensity revealed in the present work will play an essential role in accurate evaluation of the greenhouse effect of water, which is one of the major topics in atmospheric and environmental science.

We appreciate support from the Japan Society for the Promotion of Science (JSPS) KAKENHI Grant-in-Aid for Early-Career Scientists (No.JP18K14182).

(Koichiro Yamakawa)

Reference

Yamakawa, K. et al., Terahertz and Mid-Infrared Spectroscopy of Matrix-Isolated Clusters and Matrix-Sublimation Ice of D_2O , *The Journal of Chemical Physics*, vol.152, issue 17, 2020, 174310, 13p.

3-6 Exploration of the Exotic Structure of P_c

— Hybrid State with a Mixture of Compact State and Hadron Molecule —

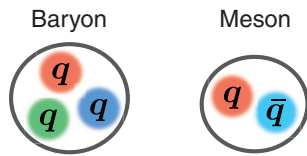


Fig.3-11 Ordinary hadrons; baryons and mesons

Baryon (qqq) and meson ($q\bar{q}$) comprise quarks, where q and \bar{q} denote a quark and an antiquark, respectively. Many experimentally observed hadrons can be classified as either baryons or mesons.

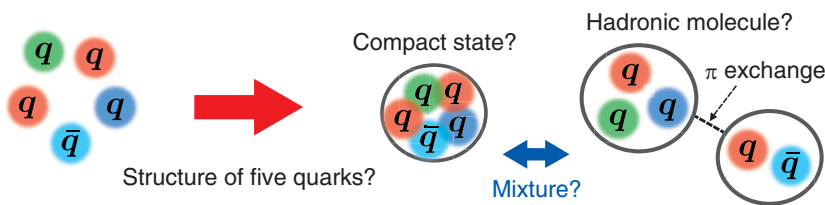


Fig.3-12 Possible five-quark structures: compact state and hadronic molecule

Five quarks are assumed to form a compact state or hadronic molecule. Hadron interactions such as the π exchange force work in the hadronic molecule. Here, P_c was considered a mixture of these two states.

Recently, unusually structured hadrons have been reported from accelerator experiments. Ordinary hadrons are classified into baryons and mesons; a baryon comprises three quarks, and a meson comprises a quark and an antiquark (Fig.3-11). Quarks are the elementary building blocks of hadrons, and antiquarks are the antiparticles of quarks. Researchers have discovered hundreds of hadrons have been found. For example, protons and neutrons, which form atomic nuclei, are described as baryons comprising three quarks.

Exotic hadrons, which cannot be explained by the ordinary meson or baryon structure, have been reported recently. Of note is the hadron " P_c " discovered during an experiment at the Large Hadron Collider in Europe, where P_c denotes a pentaquark, i.e., a hadron comprising five quarks. A pentaquark was first reported by SPring-8 in Hyogo, Japan as Θ^+ , but its existence was not confirmed. Thus, the observed P_c may represent the first discovered pentaquark.

However, it is not yet understood how the five quarks of P_c form their hadron structure. Therefore, this work aimed to develop a model to theoretically describe the P_c 's structure and understand its nature by comparing model predictions with the experimental results.

Two models have been proposed by previous researchers: a compact pentaquark ($c5q$) state in which five quarks form

a densely bound state and a hadron molecule in which five quarks are divided into baryon and meson clusters that are loosely bound, similarly as in a molecule (Fig.3-12). However, the $c5q$ state can split into two hadrons of which one is a hadron molecule, thus implying that the two states can mix. Therefore, we have proposed a hybrid model that considers a mixture of the $c5q$ states and hadron molecules. The π exchange force, known to produce attraction binding atomic nuclei, was also introduced in the hadronic molecules.

The energy of the pentaquarks was then predicted using the proposed hybrid model introducing state mixtures (Fig.3-13). The dashed arrows in Fig.3-13 show that the model accurately reproduced the observed mass and lifetime of P_c hadrons. These results indicate that P_c is indeed an exotic state that comprises a mixture of the $c5q$ state and hadron molecule. In addition to these three P_c states, we predict that more pentaquarks are yet to be discovered; future efforts will aim to explore such options and further verify the developed model by analyzing such pentaquarks. Future endeavors will also aim to further understand the P_c structure and continue progressing toward the fundamental problem of how matter of the universe is created from quarks with dynamical processes, such as spontaneous chiral symmetry breaking and confinement.

(Yasuhiro Yamaguchi)

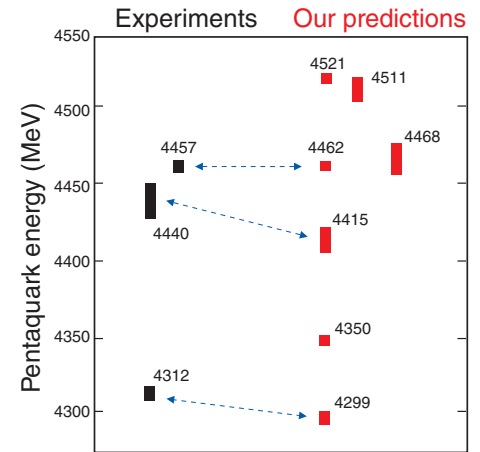


Fig.3-13 Predicted masses and lifetimes of the pentaquarks

Experimental (■) and predicted (■) energies (in mega electron volts (MeV)) are shown, where the center positions of the box corresponds to the mass of the pentaquark (shown next to the box) and the height of the box corresponds to the reciprocal of the lifetime.

Reference

Yamaguchi, Y. et al., P_c Pentaquarks with Chiral Tensor and Quark Dynamics, Physical Review D, vol.101, issue 9, 2020, 091502, 7p.

Fundamental Technologies for Nuclear Energy Innovation

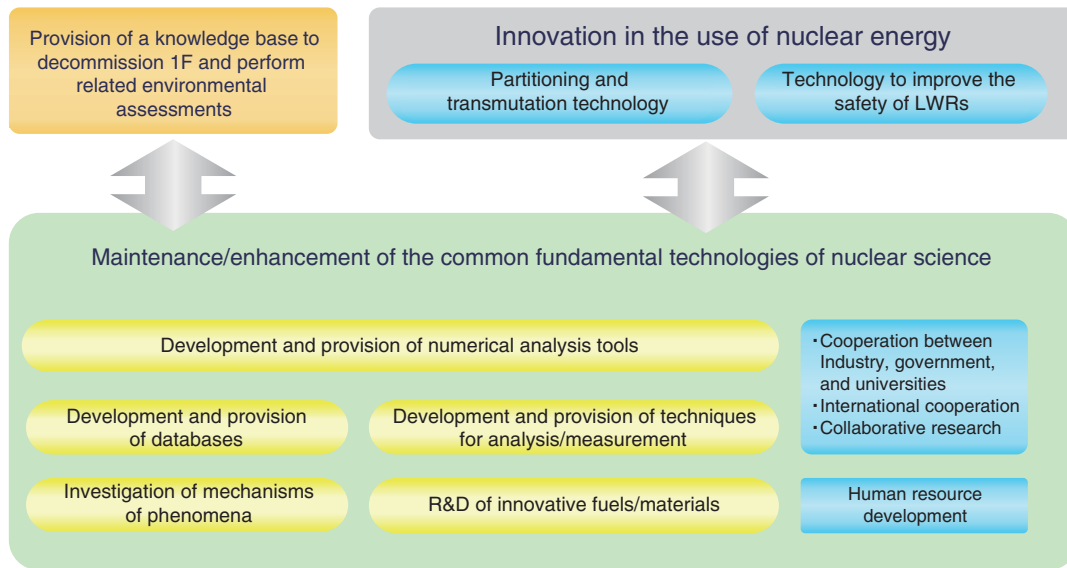


Fig.4-1 Overview of nuclear science and engineering research

NSEC maintains and enhances fundamental technologies for the use of nuclear energy and radiation. The center also aims to provide a knowledge base for decommissioning TEPCO's Fukushima Daiichi NPS (1F), contribute to improving the safety of light water reactors (LWRs), and develop partitioning and transmutation technologies to reduce the impact of radioactive wastes.

Common fundamental technologies and knowledge platforms, such as databases, numerical analysis tools, analytical technologies, and knowledge of phenomena mechanisms, are necessary to support the use of nuclear energy and radiation. As summarized in Fig.4-1, the Nuclear Science and Engineering Center (NSEC) aims to maintain state-of-the-art fundamental technologies and nuclear science knowledge and provides them to industry, universities, and governmental agencies. The NSEC has also contributed to safety improvements of LWRs and the development of partitioning and transmutation technology to reduce the impact of radioactive wastes. Recent results of the ongoing research and development (R&D) activities at NSEC are introduced in this chapter.

The cross-sections of nuclear reactions by deuterons were calculated using a new method considering quantum mechanical effects and have been compiled as a database, JENDL/DEU-2020. This database is expected to facilitate the use of intensive high-energy neutron sources using a deuteron accelerator (Topic 4-1).

High-quality nuclear data is indispensable when using nuclear energy and radiation. Therefore, we proposed a method using a machine learning technique to estimate nuclear data that are difficult to predict using theoretical nuclear reaction models. This method is expected to contribute to the development of high-quality nuclear data that is accurate and addresses uncertainty (Topic 4-2).

Proper decommissioning of 1F requires an understanding of the properties of the nuclear fuel debris. Micro-Raman spectroscopy can be used to analyze the debris because of its applicability to highly radioactive samples. Using this technique, we visualized the generation of two types of uranyl peroxide from the reaction between uranium oxide and hydrogen peroxide. Micro-Raman spectroscopy is expected to contribute to understanding the debris properties (Topic 4-3).

Organ doses were reevaluated using the latest computational

techniques and new data sets of human bodies being developed for more precise estimation. The reevaluated doses and doses derived from the current dosimetry system were consistent for most organs within a difference of 10%. The reevaluated doses will be used for future updates to the dosimetry system (Topic 4-4).

The Worldwide version of System for Prediction of Environmental Emergency Dose Information (WSPEEDI) is a sophisticated model that has been used for atmospheric dispersion analysis in nuclear emergencies; however, the calculation time required made comparing calculation results for various conditions cumbersome. Thus, we developed an atmospheric dispersion database system, WSPEEDI-DB, based on a proposed calculation method that can rapidly produce results calculated by WSPEEDI. This developed database for various release and weather conditions can be used for optimizing monitoring plans and disaster prevention drills (Topic 4-5).

Hydrogen embrittlement is known as a typical fracture mode of high-strength aluminum (Al) alloys. Our performed experimental observations of fractured Al alloy samples and theoretical calculations indicated that deterioration of the cohesivity on the interface of the alloy by the increase of hydrogen occupancy leads to spontaneous microcracking. Computational simulations are expected to play a more important role in designing new alloys (Topic 4-6).

Finally, displacement cross-sections were measured to evaluate the damage to materials caused by the proton beam. The first experimental data for iron were obtained, which are crucial to reducing the hazard of high-level radioactive wastes in accelerator-driven systems (ADSs). The results calculated using PHITS with the latest displacement model showed good agreement with the experimental results. Precise evaluation of radiation damage using cross-sections is expected to lead to safer ADSs and other high-energy accelerator facilities (Topic 4-7).

4-1 Toward High-Energy Neutron Applications

— Development of Nuclear Reaction Database for Basic Sciences and Medicine —

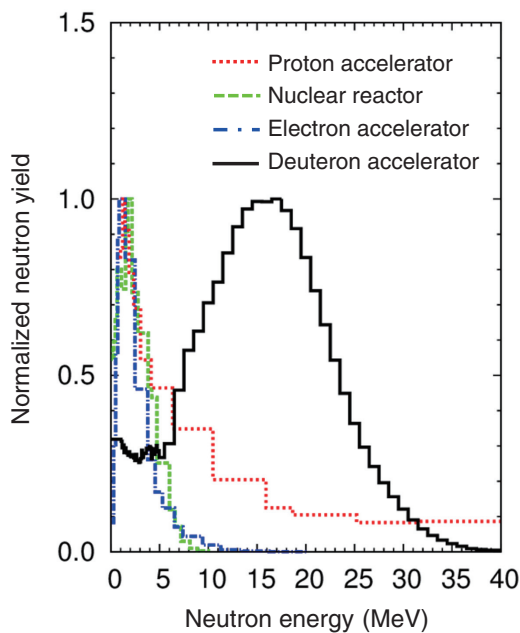


Fig.4-2 Neutron energy distributions of typical neutron sources (Each distribution is normalized to have a maximum value of 1.0, low energy component of nuclear reactor is omitted)

Most neutrons obtained from proton accelerators (e.g., J-PARC), nuclear reactors, and electron accelerators have energies below 10 MeV. On the other hand, a deuteron accelerator can produce high-energy neutrons above 10 MeV (solid line: experimental neutron energy distribution from a lithium target bombarded by a 40-MeV deuteron).

Applications of neutrons have expanded widely from basic science to industrial applications. In fields like experimental nuclear physics, medicine, and fusion reactor development, intensive neutron beams with energies above 10 MeV are required. However, conventional neutron sources, such as nuclear reactors, cannot satisfy these requirements, as shown in Fig.4-2. Thus, neutron sources using a deuteron accelerator have been proposed.

Designing such facilities requires that the amount and energy distribution of neutrons generated from the nuclear reactions induced by deuterons under various conditions (e.g., target material and kinetic energy of incident deuteron) are accurately predicted. However, the calculation methods used in existing software have shown poor prediction accuracy because the quantum mechanical wave properties of deuterons are not appropriately considered.

Therefore, we developed a calculation method by integrating several theoretical models taking quantum mechanical effects into account. The calculated results were

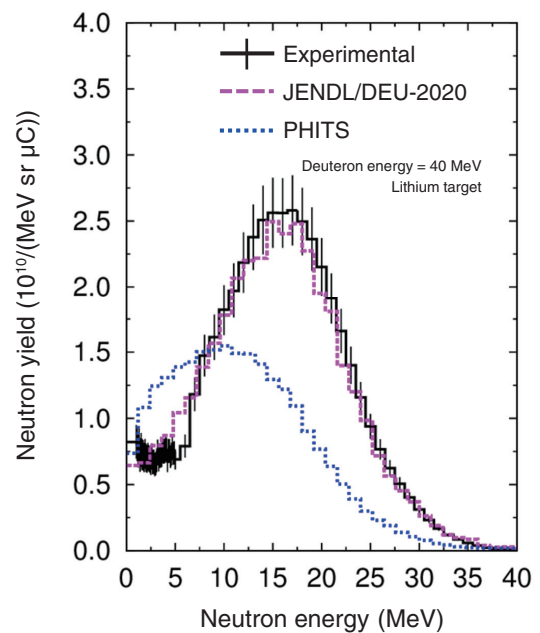


Fig.4-3 Simulation results of deuteron accelerator neutron source

Solid line: experimental data shown in Fig.4-2 including experimental error. Dashed line: data calculated by the simulation software PHITS using the JENDL/DEU-2020 database. Dotted line: data calculated using the nuclear reaction models implemented in PHITS.

compiled into a database that is applicable to the simulation software employed in the design studies of neutron sources; this database, JENDL/DEU-2020, can be used to design neutron sources with deuteron accelerators.

Example simulation validation results using JENDL/DEU-2020 are shown in Fig.4-3. Using JENDL/DEU-2020, the experimental data was reproduced more accurately than when using the models implemented in the simulation software PHITS. Similar improvements were demonstrated under various conditions, including beryllium and carbon targets.

Overall, the proposed calculation method and database improves the simulation reliability, thus making targeted neutron source design easier. JENDL/DEU-2020 is expected to promote the use of intensive high-energy neutrons in various fields, including basic sciences, medicine, and reactor design.

This work was partially supported by the Japan Society for the Promotion of Science (JSPS) KAKENHI Grant-in-Aid for Young Scientists (No.JP19K15483).

(Shinsuke Nakayama)

Reference

Nakayama, S. et al., JENDL/DEU-2020: Deuteron Nuclear Data Library for Design Studies of Accelerator-Based Neutron Sources, Journal of Nuclear Science and Technology, vol.58, issue 7, 2021, p.805–821.

4-2 Estimating Nuclear Data Using a Machine Learning Technique — Toward the Development of a High-Quality Nuclear Reaction Database —

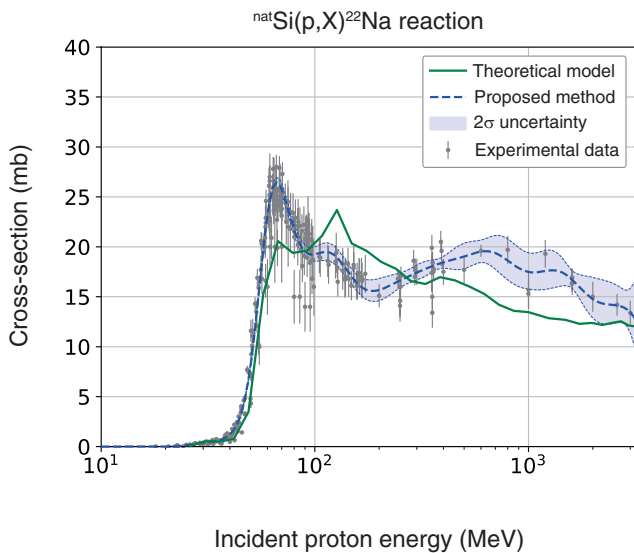


Fig.4-4 Estimated ${}^{\text{nat}}\text{Si}(p,X){}^{22}\text{Na}$ cross-section using the theoretical model and proposed ML method

The light blue band indicates the uncertainty (two standards of deviation, 2σ) of the estimated cross-section. Even with the latest theoretical models, predicting the high-energy nuclear reaction cross-sections is difficult.

Nuclear data are indispensable when simulating particle transport to estimate radiation doses, radioactive isotope production, and safety parameters of nuclear systems. The quality and quantity of nuclear data in the nuclear data libraries have been steadily enhanced owing to physicists' strenuous efforts; however, discrepancies between experimental data and model calculations remain, particularly at high incident energies. Further, conventional approaches used to improve theoretical models require a substantial amount of time and effort. In such cases, a machine learning (ML) technique based on Gaussian processes may serve a useful role in estimating nuclear data.

Experimental and calculated data using the conventional and proposed methods of the proton-induced sodium-22 (${}^{22}\text{Na}$) production cross-section produced from a silicon (${}^{\text{nat}}\text{Si}$) nucleus, which is a key material of semiconductor devices, are summarized

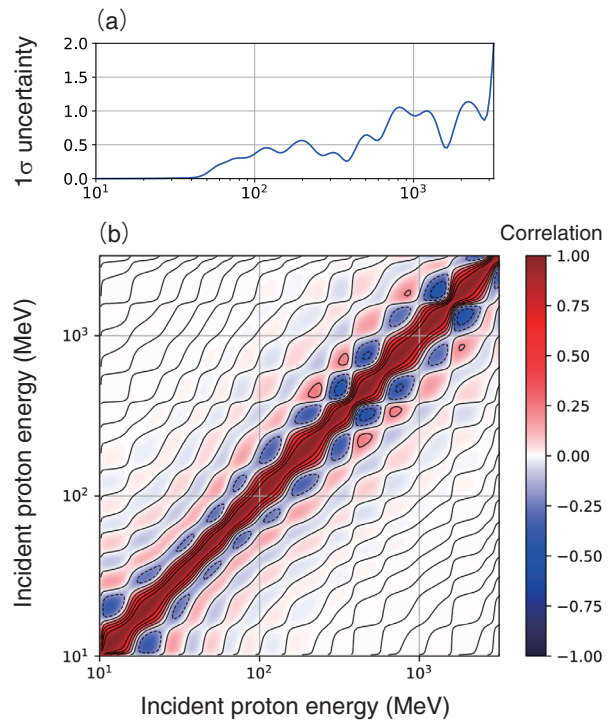


Fig.4-5 Uncertainty of the ${}^{\text{nat}}\text{Si}(p,X){}^{22}\text{Na}$ cross-section estimated by the proposed ML method

(a) 1σ uncertainty of the evaluated cross-section at varying incident energies. (b) Correlation matrix, which clarifies the strength of the linear relationship between the cross-sections at different energy points.

in Fig.4-4. Even with the latest theoretical models, it is difficult to account for nuclide-production cross-sections at incident energies above 10 MeV. In contrast, since the proposed method estimates the cross-section while learning from the experimental data based on Gaussian processes, no significant discrepancies were found between the estimated and experimental values.

As illustrated in Fig.4-5, the proposed method also provides information regarding the uncertainty of the estimated cross-sections; in conventional methods, such calculations are cumbersome to obtain. The obtained uncertainty information allows us to discuss the effectiveness of experiments to improve the accuracy of nuclear data. This method is expected to contribute to the development of an accurate, high-quality nuclear reaction database that contains uncertainty information.

(Hiroki Iwamoto)

Reference

Iwamoto, H., Generation of Nuclear Data Using Gaussian Process Regression, Journal of Nuclear Science and Technology, vol.57, issue 8, 2020, p.932–938.

4-3 Toward Clarifying the Chemical States of Nuclear Fuel Debris — Applicability of Micro-Raman Spectroscopy —

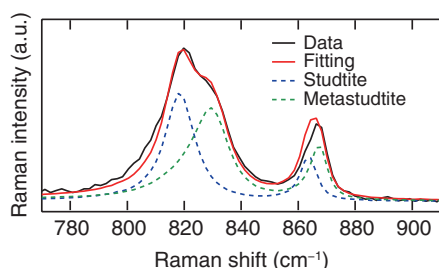


Fig.4-6 Raman spectra of U_3O_8 immersed in a hydrogen peroxide solution

Two types of uranyl peroxide were observed: studtite $[(UO_2)(O_2)(H_2O)_2]$ and metastudtite $[(UO_2)(O_2)(H_2O)_2]$.

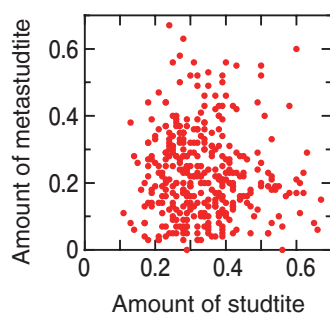


Fig.4-8 Scatter plot showing the amount of generated studtite (x-axis) and metastudtite (y-axis)

No correlation was observed, suggesting that these compounds were independently generated.

Nuclear fuel debris at TEPCO's Fukushima Daiichi NPS is considered an uncertain, complex, solid mixture generated from the melting and cooling of nuclear fuel, zirconium cladding, structural materials, etc. Detailed knowledge of the chemical state of the debris, such as the chemical substances comprising the fuel debris, is necessary for safe and effective decommissioning processes, including removal from the reactor, storage, processing, and disposal. However, clarification methods for the chemical states of the fuel debris have not been well established.

Therefore, we proposed a method using micro-Raman spectroscopy to clarify the chemical states of fuel debris. During micro-Raman spectroscopy, a sample is irradiated with a laser through an objective lens; information regarding the vibrational structure of the sample is obtained by detecting the scattered light. This method does not require sample pretreatment and can be performed on small samples and thus can be used to examine radioactive fuel debris safely and easily.

Since the fuel debris is in contact with water in the reactor, it is expected to react with the hydrogen peroxide generated by the radiolysis of water and be in a chemical state different from that immediately following the accident. Therefore, the aging reaction of U_3O_8 , which is one of the fundamental uranium oxides, by hydrogen peroxide was investigated.

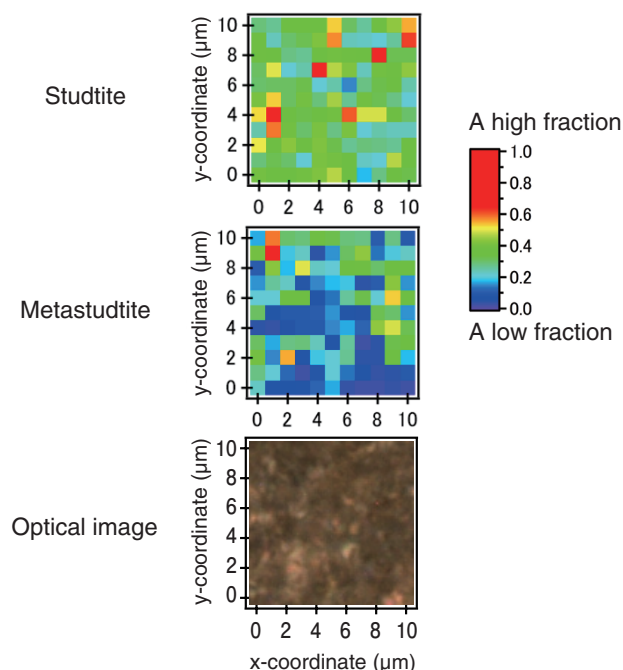


Fig.4-7 Distribution of uranyl peroxides generated on the surface of U_3O_8 and an optical microscope image

More studtite was generated than metastudtite.

The performed measurements clarified that two types of uranyl peroxides (studtite and metastudtite) with different hydration numbers were observed on the surface of U_3O_8 by the reaction with hydrogen peroxide (Fig.4-6). The distribution of the products on the sample surface indicates that more studtite was formed (Fig.4-7). No correlation was observed between the amount of studtite and metastudtite generated (Fig.4-8), suggesting that these two types of uranyl peroxides were generated independently.

Uranyl peroxide is also known to be generated by the oxidation reaction of spent nuclear fuel and UO_2 . Recently, it has been found that uranyl peroxides are also generated by the oxidation reaction of simulated debris of uranium-stainless steel-zirconium system, which is closer to the actual fuel debris. Therefore, as uranyl peroxides may be generated in actual fuel debris, analyzing uranyl peroxides will provide information on the aging of fuel debris. Furthermore, since micro-Raman spectroscopy can be used to analyze compounds other than uranyl peroxides, the proposed methodology could contribute to the accurate understanding of the chemical properties of fuel debris.

This work was supported by JAEA Nuclear Energy S&T and Human Resource Development Project (No. JPJA18P18071886).

(Ryoji Kusaka)

Reference

Kusaka, R. et al., Distribution of Studtite and Metastudtite Generated on the Surface of U_3O_8 : Application of Raman Imaging Technique to Uranium Compound, Journal of Nuclear Science and Technology, vol.58, issue 6, 2021, p.629-634.

4-4 Reassessment of Atomic Bomb Survivor Doses

— Joint Japan–U.S. Study to Improve Epidemiological Research Accuracy —

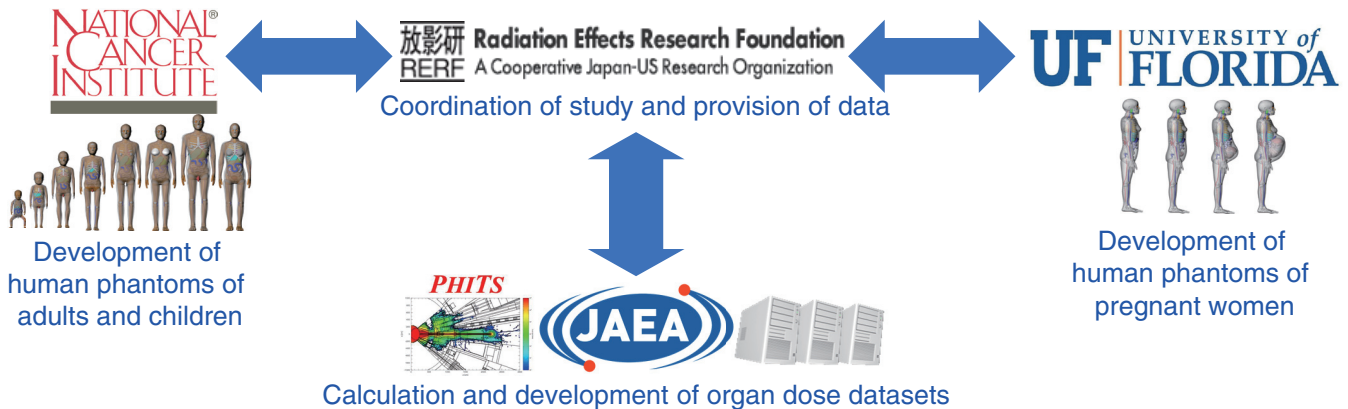


Fig.4-9 Structure of this study

The RERF coordinates the project and provides data, JAEA calculates and develops the organ dose datasets, the NCI develops human phantoms of adults and children, and the UF develops human phantoms of pregnant women.

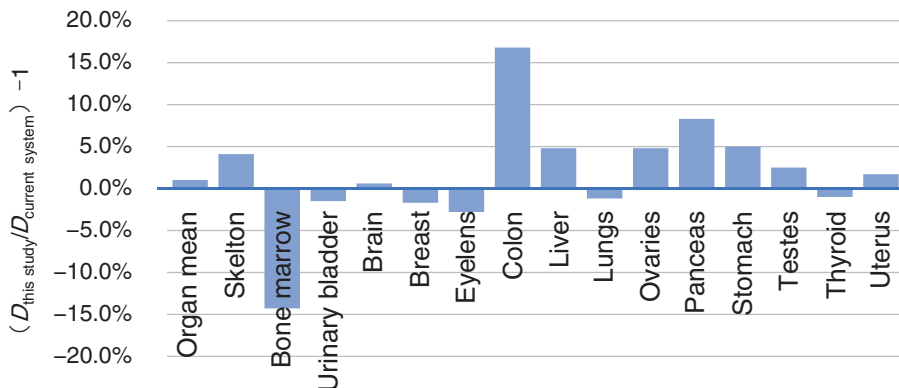


Fig.4-10 Percentage difference between organ doses obtained from this study ($D_{\text{this study}}$) and current dosimetry system ($D_{\text{current system}}$)

Positive values indicate that the organ dose obtained from this study is larger than that obtained from the current dosimetry system.

Epidemiological studies of atomic bomb (A-bomb) survivors conducted by the Radiation Effects Research Foundation (RERF) are some of the most important resources for data on the effects of radiation on human health. The precise estimation of the organ doses is key to these studies, and the dosimetry system used to estimate the doses received by individual organs in each survivor has evolved and improved over the years. A joint Japan–U.S. project team comprising the Nuclear Science and Engineering Center of JAEA, RERF, the University of Florida (UF), and the U.S. National Cancer Institute (NCI) was formed to further refine the dosimetry estimation system (Fig.4-9).

Members of this project team developed a set of models of the human body (known as phantoms) for adults, children, and pregnant women by precisely reproducing the standard body dimensions of Japanese people in 1945, modeled in detail using the latest-available CT images and other information. The project team also established a method for more accurately estimating

the organ doses of A-bomb survivors with these phantoms using the latest computational techniques, such as PHITS, which was developed mainly by JAEA. Based on idealized conditions in hypothetical survivors, our initial comparisons of doses using the developed phantoms and methods with doses derived from the current dosimetry system found that doses were generally consistent, although dose estimates for some organs changed by as much as $\pm 15\%$ (Fig.4-10).

The results of this collaborative effort have been published in the journal “Radiation Research” as a series of three articles. They will be used to continue updating organ doses within the epidemiological study of the atomic bomb survivors.

This research is part of the results of the joint research with Radiation Effects Research Foundation (RERF), “Joint research on the development of exposure dose calculation methods for atomic bomb survivors”.

(Tatsuhiko Sato)

Reference

Sato, T. et al., Dosimetric Impact of a New Computational Voxel Phantom Series for the Japanese Atomic Bomb Survivors: Methodological Improvements and Organ Dose Response Functions, Radiation Research, vol.194, issue 4, 2020, p.390–402.

4-5 Quicker Calculation of Atmospheric Dispersion of Radioactive Materials under Various Conditions — Development of the Atmospheric Dispersion Database System WSPEEDI-DB —

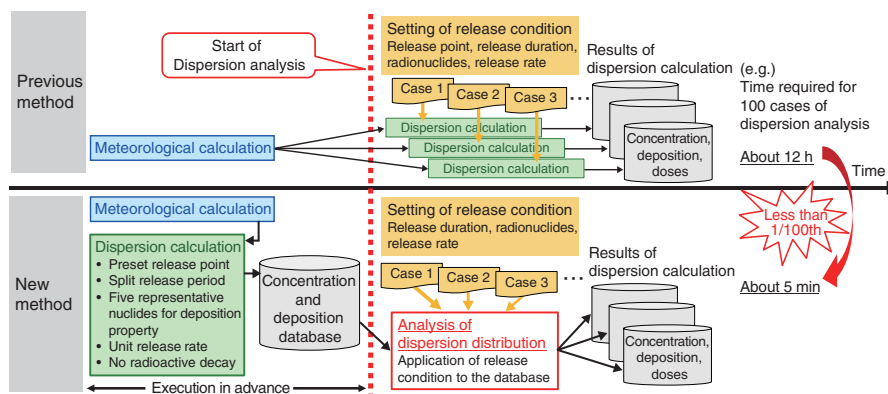


Fig.4-11 Comparison of the previous method (upper) and new method (lower)

The new method makes it unnecessary to perform dispersion calculations for each release condition required by the previous method. The results of a 1-day test calculation with the previous method, which required about 7 minutes per case, was obtained in 3-4 seconds with the new method, i.e., the results can be provided in less than 1/100th of the time needed for the previous method.

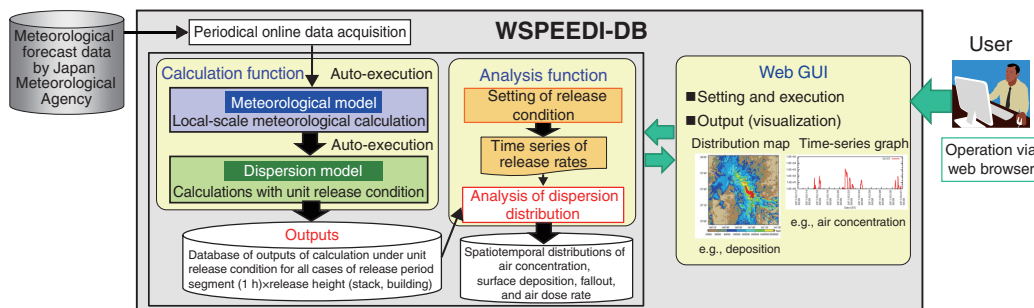


Fig.4-12 Structure and calculation flow of WSPEEDI-DB

The calculation function creates an output database; the analysis function applies release conditions to this database to create dispersion analysis results. The results can be visualized by creating various figures. These functions can be easily operated using a web browser.

According to the basic disaster management plan issued by the National Disaster Management Council, the Government of Japan provides professional and technical support to local governments when they use atmospheric dispersion calculations to improve their regional disaster prevention and evacuation plan. To contribute to this, it is necessary to efficiently provide the detailed dispersion calculation results using the Worldwide version of System for Environmental Emergency Dose Information, WSPEEDI, which has been used for source term estimation and atmospheric dispersion analysis in nuclear emergencies. However, this sophisticated numerical model requires computation time, making it difficult to quickly compare calculation results under various conditions, including meteorological conditions.

Therefore, we developed a new calculation method as summarized in Fig.4-11. Using this method, if a release point (e.g., a nuclear facility) is known, the prediction results could be rapidly obtained by applying a source term (radionuclides, release rate, and release period) to the database of dispersion calculation results that is prepared in advance without specifying the source term. Each dispersion calculation is conducted under a unit release condition (1 Bq/h) for each release segment divided by a fixed time interval, and all calculated release segment results are saved. Five radionuclides, which represent five groups classified by diffusion behavior, are calculated without

radioactive decay; the decay rate for each specific radionuclide is applied later. These calculations are conducted regularly along with daily meteorological data updates to construct a continuous database that includes past data and predictions for the next few days. By applying a release condition of each release segment to the database and aggregating the results of all release periods, calculation results can be quickly created for arbitrary release conditions. We then developed the atmospheric dispersion database system WSPEEDI-DB using a user-friendly interface for easy function operation, as summarized in Fig.4-12. Dispersion calculation results under various release and weather conditions can be used for optimization of monitoring plans and drills by creating simulated monitoring data. As an example, the deployment of monitoring posts around the Shimane Nuclear Power Station was assessed by analyzing the past 1-year dispersion calculation results. We could demonstrate that the present monitoring post deployment can capture the distribution of air dose rates during periods without rainfall. For periods with precipitation, however, high-dose-rate areas are assumed not to be grasped.; mobile measurement is effective in such areas.

This study includes the results of the FY2016–2019 joint research with the Shimane Prefectural Nuclear Power Environmental Center.

(Hiroaki Terada)

Reference

Terada, H. et al., Atmospheric-Dispersion Database System that Can Immediately Provide Calculation Results for Various Source Term and Meteorological Conditions, *Journal of Nuclear Science and Technology*, vol.57, issue 6, 2020, p.745–754.

4-6 Clarification of the Spontaneous Microcracking of Aluminum Alloys — Toward the Realization of High-Strength Alloys through Computational Science —

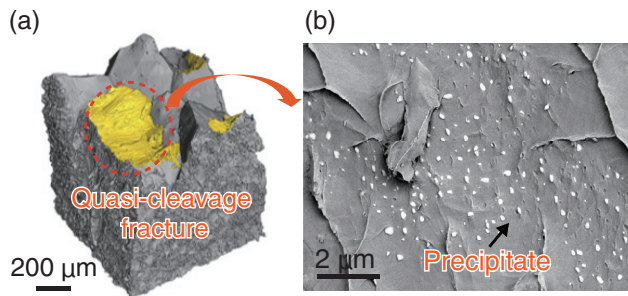


Fig.4-13 Experimentally observed fracture surface of an Al-Zn-Mg alloy

Aluminum alloys show a quasi-cleavage fracture mode. (a) Three-dimensional tomographic images of fractured Al-Zn-Mg alloy samples captured by synchrotron X-ray tomography. (b) Low-voltage SEM images of this fracture surface, indicating interfacial fracture due to numerous precipitates at the interface.

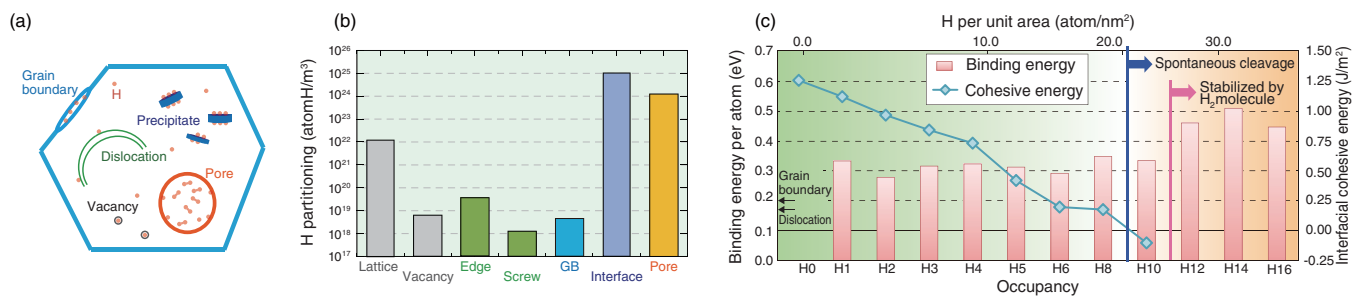


Fig.4-14 Hydrogen partitioning and spontaneous cracking

(a) Various defect structures in aluminum alloy; (b) hydrogen partitioning at various defect sites; and (c) binding energy per atom and interfacial cohesive energy as a function of occupancy. Spontaneous cleavage occurred when the concentration of hydrogen atoms reached 22.7 H atoms/nm², according to the negative value of the cohesive energy.

Aluminum alloys are considered the most feasible material to satisfy lightweight structural and industrial needs. Highly concentrated precipitates generated by age hardening play a dominant role in shaping the mechanical properties of aluminum alloys. It is commonly believed that the coherent interface between the matrix and precipitate does not contribute to crack initiation and embrittlement. High-strength lightweight aluminum alloys have been expected for a long time.

Therefore, we performed a three-dimensional observation technique and atomistic simulations to clarify the hydrogen embrittlement mechanism related to the quasi-cleavage fracture unique to Al alloys. Synchrotron X-ray imaging and scanning electron microscopy (SEM) with energy-dispersive X-ray spectroscopy analysis were used to capture the characteristic features of the fracture and, in particular, elucidate the relationship between the fracture and coherent surface planes of the η -phase precipitates.

The fracture surface obtained by synchrotron X-ray tomography corresponded to a brittle fracture, as shown in Fig.4-13(a). The crack propagated gradually and undulatory along various quasi-cleavage facets where hydrogen atoms were sufficiently trapped. Low-voltage SEM images on this surface are shown in Fig.4-13(b). Surprisingly, very dense white particles were observed, indicating that the fracture occurred along the Al–MgZn₂ precipitate interface.

The binding energy between hydrogen atoms and various

defect structures, such as vacancies, edge/screw dislocations, grain boundaries, and precipitates, were then investigated, as summarized in Fig.4-14(a). The theoretically estimated hydrogen partitioning (i.e., site occupancy) is provided in Fig.4-14(b). Site occupancy differed widely, reflecting the exponential contribution of the binding energies. Hydrogen partitioning was found at the interface of the precipitate and aluminum matrix. DFT calculations were performed again to explore the relationship between cohesive energy and occupancy at this interface; the resulting binding energy per atom and interfacial cohesive energy in terms of occupancy is shown in Fig.4-14(c). Despite the coherent interface, the binding energy did not decrease, even at maximum occupancy. Once occupancy exceeded a certain limit, hydrogen atoms tended to stably nucleate as hydrogen molecules. Thus, the interface cohesivity deteriorates significantly with increasing hydrogen occupancy, whereas hydrogen atoms can be stably trapped up to an extremely high occupancy that is equivalent to spontaneous cleavage.

Computational simulations are expected to aid in the design of alloys to serve industrial needs.

This study was supported by Japan Science and Technology Agency (JST) Strategic Basic Research Programs (CREST, JPMJCR1995), and Industry-Academia Co-creation Basic Research Program (Project 20100114).

(Tomohito Tsuru)

Reference

Tsuru, T. et al., Hydrogen-Accelerated Spontaneous Microcracking in High-Strength Aluminium Alloys, Scientific Reports, vol.10, 2020, 1998, 8p.

4-7 Extent of Damage to Material when Exposed to Proton Beam — Contribution to the Safety of Accelerator-Driven Systems —

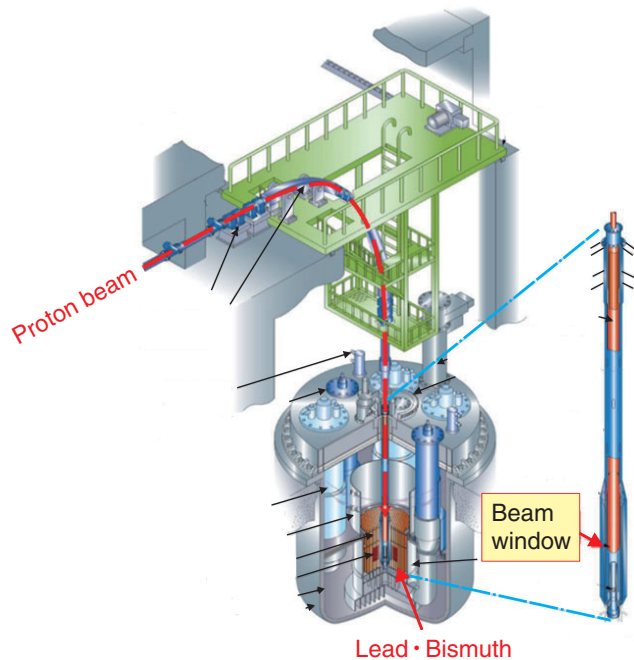


Fig.4-15 Overview of ADS proposed by JAEA

The steel beam window is a vital component that affects the feasibility of ADS; however, no experimental data on displacement cross section were available for radiation damage evaluation.

JAEA is developing Accelerator-Driven Systems (ADSs) for efficiently reducing the hazards and amount of high-level radioactive waste generated by nuclear reactors. Steel is used for fabricating the beam window in an ADS, introducing a high-energy proton beam with billions of electron volts (GeV) (Fig.4-15). “Displacement damage” occurs when protons are injected into materials, displacing the positions of atoms in the lattice and consequently deteriorating the material strength. The displacement per atom (dpa) is usually used as an index to evaluate the displacement damage of materials. The displacement cross section is used to estimate the number of displacements produced in the material. Owing to very limited experimental data of the cross section, validating the calculation model for estimating the number of displacements is difficult.

In this study, the displacement cross sections of iron and copper, which are essential in ADS, were measured using the accelerator at the Japan Proton Accelerator Research Complex (J-PARC). Based on Matthiessen’s rule, the displacement damage is found to be proportional to the increase in the electrical resistance of metal samples irradiated by the proton beam. To prevent the damage from being recovered by thermal motions, the sample was cooled to approximately $-269\text{ }^{\circ}\text{C}$ (4 K), and the increase in the electrical resistance was measured after irradiation. Through this experiment, we obtained the world’s

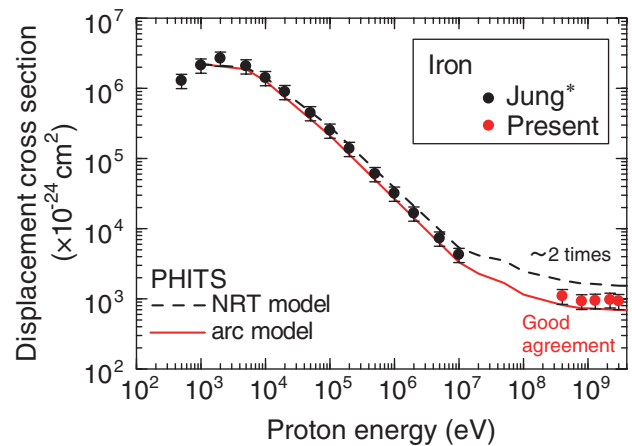


Fig.4-16 Comparison of the present experimental data with calculation data using PHITS

No previous measurements have been performed on iron in the energy region above 10 MeV, which is important for ADS. In this study, we obtained the world’s first experimental data in this energy region.

first displacement cross section of iron in the GeV energy region.

The displacement cross sections were calculated by incorporating the displacement model into Particle and Heavy Ion Transport code System (PHITS), and the calculation results were compared with the experimental data (Fig.4-16). Although the calculation results obtained using the widely used NRT model were in relatively good agreement with the experimental cross sections for protons below 10 MeV, they are larger than the experimental cross sections by a factor of 2 in the GeV energy region. Alternatively, the latest athermal-recombination-corrected (arc) model based on the molecular dynamics results showed excellent agreement with the experimental data.

This study is expected to improve the accuracy of damage evaluation for ADS-related and other materials used in high-energy accelerator facilities, such as J-PARC, and further enhance their safety.

This study was supported by MEXT (Ministry of Education, Culture, Sports, Science and Technology, Japan) Innovative Nuclear Research and Development Program (No.JPMXD0216815810).

(Shin-ichiro Meigo)

* Jung, P., Atomic Displacement Functions of Cubic Metals, Journal of Nuclear Materials, vol.117, 1983, p.70–77.

Reference

Matsuda, H., Meigo, S. et al., Measurement of Displacement Cross-Sections of Copper and Iron for Proton with Kinetic Energies in the Range 0.4 – 3 GeV, Journal of Nuclear Science and Technology, vol.57, issue 10, 2020, p.1141–1151.

Contributions to Innovative Achievement in Science and Technology

In accordance with the Science and Technology Basic Plan formulated by the Government of Japan, we have aimed to contribute to the advancement of science and technology and the promotion of industry in Japan through innovative research into neutron and synchrotron radiation. This has included using the high performance and multipurpose research reactor JRR-3, the high-intensity proton accelerator at the Japan Proton Accelerator Research Complex (J-PARC) and JAEA's synchrotron radiation beamlines at the Super Photon ring-8 GeV (SPring-8), upgrading neutron facilities and devices, and pursuing world-leading research in fields that use neutron and synchrotron radiation, such as nuclear energy and materials sciences.

(1) Research and development at J-PARC

J-PARC comprises three proton accelerators, including a linear particle accelerator (linac), a 3-GeV rapid-cycling synchrotron (RCS), and a main ring synchrotron, and three experimental facilities. The facilities include the Materials and Life Science Experimental Facility (MLF) for a wide range of research fields using neutron and/or muon beams, the Hadron Experimental Facility for nuclear and particle physics experiments using K-mesons and other particles, and the Neutrino Experimental Facility for T2K particle physics experiments using neutrinos. These experimental facilities are open to researchers worldwide.

We have made accelerator equipment improvements and performed beam studies toward stable operation at 1 MW proton beam power. Recently, 38 hours of continuous operation at the designed power of 1 MW with an availability of more than 90% was achieved, thereby meeting this target. To achieve longer continuous stable operation, we recently developed a system in which the state of consumption of the carbon thin film used for charge-exchange beam injection in the 3 GeV RCS can be remotely measured. This development allows the carbon thin film to be replaced as preventive maintenance before being damaged and is thus expected to further improve the operation rate (Topic 5-1).

During FY2020, a stable, 600 kW beam operation was achieved at the MLF. Due to the spread of the new coronavirus, the user program for 7.2 scheduled run cycles (159 days) was adjusted to 144 days.

A wide range of experiments related to material and life sciences were conducted at MLF this past year, including the operation of 21 neutron spectrometers and 2 muon instruments. Using the neutron diffractometer “TAKUMI” (BL19), shown in Fig.5-1, spheroidal graphite cast iron, which is widely used in the castings of the parts for construction machinery, automobiles, nuclear fuel casks, etc., was studied to reveal the mechanism behind the increase in strength caused by cyclic tensile–compressive deformation (Topic 5-2). Furthermore, with the Accurate Neutron-Nucleus Reaction Measurement Instrument “ANNRI” (BL04), the energy-dependent angular distribution of γ rays was revealed in the high-energy range of 0.74 eV p-wave resonance in the $^{139}\text{La}(n,\gamma)^{140}\text{La}$ reaction using a high performance He-3 spin filter (Topic 5-3). This experiment represents a first step toward investigating CP-violations within nuclei. Further, this technology can be applied to analyze the magnetic structure of spintronics devices, determine hydrogen positions in substances, perform basic physics experiments, etc. We expect that this optical device will be used to obtain wide-ranging scientific results.

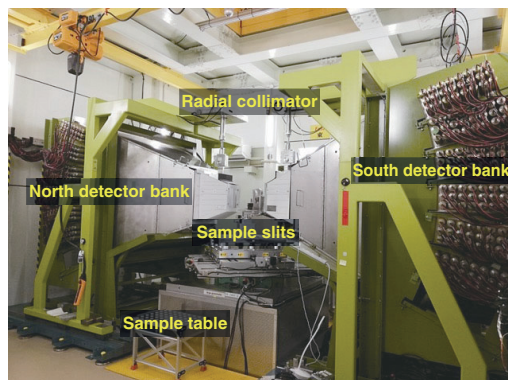


Fig.5-1 Engineering materials diffractometer “TAKUMI” (BL19) at J-PARC MLF

(2) Research and development at the Materials Sciences Research Center (MSRC)

Researchers at the MSRC aim to provide innovative results and seed research in a wide range of scientific, technological, and academic fields by developing and improving neutron and synchrotron radiation instruments for advanced structural and functional analysis in Tokai (JRR-3 and J-PARC) and in Harima (SPring-8).

In FY2020, we discovered a phase of partial short-range order of conduction-electron spins that is phase-separated from the paramagnetic phase at a record high temperature in the newly synthesized metal magnet, Mn_3RhSi , from the neutron diffraction and muon spin resonance experiments (Topic 5-4). This phenomenon can be realized in other metal magnets; further examination of this phenomenon is expected to lead to further understanding of the partial order of conduction-electron spins, whose origin has not been clarified. We also developed a powerful strategy to produce eco-friendly, high-performance metal adsorbents that can adsorb biohazardous ions from their environment (Topic 5-5). This simple method allows highly carbonated nanohydroxyapatites (C-NHAPs) to be obtained from biological hydroxyapatite, which can be extracted from animal bones (e.g., from food waste); the obtained C-NHAPs exhibit high adsorptivity of toxic ions, such as ^{90}Sr and Cd. Additionally, neutron instruments and related devices have been set up at JRR-3 to prepare for operations to resume in FY2021 to produce valuable results at this reactor.

Our synchrotron radiation studies have included efforts to describe the permeation of oxygen through graphene, which is a remarkable functional material (Topic 5-6). Although graphene is a net comprising only a single layer of carbon atoms, it is known as an excellent gas barrier: very few gas molecules, including hydrogen, are known to penetrate it. However, we have discovered that fast oxygen molecules can penetrate graphene nondestructively. It is expected to develop novel protective films considering the discovered mechanism. Ferromagnetic semiconductors have also attracted attention for their use in efficient spintronics materials. An electronic state of an element bearing magnetic properties of a sample was investigated in detail to clarify the mechanism of the magnetism ordering process (Topic 5-7). This work will contribute to settling the controversy over the origin of ferromagnetism and guide the application of ferromagnetic semiconductors to room-temperature spintronics devices.

5-2 Strengthening Mechanism of Cast Iron Elucidated by a High-Intensity Pulsed Neutron Beam — Deformation Response of Each Constituent Phase Monitored by Neutron Diffraction —

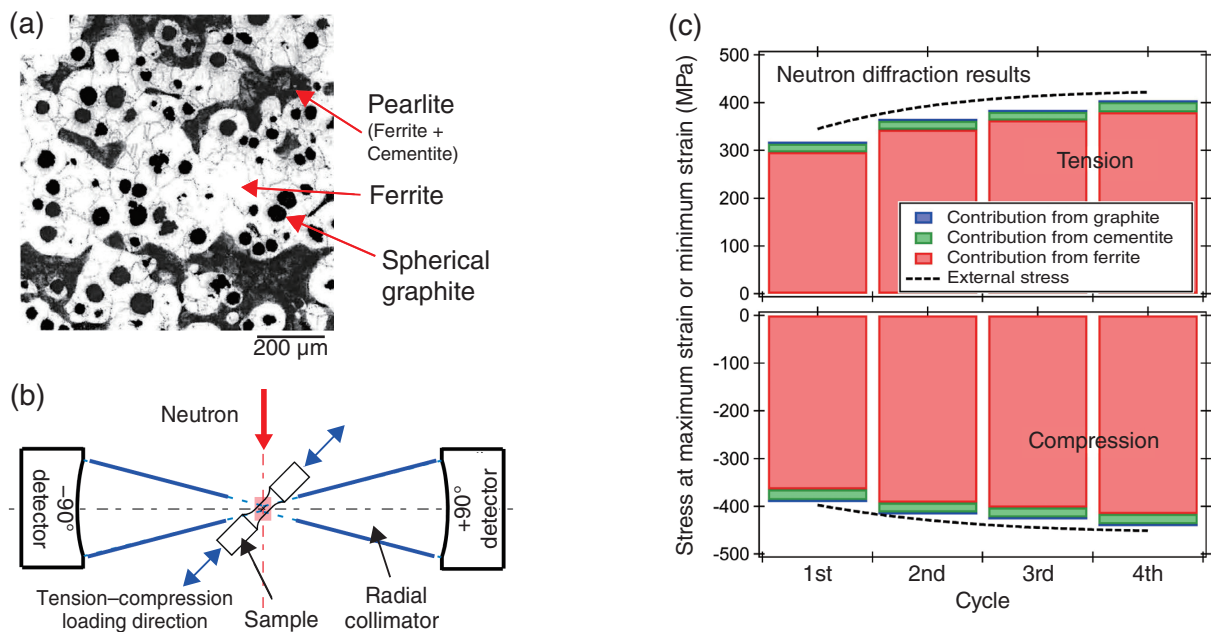


Fig.5-4 (a) Cast iron microstructure, (b) schematic of *in situ* neutron diffraction experiment, and (c) the obtained results
 (a) The microstructure of the cast iron used in the experiment comprised ferrite, pearlite (layered structure of ferrite and cementite), and spheroidal graphite. (b) The *in situ* neutron diffraction experiment during cyclic tensile–compressive deformation was performed using the Engineering Materials Diffractometer TAKUMI at J-PARC. The diffraction lines in the loading direction ($+90^\circ$) and the direction perpendicular to the loading direction (-90°) were measured simultaneously. (c) The obtained results revealed that the contribution of ferrite to the external stress increased as the number of cycles increased, thereby increasing the overall strength of cast iron. Meanwhile, the contributions of cementite and spheroidal graphite were minor.

Cast iron is an iron-based material comprising three constituent phases (i.e., structures), as shown in Fig.5-4(a): ferrite, pearlite, and spheroidal graphite. Cast iron is known for its ability to withstand high external forces and can easily be cast into complicated shapes; it is thus widely used in the casing of hydraulic equipment for construction machinery, various parts of automobiles, and spent nuclear fuel casks. Cyclic tensile–compressive deformation tests are often performed to simulate use in a harsh environment. Although the strength of cast iron is known to increase with increasing cycle number during cyclic tensile–compressive deformation, the mechanism behind this increase in strength has remained unclear.

Therefore, an *in situ* neutron diffraction experiment was designed to observe the forces and microstructural changes occurring in each of the constituent phases of cast iron and clarify this mechanism; a schematic of this experiment is shown in Fig.5-4(b). Here, the stress (strength) and crystal defects carried by each constituent phase could be obtained in diffraction experiments using neutrons with high penetrating power by quantitatively analyzing the diffraction lines related to the atomic arrangement of each constituent phase inside the sample.

The obtained results are summarized in Fig.5-4(c). As the number of cycles increased during the cyclic tensile–compressive deformation test, crystal defects (i.e., dislocations) accumulated in ferrite, thus increasing its strength. This increase in strength led to an increase in the overall strength of the cast iron, because ferrite was the major constituent phase in the cast iron. On the other hand, the cast iron contained a very small fraction of

cementite (a constituent of pearlite), so its contribution to the overall strength was limited. Additionally, spheroidal graphite accommodated low stress and thus provided only a negligible contribution to the strength.

Overall, a detailed analysis of the behavior of each phase of cast iron was analyzed in detail via diffraction using the high-intensity pulsed neutron beam of the Materials and Life Science Experimental Facility at J-PARC, thereby allowing us to successfully elucidate the mechanism behind strength increases during cyclic tensile–compressive deformation. Further, the method developed using the TAKUMI diffractometer enabled *in situ* neutron diffraction experiments during continuous deformation.

Cast iron is an important material supporting daily life; by changing the morphology and distribution of the constituent phases by heat treatments or other processes, a wide range of material properties can be tuned to cover a wide range of applications. Our achievements toward understanding the phenomena occurring in cast iron may advance calculation and processing methods and support the design of materials for various applications.

This study was supported by the Japan Society for the Promotion of Science (JSPS) KAKENHI Grant-in-Aid for Scientific Research on Innovative Areas (Research in a proposed research area) (No.JP18H05479) “Solving kink formation/strengthening mechanism through precise structure analyses”.

(Stefanus Harjo)

Reference

Harjo, S. et al., Neutron Diffraction Monitoring of Ductile Cast Iron under Cyclic Tension-Compression, *Acta Materialia*, vol.196, 2020, p.584–594.

5-3 Realization of a Highly Polarized Neutron Beam across a Wide Energy Range

— Development and Application of a Neutron Polarization Device Using Highly Polarized ^3He —

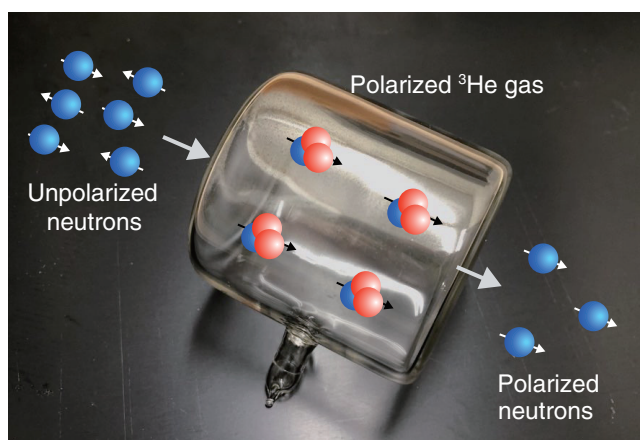


Fig.5-5 Fabricated ^3He spin filter

The developed ^3He spin filter is a neutron polarization device composed of polarized gaseous ^3He gas and alkali metal encapsulated into a special glass cell that does not include boron. ^3He has a large absorption cross-section (10666 b) of neutrons with an anti-parallel spin state; nevertheless, the absorption cross-section of neutrons with a parallel spin state is approximately zero. The neutron beam is polarized as it passes through a glass cell containing polarized ^3He . The ^3He spin filter can polarize neutrons over a wide energy range, including high-energy neutrons over 100 meV.

Neutrons have important characteristics such as having no electric charge, high transmittance, and a large cross-section for light elements, as well as having a spin. However, magnetic supermirrors, widely used to polarize neutrons, can only polarize neutrons below several tens of meV. The pulsed neutron source at the Materials and Life Science Experimental Facility in J-PARC can provide neutrons across a wide energy range (from 1 meV to 1 keV), unlike reactor neutron sources.

To further broaden this range, we developed a ^3He spin filter, which is a neutron polarization device comprising nuclear spin-polarized gaseous ^3He encapsulated in a glass cell (Fig.5-5). The ^3He spin filter can polarize neutrons with energies ranging from 1 meV to 10 eV by adjusting the amount of ^3He gas and is suitable to analyze the spin of neutrons scattered by a sample due to its large solid angle coverage. The key to developing this device was determining how to polarize the ^3He gas with a high polarization ratio while maintaining the polarization on the neutron beamline. Since impurities in the glass cell reduce the ^3He polarization, we constructed a vacuum system to supply ^3He gas to the glass cell while minimizing contamination. A laser irradiation system of approximately 100 W was also constructed to polarize the ^3He gas. Finally, the developed ^3He spin filter demonstrated a ^3He polarization of 85%, representing the highest

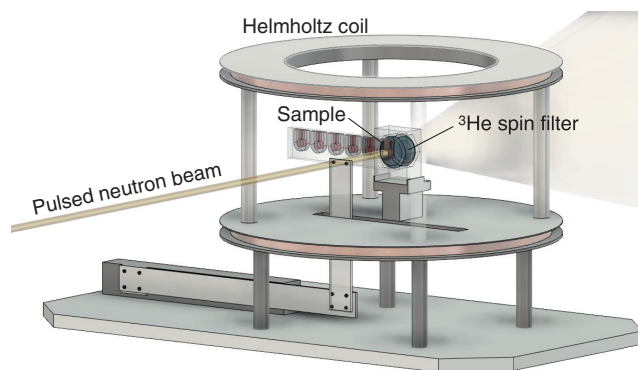


Fig.5-6 Instrument used for neutron polarization analysis that uses the ^3He spin filter in a small-angle neutron scattering experiment

The spin of neutrons scattered by a sample was analyzed using the ^3He spin filter. A magnetic field was applied to the ^3He spin filter with a Helmholtz coil to maintain ^3He polarization during the experiment. By installing this instrument to beamline BL15 (i.e., TAIKAN), we verified the usefulness of the ^3He spin filter to determine the structure of a material containing hydrogen atoms.

documented neutron polarization. Generally, ^3He polarization gradually decreases when laser irradiation is stopped due to impurities inside the glass cell and the surrounding non-uniform magnetic field. Therefore, we established a gas filling procedure to remove impurities inside the glass cell and developed a uniform magnetic field environment on the beamline to maintain a long-lasting ^3He polarization.

The developed ^3He spin filter was installed in beamlines BL04, BL06, BL10, BL15, and BL21, and experiments using neutron beams were performed. A neutron beam of approximately 1 eV was successfully polarized in BL04: Accurate Neutron-Nucleus Reaction measurement Instrument (ANNRI); this allowed us to discover the angular distribution of the γ -rays emitted in the polarized neutron absorption reaction of ^{139}La . Additionally, we verified that neutron polarization analysis using the ^3He spin filter can be used to determine the position of hydrogen atoms in materials in pulsed neutron small-angle scattering experiments (Fig.5-6) during experiments performed using the small and wide-angle neutron scattering instrument “TAIKAN” (BL15). Many experiments using ^3He spin filters have since been performed, and various scientific results are expected to be obtained in the future.

(Takuya Okudaira)

Reference

Okudaira, T. et al., Development and Application of a ^3He Neutron Spin Filter at J-PARC, Nuclear Instruments and Methods in Physics Research Section A, vol.977, 2020, 164301, 8p.

5-4 Strange Short-Range Order of Conduction Electron Spins Realized at High Temperatures — Unexpected State Found in the Newly Synthesized Magnet, Mn_3RhSi —

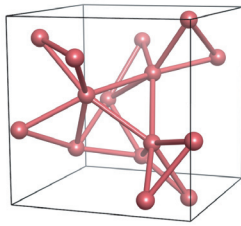


Fig.5-7 Arrangement of magnetic Mn atoms in the Mn_3RhSi lattice without special inversion symmetry

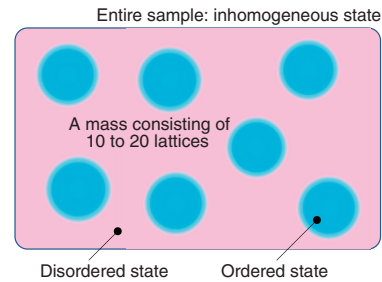


Fig.5-9 Schematic of the expected magnetic SRO state in Mn_3RhSi

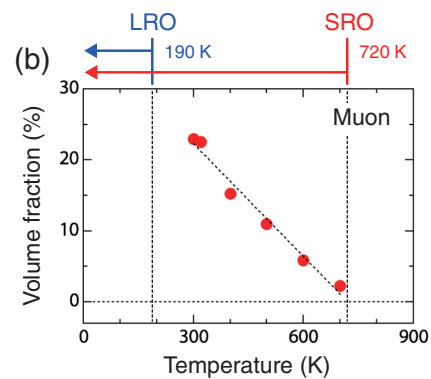
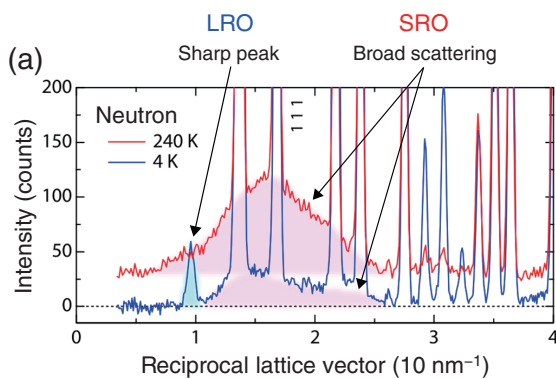


Fig.5-8 Observation of ordered states by complementarity use of neutron scattering and muon spin relaxation

(a) Neutrons reveal the state and structure of the magnetic order, whereas (b) muons reveal the temperature dependence of the volume fraction for the region of the magnetic short-range order (SRO) in the sample. LRO = long-range order.

Electron spins contribute to the magnetism of materials at the atomic level. In the paramagnetic phase of magnetic materials, the electron spins are in a disordered state; however, the spins shift to a long-range order (LRO) state in the ordered phase at low temperatures. Although this state change occurs as the development of order parameters from the phase transition temperature to lower temperatures in most cases, a local high-order state, known as short-range order (SRO), can emerge as a precursor phenomenon at temperatures above the phase transition temperature. However, several intermediate states that cannot be regarded as precursor states have been found in metallic magnets, in which locally ordered regions are phase-separated inhomogeneously. The origin of these states, however, has remained a mystery for many years.

We considered that the inhomogeneity of order parameters might owe to the spatial inversion symmetry breaking and then searched for materials to verify this hypothesis. As a result, we successfully synthesized a novel cubic metallic magnet without spatial inversion symmetry, Mn_3RhSi (Fig.5-7).

Using a neutron scattering technique, we observed long-range and short-range antiferromagnetic magnetic orders occurring

in Mn_3RhSi (Fig.5-8(a)). In neutron scattering, the intensities and periodicity of sharp peaks can be used to determine the average size and arrangement of magnetic moments of the entire sample. Additionally, the volume fraction of the short-range ordered state was investigated using the muon spin relaxation (μSR) in a complementary use as a microscopic local probe (Fig.5-8(b)). Thus, the phase separation and magnitude of the magnetic moment in the short-range ordered state were determined. Finally, the short-range magnetic order phase separation in Mn_3RhSi from the paramagnetic phase was maintained up to a temperature of 720 K, which is much higher than the antiferromagnetic transition temperature of 190 K (Fig.5-9). Moreover, even below the antiferromagnetic transition temperature, a novel phase-separation state was observed in which the SRO coexists with the LRO of a different structure. These findings will help us understand the inhomogeneous ordering of conduction electrons in metallic magnets.

This work was supported by the Japan Society for the Promotion of Science (JSPS) KAKENHI Grant-in-Aid for Scientific Research (C) (No.JP25390133).

(Hiroki Yamauchi)

Reference

Yamauchi, H. et al., High-Temperature Short-Range Order in Mn_3RhSi , *Communications Materials*, vol.1, 2020, 43, 6p.

5-5 Development of a Metal Adsorbent Using Bone Waste

— A Low-Cost and High-Performance Metal Adsorbent Prepared from Food Waste —

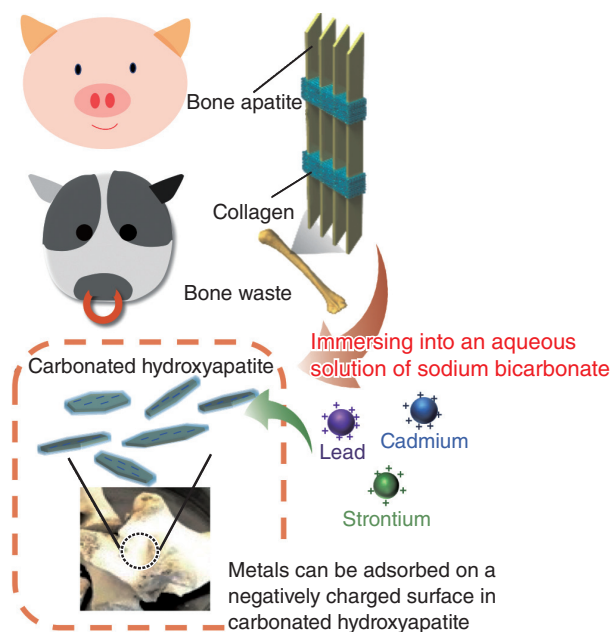


Fig.5-10 Schematic of metal adsorbents using bone waste
Carbonated hydroxyapatites prepared from bone waste-adsorbed metal ions such as strontium and cadmium with high efficiency.

Decontamination of a wide range of pollutants has been identified as a key challenge for building a sustainable and safe society, especially after the accident at TEPCO's Fukushima Daiichi NPS in 2011. The development of effective methods for removing pollutants from the environment remains an important research topic.

Biological hydroxyapatite (HAP) that can be extracted from animal bone is an interesting material because it exhibits greater adsorptivity for cadmium (Cd), strontium (Sr), and uranium (U) than those exhibited by synthetic HAPs. However, the ion-adsorption performance is lower than that of other conventional materials. The ion adsorptivity of biological HAP has been considered to depend on its highly substituted carbonate ions, but the adsorption mechanisms have not yet been fully elucidated.

This study aims to use bone waste to develop low-cost effective metal adsorbents that can adsorb ^{90}Sr and heavy metals (Fig.5-10). In this study, we focused on the correlation between the high carbonation substitution ratio, which is the most characteristic property of biological HAP, and adsorption

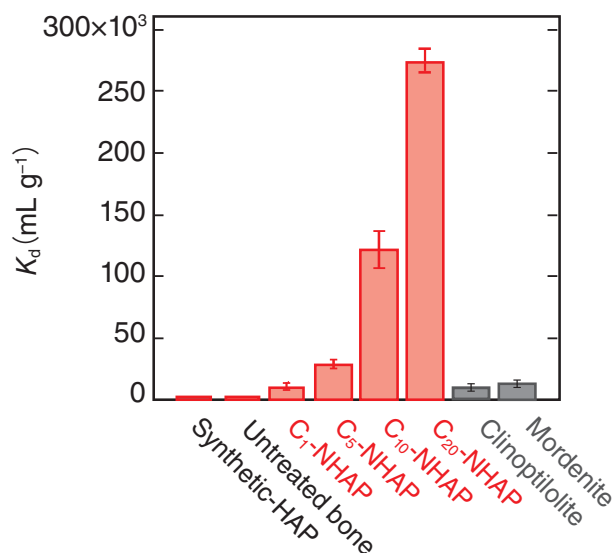


Fig.5-11 Distribution coefficients (K_d) of C_x -NHAPs, natural bone, synthesized HAPs, clinoptilolite, and mordenite
 x in C_x -NHAPs corresponds to the concentration of NaHCO_3 (wt%) in the immersion solution.

performance. First, bulk pig bone was immersed in water and autoclaved to eliminate the residual organic compounds. Then, the heat-treated bone was immersed in aqueous sodium bicarbonate (NaHCO_3) solutions to obtain highly carbonated nanohydroxyapatites (C-NHAP). We investigated its performance with respect to the adsorption of Sr^{2+} and Cd^{2+} . The distribution coefficient (K_d) of the C-NHAP for Sr^{2+} was approximately 20 and 250 times greater than those of clinoptilolite and the untreated bone, respectively (Fig.5-11). The K_d value of the C-NHAP for Cd^{2+} was approximately 370 and 23 times greater than those of the untreated bone and clinoptilolite, respectively. The amount of introduced CO_3^{2-} into C-NHAP increased with the increasing NaHCO_3 concentration in the immersion solution. With the increasing amount of CO_3^{2-} ions introduced into the C-NHAP, it exhibited a greater ion-adsorption performance.

The CO_3^{2-} substitution approach presented in this study would be a useful strategy for the development of high-performance HAP adsorbents for toxic ions, especially ^{90}Sr , by efficiently using waste bones.

(Yurina Sekine)

Reference

Sekine, Y. et al., Carbonated Nanohydroxyapatite from Bone Waste and Its Potential as a Super Adsorbent for Removal of Toxic Ions, Journal of Environmental Chemical Engineering, vol.9, issue 2, 2021, 105114, 12p.

5-6 Fast Molecules Passing through Carbon-Atom Net — Discovery of Oxygen Molecules Slipping through Graphene —

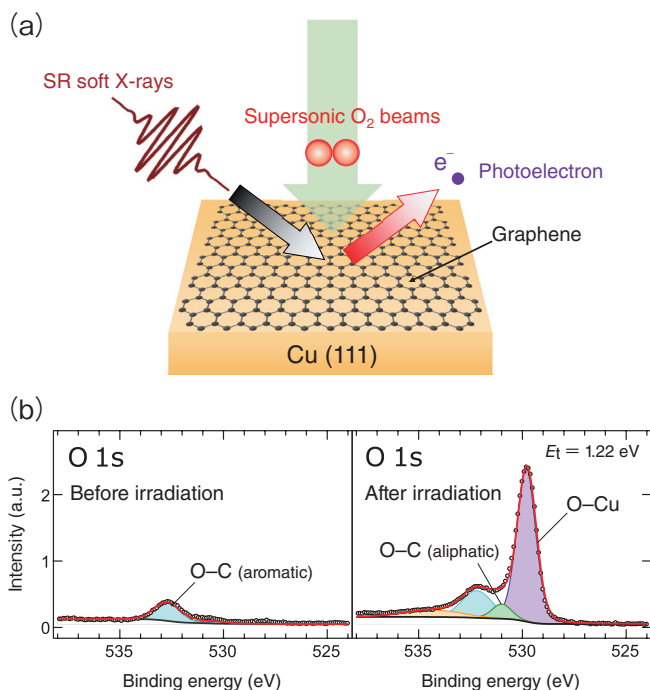


Fig.5-12 Gas barrier experiment by using real-time synchrotron radiation X-ray photoelectron spectroscopy (SR-XPS) combined with supersonic molecular beams and experimental evidence of O₂ permeation through graphene

(a) Conceptual diagram of SR-XPS measurements for irradiating graphene on a Cu substrate with oxygen beams. (b) X-ray photoelectron spectral change after irradiation with O₂ beams with the translational energy of 1.22 eV. The increase in the O-Cu component (purple) is evidence that O₂ penetrates graphene and oxidizes the Cu surface.

Graphene, a carbon-atom net, has been attracting attention as a next-generation functional material because of its excellent physical properties such as low electrical resistance. Due to its unique physical properties, the Nobel Prize in Physics was awarded in 2010 for its discovery. Furthermore, as it is known that graphene has excellent gas barrier property, it is expected to be used as a protective film for easily oxidized transition metal catalysts (Ni, Cu, etc.). However, details of gas barrier properties remain unclear.

As is well known, the majority of O₂ in an environment such as the atmosphere have kinetic energy (Et) of about 26 meV, however there are also small amounts of O₂ with higher energies, which may overcome activation barriers in reaction pathways. Real-time SR-XPS using X-rays at 700 eV was applied to analyze the graphene/Cu(111) after O₂ irradiation with various Et controlled by the supersonic molecular beams technique (Fig.5-12(a)). All experiments were conducted at the surface experimental station of the JAEA soft X-ray beamline (BL23SU) at SPring-8.

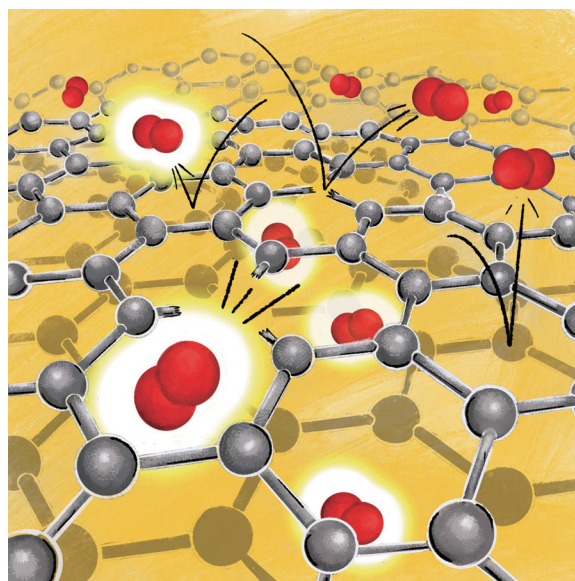


Fig.5-13 An image of an oxygen molecule passing through graphene (a net made of a single layer of carbon atoms)

A slow oxygen molecule bounces off the carbon net and cannot pass through, while a fast molecule (> 0.8 eV) can pass through.

Fig.5-12(b) shows O 1s photoelectron spectra before (left) and after (right) irradiation for O₂ with 1.22 eV. An increase in the peak exhibiting surface oxidation was clearly observed. A similar change in the spectrum was observed for O₂ higher than 0.8 eV. Furthermore, it was found that the gas barrier property was maintained even after permeation. In addition to synchrotron experiments, computer simulations clarify that the permeation of O₂ with higher energies occurs nondestructively with the aid of defects in graphene (Fig.5-13). The discovery of nondestructive transmission of O₂ with high incident energies is expected to be applied to molecular filters. Since high-speed O₂ are all around us, it is expected to produce a new type of protective films that prevent food deterioration, metal rusting and so on.

This research is part of the results of a joint research project with Tohoku University entitled “Synchrotron Radiation Realtime Photoemission Spectroscopic Study of Material Surface Processes”.

(Akitaka Yoshigoe)

Reference

Ogawa, S., Yoshigoe, A. et al., Gas Barrier Properties of Chemical Vapor-Deposited Graphene to Oxygen Imparted with Sub-electronvolt Kinetic Energy, The Journal of Physical Chemistry Letters, vol.11, issue 21, 2020, p.9159–9164.

5-7 Atomic-Level Observation of Magnetic Ordering Process in Ferromagnetic Semiconductors

— Exploring the Mechanism of Ferromagnetism for Its Practical Use in Spintronics Devices —

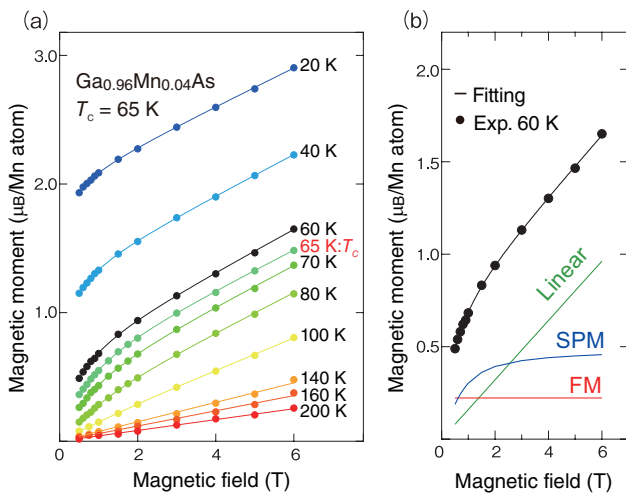


Fig.5-14 Temperature and magnetic field dependence of the XMCD for $\text{Ga}_{0.96}\text{Mn}_{0.04}\text{As}$

(a) Experimental and fitting results are represented by solid circles and lines, respectively. (b) Red, green and blue lines show the extracted FM, Linear magnetic, and SPM components, respectively; the black solid line shows the sum of these three components.

Ferromagnetic semiconductors (FMSs), which possess both semiconductor and ferromagnetic (FM) properties, have attracted attention as next-generation spintronics materials. The discovery of ferromagnetism in manganese-doped gallium arsenide ($\text{Ga}_{1-x}\text{Mn}_x\text{As}$; (Ga, Mn)As) broadened the research field of FMSs. Despite enthusiastic investigations, however, there has been controversy over the origin of ferromagnetism for over 20 years. Ferromagnetism appears below the Curie temperature (T_C); to apply FMS to spintronics devices, it should be achieved at room temperature. The highest reported T_C of (Ga, Mn)As, however, is -73°C .

To understand the mechanism of ferromagnetism, it is necessary to clarify the element-selective spin states of Mn responsible for the magnetic properties of (Ga, Mn)As and investigate how ferromagnetism develops. Therefore, we performed X-ray magnetic circular dichroism (XMCD) experiments at JAEA's beamline BL23SU of SPring-8 to observe the magnetic ordering process.

The observed dependence of the magnetic moment of the Mn 3d electrons on the temperature and magnetic field are shown in Fig.5-14(a), as estimated from the XMCD intensity for $\text{Ga}_{0.96}\text{Mn}_{0.04}\text{As}$ with $T_C = 65\text{ K}$. The magnetic moment becomes large as the temperature decreases and magnetic field increases, as shown in Fig.5-14(a). This behavior clearly shows development of the FM state at the low temperatures and high

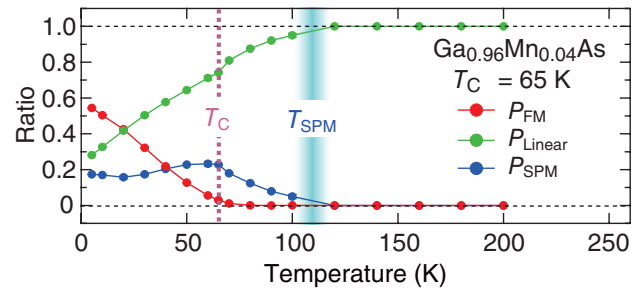


Fig.5-15 Temperature dependence of the ratio of each magnetic component

As the temperature continued to decrease after reaching the Curie temperature (T_C), the FM component (P_{FM}) increased. On the other hand, the SPM component (P_{SPM}) began increasing around a certain temperature (T_{SPM}), which is well above T_C .

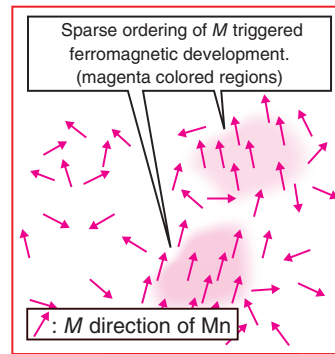


Fig.5-16 Schematic of the magnetic ordering process around T_{SPM}

Arrows represent the magnetic moment (M) of Mn atoms. FM domains (magenta-colored regions) begin developing sparsely around T_{SPM} and then overlap at T_C .

magnetic fields.

Fitting allowed three magnetic components to be identified: FM, linear, and superparamagnetic (SPM). Against the magnetic field, these components were constant, increased linearly, and increased non-linearly, respectively, as shown in Fig.5-14(b). The ratio of each component to the total magnetic moment was then defined as P_{FM} , P_{Linear} , and P_{SPM} , respectively (i.e., $P_{\text{FM}} + P_{\text{Linear}} + P_{\text{SPM}} = 1$ for each measured temperature). The observed temperature dependence of P_{FM} , P_{Linear} , and P_{SPM} is shown in Fig.5-15. Here P_{FM} began increasing as the temperature decreased below T_C . On the other hand, P_{SPM} began increasing around a certain temperature (T_{SPM}) above T_C , reached a maximum near the T_C , and then decreased. This behavior was also observed in other samples with different Mn concentrations and values of T_C . These results indicate that SPM regions begin forming at temperatures above T_C , i.e., T_{SPM} , and that SPM regions overlap at the T_C (Fig.5-16).

This result was selected as a featured paper and the cover of the issue, and an explanatory article was also published.

This work is a part of the results of a joint research project with the University of Tokyo and Kyoto Sangyo University, entitled "Development of functional magnetic semiconductor thin films and study of their electronic states using synchrotron radiation".

(Yukiharu Takeda)

Reference

Takeda, Y. et al., Direct Observation of the Magnetic Ordering Process in the Ferromagnetic Semiconductor $\text{Ga}_{1-x}\text{Mn}_x\text{As}$ via Soft X-ray Magnetic Circular Dichroism, Journal of Applied Physics, vol.128, issue 21, 2020, 213902, 11p.

Research and Development on HTGR, Hydrogen Production, and Heat Application Technologies

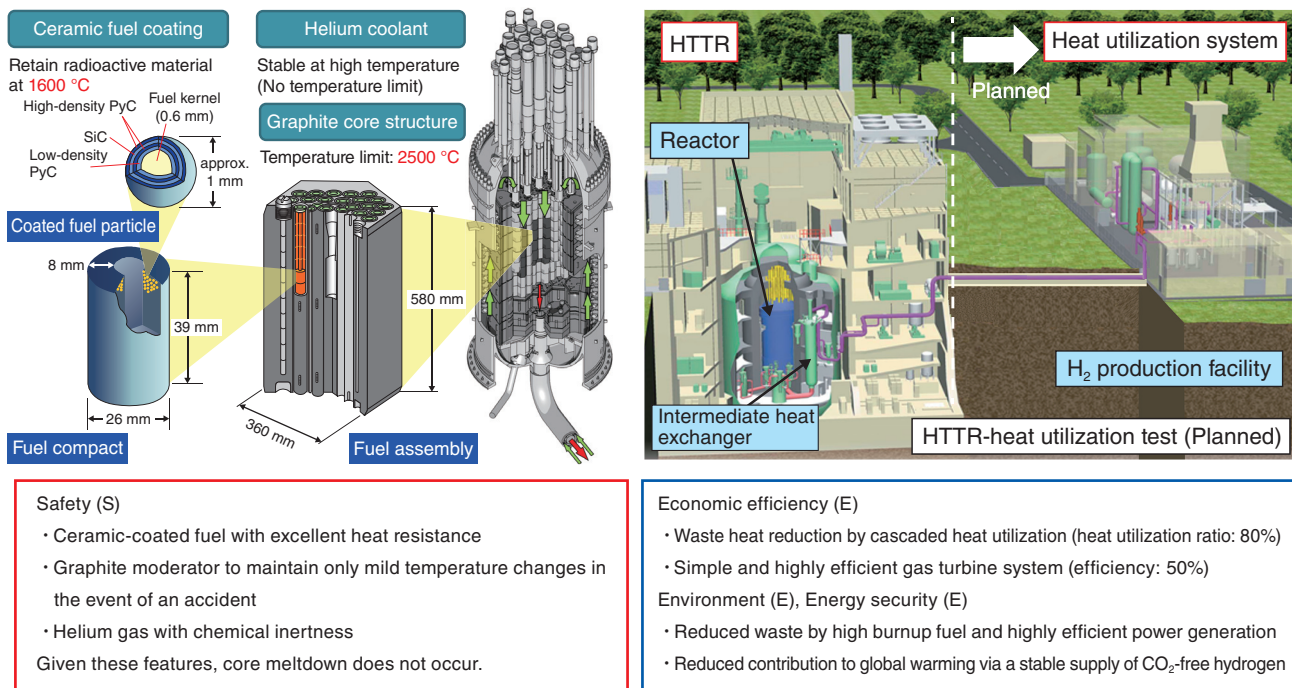


Fig.6-1 Features of the HTGR and plan of the HTTR-heat utilization test

A high temperature gas-cooled reactor (HTGR) is a helium gas-cooled and graphite-moderated thermal-neutron reactor with excellent inherent safety features. The HTGR meets various heat application requirements, including hydrogen production and power generation. The HTGR also meets the 3E+S policy targets in Japan's Strategic Energy Plan. JAEA's final target is the successful demonstration of coupling a nuclear reactor and heat application systems by connecting a gas turbine and hydrogen production facilities to Japan's first HTGR, that is, the high temperature engineering test reactor (HTTR).

A high temperature gas-cooled reactor (HTGR) is a nuclear reactor with various industrial uses, including high-efficiency power generation and hydrogen production (Fig.6-1). Japan Atomic Energy Agency (JAEA) has been conducting various demonstration tests using the high temperature engineering test reactor (HTTR), developing the hydrogen production technology and gas turbine that utilize high-temperature heat, researching on commercial HTGRs for practical uses, and promoting international cooperation.

In 2004, the HTTR was the only nuclear reactor in the world that can supply high-temperature heat up to 950 °C. In 2010, the reactor outlet temperature of 950 °C was stably supplied in 50 days of continuous operation, demonstrating the HTGR's stable supply of high-temperature heat. The inherent safety feature of the HTGR was also confirmed in a loss-of-forced-cooling test without a reactor scram. Even if the cooling and shutdown functions were not activated in the test, the reactor power dropped to zero, and the decay heat was naturally removed. After the Great East Japan Earthquake in 2011, the HTTR operation was stopped for a long time due to the safety review by the Nuclear Regulation Authority of Japan against the new nuclear regulatory standards established in 2013. In June 2020, the HTTR obtained permission to change the reactor installation, and restarted in July 2021.

In December 2020, the Ministry of Economy, Trade and Industry executed leadership and formulated an industrial policy, called the "Green Growth Strategy Through Achieving Carbon Neutrality in 2050", in response to the "2050 carbon-neutral and a carbon-free society" declared by Prime Minister Yoshihide Suga in October 2020. In this green growth strategy, the nuclear

industry is designated as one of 14 important fields, where future growth is expected. The targets of the nuclear industry are small modular reactors, high temperature gas-cooled reactors, and fusion energy. The future efforts of the HTGR include: (1) utilization of the HTTR, in which the government will support, in addition to international safety demonstration, the necessary technology development for massive and low-cost carbon-free hydrogen production by 2030; (2) government's participation in technology development and demonstration while giving thoughts to safety, economy, supply chain construction, regulatory compliance, and so on and government's creation of overseas joint projects based on the status of preceding overseas projects; and (3) promotion of cooperation with the related organizations of other countries to disseminate Japanese standards through construction, operation.

JAEA is steadily advancing the research and development of the HTGR-related technology with great expectation. The research and development for practical uses include the prediction of the heat flow behavior in the HTGR during normal operation and accidents, nuclear design policy for maintaining the integrity of coated fuel particles, and reduction of excess plutonium (Topics 6-1-6-3). Regarding the development of hydrogen production using the IS process, JAEA is developing the corrosion test for corrosion-resistant metal materials and separation membranes and electrode materials for improving the hydrogen production efficiency (Topics 6-4-6-6). For the technical development related to the HTTR operation, a utility tool has been developed to automatically seek for the critical control rod position during a normal operation (Topic 6-7).

6-1 Prediction of Thermal-Hydraulic Behavior in HTGR Accidents

— Development of Evaluation Methodology of Air-Ingress Behavior in HTGR —

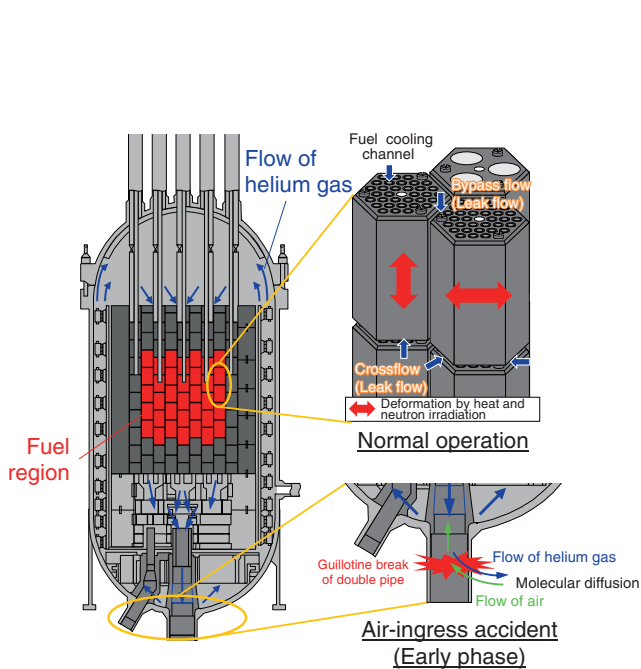


Fig.6-2 Illustration of the thermal-hydraulic phenomena in the HTGR

Leak flow between the gaps generated by the graphite block deformation as a result of the thermal and neutron irradiation effect and air-ingress into the reactor by molecular diffusion in the beginning of the air-ingress accident in the HTGR.

We are developing high temperature gas-cooled reactors (HTGRs) with inherent safety features for the multi-purpose use of nuclear energy. The air-ingress accident causing the graphite structure oxidation inside a reactor is one of the specific accidents in HTGRs. It is important to predict the onset time of the natural circulation in the reactor following the air-ingress in the safety analysis for the accident. However, the safety analysis has been performed in a conservative manner, assuming the onset time of the natural circulation to overestimate the amount of graphite oxidation due to the difficulties in evaluating the flow resistance and the air concentration distribution. Adjusting the conservativeness in the evaluation method and accurately predicting the delay of the onset time of the natural circulation will further improve the economic performance of the HTGR while keeping its safety features. The present study develops an evaluation method of the air-ingress behavior during the air-ingress accident in the HTGR using a nuclear system analysis code (RELAP5) by utilizing experiences on high temperature engineering test reactor (HTTR) construction.

The leakage flow in the HTGR is observed as shown in Fig.6-2, which depicts the helium gas flow through the gaps between the graphite blocks deformed by thermal expansion and neutron irradiation avoiding the fuel cooling channel. The temperature and pressure loss distributions at the fuel cooling, bypass flow, and crossflow channels must be precisely

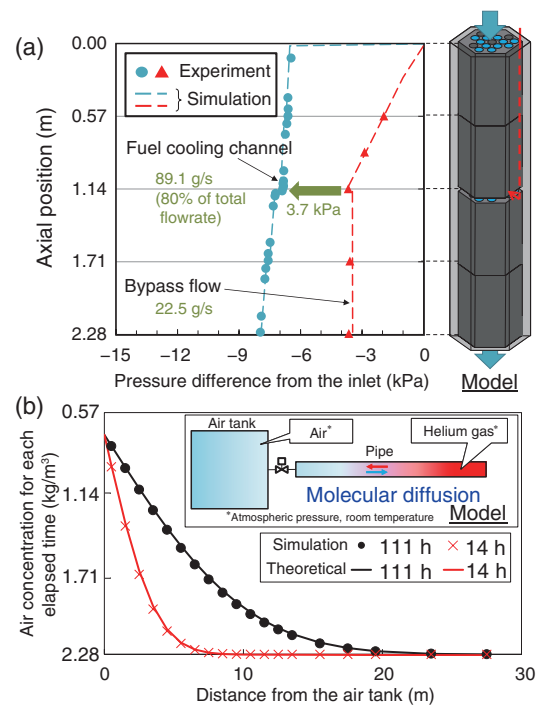


Fig.6-3 (a) Model and results of the leak flow simulation and (b) model and results of the molecular diffusion simulation

The simulation results agreed well with the experimental and theoretical results by the leak flow improvement and the molecular diffusion simulations.

evaluated for realistic evaluations of the leakage flow and the fuel temperature. The code was improved by installing the pressure loss evaluation models formulated by previous experiments and the detailed heat transfer distribution of radiation. A model was newly installed to the code to treat one-dimensional molecular diffusion to predict the air concentration in the reactor in the air-ingress accident.

The simulation results were compared with the experimental results and theoretical solutions to validate the developed method. Fig.6-3(a) shows model and the results of the leak flow simulation. The comparison of the simulation and experimental results obtained for a mock-up test composed of four piled blocks simulating fuel cooling, bypass flow, and crossflow channels showed a good agreement of the pressure loss in the crossflow with the experimental results. Fig.6-3(b) illustrates the simulation model and results for the validation of the molecular diffusion model. The calculated air concentration was compared with the theoretical solution in the air-helium mixing process by molecular diffusion between two volumes initially filled with each gas. The results agreed with the theoretical solution in the range of $\pm 2\%$ for the initial air concentration.

The evaluation model regarding the local three-dimensional natural convection phenomena will be developed for further development of the evaluation methodology.

(Takeshi Aoki)

Reference

Aoki, T. et al., Methodology Development for Transient Flow Distribution Analysis in High Temperature Gas-Cooled Reactor, Proceedings of 2020 International Conference on Nuclear Engineering (ICONE 2020), online, U.S.A., 2020, ICONE2020-16199, 6p.

6-2 Nuclear Design Policy to Maintain the Integrity of Coated Fuel Particles

— Derivation of the Ideal Power Distribution to Minimize the Kernel Migration Rate —

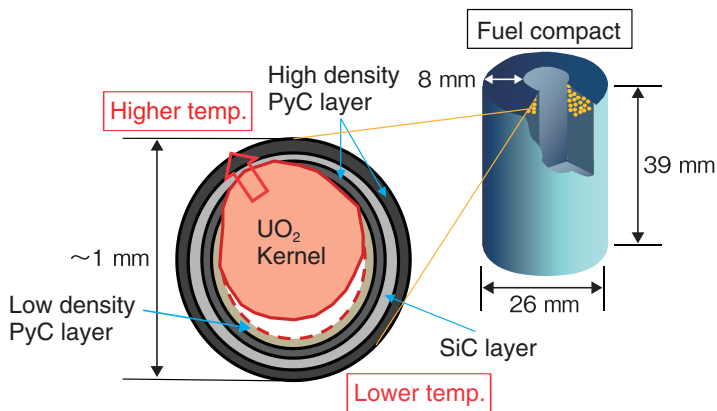


Fig.6-4 Kernel migration mechanism

As the burnup proceeds, the carbon in the coating layer reacts with the free oxygen from the UO_2 kernel, vaporizes in the higher-temperature region, and accumulates in the lower-temperature region. Kernel migration is a phenomenon, in which the kernels are pushed out into the gap created in the high-temperature region. The kernel migration rate (KMR) depends on the temperature and the temperature gradient in the fuel compact.

Coated fuel particles (CFPs) are used in high temperature gas-cooled reactors (HTGRs). They consist of a uranium dioxide (UO_2) kernel coated with multiple layers of pyrolytic carbon and silicon carbide. This coating layer retains the fission products (FPs) within the CFPs. Kernel migration is known as one of the major CFP failure modes for impairing this FP retention function of the coating layer (Fig.6-4). The kernel migration magnitude is evaluated as an integral of the kernel migration rate (KMR) with respect to time. Therefore, to maintain the CFP integrity from the viewpoint of weakening kernel migration and further improve the burnup in the future, the reactor must be designed such that the KMR is reduced as much as possible. However, the nuclear design policy to maintain the CFP integrity in terms of weakening kernel migration has not been explicitly proposed before. Therefore, we first focus herein on the condition of the ideal power distribution that minimizes the KMR. If the conditions for such an ideal power distribution can be clarified, an actual power distribution can be brought closer to the ideal power distribution by optimizing the arrangement of the fuel enrichment.

The ideal power distribution that minimizes the KMR can

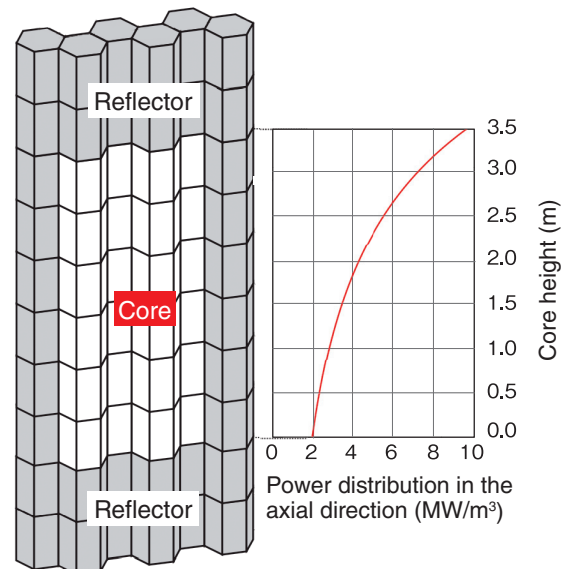


Fig.6-5 Ideal power distribution minimizing the kernel migration rate

The ideal power distribution is obtained for a high temperature gas-cooled reactor (HTGR) with 50 MWth. The power density is lower at the bottom of the core and higher at the top of the core.

be expressed as the power distribution that realizes the state where the KMR maximum value is the smallest. First, by utilizing the Lagrange undetermined multiplier method, the ideal power distribution that minimizes the KMR can be realized when the KMR distribution takes a constant value (i.e., when the KMR distribution becomes flat). Second, we developed a numerical method to gradually flatten the KMR distribution by iteratively updating the power distribution because it was difficult to analytically determine the shape of the ideal power distribution due to the complexity of the equations to be solved.

After the abovementioned procedure, we obtained the power distribution that flattened the KMR distribution in the axial direction (Fig.6-5). This allowed us to derive the ideal power distribution to minimize the KMR and propose a nuclear design policy to maintain the CFP integrity (e.g., optimization of the fuel enrichment arrangement from the viewpoint of weakening kernel migration). In the future, we will work on the design study of a commercial HTGR with a long-term burnup by optimizing the fuel enrichment arrangement, reflecting the findings of this study.

(Shoichiro Okita)

Reference

Okita, S. et al., Derivation of Ideal Power Distribution to Minimize the Maximum Kernel Migration Rate for Nuclear Design of Pin-in-Block Type HTGR, *Journal of Nuclear Science and Technology*, vol.58, issue 1, 2021, p.9-16.

6-3 Toward the Realization of High Temperature Gas-Cooled Reactor for Safe Reduction of Plutonium Inventory — Microstructure Observation of a Simulated Fuel Kernel —

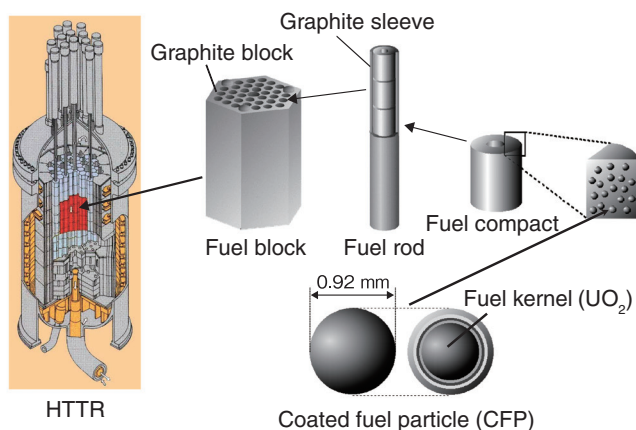


Fig.6-6 Fuel of the High Temperature Engineering Test Reactor (HTTR) in Japan Atomic Energy Agency^{*1,*2}

A UO_2 fuel kernel was coated with four-layered coating layers to form a coated fuel particle (CFP) with a diameter of approximately 1 mm. Compacts were put into a graphite sleeve to form a fuel rod.

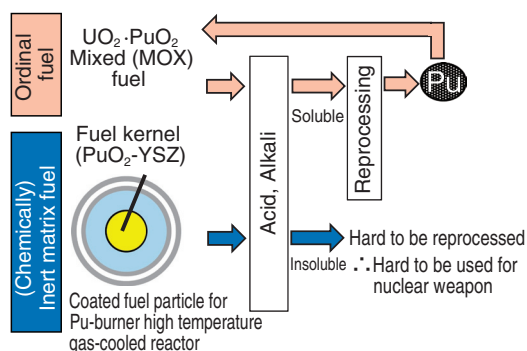


Fig.6-7 Structure of the CFP with (chemically) inert matrix fuel and its nuclear proliferation resistance

The yttria-stabilized zirconia (YSZ) used in this CFP as the inert matrix is chemically stable and insoluble in acid and alkali. YSZ makes the fuel difficult to reprocess and increases the nuclear proliferation resistance of fuel.

The Japanese government made an international commitment not to possess excess amount of plutonium (Pu) in its utilization plan. A high temperature gas-cooled reactor (HTGR) has inherent safety features; hence, the concept of the Pu-burner HTGR was proposed to safely reduce the amount of recovered Pu.

The minimum unit of the HTGR fuel is coated fuel particle (CFP) with a diameter of approximately 1 mm. Fissile materials and fission products are contained in each CFP. The CFP used in the High Temperature Engineering Test Reactor (HTTR), which is a HTGR test reactor constructed in Oarai Research and Development Institute in JAEA, employs a UO_2 fuel kernel coated with four-layered coating layers (Fig.6-6). In the Pu-burner HTGR concept, the CFP, whose fuel kernel consists of inert matrix fuel, is employed. The inert matrix fuel should be chemically stable and should be hard to reprocess (Fig.6-7). The nuclear proliferation resistance of the CFP with inert matrix fuel kernel should be high. In this study, yttria-stabilized zirconia (YSZ) containing PuO_2 (PuO_2 -YSZ) was employed as the fuel kernel.

The Nuclear Fuel Industries, Ltd. took charge of the development of fabrication technology of the PuO_2 -YSZ kernel and fabricated the simulated PuO_2 -YSZ kernels. We observed the microstructure of a fabricated simulated PuO_2 -YSZ kernel as a part of the inspections.

Cerium (Ce) was used as the material simulating Pu. The

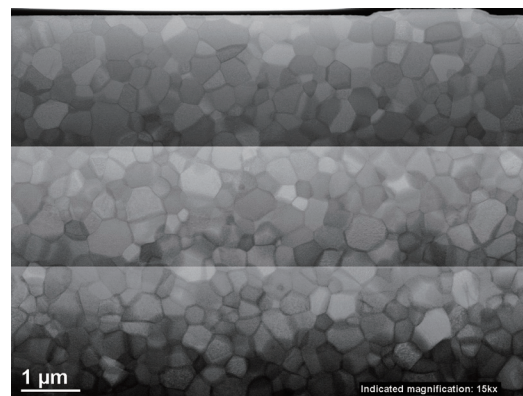


Fig.6-8 Microstructure of the center region of the CeO_2 -YSZ kernel (scanning transmission electron microscopic bright-field image)

There are hardly spaces between crystal grains. If the crystal grains are not densely distributed, the fuel kernel may not contain enough Pu.

(reprinted from Aihara, J. et al., Influences of the ZrC Coating Process and Heat Treatment on ZrC-coated Kernels used as Fuel in Pu-burner High Temperature Gas-cooled Reactor in Japan, Journal of Nuclear Science and Technology, Vol.58, 2021, p.107-116. Published online: 23 Aug 2020, Taylor & Francis Ltd, by permission of Taylor & Francis Ltd, <http://www.tandfonline.com>)

chemical properties of Ce imitate those of Pu. A solution was prepared by dissolving Ce, Y, and Zr nitrate powders in water. The prepared solution was dropped into ammonia water to form gelled particles. These gelled particles were then sintered to form the CeO_2 -YSZ kernels.

We observed the center region of the fabricated CeO_2 -YSZ kernel and found that the crystal grains were densely distributed (Fig.6-8). This result indicates the possibility that the fabrication method of the fuel kernel similar to that described above is proper. If the crystal grains are not densely distributed, the fuel kernel may not contain enough Pu.

This study includes the results of the “Development of Security and Safety Fuel for Plutonium Burner HTGR” performed under the Innovative Nuclear Research and Development Program by the Ministry of Education, Culture, Sports, Science and Technology (MEXT), Japan.

(Jun Aihara)

*1 Goto, M. et al., Conceptual Design of Small-Sized HTGR System (II) - Nuclear Design -, JAEA-Technology 2012-017, 2012, 29p.

*2 HTGR Research and Development Center, Japan Atomic Energy Agency, What is HTGR?, <https://www.jaea.go.jp/04/o-arai/nhc/en/faq/index.html> (accessed October 14th, 2021).

Reference

Aihara, J. et al., Influences of the ZrC Coating Process and Heat Treatment on ZrC-Coated Kernels Used as Fuel in Pu-Burner High Temperature Gas-Cooled Reactor in Japan, Journal of Nuclear Science and Technology, vol.58, issue 1, 2021, p.107-116.

6-4 Toward Metallic Sulfuric Acid Decomposers in the IS Process

— Discovery of Steel Materials with Corrosion Resistance Equivalent to Ceramics in a Sulfated Gas Environment —

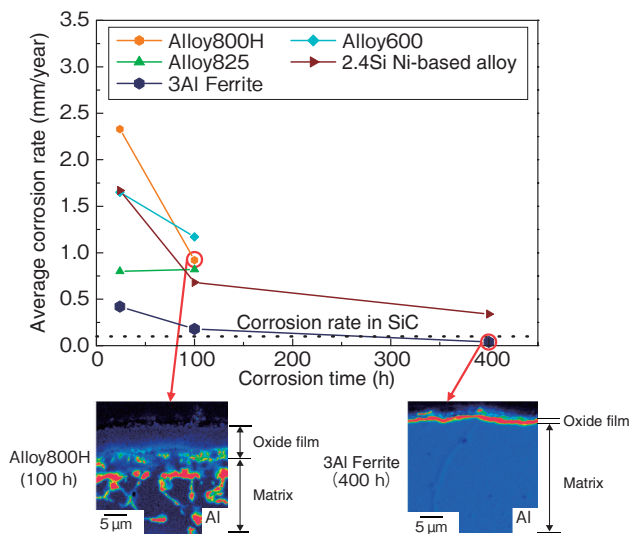


Fig.6-9 Average corrosion rate change with the increasing corrosion time of each material and Al map of the oxide film/matrix cross-section in Alloy800H and 3Al Ferrite

The corrosion rate of 3Al Ferrite at 400 h was equivalent to that of SiC. The material cross-section after the corrosion test showed that unlike Alloy800H, an Al oxide film with a uniform thickness was observed.

The iodine sulfur (IS) process, which is a thermochemical hydrogen production method that is a potential heat-application technology of high temperature gas-cooled reactors, treats highly corrosive hydrogen iodide (HI) and sulfuric acid at high temperature. Any material involved in the process must have excellent heat and corrosion resistance. In particular, the temperature inside the pressure vessel that decomposes sulfuric acid (i.e., sulfuric acid decomposer) reaches the maximum temperature in the IS process of 850 °C. Thus, ceramics (e.g., SiC) have been considered for use as sulfuric acid decomposers.

However, assuming the operation of a practical plant that will require a large amount of hydrogen production in the future, SiC is a brittle material in addition to being difficult to increase in size due to dimensional restrictions on the sintering furnace to be manufactured and difficult welding. Therefore, we started to use metallic materials that can achieve a corrosion rate of 0.1 mm/year, which is equivalent to that of SiC.

How to form the oxide film on the matrix surface when heated at a high temperature is considered to be the key point in improving the corrosion resistance. We mainly selected the following alloys: Alloy800H; Alloy825, an iron (Fe)-based alloy that forms an Fe and chromium (Cr) oxide film; 3Al Ferrite, a ferritic stainless steel that contains a large amount of aluminum (Al) that forms an Al oxide film; Alloy600, a nickel (Ni)-based alloy that forms a Ni oxide film; and 2.4Si Ni-based alloy, which contains silicon (Si) that forms a Si-based oxide film.

In the corrosion test, a 96wt% sulfuric acid solution was heated and evaporated, then further heated to 850 °C to simulate an environment similar to that of an actual plant.

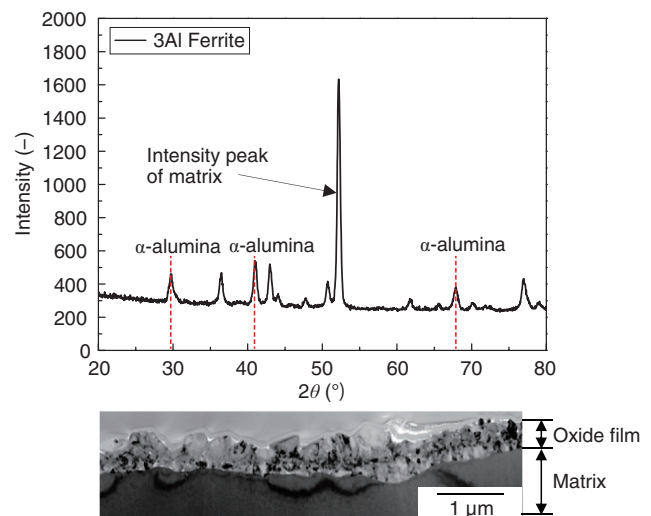


Fig.6-10 Surface structural analysis by X-ray diffraction with 3Al Ferrite and TEM-magnified observation photograph of the cross-section of the same material

The intensity peak of α -alumina was confirmed for 3Al Ferrite. In addition, the cross-section of the same material showed that the oxide film of α -alumina was a dense 1 μ m-thick film without gaps.

Fig.6-9 shows the change in the average corrosion rate with the increasing corrosion test time for each material. Alloy800H showed the worst corrosion rate after 24 h. In contrast, 3Al Ferrite was 0.42 mm/year. After 100 h, all materials had a corrosion rate lower than that after 24 h, especially 3Al Ferrite, which was 0.18 mm/year. After 400 h, the corrosion rate of 3Al Ferrite was almost the same as that of SiC.

To confirm the situation of the oxide film after the corrosion test, the Al element mapping of the film/matrix cross-section was implemented after 100 h of Alloy800H, which was severely corroded, and after 400 h of 3Al ferrite, which had excellent corrosion resistance. The Al layer existing under the Cr-based oxide film was completely destroyed in Alloy800H, while a uniform-thickness Al layer was formed in 3Al Ferrite. Fig.6-10 shows the surface structural analysis by X-ray diffraction after the corrosion test on 3Al Ferrite and the magnified microstructure observation photograph of the cross-section of the same material with a transmission electron microscope (TEM). The intensity peaks of the ferrite phase of the matrix and α -alumina of the oxide film were detected by X-ray diffraction. The TEM observation of the same material confirmed a dense 1 μ m-thick oxide film without gaps. In short, the excellent corrosion resistance of 3Al Ferrite was caused by the uniform formation of α -alumina on the matrix surface.

This research is a part of the result of the joint research “Research on corrosion resistant alloy development in IS process environment” with Nippon Steel Corporation.

(Noriaki Hirota)

Reference

Hirota, N. et al., Corrosion Resistance and Oxide Film Structure of Stainless Steels and Ni-Based Alloys under Sulfuric Decomposition Gas at High Temperature, Zairyo-to-Kankyo, vol.70, issue 3, 2021, p.68–76 (in Japanese).

6-5 Membrane Technique Advancing the IS Process

— Enhancement of the HI Conversion by Silica-Based Membrane Reactor —

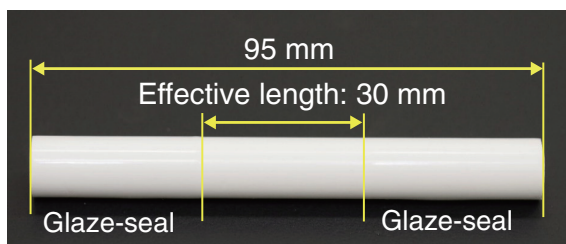


Fig.6-11 Image of a silica membrane

Silica membranes were prepared via counter-diffusion chemical vapor deposition on γ -alumina-coated α -alumina support tubes.

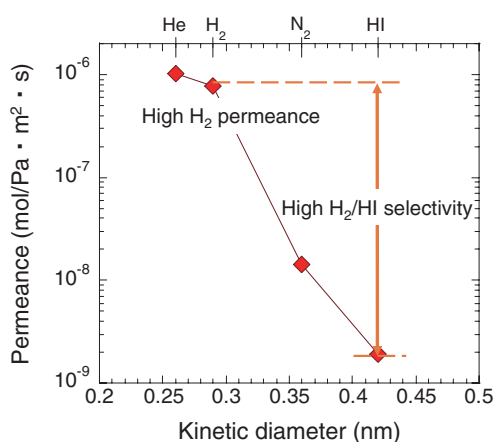


Fig.6-12 Single-gas permeation performance of the silica membrane

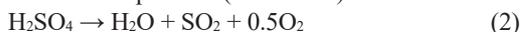
The prepared silica membrane showed a high H₂ permeance of 7.7×10^{-7} mol/Pa · m² · s and a high H₂/HI selectivity of 403.6.

The thermochemical sulfur-iodine (IS) process is studied by the JAEA to realize massive hydrogen production using nuclear heat at high temperature. This process consists of three coupled chemical reactions:

Bunsen reaction (ca. 100 °C):



Sulfuric acid decomposition (ca. 850 °C):



Hydrogen iodide decomposition (ca. 400 °C):



The HI decomposition (Eq. 3) is a key reaction in the IS process. However, the equilibrium conversion of HI to H₂ and I₂ is very low (e.g., approximately 20% at 400 °C), leading to an increase in the amount of recycled materials and a decrease in the thermal efficiency of the process. The usage of a membrane reactor that combines a catalytic reaction and H₂ separation in one unit can shift the equilibrium and enhance the HI conversion. The membrane reactor demonstration comprises two stages: i) fabrication of a membrane possessing high H₂ separation performance and high corrosion stability; and ii) reactor assembly with membrane and catalyst integration.

In this study, silica membranes consisting of a three-layer structure comprising a porous α -alumina ceramic support, an intermediate γ -alumina layer, and a top silica layer that is H₂

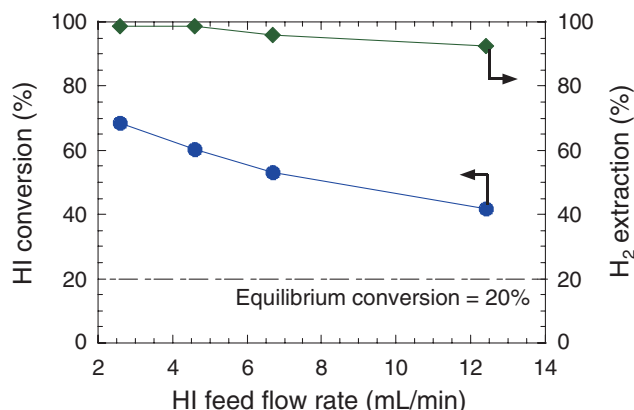


Fig.6-13 HI decomposition performances of the silica membrane reactor at T = 400 °C and HI feed flow rates of 2.6–12.4 mL/min

HI conversion greater than 70% was achieved, which is 3.5 times higher than the equilibrium conversion.

selective were prepared via the counter-diffusion chemical vapor deposition of hexyltrimethoxysilane (Fig.6-11).

Fig.6-12 presents the He, H₂, N₂, and HI permeances through the developed silica membranes. The silica membranes exhibited high H₂ permeance and high H₂/HI selectivity and were stable in the corrosive gas of HI for 11 h. Therefore, the research extended to the assembly of a membrane reactor with the integration of the silica membrane and active carbon catalyst and investigated its potential for H₂ production from the HI decomposition.

Fig.6-13 shows the results of the HI decomposition tests varying the HI feed flow rate. The influence of the HI feed flow rate on the membrane reactor performance was significant in the lower range of the flow rate. Moreover, better than 70% conversion of the HI decomposition and 98% H₂ extraction were attained. The results suggest that the developed membrane reactor equipped with the silica membrane would reduce the recycled flow rate in the HI decomposition by up to approximately 80% and improve the total thermal efficiency of the IS process by 1%.

We are currently working on the improvement of the thermal efficiency of the IS process by developing a membrane reactor equipped with industrial-size silica membranes in HI decomposition.

(Odtsetseg Myagmarjav)

Reference

Myagmarjav, O. et al., Comparison of Experimental and Simulation Results on Catalytic HI Decomposition in a Silica-Based Ceramic Membrane Reactor, International Journal of Hydrogen Energy, vol.44, issue 59, 2019, p.30832–30839.

6-6 Energy Saving of the Main Reaction in the IS Process

— Membrane and Electrode Development for the Bunsen Reaction Overvoltage Reduction —

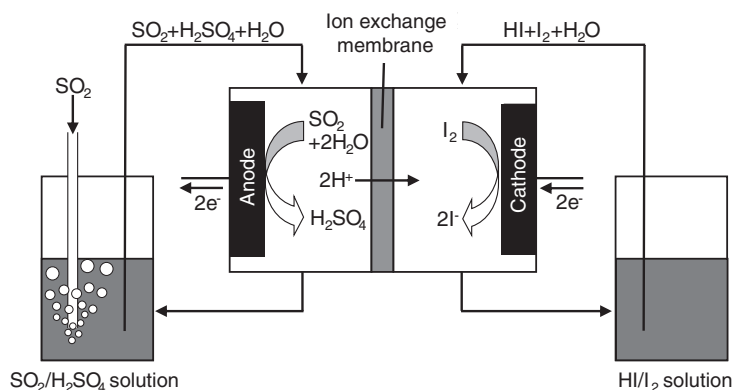


Fig.6-14 Schematic of the Bunsen reaction using the ion-exchange membrane

Hydriodic and sulfuric acids were produced on the cathode and the anode, respectively, in an electric cell equipped with an ion-exchange membrane.

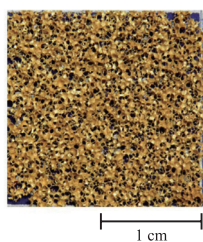


Fig.6-15 Microscopic outlook of the porous Au electrode

The porous Au surface increases the effective reaction area and allows the anode reaction to easily proceed. Consequently, the overvoltage that originated from the electrode reaction can be reduced.

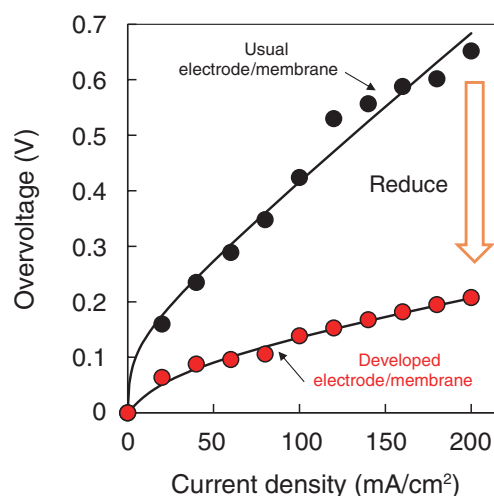


Fig.6-16 Current density dependence of the Bunsen reaction overvoltage

The overvoltage was reduced to less than 1/3 using the electric cell assembled with the developed electrode and membrane compared to that with the usual setup cell.

The iodine–sulfur (IS) water-splitting H₂ production process as the heat application of high temperature gas-cooled reactors is investigated to realize the hydrogen (H₂) economy. The IS process is composed of sulfur and iodine chemical reactions.

The Bunsen reaction, which is a starting reaction of the IS process, produces sulfuric and hydriodic acids by mixing iodine and sulfur dioxide with water. The membrane for the Bunsen reaction method is investigated to allow the Bunsen reaction to proceed using an electric cell equipped with an ion-exchange membrane (Fig.6-14). The conventional Bunsen reactor required the separation process of two acid solutions after a reaction. In contrast, no solution separation process is needed because the two acids can be separately produced in a cell partitioned into two channels by the membrane. However, in the membrane for the Bunsen reaction assembled with the usual electrodes and membrane, the overvoltage was excessively high for practical application to the IS process. The overvoltage originated from the anode reaction at the anode electrode and the membrane resistance caused by the proton permeation. Therefore, the novel electrode and the ion-exchange membrane were developed to reduce the overvoltage.

First, the porous Au electrode was developed in collaboration with Shibaura Institute of Technology (Fig.6-15). The porous electrode that enhanced the effective surface area allowed the anode reaction to easily proceed, indicating that the overvoltage was reduced.

Second, the ion-exchange membrane, which introduced many ion-exchange groups compared with the usual membrane to improve the conductivity, was prepared through the National Institutes for Quantum Science and Technology technique. The prepared membrane enabled the reduction of the membrane resistance.

Finally, the membrane for the Bunsen reaction was operated using the electric cell assembled with the developed electrode and membrane. The stoichiometric Bunsen reaction was confirmed to proceed. Moreover, the overvoltage was 0.21 V at 200 mA/cm², which is 1/3 lower than that of the usual setup (Fig.6-16). In summary, the practical process efficiency for the technical applicability of the membrane for the Bunsen reaction can be achieved.

This work was supported by the Strategic Innovative Promotion (SIP) program of the Council for Science, Technology and Innovation (Cabinet Office, Government of Japan).

(Nobuyuki Tanaka)

Reference

Sawada, S., Tanaka, N. et al., Overvoltage Reduction in Membrane Bunsen Reaction for Hydrogen Production by Using a Radiation-Grafted Cation Exchange Membrane and Porous Au Anode, *International Journal of Hydrogen Energy*, vol.45, issue 27, 2020, p.13814–13820.

6–7 Shortening the Calculation Working Time for the Criticality Control Rod Position — Development of a Utility Tool for Auto Seeking the Critical Control Rod Position —

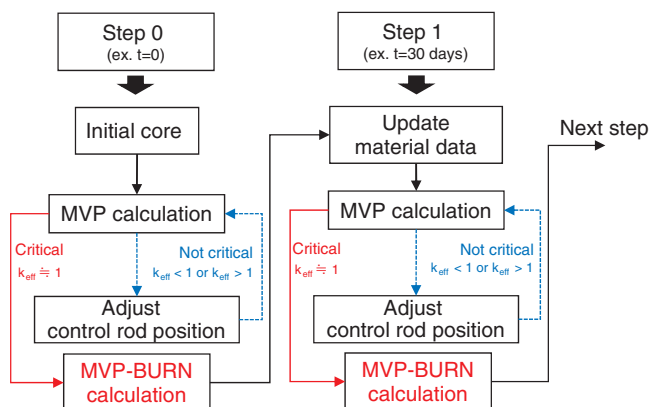


Fig.6-17 Flow chart of the utility tool

The utility tool adjusts the control rod to a critical position before executing the burnup calculation. Subsequently, the burnup calculation is performed by MVP-BURN; the fuel composition changed by the burnup is updated to the next step; the critical control rod position is automatically searched again; and these steps are repeated until the end of the burnup.

The criticality control rod position, which can directly be measured during the operation, is one of the important parameters in confirming the validity of the nuclear characteristic evaluation method. However, in the conventional calculation of the critical control rod position, the critical calculation must be manually performed many times to find the critical position of the control rod, which requires a large amount of calculation work time. In addition, the fuel composition changes during the burnup process; thus, searching for the critical control rod position while exchanging the fuel composition is also necessary, leading to a huge challenge. For example, when using a Monte Carlo code (e.g., MVP) to evaluate the nuclear characteristics of the high temperature engineering test reactor (HTTR), it takes more than 1 week to calculate the critical control rod position during the entire burnup period. Therefore, we developed a utility tool that can automatically search for the critical control rod positions to reduce the calculation work time and perform highly accurate calculations.

Fig.6-17 depicts the utility tool algorithm. First, the tool calculates k_{eff} using the MVP code with any initial value of the control rod position. Once the MVP calculation finishes, the tool checks whether or not the critical state is achieved ($k_{\text{eff}} \approx 1$). When the reactor is not critical ($k_{\text{eff}} < 1$ or $k_{\text{eff}} > 1$), the tool will re-adjust the control rod position and repeat the MVP calculation until the reactor becomes critical. When the k_{eff} reaches nearly unity (within a specific range), the control rod position is recorded, and the MVP-BURN calculation is performed with the designated power and operation time. Subsequently, the nuclide density that has changed as the fuel burns is read and updated to perform the calculation for the next step. As in the

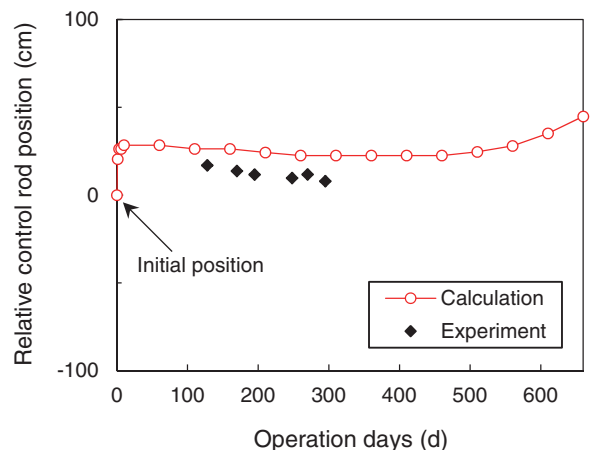


Fig.6-18 Pressure variation of metal lattices of YH₃

Change of the criticality control rod position in case the initial value is zero. The calculated results showed a good agreement compared to the experimental results, with less than 5% difference in the control rod position.

previous steps, the tool will automatically then search for the next critical control rod position and repeat the next calculation until the specified burnup.

Conventionally, the control rod was set at a fixed position during the entire burnup because the amount of calculation is enormous; however, with this utility tool, the critical control rod is always calculated. Therefore, the reactor operation can be more realistically simulated. In addition, the calculation working time can be reduced to less than 2 days by automating all calculation procedures, such as searching for the critical control rod position, updating the nuclide density, and submitting the calculation job to the computing system. The time reduction with the new tool gives a great advantage in developing more detailed calculation models.

Fig.6-18 shows the change in the critical control rod position during operation of the HTTR. The result confirmed that the calculated critical control rod position using this utility tool was in a good agreement with the measurement, with approximately 5% difference from the experimental positions.

The abovementioned results confirmed that the utility tool can accurately evaluate the critical control rod position of the HTTR, automate the complicated work required for the calculation, and reduce the calculation work time by approximately one-third. In the future, by utilizing this utility tool, we can develop more detailed calculation models, which can contribute to the improvement of the accuracy of the neutronic calculations of the HTTR. In addition, the utility value of this tool is expected to increase in the future because the calculation method can be applied not only to the HTTR, but also to other nuclear reactors.

(Hai Quan Ho)

Reference

Ho, H. Q. et al., Preparation for Restarting the High Temperature Engineering Test Reactor: Development of Utility Tool for Auto Seeking Critical Control Rod Position, Nuclear Engineering and Design, vol.377, 2021, 111161, 9p.

Development of Technology Base and Infrastructure toward Improving the Fast Reactor Cycle

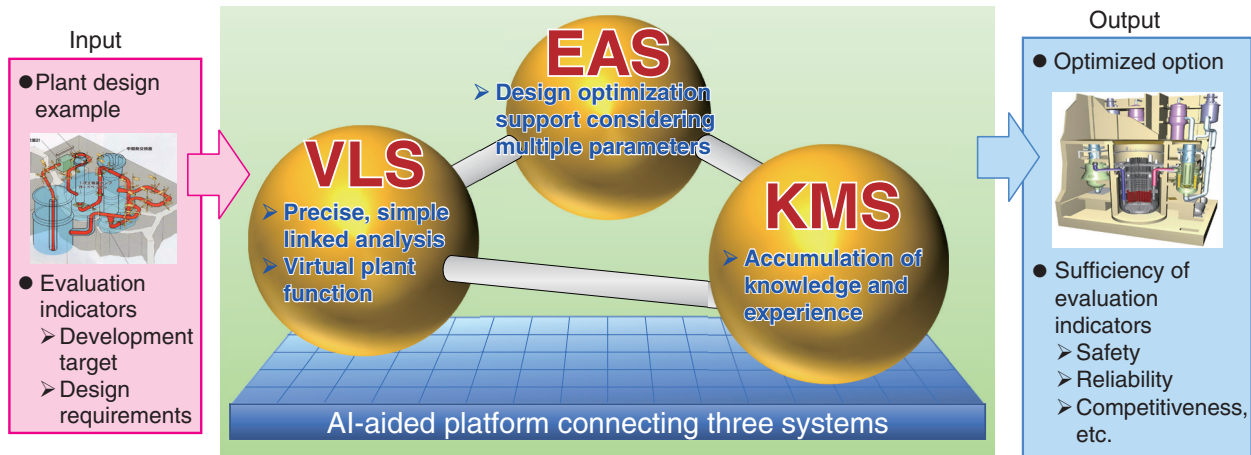


Fig.7-1 Advanced integrated design evaluation method (Advanced Reactor Knowledge- and AI-aided Design Integration Approach through the whole plant lifecycle; ARKADIA)

ARKADIA comprises three systems for fast reactor R&D, including the knowledge management system (KMS), virtual plant life system (VLS), and enhanced and AI-aided optimization system (EAS), that are integrated by an AI-aided platform. ARKADIA can evaluate the design indicators and can automatically provide optimized design options.

Fast reactor and related nuclear fuel cycles offer a promising sustainable energy supply to meet the global energy demand while protecting the environment. Fast reactors can potentially supply energy for over 1000 years by using uranium resources more effectively than traditional nuclear energy systems. Further, they can significantly reduce the exothermic heat and radiotoxicity of vitrified bodies sent to geological disposal by transmuting the minor actinides (MAs) that have a long half-life.

The R&D activities for fast reactors for the next decade were specified in the Strategic Roadmap presented by the National Inter-Ministerial Council for Nuclear Power in December 2018. According to this roadmap, back-end actions related to the reprocessing/recycling of fast reactor technology are required to establish the significance of diversifying fast reactors. Moreover, international competitiveness should be maintained via continuing R&D in the fields of nuclear power, human resource development, and research base while introducing cutting-edge technology domestically and internationally. Therefore, JAEA formulated an R&D policy in accordance with the Strategic Roadmap; the Sector of Fast Reactor and Advanced Reactor R&D (SEFARD) is now implementing an advanced integrated design evaluation method incorporating cutting-edge technologies in Japan and overseas, safety improvement technology, technology to reduce the volume and toxicity of radioactive waste, cost-effective fast reactor technology, fuel cycle technology (such as fuel fabrication and reprocessing), and the development/standardization of safety criteria, codes, and standards. The advanced integrated design evaluation method is summarized in Fig.7-1 and comprises three systems for fast reactor R&D, including the knowledge management system (KMS), the virtual plant life system (VLS), and the enhanced and AI-aided optimization system (EAS), that are integrated by an AI-aided platform to provide optimized design options by evaluating design indicators. In this chapter, some achievements from the latest R&D efforts carried out by JAEA in this area are introduced.

An extraction chromatography method using neutrons has been developed to observe nuclides adsorbed inside the column (Topic 7-1). A neutron's energy was first calculated using its

flight time from the pulse source to the detector in the proposed neutron imaging technology. The adsorption band formed inside the column was then visualized by identifying the spatial distribution and nuclide type using the decrease in the number of neutrons after passing through the column and their energy, respectively.

The ratio of the neutron adsorption reaction rate in control rods to that in peripheral fuels was then investigated to reduce the rod calculation errors for large cores (Topic 7-2), and reference solutions were calculated using the Monte Carlo method. This ratio is the main factor used in the reaction rate ratio preservation method and is multiplied by nuclear reaction data. Furthermore, the error evaluation method was improved by improving multiple fuel areas and boundary conditions in the system model for the fuel rods and peripheral fuels.

The physical properties (e.g., density and heat capacity) of melted control rods were measured in collaboration with other research institutes at a wide temperature range encompassing solid and liquid phases to evaluate the influence of temperature on composition ratio and thus improve models of the melting and transport behavior of the control rods and stainless steel eutectic reaction. Our results could aid efforts to reduce the exothermic heat of core melt materials during a core disruptive accident (CDA) in a fast reactor (Topic 7-3).

The swelling properties of core materials should be well understood to develop irradiation-resistant, long-lasting fuel cladding. Therefore, we quantified the vacancy diffusivity and concentration of an empty rectangular lattice of modified stainless steel by observing the void denuded zone width after irradiation and quantifying the relationship between the swelling and diffusivity of an empty rectangular lattice (Topic 7-4).

Finally, we developed a recovery process using a solvent extraction method that has been used in reprocessing plants worldwide to improve the recovery of trivalent MAs (MAs (III)). To do so, we developed an extraction chromatography separation flow-sheet that utilizes the difference in behavior between light and heavy rare earth elements. Using the developed method, MAs (III) were recovered with high purity in a nitric acid solution (Topic 7-5).

7-1 Observation of Nuclides Adsorbed inside the Column Using Neutrons — Non-Destructive Visualization of Nuclides by Resonance Neutron Imaging —

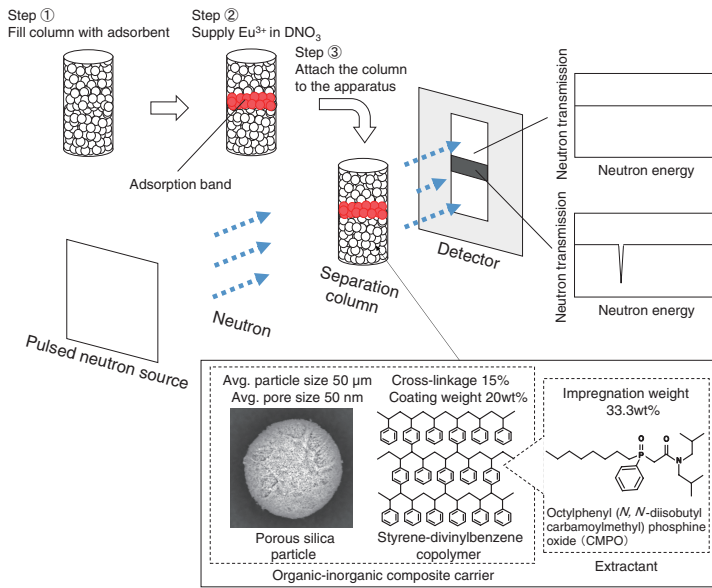


Fig.7-2 Experimental resonance neutron imaging method

The organic-inorganic composite support, in which silica particles are coated with styrene-divinylbenzene copolymer, is impregnated by a CMPO extractant (or CMPO-impregnated adsorbent) and used to fill the separation column. The nuclides and their spatial distribution can be identified without destroying the sample from the neutron energy and the decrease in number of neutrons transmitted through the column, respectively.

When reprocessing spent nuclear fuel, uranium (U) and plutonium (Pu) can be reused; all other elements are geologically disposed after vitrification. However, separating long-lived MAs from radioactive liquid waste is expected to reduce the volume and radiotoxicity of radioactive waste. Therefore, we developed extraction chromatography using a separation column filled with MA-compatible particles (i.e., CMPO-impregnated adsorbent). After the waste liquid is supplied, MAs form an adsorption band and can be separated from other elements due to their affinity to a CMPO extractant. In this manner, 99% of the MAs were separated from real waste liquid in the demonstration experiment. Our facing issue is the purity of recovered MAs, which must be improved for the nuclear fuel fabrication. We supplied europium (Eu^{3+}) to the column as a simulated MA to observe the adsorption band by resonance neutron imaging for better understanding of the phenomena inside the column.

A schematic of the neutron irradiation experiment performed at J-PARC is shown in Fig.7-2. The column was irradiated with neutrons, and the transmitted neutrons were measured by a detector. The neutron energy was determined by the flight time of neutrons from the pulsed neutron source to the detector, and the nuclides and their spatial distribution were identified from the neutron absorption energy and the decrease in the number

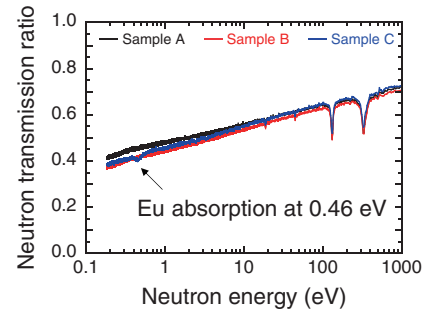


Fig.7-3 Measured neutron transmission

The ratio of neutrons transmitted through the column is shown with respect to neutron energy. The column was found to contain W, Mo, Co and Mn nuclides.

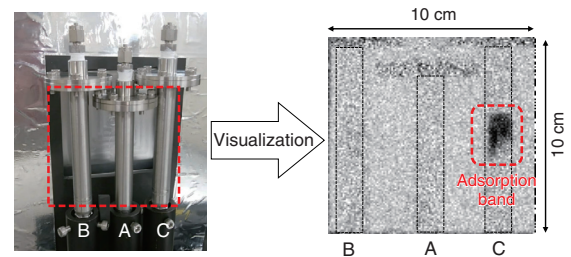


Fig.7-4 Photograph and neutron radiograph of the column

The Eu adsorption band formed inside the separation column was observed without destroying the sample.

of neutrons after transmission, respectively. These data were converted to a neutron radiograph, which allowed us to observe the internal structure of the column without destroying it.

When light water (H_2O) is used in neutron radiography, neutrons react with hydrogen, causing low transmittance and a low-resolution neutron radiograph. This problem was solved by using deuterium. The obtained neutron transmission spectra of the columns filled with (A) D_2O , (B) DNO_3 , and (C) Eu^{3+} after being prepared with DNO_3 are shown in Fig.7-3. Replacing H_2O with the deuterium solvent increased the neutron transmission from 20% to 50%. A characteristic decrease of neutrons was observed at 0.46 eV, as shown in Fig.7-3(C). This value is nuclide-specific, thereby providing evidence of the presence of Eu-151. The Eu adsorption band was also confirmed in the neutron radiograph, as indicated in Fig.7-4.

Overall, the proposed resonance neutron imaging method allows the adsorption band to be measured without destroying the sample. For future works, the time evolution of multiple adsorption bands separating during the process inside the column will be tracked and applied to construct the feasible MA separation flowsheet.

(Yasunori Miyazaki)

Reference

Miyazaki, Y. et al., Observation of Eu Adsorption Band in the CMPO/SiO₂-P Column by Neutron Resonance Absorption Imaging, JPS Conference Proceedings, vol.33, 2021, 011073, 7p.

7-2 Improvement of the Calculation Accuracy of Power Distribution for Large Fast Reactors — Refinement of Control-Rod Calculation Method —

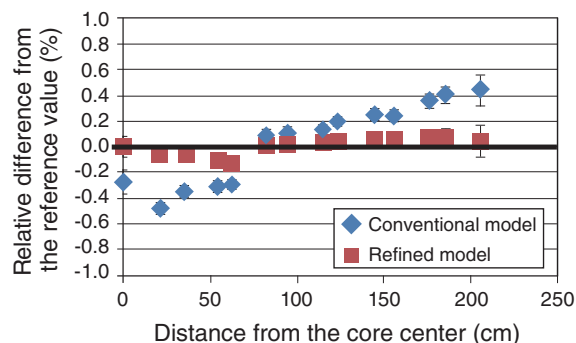
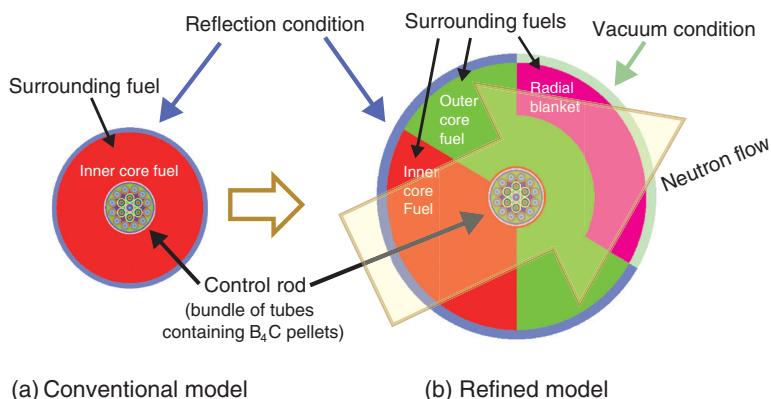


Fig.7-5 (a) Conventional and (b) refined geometric model of the control rod and surrounding fuels

The refined model treats the surrounding fuel regions (inner core fuel, outer core fuel, radial blanket) according to the location of the control rod and employs two boundary conditions (isotropic reflection and vacuum). Those improvements allowed the flow of neutrons from the center to the exterior of the core to be simulated.

Fig.7-6 Improved radial power distribution for a large core

The proposed refined model improved the calculation accuracy of power distribution, which was sensitive to the modeling of the control rod, even in the regions other than the core center. The reference values were obtained by the Monte Carlo method.

The control rod is an important device that is used to operate and control a nuclear reactor. Incorrectly estimating the neutron absorption effect of a control rod leads to an improperly designed core. In particular, the radial power distribution in radially flattened large cores is affected by control-rod calculation errors, leading to excessive allowance in core design.

The core design calculation is performed in two steps. In the first step, the detailed structure of core components is focused on individually, such as that of the control rod or fuel assembly. An overall core calculation is then performed in the second step without treating the detailed structure, where the nuclear reaction data are multiplied by a set of coefficients to reproduce the results from the first step. The reaction rate ratio preservation (RRRP) method had been established to calculate the necessary parameters of the control rods in the first step. In this method, the nuclear reaction data are multiplied by the ratio of neutron absorption reaction rate in the control rod to that of the surrounding fuels.

Conventionally, the geometric model of the control rod and surrounding fuels shown in Fig.7-5(a) is used in the first calculation step for all control rods in the core. We reconstructed this model. To evaluate the adequacy of the model, we adopted the ratio of neutron absorption reaction rate of control rod to that of the surrounding fuels (α), which is an essential component of the RRRP method. The proposed model was then verified by the Monte Carlo (MC) method that can simulate an entire core configuration with detailed control rod and fuel structures. An improvement of the conventional deterministic method was still required for core design, since the statistical MC method

requires extensive calculation time.

Simple modifications, such as adjusting the number of surrounding fuel assemblies per control rod to meet that of the target core, allowed for clear improvements to the value of α for the control rods near the core center, thereby reducing the calculation error caused by the overestimation of neutron absorption of control rods. However, the value of α for control rods further from the core center did not agree with the reference value, possibly because the control rods were surrounded by plural fuel regions (i.e., inner core fuel, outer core fuel, radial blanket); because neutrons flow from the core center to the core exterior, the neutron flow behavior depends on the direction. We then proposed a refined model, as shown in Fig.7-5(b), to address this problem and improve the overall value of α . The refined model not only simulates the surrounding plural fuel regions with sector dividing but also employs two boundary conditions, reflective and vacuum, to simulate the neutron flow.

Evaluating the resulting core design calculations with several control-rod insertion patterns demonstrated that the proposed refined model significantly improved the calculation accuracy of control-rod worth and radial power distribution. The relative error from the reference value (i.e., using the MC method) decreased below 0.13% (one-sixth of that using the conventional model) for the control-rod reactivity worth, below 0.35% (one-third) for the radial power distribution as an example shown in Fig.7-6. Overall, the proposed control-rod calculation method can be applied to large fast reactor core design with high accuracy.

(Kazuo Takino)

Reference

Takino, K. et al., An Investigation on the Control Rod Homogenization Method for Next-Generation Fast Reactor Cores, Proceedings of Joint International Conference on Supercomputing in Nuclear Applications + Monte Carlo 2020 (SNA + MC 2020), Chiba, Japan, 2020, p.92–96.

7-3 Clarification of the Relocation Behavior of Degraded Fast Reactor Core Materials under Severe Accident

— Development of Thermophysical Properties Database for Stainless Steel Containing Boron Carbide —

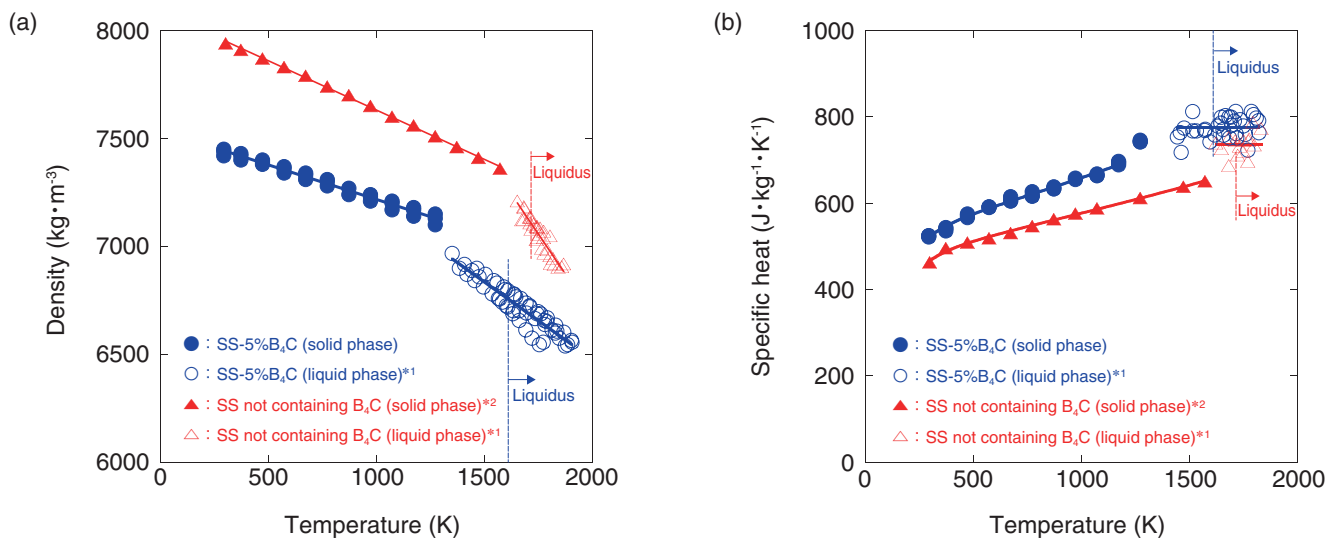


Fig.7-7 Density and specific heat of stainless steel (SS) and SS containing boron carbide (SS-B₄C)
The presence of B₄C in the SS caused the density to decrease and the specific heat to increase.

The long-term coolability of degraded core materials inside the reactor vessel must be ensured in a severe accident.

Although the melting temperature of boron carbide (B₄C), which is used as a control rod material, is 2723 K, it could melt below its melting temperature (i.e., undergo liquefaction) due to chemical interactions caused by contact with stainless steel (SS), which is used in the cladding tube. The produced liquefied stainless steel containing boron carbide (SS-B₄C) is expected to reduce the temperature increase of the degraded core material by moving throughout the core and mixing with other degraded core materials. JAEA has been developing calculation models to explain this liquefaction and relocation behavior. However, thermophysical property data (density, specific heat) of SS-B₄C are needed over a wide temperature range covering the solid-to-liquid phases at various B₄C concentrations to complete the calculation models. Therefore, we have been collaborating with other research institutes to maintain and expand the thermophysical properties database and improve the severe accident analysis code.

Thermophysical data was obtained for SS-5%B₄C, which is expected to have the lowest melting temperature in various SS and B₄C blends; the measured density and specific heat of SS-5%B₄C are shown in Figs.7-7(a) and (b), respectively. The addition of 5% B₄C to SS caused the density to decrease by approximately 6% at room temperature, although this difference decreased as the temperature was increased within

the solid and liquid range. The presence of 5% B₄C in SS caused the specific heat to increase by approximately 7% at room temperature, although the specific heat of both materials in the solid state had a similar temperature dependence. On the other hand, the specific heat did not vary with temperature once in the liquid phase. Overall, we successfully acquired the thermophysical property data of SS-5%B₄C over a temperature range encompassing both solid and liquid phases. Future experimental work will focus on evaluating thermophysical properties of various B₄C concentrations in SS. Together, these efforts will allow for a thermophysical property database that can be used to develop and improve calculation models used to analyze severe accidents.

The present study is the result of the “Technical Development Program on a Fast Reactor International Cooperation, etc.”, entrusted to the JAEA by the Ministry of Economy, Trade and Industry (METI), Japan.

(Toshihide Takai)

*1 Fukuyama, H. et al., Thermophysical Properties of Molten Stainless Steel Containing 5 mass % B₄C, Nuclear Technology, vol.205, issue 9, 2019, p.1154–1163.

*2 Japan Nuclear Energy Safety Organization, Project of Integrity Assessment of Flawed Components with Structural Discontinuity (IAF) Material Properties Data Book at High Temperature for Dissimilar Metal Welding in Reactor Pressure Vessel, JNES-RE-2012-0024, 2013, 122p.

Reference

Takai, T. et al., Thermophysical Properties of Stainless Steel Containing 5 mass % B₄C in the Solid Phase, Nuclear Technology, vol.205, issue 9, 2019, p.1164–1174.

7-4 Optimization of Alloying Components of Nuclear Core Materials

— Development of an Estimation Method for Irradiation-Induced Point Defect Behavior —

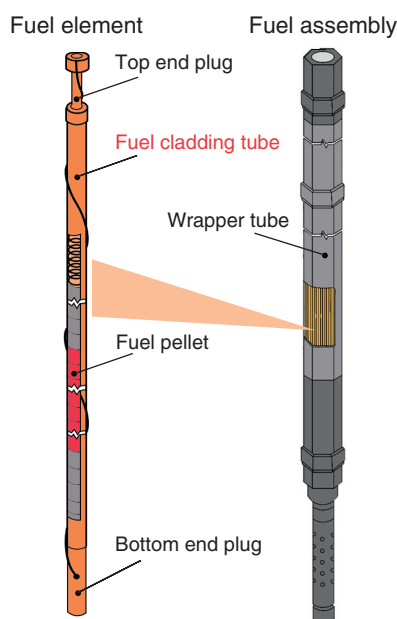


Fig.7-8 Example fuel structure design in a sodium-cooled fast reactor

Fuel pellets and their fission products are covered in a fuel cladding tube and top/bottom end plugs. This integrated structure is called the fuel element and is bundled in a fuel assembly and loaded into the core.

Fuel pellets inside a nuclear reactor are covered with a thin metal tube, i.e., the fuel cladding tube, to prevent the leakage of radioactive materials released by nuclear fission (see Fig.7-8). The material used for the fuel cladding tube must be resistant to irradiation and not deteriorate in the presence of the neutron irradiation occurring in the reactor.

We are currently developing long-life cladding tubes that exceed the performance of the existing modified SUS316 steel cladding to reduce radioactive waste and support research into fast reactors. In particular, swelling causes material deterioration and must be reduced. Swelling is due to the behavior (diffusion and quantity) of irradiation-induced point defects (vacancies and self-interstitial atoms) in the material. Therefore, the behavior of these defects must be understood and controlled to suppress swelling; however, the quantitative relationship between defect behavior and swelling has not been addressed. Further, methods to evaluate these behaviors have not yet been established. Clarifying the relationships between defect behavior and swelling in various steel types with different alloy components thus would allow an appropriate design strategy for selecting major alloy components and additional elements to be constructed to supplement the existing cladding design method.

Therefore, we aimed to develop a method to estimate the behavior of defects in Fe–Cr–Ni austenitic steel (i.e., the base

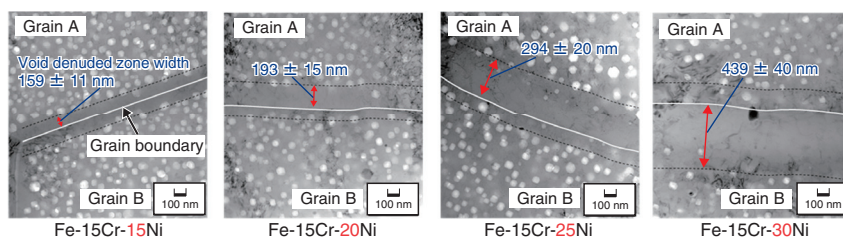


Fig.7-9 Void denuded zone formed in neutron-irradiated Fe–Cr–Ni austenitic steels (476 °C, 18 dpa*)

The void denuded zone (VDZ) of each steel sample was measured using the average width formed between grains A and B at multiple points. The width of the VDZ, which depends on the vacancy diffusion behavior, increased with increasing Ni concentration, indicating that the vacancy diffusion differs depending on the steel type.

* The dpa (displacement per atom) represents a unit of neutron irradiation dose.

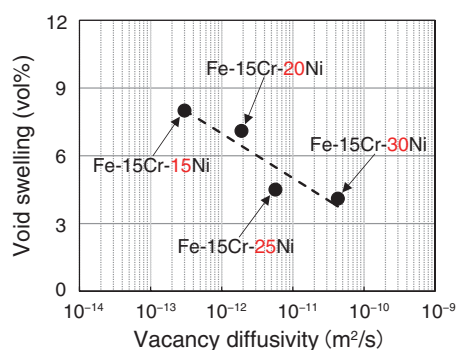


Fig.7-10 Relationship between vacancy diffusivity and void swelling of each steel sample

Using the widths of the VDZs presented in Fig.7-9, the vacancy diffusivities were estimated to establish a quantitative relationship between them and the void swelling. For the four types of steel studied, increasing the Ni concentration caused the void swelling to decrease due to the high vacancy diffusivity.

material of modified SUS316 steel) by focusing on the void denuded zone (VDZ) at grain boundaries by irradiation. The width of the VDZ depending on the vacancy diffusion behavior was measured using transmission electron microscopy. Using the measured widths and calculations combining the existing VDZ formation theory (i.e., diffusivity dependence) and the existing rate theory (i.e., concentration dependence), we estimated the vacancy diffusivity and concentration. The observed VDZ formation within four steel samples irradiated in Joyo is shown in Fig.7-9, where the Cr content of these samples was fixed at 15wt%, and the Ni content was ranged from 15 to 30wt%. The VDZ width varied with Ni concentration. The relationship between the vacancy diffusivity and the void swelling is shown in Fig.7-10. Our methodology thus quantitatively clarified that the swelling suppression in the four steels was due to the increase of vacancy diffusivity. Future efforts will focus on using neutron-irradiated samples with various alloy components to improve the accuracy of the observed relationship, thereby contributing to efforts to optimize the design of alloy components.

This research is a part of the results from the joint research with Hokkaido University, “Research on quantitative evaluations of point defect behavior in Fe–Cr–Ni steel”.

(Yoshihiro Sekio)

Reference

Sekio, Y. et al., Effect of Nickel Concentration on Radiation-Induced Diffusion of Point Defects in High-Nickel Fe–Cr–Ni Model Alloys during Neutron and Electron Irradiation, *Materials Transactions*, vol.60, issue 5, 2019, p.678–687.

7-5 Improvement and Demonstration of an Extraction Chromatography Flow-Sheet to Recover Trivalent Minor Actinides

— Efficient MA(III)/Ln(III) Separation Process —

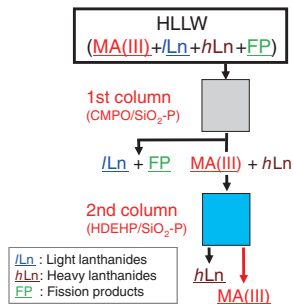


Fig.7-11 Improved MA(III) recovery process

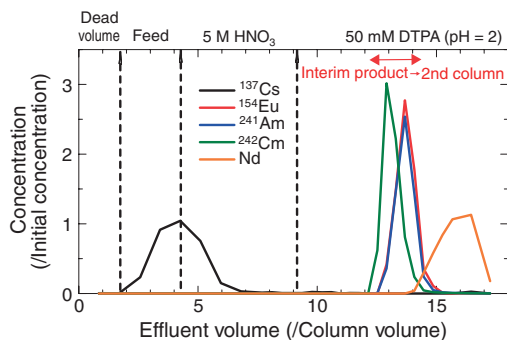


Fig.7-13 Elution curves obtained by the CMPO column
MAs(III) and heavy lanthanides (*h*Lns) were separated from light lanthanides (*l*Lns) by supplying DTPA solution.

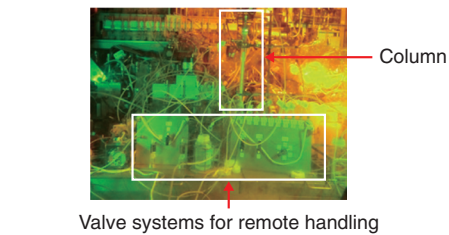


Fig.7-12 Experimental setup inside the hot cell

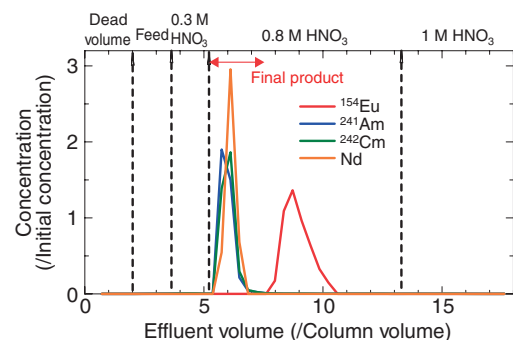


Fig.7-14 Elution curves obtained by the HDEHP column
MAs(III) were successfully recovered in an 0.8 M (mol/dm³) nitric acid solution separated from *h*Ln.

Partitioning and transmuting minor actinides (MAs(III)), including Am and Cm, may reduce the volume and radiotoxicity of radioactive wastes owing to their long half-life and heat generation natures. Many researchers worldwide have aimed to separate MA(III) from high-level liquid wastes (HLLW) containing various metals. The main challenging task for selective MA(III) recovery is their separation from trivalent lanthanides (Lns(III)) because of the chemical similarity between MAs(III) and Lns(III) in solution.

Solvent extraction is a proven methodology that is commonly studied for MA(III) separation worldwide. We have focused on developing an extraction chromatography technology that is based on the principles of solvent extraction but is expected to generate less secondary waste. This technology uses porous silica particles coated with a polymer (SiO₂-P)-impregnating solvent to adsorb MAs(III), thereby allowing MAs(III) to be recovered from the HLLW through column separation. Our proposed two-step column operation uses CMPO and HDEHP extractants as adsorbents in the first and second columns, respectively. Here, MAs(III) and Lns(III) are recovered in the first column; MAs(III) are then separated from Lns(III) in the second column. Using the proposed method, MAs(III) were separated from Ln(III) successfully. However, the recovery ratio of Mas(III) was relatively low (70%), and the product solution contained the complexing reagent used for MA(III) elution, thereby

requiring a separate removal step.

To improve MA(III) recovery, therefore, we designed a separation process using the difference in affinity of Lns(III) to CMPO and HDEHP, as shown in Fig.7-11, by focusing on the difference between light Lns (*l*Lns: La-Nd) and heavy lanthanides (*h*Lns: Sm-Gd). DTPA, which was used in the second column of the original method, was used in the first column of the modified one, and MA(III) was expected to be recovered in a solution of pure nitric acid. The proposed methodology was then demonstrated on real HLLW, as shown in Fig.7-12, after minor modifications were obtained from column separation experiments using simulated HLLW. Using the proposed methodology, *l*Lns and other fission products were removed in the first column, and MAs(III) were then separated from *h*Lns in the second column, as shown in Figs.7-13 and 7-14, respectively. Decontamination factors of Lns(III) were larger than the target value 10² although Nd was not decontaminated by the second column. Overall, we successfully designed and demonstrated a MA(III) recovery process that achieved over 90% MA(III) recovery in nitric acid solution with high purity.

A part of this study was carried out through collaboration with the Shibaura Institute of Technology under the project “Optimization in adsorbent for MA(III) recovery”.

(Sou Watanabe)

Reference

Watanabe, S. et al., Improvement in Flow-Sheet of Extraction Chromatography for Trivalent Minor Actinides Recovery, Journal of Radioanalytical and Nuclear Chemistry, vol.322, issue 3, 2019, p.1273–1277.

Toward Decommissioning Nuclear Facilities and Managing Radioactive Waste

To maintain and develop its research and development (R&D) capabilities by strengthening the safety of its nuclear facilities and ensuring steady implementation of back-end measures, JAEA issues the “Medium- and Long-Term Management Plan of our Facilities” (issued on April 1, 2017, and amended on April 1, 2020) as a comprehensive plan detailing the following three points:

- The selection and consolidation of facilities,
- safety measures, and
- the management of back-end issues.

In the plan, 89 nuclear facilities were chosen to be decommissioned.

Among the large facilities, JAEA submitted an application to the Nuclear Regulation Authority (NRA) for permission to decommission MONJU and the Tokai Reprocessing Plant (TRP), which led to the NRA granting permission for the decommissioning of MONJU on March 28, 2018 and for that of TRP on June 13, 2018. The application to the NRA for permission to decommission the Uranium Enrichment Demonstration Plant is ongoing.

The implementation of back-end measures requires long-term prospects and policies, including those regarding the processing and disposal of radioactive waste; the decommissioning of TRP is expected to take approximately 70 years to complete. Therefore, JAEA published a long-term prospect and policy for back-end measures, the “Back-end Roadmap”, on December 26, 2018.

To ensure safe and appropriate nuclear facility decommissioning and radioactive waste management, it is necessary to introduce new technologies and knowledge and to promote the development of technologies for advanced safety and cost reduction. Technologies for the safe and effective dismantling of nuclear facilities, the minimization and stabilization of radioactive wastes, and the disposal of radioactive wastes are under development (Fig.8-1). The proposed disposal project applies to low-level radioactive wastes from research facilities of universities, private organizations, and JAEA facilities.

TRP has entered the decommissioning stage. In the TRP, in an effort to reduce risk to the facilities, the vitrification of high-level radioactive waste (HLW) is promoted with a primary focus on safety. JAEA has also developed advanced vitrification techniques.

Specifically, this year saw the making of the “Radioactivity Concentration Equivalent Dose Criteria” as important nuclide selection criteria for smooth implementation of low-level radioactive waste disposal projects generated at research facilities, etc. (Topic 8-1), development of a technique for recovering nuclear material from used extraction solvent using solid adsorbent (Topic 8-2), investigation of radioactive aluminum waste treatment technology using the Bayer process aimed at converting difficult-to-treat waste into a stable waste package (Topic 8-3), and the development of a fireproof sheet on glove box panels toward safety improvement of plutonium handling facilities (Topic 8-4).

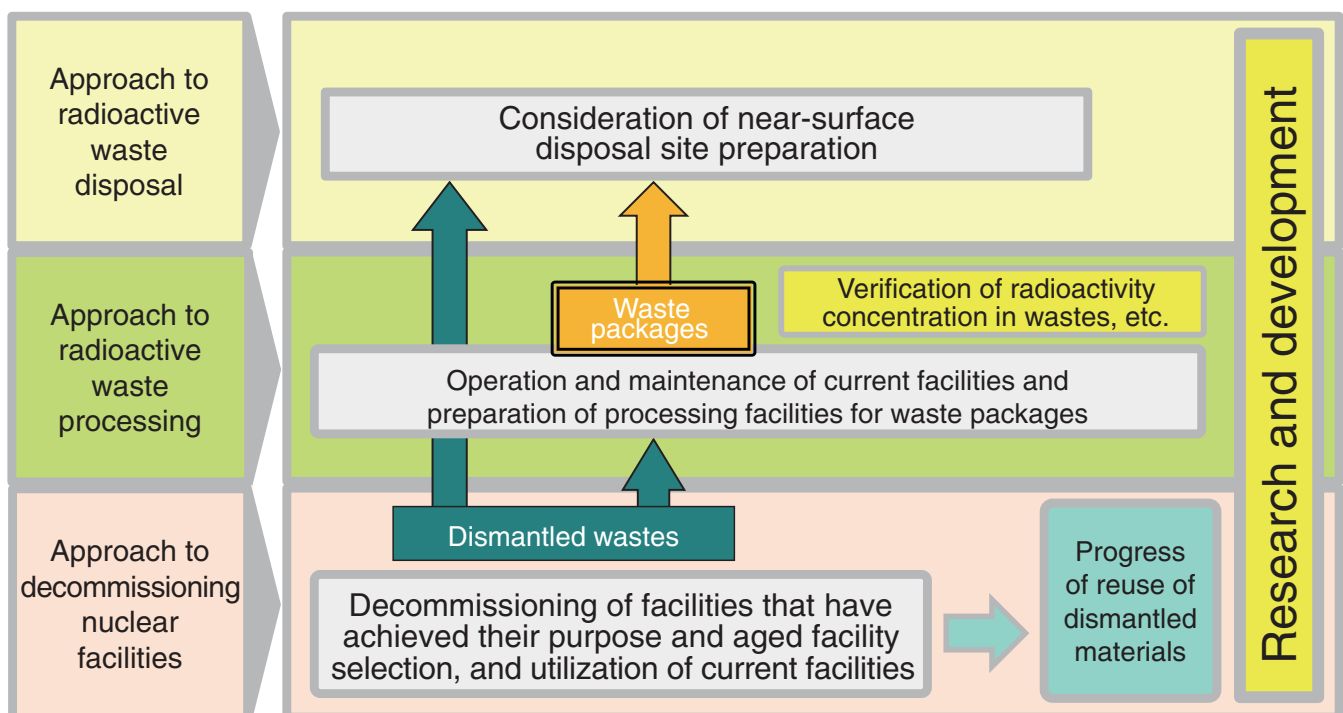


Fig.8-1 Outline of low-level radioactive waste management

R&D of the decommissioning of nuclear facilities and processing of radioactive wastes, including waste treatment and waste characterization, has been promoted.

R&D to Improve Technology and Reliability of Geological Disposal in Japan

Geological disposal is internationally recognized as the most practical method currently available for the long-term isolation of HLW, which is produced during the generation of nuclear power, from human environments. This critical issue must be approached sensibly by the present generation and will remain crucial regardless of any revision of the national nuclear energy policy.

In Japan, the spent fuel discharged from a nuclear reactor is reprocessed to extract the reusable uranium and plutonium for power generation. The liquids separated from the spent fuel during chemical reprocessing are consolidated into a stable glass form. In accordance with the Japanese disposal policy, vitrified waste is then encapsulated in a thick steel overpack, surrounded by highly compacted bentonite, and emplaced in a stable geological environment at a depth of more than 300 m below the surface (Fig.8-2).

R&D in relevant fields such as geoscience, repository engineering, and safety assessments of the disposal system are ongoing, as summarized in Fig.8-3, and are vital in improving their sound technical basis and be reflected in the implementation and regulatory activities.

The Horonobe Underground Research Center for sedimentary rock carries out R&D including Study on near-field system performance in geological environment (Topics 8-5 and 8-6).

At the Tono Geoscience Center, the Toki Research Institute of Isotope Geology and Geochronology is engaged in a study of the long-term stability of the geological environment (Topics 8-7 and 8-8), while the Mizunami Underground Research Laboratory project for crystalline rock is continuing work on the backfilling of underground facilities.

To expand further the knowledge regarding geological disposal, extensive studies to assess the behavior of the engineered barrier system, and key processes constraining the release and the migration of radionuclides are being studied (Topics 8-9 and 8-10). These studies exploit the data regarding geological environments that were obtained through geoscientific research at underground research laboratories.

Results of the R&D activities have been summarized as a web-based report (CoolRep), which has been made available on JAEA's public website:

CoolRep: <https://kms1.jaea.go.jp/CoolRep/english.html>.

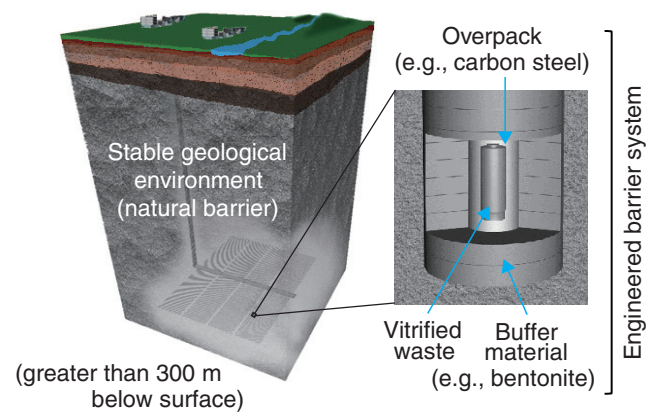


Fig.8-2 Schematic view of the basic concept for the geological disposal of high-level waste

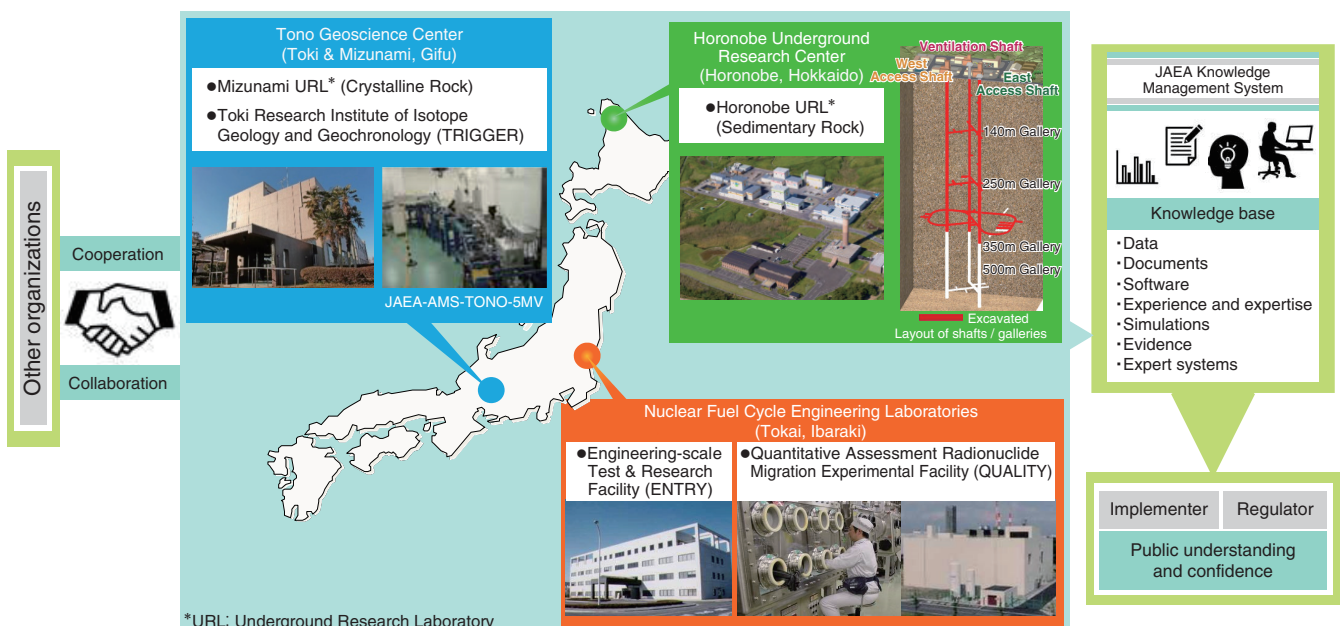


Fig.8-3 Structure of JAEA R&D activities

8-1 Implementation of Disposal Project of LLW Generated in Research, Medical, and Industrial Facilities

— Preparation of “Concentration Equivalent Dose Criteria” as the Standard for the Selection of Important Nuclides —

National requirements in safety reviews

- National requirements in the safety reviews of a disposal facility project, the dose standards specified by the government should be satisfied by the dose assessment (safety assessment) based on the assumption (scenario) that the general public will be exposed to radiation from the disposal facility.
- The nuclides that contribute significantly to the radiation dose (important nuclides) shall be selected, and the maximum radioactivity concentration and total amount of radioactivity for the important nuclides shall be indicated.

Current responses

- © Site selection is in progress, the safety assessment under site environmental conditions has not yet been conducted.

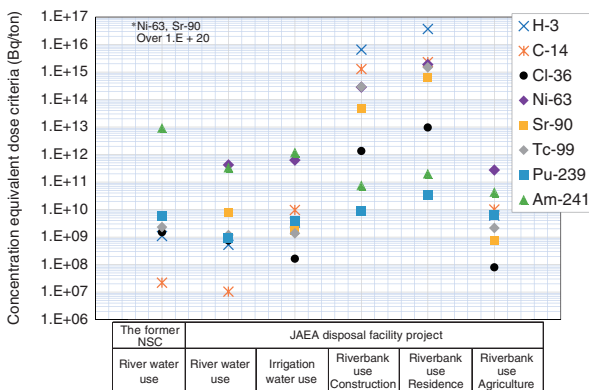
↓

Selection of important radionuclides using concentration equivalent dose criteria (radioactivity concentrations of each radionuclide that cause reference doses specified by the government) under general site environmental conditions that set upper limits for disposal.

↓

Calculating concentration equivalent dose criteria considering various future site environments and studying the impact on the safety assessment.

Fig.8-4 National requirements in safety reviews and current responses
Site selection is in progress; in the meantime, we are calculating the concentration equivalent dose criteria for each nuclide, taking into account various future site environments and examining the impact on the safety assessment.



We are implementing the project (trench-type and pit-type disposal) at JAEA to dispose low-level radioactive wastes (LLW) generated from JAEA and domestic research, medical, and industrial facilities. National requirements in safety reviews of the disposal facility project, it is necessary to show that the dose standards specified by the government are satisfied by the dose assessment (safety assessment) based on the estimation that the general public will be exposed to radiation from the disposal facility (scenario), and to select the nuclides that contribute significantly to the exposure dose (important nuclides) and show the maximum radioactivity concentration and total radioactivity for the important nuclides.

Additionally, these important nuclides must be selected to promote the smooth implementation of the disposal project, as they are also considered when examining waste treatment methods and measurement and analysis methods of waste. An overview of these requirements and our responses are shown in Fig.8-4.

Important nuclides have been selected from nuclides that have a large ratio between the radioactivity concentration of each nuclide that causes exposure to the dose criterion set by the government (i.e., the concentration equivalent dose criteria) and the radioactivity concentration of the nuclide contained in the waste. Nuclides having a low concentration equivalent dose criterion are more likely to be important nuclides because their exposure doses are high even if the radioactivity concentration in the waste is low.

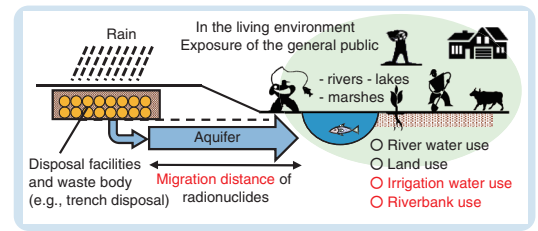


Fig.8-5 Estimation of exposure (scenarios) used in the calculation of concentration equivalent dose criteria

During the safety assessment of disposal facilities, exposure doses are evaluated based on the assumption that the general public will be exposed to the waste from the disposal facilities, and the concentration equivalent dose criteria is calculated. For example, a scenario involving river water use must account for exposure caused by drinking contaminated river water and eating livestock raised on the water.

Fig.8-6 Evaluation of the concentration equivalent dose criteria for trench disposal

The minimum value of C-14 was lower than that found by the NCS in the case of river water use. New nuclides (e.g., Cl-36) with high contribution to exposure were found in water used for irrigation on the riverbank. The established criteria will result in the selection of a wide range of nuclides that are likely to be selected based on the safety assessment that reflect actual site conditions, which will improve the reliability of safety reviews conducted by the government.

The concentration equivalent dose criteria established by the former Nuclear Safety Commission (NSC) has been used as the basis for determining the legal upper limit of radioactivity concentration for near-surface disposal. Efforts to select a location for the disposal facility are underway; as such, we established several scenarios that take various future site environments into account to calculate the concentration equivalent dose criteria in each scenario and study their impact on the safety assessment, as summarized in Fig.8-5.

An example of our calculated concentration equivalent dose criteria for representative nuclides assuming trench disposal is shown in Fig.8-6. In the scenario of river water use, the value of C-14, which was previously the minimum value, was found to be even lower due to the estimation of location environmental conditions (e.g., close living area, short migration distance) that would result in higher exposure doses. Additionally, scenarios that account for various site environments (irrigation water use, riverbank use) revealed several other nuclides that contribute significantly to exposure (e.g., Cl-36).

Based on the results of this study, we believe that the use of the concentration equivalent dose criteria based on a wide range of site environments will enable the selection of a wide range of nuclides that are likely to be selected in the safety assessment that reflect actual locations, and will improve the reliability for safety reviews conducted by the government.

(Toshikatsu Sugaya)

Reference

Sugaya, T. et al., Evaluation of Radioactivity Concentration Corresponding to Dose Criterion for Near Surface Disposal of Radioactive Waste Generated from Research, Medical, and Industrial Facilities, Volume 1, JAEA-Technology 2021-004, 2021, 79p. (in Japanese).

8-2 Recovery of Nuclear Materials from Spent Extraction Solvent Using Solid Adsorbent

— Investigation of Complex Formation Reaction of Iminodiacetic Acid Group in Solvent —

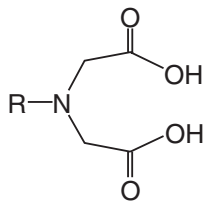


Fig.8-7 Structural diagram of iminodiacetic acid group

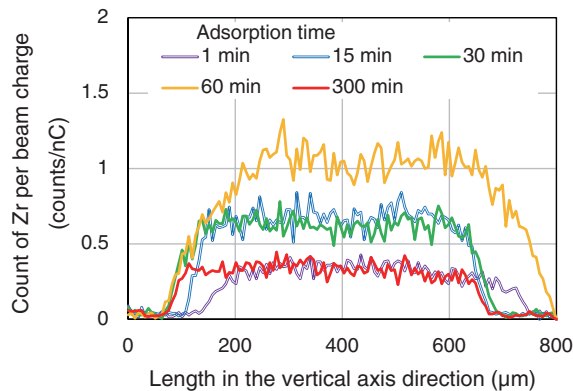


Fig.8-9 Zr detection strength of adsorbent (micro-PIXE analysis) Zr detection intensity (vertical axis) as a function of the distance from the top to bottom of PIXE image (horizontal axis). Zr was distributed throughout the adsorbent after only one minute of adsorption treatment.

Radioactive waste liquids generated in nuclear facilities sometimes contain reactive chemical reagents in addition to radioactive elements. Some such waste liquids are currently stored inside nuclear facilities due to a lack of appropriate treatment processes. The spent extraction solvent, which mainly comprises tributyl phosphate (TBP) and normal dodecane, contains U and Pu and is generated during plutonium uranium redox extraction (PUREX) process. The spent extraction solvent is degraded by radiation from the extracted nuclear fuel material. Due to the risk of explosive substances being generated as products of radiolysis (e.g., hydrogen and nitrogen compounds), stabilization treatment must be performed promptly. Thus, nuclear materials must be removed from the organic liquid to ensure safety. One commonly used back extraction method used to recover nuclear fuel material from the spent extraction solvent uses a sodium carbonate solution; however, using this method generates a large amount of alkaline liquid waste. To design a recovery process that releases less secondary waste, we are focused on developing a process using an adsorbent containing iminodiacetic acid (IDA) functional groups, the structure of which is shown in Fig.8-7.

Here, we investigated the complex formation reaction of an IDA-type adsorbent with simulated nuclear fuel materials in the spent extraction solvent. The simulated spent extraction solvent was prepared by diluting TBP and dibutyl phosphate (DBP), which is produced by radiolysis or hydrolysis of TBP, with normal dodecane. Subsequently, a nitric acid (HNO_3) solution

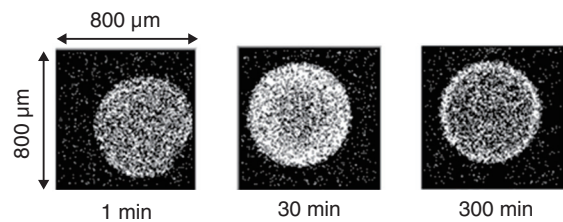


Fig.8-8 PIXE images of Zr adsorbed from simulated spent extraction solvent

Table 8-1 Local structural parameters around adsorbed Zr (EXAFS analysis)

The Zr ion was surrounded by NO_3 ions in solution, and $\text{ZrO}(\text{NO}_3)_2$ forms a complex with the IDA group. The Zr extracted in the simulated spent extraction solvent is complexed with the chemical forms of ZrO^{2+} .

Sample	Atom	Number of Atom	Atomic distance (10^{-10} m)
HNO_3 solution	O	8.2	2.16
	N	4.2	2.28
Adsorbed Zr in HNO_3 solution (300 min)	O	4.0	2.14
	N	2.2	2.35
Simulated spent extraction solvent	O	4.0	2.05
	N	1.8	2.18
Adsorbed Zr in simulated spent extraction solvent (300 min)	O	3.8	2.06
	N	–	–

containing Zr was mixed with the same solvent to load Zr onto the solvent, where Zr was used to simulate Pu. As a control, the HNO_3 solution was also used as a feed solution to load Zr onto the adsorbent from the aqueous solution. The IDA-type adsorbent (CR11, Mitsubishi Chemical) was contacted with the liquid in a vial and shaken for 1 to 300 minutes. The distribution of Zr and the chemical form of the complex were then analyzed using micro-particle induced X-ray emission (PIXE) and extended X-ray absorption fine structure (EXAFS), respectively, to clarify the adsorption reaction of the IDA-type adsorbent.

The resulting distribution of Zr adsorbed on the adsorbent and Zr detection strength of adsorbent by micro-PIXE analysis are summarized in Figs.8-8 and 8-9, respectively. Micro-PIXE analysis revealed that Zr was distributed inside the adsorbent within one minute. The local structural parameters around the adsorbed Zr are detailed in Table 8-1. EXAFS analysis suggested that the chemical species of Zr trapped in adsorbent from the HNO_3 solution and simulated spent extraction solvent were $\text{ZrO}(\text{NO}_3)_2$ and ZrO^{2+} , respectively. Since the IDA-type adsorbent can form complexes with Zr atoms in the solvent, this suggests that an IDA-type adsorbent can be used to treat spent solvent.

The micro-PIXE and EXAFS analyses were performed at Takasaki Ion Accelerators for Advanced Radiation (TIARA) of National Institutes for Quantum and Radiological Science and Technology and the BL11S2 beamline of Aichi SR, respectively. (Yoichi Arai)

Reference

Arai, Y. et al., Microscopic Analyses on Zr Adsorbed IDA Chelating Resin by PIXE and EXAFS, Nuclear Instruments and Methods in Physics Research Section B, vol.477, 2020, p.54–59.

8-3 Turning Difficult-to-Treat Wastes into Stable Waste Packages

— Investigation of Radioactive Aluminum Waste Treatment Technology Using the Bayer Process —

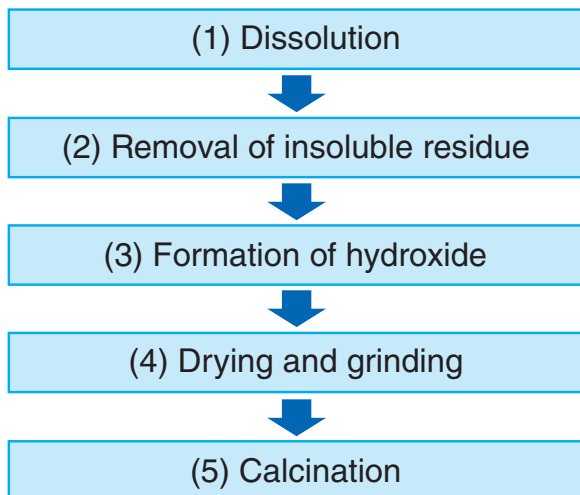


Fig.8-10 Basic process flow diagram of the Bayer process

(1) Al is dissolved in an alkaline solution. (2) The insoluble residue is removed by filtration. (3) Hydrochloric acid is added (neutralization) to generate hydroxide. (4) The hydroxide is then dried and crushed. (5) Calcining is performed using an electric furnace to convert it into stable alumina.

Solid radioactive wastes generated by nuclear facilities are generally disposed of by being converted into waste packages using concrete. Aluminum (Al) and its alloys are often used as structural materials in research reactors, such as the Japan Materials Testing Reactor (JMTR); however, Al and Al alloys can react with the concrete to produce hydrogen gas, which affects the integrity of the waste package. Therefore, we converted Al into a substance that does not react with concrete, thereby ensuring the stability of waste packages comprising Al.

Aluminum oxide (alumina) does not react with concrete and is commonly used as a quick-drying material for concrete. The Bayer process, which is used in industrial manufacturing, was applied to convert Al to alumina. However, the Al alloy used in the JMTR contains nuclides with a longer half-life than Al derived from additive elements and impurities, which increases the radioactivity of the Al waste. As Al is an amphoteric metal that reacts with both acid and base, the Al alloy is first dissolved in a strongly alkaline NaOH solution to separate it from the additive elements and impurities in the proposed method.

A summary of the proposed method is shown in Fig.8-10. X-ray diffraction was then used to analyze the calcined sample;

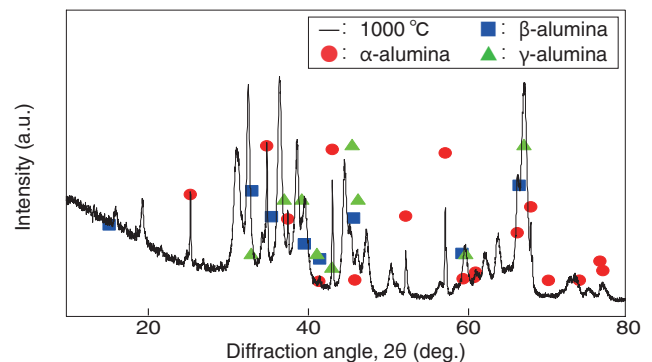


Fig.8-11 X-ray diffraction spectrum of calcining at 1000 °C
Samples calcined at 1000 °C were confirmed by X-ray diffraction to comprise three types of alumina containing α , β , and γ crystal structures.

Table 8-2 Percentage change of radioactivity of samples generated in each process

Using the irradiated Al alloy, the total radioactivity of the sample generated by the basic process was normalized by 100% and the percentage of radioactivity in each process was calculated. The results showed that more than 99% of the radioactivity was contained in the insoluble residue.

	Insoluble residue (%)	Hydroxide (%)	Waste fluid (%)
Cr-51	99.3	0.5	0.2
Fe-59	100.0	LTD	LTD

LTD: Less than detectable

our results suggested the presence of three types of alumina, as shown in Fig.8-11. Among them, α -alumina and γ -alumina are highly pure and stable, whereas β -alumina contains Na. Most importantly, these three types of alumina have a low reactivity with concrete.

The Al alloys irradiated in the Kyoto University Research Reactor were then used to measure the radioactivity of the samples generated during each step of the proposed method. More than 99% of the nuclides produced by the activation of Cr and Fe in the Al alloy could be removed by the insoluble residue removal process, as summarized in Table 8-2, thereby reducing the radioactivity of the alumina produced during calcination.

In summary, the proposed waste treatment method can effectively convert radioactive Al into a stable waste package. Future efforts will include further studies on the properties of the alumina when mixed with concrete and the consequences on the behavior and properties of the produced waste package.

This research includes the results obtained through the joint use of the Institute for Integrated Radiation and Nuclear Science, Kyoto University.

(Misaki Seki)

References

- Seki, M. et al., Development of the Treatment Method for Difficult Wastes Aimed at Decommissioning of JMTR - Structural Materials of Reactor and Used Ion-Exchange Resins -, Journal of RANDEC, no.62, 2020, p.9-19 (in Japanese).
 Seki, M. et al., Radioactive Aluminum Waste Processing Method, Patent Application Publication, 2021-32570, 2021-03-01 (in Japanese).

8-4 Safety Improvements for Plutonium-Handling Facilities

— Development of Fireproof Sheet on Glove Box Panels —

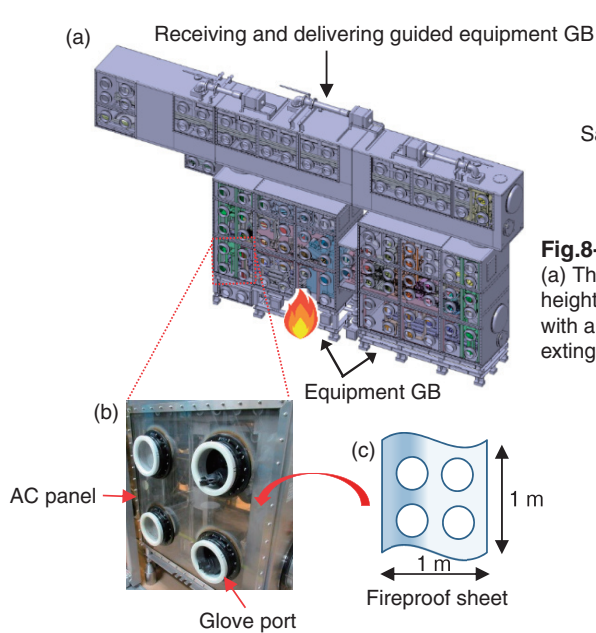


Fig.8-12 Schematic of fire-retardant measures

(a) Typical GB configuration in the PFPF, including one receiving and delivering guided equipment GBs (approx. $10 \times 1 \times 1 \text{ m}^3$) and two equipment GBs (approx. $3 \times 3 \times 1 \text{ m}^3$). (b) Measures were implemented to attach the (c) developed fireproof sheet to the AC panel of each GB.

The Plutonium Fuel Production Facility (PFPF) produces mixed oxide (MOX) fuel for fast reactors and contains many large glove boxes (GBs) for handling plutonium. Acrylic (AC) resin (flammable) is used for the window panels that constitute the GB, after confirming its safety through past fire tests. However, from the perspective of preventing the spread of fire in the event of a fire in the process room, direct fire prevention was an issue. In the PFPF, fire-retardant polycarbonate (PC) resin is to be used for the panels of GBs to be newly installed after the new regulatory requirements took effect (December 2013). However, replacing the AC panels of the existing GBs (approx. 2300 panels) with fire-retardant PC panels is impractical in terms of contamination risk, cost, and work period. Therefore, we developed a fireproof sheet made of PC that does not deteriorate under radiation, is effectively prevents fire damage, and can be attached to existing AC panels, as shown in Fig.8-12.

During the development and testing of the developed method, we conducted flammability tests and usage environmental (gamma rays, ultraviolet rays) influence tests to confirm its feasibility. The samples are 10 mm thick AC plate (as same as existing GBs) with fireproof sheet (this sample) and 10 mm thick PC plate for the purpose of comparison. For this sheet, we selected a transparent PC fire-retardant sheet (0.38 mm thick) with V-0 rating that is the highest fire-retardant in the U.S. UL94 standard, which is widely used for flammability testing of polymer materials. In addition, a special adhesive agent was used to make it easier to attach on the AC panel and remove for replacement.

Following the guidelines set by equivalent to the UL94 standard 5V during flammability testing, each sample was fixed horizontally, and flames were intermittently applied from below

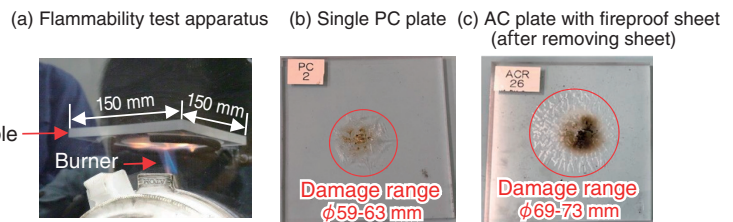


Fig.8-13 Flammability test equivalent to the UL94 standard 5V

(a) The sample was fixed horizontally and burned intermittently from below with a flame height of 125 mm. (b) After releasing the burner, the sample self-extinguished within 1 s with a maximum damage range of 63 mm. (c) After releasing the burner, the sample self-extinguished within 1 s with a maximum damage range of 73 mm.

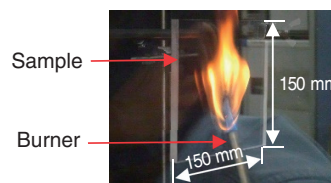


Fig.8-14 Forced combustion test

The sample was fixed vertically and burned continuously for 90 s from the side using a burner with a flame height of 125 mm. The PC plate was self-extinguished within 7 s after releasing the burner, whereas the AC plate containing the sheet was self-extinguished within 1 s.

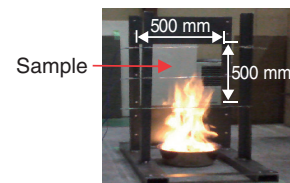


Fig.8-15 Fire test

As a result of burning the sample with the fire almost touching the sample, neither the PC plate alone nor the AC plate with this sheet attached did not ignite.

with a burner five times for 5 s each, as shown in Fig.8-13. By applying the proposed fire-retardant sheet, the AC panel self-extinguished within the same amount of time as the PC plate. We also performed forced combustion tests and fire tests, as shown in Figs.8-14 and 8-15. During forced combustion tests, the sample was fixed vertically and continuously exposed to a burner under severe conditions similar to the actual installation of a window panel; during fire tests, 1.5 kg of 62wt% ethanol (equivalent to the total calorific value of 1.5 kg of paper towels) was used to simulate a fire in a process room. In all cases, the results of the proposed system were comparable to those of a single PC plate.

Usage environmental influence tests were then performed to confirm that there were no significant property changes (e.g., in fire retardance or visibility) after 5–60 years of accelerated gamma irradiation from nuclear fuel materials in the GB and 10–20 years of accelerated ultraviolet irradiation from fluorescent lights installed near the window panels.

From the results of these tests, we found that attaching this sheet to the AC panel of the existing GB has self-extinguishing properties equivalent to those of PC plates, and is expected to prevent fire damage, as well as providing the prospect of application in actual radiation environments.

Currently, this sheet has been attached to the window panels of the existing GBs in PFPF and is in operation. This development is expected to be widely applied not only to nuclear facilities but also to every place using AC panels such as GBs in the chemical and pharmaceutical industries, as a fire-retardancy measure and as a surface protection measure.

(Kohei Kawasaki)

Reference

Kawasaki, K. et al., Development of Fireproof Sheet on Glove Box Panels, JAEA-Technology 2020-025, 2021, 80p. (in Japanese).

8-5 Direct Observation of the Fracture Induced by Gallery Excavation — Visualization Technology Using a Resin Injection Method —

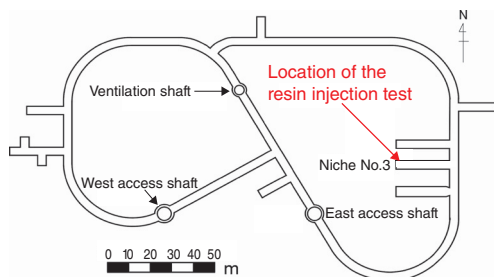


Fig.8-16 Location of the resin injection test
An in situ resin injection test was performed in the gallery 350 m below ground in the Horonobe URL.

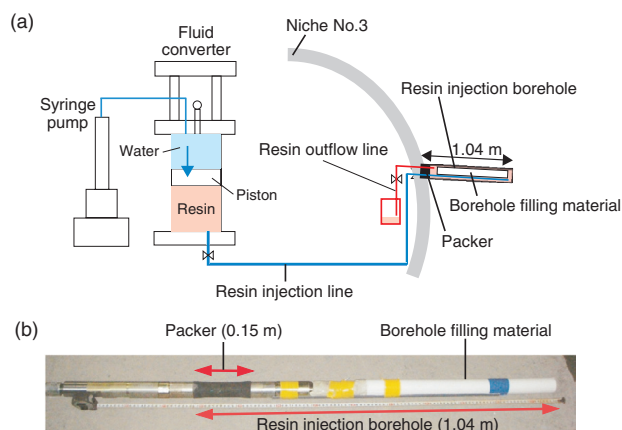


Fig.8-17 (a) Experimental setup for resin injection tests and (b) photograph of the packer system used in the resin injection borehole
Resin was injected into the borehole through a fluid converter using a syringe pump. The injection was made at constant pressure (approximately 0.1 MPa).

Artificial fractures can develop around the gallery wall of high-level radioactive waste (HLW) disposal repositories because of the resultant stress redistribution occurring during excavation. Zones containing these artificial fractures are identified as excavation-damaged zones (EDZs). The hydraulic conductivity in an EDZ can increase and cause the fracture to become a migration pathway for the radionuclides from the disposal facilities. Thus, the distribution and aperture of fractures in the EDZ must be understood quantitatively to assess the safety of HLW disposal.

Therefore, we performed an in situ resin injection experiment in the gallery of Niche No. 3 at a depth of 350 m in the Horonobe Underground Research Laboratory (URL) to observe EDZ fractures, as summarized in Fig.8-16. Previously, high-viscosity resins (i.e., with a viscosity 90–800 times that of water) were injected into the EDZ fractures. However, high-pressure injections cause the re-opening of existing fractures and/or the expanding of EDZ fractures. Therefore, we developed a low-viscosity resin (i.e., with a viscosity 7 times that of water) that can be polymerized at room temperature and in a water-rich condition. The resin included a fluorescent substance and was injected using the packer system shown in Fig.8-17. Based on a previous study on the EDZ, the EDZ around Niche No.3 was assumed to be within 0.6 m from the surface of the

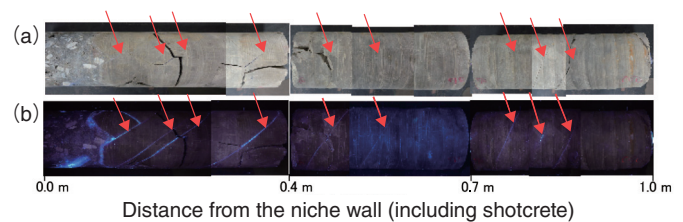


Fig.8-18 Photographs of the injection borehole taken under (a) natural and (b) UV light
Resin-fixed fractures, indicated as red arrows, were recognized as EDZ fractures based on the observation of the rock core surface at the injection borehole.

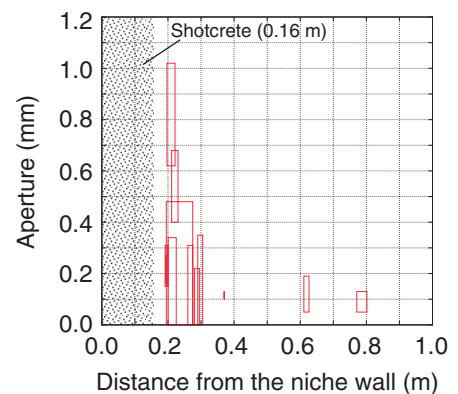


Fig.8-19 Relationship between the fracture aperture and distance from the niche wall
Fractures with a relatively large aperture developed within 0.3 m into the niche wall.

niche wall. Therefore, the length of the injection borehole was approximately 1.0 m, including the shotcrete thickness. After the resin polymerized, rock samples containing injected resin were overcored. The resin in the fractures was confirmed to be successfully polymerized by observation under ultraviolet (UV) light, as shown in Fig.8-18.

The aperture of the EDZ fractures was measured using a close-up photograph of the fracture that had been filled with resin taken under UV light. The relationship between the aperture and distance from the niche wall is shown in Fig.8-19. In the region within 0.3 m from the niche wall, fractures with large apertures were observed; the maximum aperture was approximately 1.02 mm. Many fractures developed in that region. On the other hand, there were very few fractures past 0.3 m from the niche wall, and the maximum aperture was 0.19 mm.

These results are expected to support model development to estimate the future change in the hydraulic conductivity of the EDZ fracture considering the increase in swelling pressure of the backfilling material after the repository is closed. Our study provided data fundamental to improving the reliability of HLW disposal safety assessments.

Our research was performed in collaboration with Kyoto University.

(Akitaka Sakurai)

Reference

Aoyagi, K., Sakurai, A. et al., Visualization of Fractures Induced around the Gallery Wall in Horonobe Underground Research Laboratory, Proceedings of 5th ISRM Young Scholars' Symposium on Rock Mechanics and International Symposium on Rock Engineering for Innovative Future (YSRM 2019 and REIF 2019), Ginowan, Japan, 2019, 6p., in USB Flash Drive.

8-6 Factors Affecting Rock Desaturation in Tunnel Excavation

— Numerical Simulation on the Effects of Dissolved Gas and Rock Permeability —

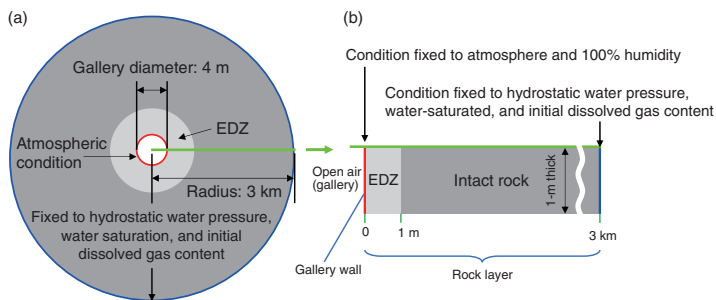


Fig.8-20 Conceptual model and boundary conditions
 (a) Horizontal cross section. (b) Vertical cross section at the green line.

Table 8-3 Parameters used in base case

Permeability and effective porosity were derived from monitoring data. The initial dissolved gas contents were calculated as saturated at the initial water pressure.

Permeability of EDZ (m^2)	5.1×10^{-15}	CH ₄ content (mol/L)	3.3×10^{-2}
Permeability of intact rock (m^2)	5.2×10^{-17}	CO ₂ content (mol/L)	6.0×10^{-3}
Effective porosity (%)	50	Water pressure (Pa)	2.45×10^6

Excavating underground facilities to dispose of high-level radioactive waste (HLW) geologically is expected to cause the rock around galleries to desaturate, especially near the newly created fractures of the EDZ. Desaturation affects rock's hydraulic properties, increasing gas mobility relative to groundwater, leading to air infusion into rocks, and increasing the solubility and mobility of radionuclides. However, a significant amount of dissolved gas has been shown to emanate from the gallery walls, suggesting that this dissolved gas inhibits air entry into the surrounding rock and plays an important role in the desaturation process. Therefore, we aimed to clarify the factors contributing to rock desaturation. Thus, the effects of dissolved gas and rock permeability on desaturation were investigated using numerical simulation.

A sensitivity analysis of gas content and rock permeability was performed using a numerical simulator for the two-phase flow of the groundwater and gas in the model mimicking the gallery of the Horonobe URL; this model is summarized in Fig.8-20. As an initial condition, the rock was assumed to be saturated with groundwater that was saturated with dissolved CH₄ and CO₂ gases at hydrostatic pressure. The two-phase flow of groundwater and gas, which is caused by a large pressure gradient between atmospheric pressure at the gallery and hydrostatic pressure, was calculated for 50 years. The parameters used for the base case demonstrating the conditions in the 250 m

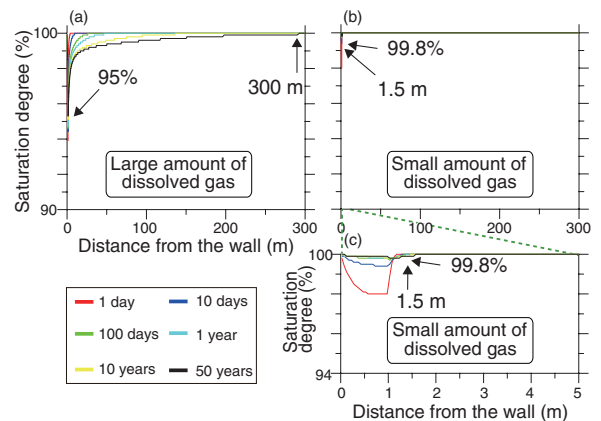


Fig.8-21 Results for cases mimicking the 250 m gallery
 (a) Base case. (b) Initial dissolved gas content decreased to one tenth. (c) Magnification of area within 5 m from the wall in (b). Arrows indicate the values at 50 years. Both the saturation degree and spatial extent of desaturation differed between (a) and (b).

gallery are shown in Table 8-3 as an example. To assess the effects of the dissolved gas content and the rock permeability on desaturation, several cases were calculated assuming various amounts of dissolved gas and permeability.

The results of the base case and a case assuming a low amount of dissolved gas are shown in Figs.8-21(a) and 8-21(b), respectively. In the base case, there was a minimal degree of saturation near the EDZ, and the spatial extent (i.e., distance from the wall) of desaturation reached approximately 300 m after 50 years. Decreasing the amount of dissolved gas caused almost no decrease in saturation degree within 50 years and reduced the spatial extent of desaturation near the EDZ. When the permeability of intact rock was increased, the degree of saturation was similar to that of the base case, but the extent of desaturation increased.

Overall, we determined that the initial dissolved gas content affects both the degree and spatial extent of rock desaturation. Further, rock permeability can affect the spatial extent of desaturation but has little effect on the degree of saturation. These results will advance investigation efforts into the mechanism of O₂ infusion into rock and R&D efforts to secure and ensure the retrievability of HLW, thereby ensuring the long-term safety of the underground facility.

(Kazuya Miyakawa)

Reference

Miyakawa, K. et al., The Effect of Dissolved Gas on Rock Desaturation in Artificial Openings in Geological Formations, Proceedings of 5th ISRM Young Scholars' Symposium on Rock Mechanics and International Symposium on Rock Engineering for Innovative Future (YSRM 2019 and REIF 2019), Ginowan, Japan, 2019, 6p., in USB Flash Drive.

8-7 From Micro to Macro: Approaching Mountain Formation Processes Based on Age Determinations of Minerals

— Insights to the Ou Backbone Range Obtained from Low-Temperature Thermochronology —

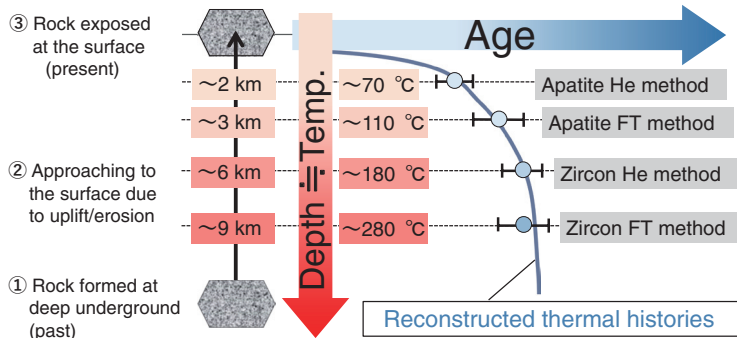


Fig.8-22 Reconstructing the time-temperature history involving uplift and cooling of a rock sample based on multi-thermochronometers

After formation, a rock gradually approaches the surface due to uplift/erosion before finally becoming exposed at the surface. Multiple dating methods having various closure temperatures were applied to a single rock sample collected at the present surface. The obtained ages should vary depending on the closure temperatures/depths of the applied methods. The curve connecting each point represents a time–temperature history of the rock, i.e., a cooling history.

Sites selected for geologic disposal of high-level radioactive waste (HLW) should be stable in the long term (i.e., 10^5 yr). At the Tono Geoscience Center (TGC), techniques for evaluating and investigating the long-term geosphere stability have been developed. In particular, estimating the uplift/erosion mechanisms plays a key role in evaluating risks of HLW approaching biospheres and simulating groundwater flow conditions related to topographic evolution, thereby contributing to the design and safety assessment of a disposal facility.

Thermochronology, a branch of radiometric dating, is a useful method to evaluate the temperature of a rock sample changing over time (i.e., the cooling history). Radiometric dating employs radioactive decay, in which radionuclides (e.g., uranium) naturally decompose into other nuclides at certain rates. At TGC, fission-track (FT) and (U–Th)/He (He) thermochronometers are available. These instruments can be used to determine the age of a sample by analyzing the chemical composition or crystal structure subject to micro-scale (<0.1 mm) minerals, such as apatite and zircon. Closure temperatures, below which dating methods begin to record their ages, have been determined theoretically and experimentally. The obtained age indicates when the sample was cooled to its closure temperature. Thus, an uplift/erosion history of rock can be represented by a cooling history from the hot to the cold domain (i.e., deep underground to the surface), as shown in Fig.8-22. Young ages indicate short transfer durations, implying that the rock was recently located in a warmer (i.e., deeper) location. By assuming thermal

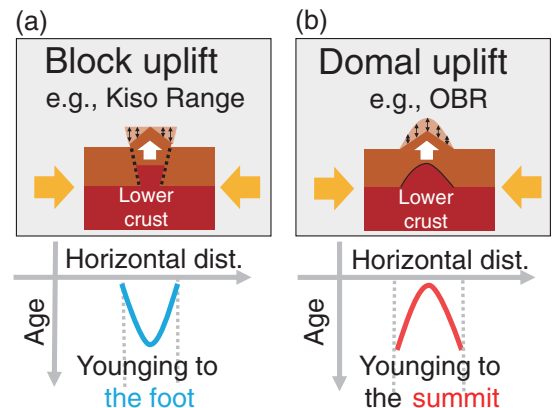


Fig.8-23 Comparing uplift mechanisms and the spatial age distributions between two mountains

The spatial patterns of ages across mountains can be useful indicators to estimate the uplift mechanisms of mountains. (a) Samples closer to the foot of a mountain formed from block uplift are younger because the unstable topographies along both margins are extremely eroded. (b) Samples closer to the summit of a mountain formed by domal uplift are younger because the steepest topographies at the center are selectively eroded.

gradients, uplift/erosional histories (i.e., how quickly the rock was moved to the surface) can be reconstructed. Furthermore, a large sampling of ages across a mountain can provide a macro-scale (i.e., a few to a dozen km) uplift/erosion pattern over the entire mountain.

The Tohoku district has been affected by the E–W compression for three million years due to the subduction of the Pacific Plate at the Japan Trench, which triggered the 2011 off the Pacific coast of Tohoku Earthquake. This compression has also caused the uplift of the Ou Backbone Range (OBR) along the central axis of Tohoku; however, the mechanism of uplift has not yet been clarified. Therefore, we obtained FT and He thermochronometric data at densities higher than previous studies. Our results suggested a domal uplift model of the OBR, which differs from other Japanese mountain ranges, such as the Kiso Range, as summarized in Fig.8-23. The Kiso Range is mainly uplifted by reverse faults at the foot, whereas the OBR is uplifted by the hot zone underneath it. We will continue to investigate whether such domal uplift commonly occurs in other subduction zones in Japan and overseas.

This study was supported by the Japan Society for the Promotion of Science (JSPS) KAKENHI Grand-in-Aid for Scientific Research on Innovative Areas, “Resolution of crustal deformation of the Japan Islands in various spatio-temporal scales” (No.JP26109003).

(Shoma Fukuda, Shigeru Sueoka)

References

- Fukuda, S., Sueoka, S. et al., (U–Th)/He Thermochronometric Mapping Across the Northeast Japan Arc: Towards Understanding Mountain Building in an Island-Arc Setting, *Earth, Planets and Space*, vol.72, issue 1, 2020, 24, 19p.
 Fukuda, S., Sueoka, S. et al., Thermochronometric Studies of Mountains in Island Arc Settings Based on Fission-Track Method: A Review, *RADIOISOTOPES*, vol.70, issue 3, 2021, p.173–187 (in Japanese).

8-8 Reduced Geological Sample Size for Radiocarbon Dating at JAEA-AMS-TONO

— Preparation Techniques Using One-Twentieth the Sample Size of the Conventional Method —

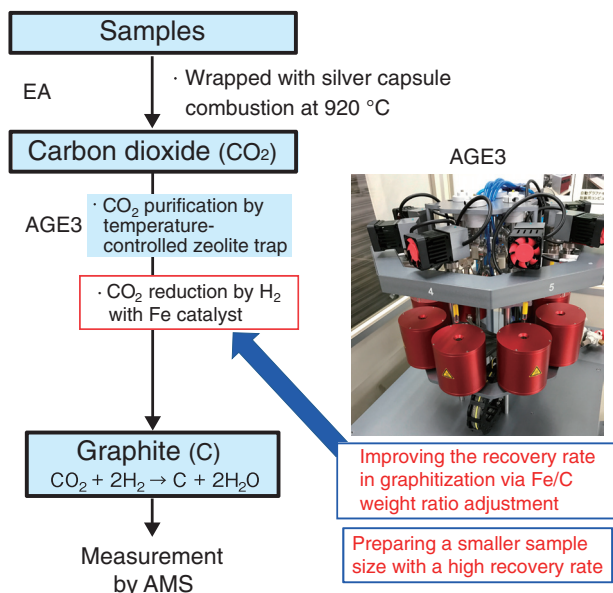


Fig.8-24 Process for graphitization of a small sample
Graphitization of a sample with a carbon weight of 0.1–0.05 mg (one-twentieth of the conventional method) was performed.

Accelerator mass spectrometry (AMS) is a technique widely used for measuring the radiocarbon (^{14}C) concentration in geochronological studies focused on the last 50000 years. AMS- ^{14}C measurements of organic materials and carbonate minerals in natural samples have been applied to geological studies, such as the estimation of paleoenvironmental changes. However, suitable geological samples for ^{14}C dating, such as plant residues, are often limited in volume. Therefore, ^{14}C measurements using less than 0.1 mg of carbon are required to date geological samples.

Sample preparation procedures have included CO_2 gas purification and graphitization from solid samples using third-generation automated graphitization equipment (AGE3, IonPlus AG) combined with an elemental analyzer (EA), as shown in Fig.8-24. The EA-AGE3 can be utilized as an automated sample preparation system for ^{14}C measurements of standard sample volume (approximately 1 mg of carbon).

Here, we developed preparation procedures using the EA-AGE3 system for AMS- ^{14}C measurements using a smaller amount of carbon (0.1 and 0.05 mg). Notably, the recovery rates

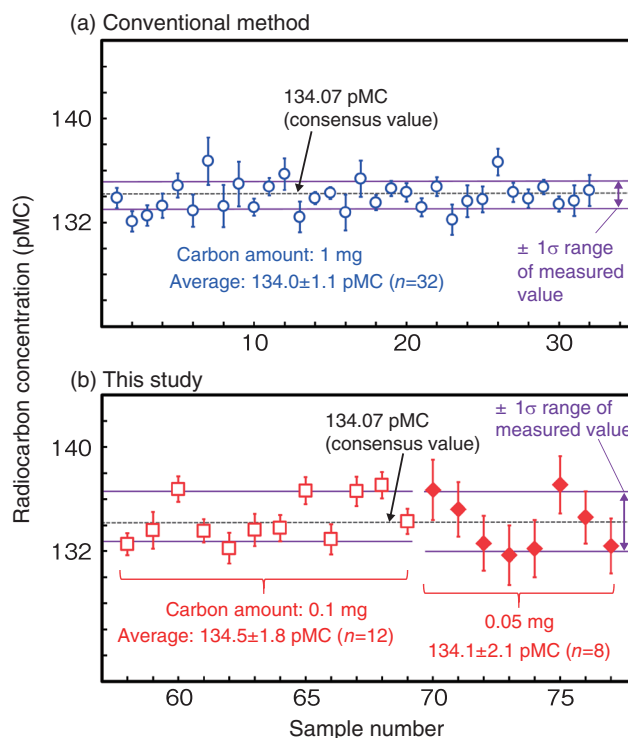


Fig.8-25 ^{14}C measurements of standard materials using small samples

^{14}C measurements of standard materials containing (a) 1 and (b) 0.1–0.05 mg of carbon.

during graphitization were improved by adjusting the ratio of iron catalyst to carbon sample size in the EA-AGE3 system. The resulting average ^{14}C concentrations (percent modern carbon: pMC) in the standard reference materials prepared by the EA-AGE3 system were close to their consensus values, as shown in Fig.8-25, thereby implying that the proposed preparation technique using only one-twentieth of the carbon sample of the conventional method can be used. Furthermore, the carbon background values were nearly cut in half after the capsules had undergone pre-baking at 500 °C for 5 h. We expect that the recovery rate and mass-dependent background corrections of the EA-AGE3 system can be further refined to graphitize small samples as more data are accumulated.

This study was conducted as a part of the public offered project, a commission investigation of geological disposal technology “Development of enhancing the disposal system in the coastal region” under the contract with the Agency for Natural Resources and Energy (ANRE), Ministry of Economy, Trade and Industry, Japan (JFY2016–2018).

(Takahiro Watanabe)

Reference

Watanabe, T. et al., Preliminary Report on Small-Mass Graphitization for Radiocarbon Dating Using EA-AGE3 at JAEA-AMS-TONO, *Geochemical Journal*, vol. 55, no.4, 2021, p.277–281.

8–9 Safety Assessment Considering the Evolution of Topography and the Depth of the Disposal Facility

— Development of an Analysis Tool to Evaluate the Topography and Depth of a Disposal Facility —

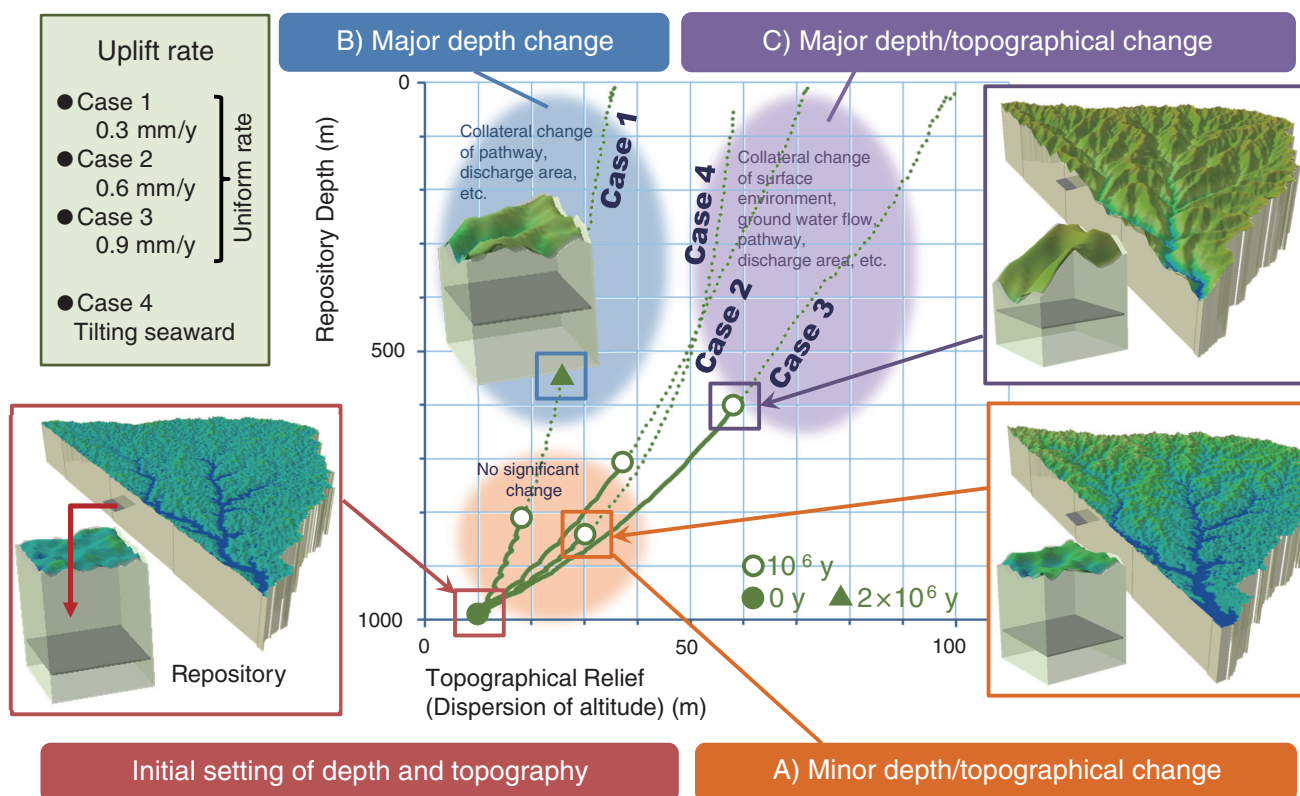


Fig.8-26 Example of topographical and repository depth change calculated using the developed tool

Changes to the topography and repository depth were calculated for multiple uplift rate settings (i.e., Cases 1–4). Several patterns can be used to describe the topography and repository depth; by estimating which pattern best represents the calculated results, the impact to be focused on during safety assessment can be assessed.

Sites for geological disposal of high-level radioactive waste (HLW) are selected based on exclusion requirements to avoid significant effects from natural phenomena, such as volcanic/igneous activity, uplift/erosion, and earthquake/fault activity. On the other hand, the potential effects of climate change and slow uplift/erosion affecting wide areas should also be studied.

Therefore, we developed a method to assess the temporal changes in topography and depth of a disposal facility due to uplift/erosion to make it possible to evaluate the effects of uplift/erosion on the performance of geological disposal systems, including location-dependent effects. The developed tool can quickly calculate topographical and repository depth change by changing the conditions such as the topography, uplift rate and distribution, and location of the disposal site. Changes in the topography and repository depth caused by uplift/erosion likely influence the nuclide migration behavior, including the pathway from the disposal to the surface and the discharge area. On the other hand, these changes depend on the initial conditions, such as the initial topography, disposal site location, and uplift rate. Three patterns of topographical and depth changes were

identified based on the result depending on the initial conditions.

- A) minor changes in topography and repository depth,
- B) major changes in repository depth, and
- C) major changes in topography and repository depth.

The calculated repository depth and topographical changes assuming multiple uplift rate settings (i.e., Cases 1–4) using the tool are summarized in Fig.8-26. By applying this tool to various conditions, calculating the temporal changes in topography and repository depth, and estimating which pattern they follow, the impact of uplift and erosion on safety assessment can be estimated. The developed tool can also be used to estimate which conditions should be focused on the safety assessment when considering the influence (e.g., changes in the migration pathway changes or the discharge area to the surface). Additionally, the quantitative information on topographical and depth changes provided by this tool can be used to evaluate groundwater flow or nuclide migration pathways to the surface.

Overall, the developed tool improves nuclide migration analyses and biosphere assessments.

(Masaaki Yamaguchi)

Reference

Yamaguchi, M. et al., Analytical Tool of Evolution of Topography and Repository Depth to Assess Impacts of Uplift and Erosion for HLW Disposal, Journal of Nuclear Fuel Cycle and Environment, vol.27, issue 2, 2020, p.72–82 (in Japanese).

8-10 Electrochemical Methods to Evaluate Overpack Corrosion

— Search for Passivation Conditions of Carbon Steel Surrounded by Buffer Material —

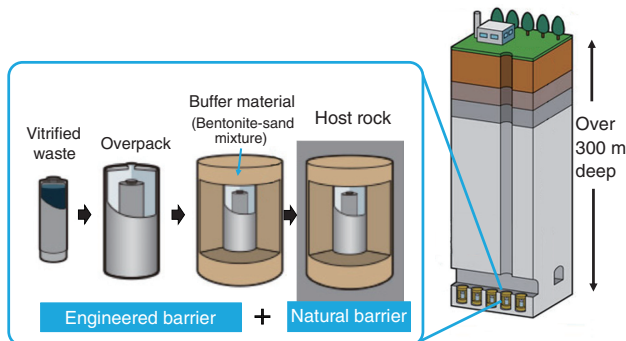


Fig.8-27 Basic concept of HLW disposal

Carbon steel overpacks are expected to have the function of preventing contact between the vitrified materials and groundwater during periods of high radioactivity and heat generation (1000 years).

Current designs for barriers for geological disposal sites of high-level radioactive waste (HLW) in Japan use carbon steel overpack containers surrounded by a bentonite-sand buffer material, as shown in Fig.8-27. Passivation is a process in which a corrosion-resistant thin oxide film (i.e., passivation film) is formed on the metal surface. If carbon steel is passivated, localized corrosion occurs; otherwise, general corrosion occurs. Under general corrosion, the containment life of the carbon steel overpack can be determined by the corrosion depth, which is based on the corrosion rate. On the other hand, localized corrosion can cause severe corrosion, such as pitting, which can reduce the lifespan of carbon steel overpacks. Therefore, to ensure that carbon steel overpacks that have not been passivated (and thus that do not incur localized corrosion), the conditions causing passivation to occur in the disposal environment must be understood. Researchers have thus investigated the conditions that lead to the passivation of carbon steel, such as groundwater environments rich in carbonic acid^{*1}. Considering the transportation of HLW, coastal waste disposal locations have become preferred^{*2}; thus, the corrosion behavior of steel given the groundwater environment of coastal areas should be studied.

Therefore, we studied the corrosion behavior of carbon steel with and without buffer material (bentonite) using a solution of diluted synthetic seawater (10% SSW) to mimic the groundwater in coastal areas, which comprises a mixture of water originating from seawater and freshwater. The solution pH was adjusted to 8.5, 10, and 12 to investigate the passivation behavior in a high pH environment, as carbon steel is known to passivate easily in high-pH environments. A low-oxygen atmosphere was used to simulate the underground environment. A carbon steel electrode was directly immersed in the solution or embedded in the buffer material before the solution was impregnated. The polarization

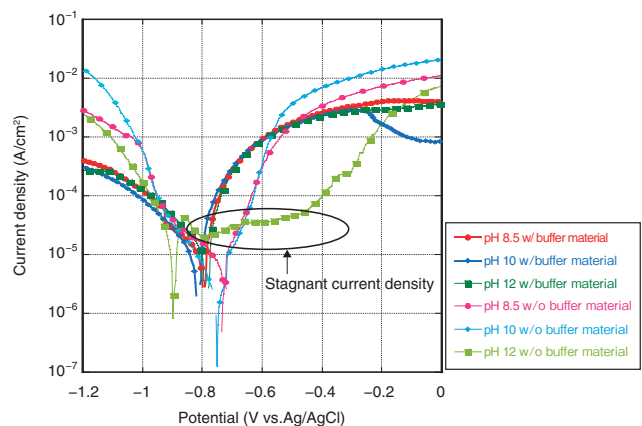


Fig.8-28 Anodic/cathodic polarization curves measured in 10% SSW with and without buffer material

The current density stagnated with passivation at pH 12 without buffer material.

measurements were performed in a low-oxygen glove box.

The resulting anodic/cathodic polarization curves are shown in Fig.8-28. Without the buffer material, current density stagnation with passivation was observed at a pH of 12; however, no passivation was observed in any condition when the buffer material was included. Even if the dilution ratio of synthetic seawater has been changed, localized corrosion was observed only at high pH without the buffer material and general corrosion was observed under the other conditions. The pH buffering function of the bentonite reduced the pH of the solution in contact with carbon steel (i.e., bentonite pore water), thereby preventing the passivation of the carbon steel even in high-pH solutions.

Overall, using a bentonite buffer prevented the passivation of carbon steel in coastal groundwater even in a high-pH environment. Our results suggest that the main corrosion mode of carbon steel surrounded by a buffer material in this environment is general corrosion. Additionally, we confirmed the applicability of the corrosion evaluation model based on general corrosion to the corrosion of carbon steel overpacks used in geological disposal in coastal areas.

This study was funded by the Ministry of Economy, Trade and Industry (METI) of Japan through the program “Advancement of the geological disposal system in coastal regions” (JFY2017–2018).

(Ayami Kitayama)

^{*1} Taniguchi, N. et al., The Assessment of Corrosion Type and Corrosion Rate of Carbon Steel in Compacted Bentonite, JNC-TN8400 99-003, 1999, 88p.

^{*2} Advisory Committee for Natural Resources and Energy, Examination Results of Requirements and Standards for Presentation of Regional Scientific Characteristics for Geological Disposal, 2017, p.59–62.

Reference

Kitayama, A. et al., Electrochemical Behavior of Carbon Steel with Bentonite/Sand in Saline Environment, *Materials and Corrosion*, vol.72, issues 1-2, 2021, p.211–217.

Computational Science for Nuclear Research and Development

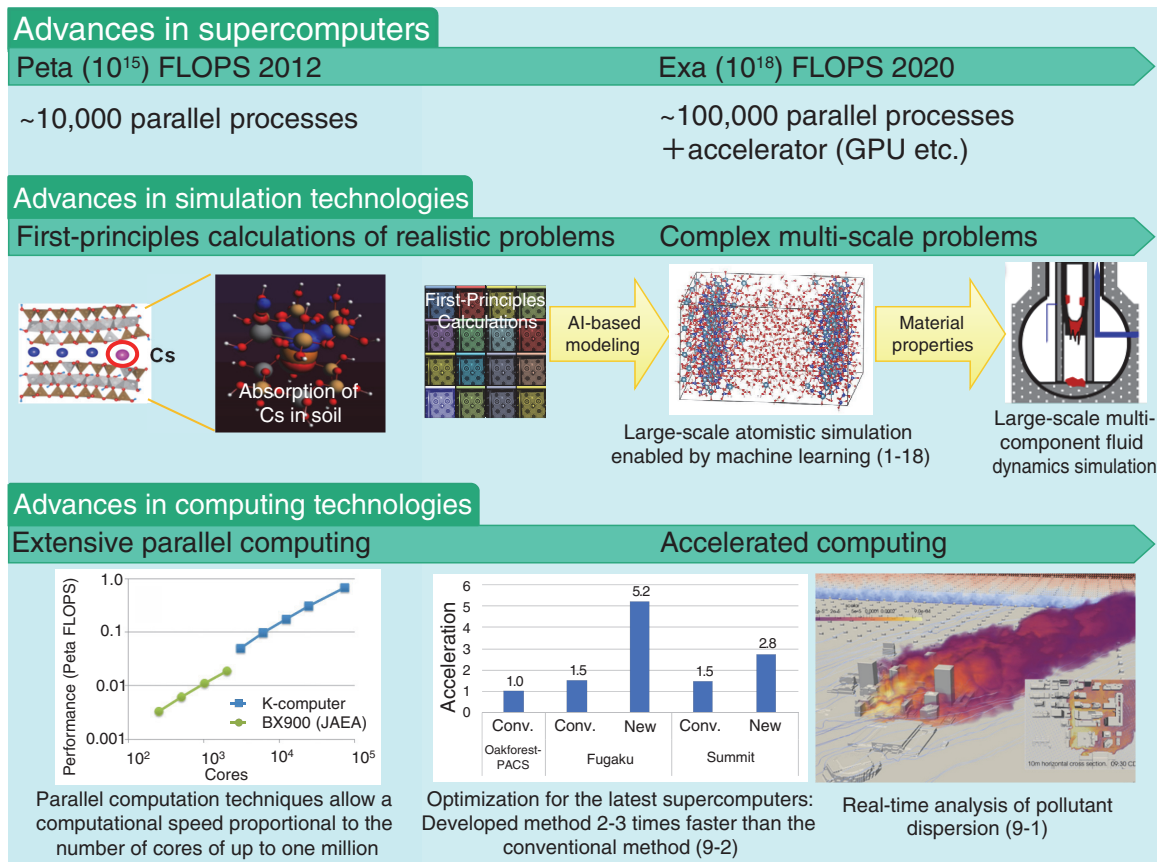


Fig.9-1 Computational science research at the Center for Computational Science and e-Systems

The performance of a supercomputer is measured by the number of arithmetic operations it can perform in one second (i.e., floating-point operations per second, FLOPS). Exascale (i.e., 10^{18} FLOPS) supercomputers are expected to be standard in the near future, as are technologies to utilize them fully (i.e., exascale computational technology). The Center for Computational Science & e-Systems applies the latest technologies, such as exascale computational technology and machine learning techniques, and promotes the development of fundamental technologies to analyze complex phenomena in nuclear engineering.

Simulation techniques used to analyze complex phenomena comprising various physics effects, such as the environmental dynamics of radioactive substances and the study of severe accidents, are essential for resolving issues created by the accident at TEPCO's Fukushima Daiichi NPS. Such techniques are also required for the research and development (R&D) of future nuclear systems. For example, predicting the spread of released radioactive substances (whether on accident or due to an act of terrorism) in real-time requires using meteorological data to reconstruct the complex wind flow around buildings. Thus, advanced fluid analysis techniques that can compute complex wind flow patterns quickly and accurately are required. Another example is material modeling required in severe accident analyses and development of next-generation nuclear reactors. Such modeling requires nanometer-scale analysis to simulate the complex arrangement of atoms in materials and centimeter-scale analysis to analyze various phenomena, such as fuel melting. Such complex phenomena analyses could be extended to a much larger scale by combining them with exascale computational technologies (i.e., computers capable of performing 10^{18} floating-point operations per second, FLOPS), such as Fugaku, which can perform several million parallel computations using many CPUs containing tens of cores.

Various simulation techniques have been developed, including

atomic/molecular and fluid simulations, which are the basis for analyzing complex phenomena, and computational technologies, such as numerical algorithms and visualization systems. Efforts to further improve these techniques and develop new simulation and computational technologies are ongoing to enable exascale simulations of complex phenomena, apply machine learning techniques for advanced simulations, and employ data-assimilation technologies to improve simulation accuracy, as summarized in Fig.9-1. Such simulation techniques for complex phenomena will become a foundation for future nuclear R&D.

In FY2020, our contributions in the field of computer science to the reconstruction and revitalization of Fukushima Prefecture included clarifying the main contributions to the air dose rate in forests in Fukushima Prefecture and established fundamental techniques of atomistic simulations to identify the mechanism of Cesium absorption to concrete (Topics 1-17 and 1-18, respectively). To advance analysis techniques of complex phenomena, we developed new simulation methods as discussed in more detail in the following sections of this chapter (Topics 9-1, 9-2, 9-3, and 9-4). We steadily promote the research of simulation and computational techniques, which are a common foundation for nuclear R&D, and provide them to the community.

9-1 Plume Dispersion Simulations Satisfying Accuracy Criteria for Environmental Assessments — Real-Time Ensemble Calculations with Meter-Order Resolution —

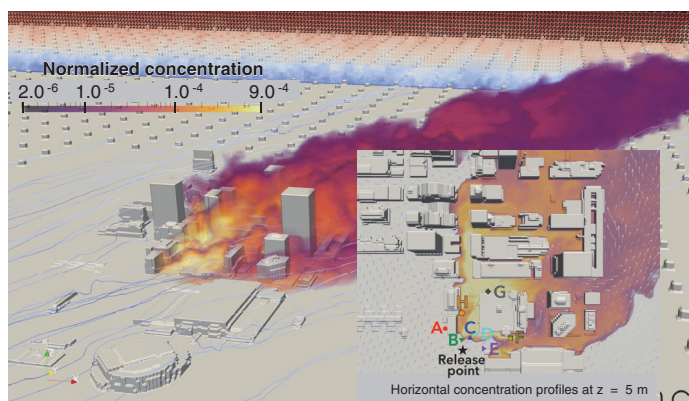


Fig.9-2 Visualization of buildings and concentration

The real-time simulation was performed over $4.2 \times 4.2 \times 2.5 \text{ km}^3$ and reflected the meteorological conditions given by the mesoscale weather prediction model and building data in the city center.

The environmental dynamics of radioactive substances is accurately predicted based on detailed simulations of local airflow and plume dispersion to ensure nuclear security. Further, these kinds of flow simulations in urban areas are important tools when designing smart cities. The presence of tall buildings and complex structures makes airflows turbulent, necessitating large-scale computational fluid dynamics (CFD) simulations to clarify airflow details. However, the computational cost can become extremely large when trying to understand detailed wind dynamics, making it difficult to achieve the real-time or faster-than-real-time simulations required in emergencies, such as accidental releases of radioactive substances.

Realizing real-time (or faster) calculations requires two problems to be addressed: higher computational speeds and greater accuracy. First, real-time high-resolution simulations several tens of times faster than existing CFD methods are required. Second, in conventional simulations, experimental and simulated results often differ by a factor of five; environmental assessments require this difference to be reduced to a factor of two.

We developed two technological solutions to address these problems, the first of which involved a speed-up technology to realize a real-time multiscale simulation. Here, the different scales of urban wind flow were focused on, and a CFD analysis code, CityLBM, was developed based on the adaptive mesh refinement (AMR) method. Since fine computational grids are arranged only around buildings where the flow becomes turbulent, the number of computational grids (i.e., the computational cost) was reduced by a factor of 10 from the original method that did not employ the AMR method. Additionally, optimizing CFD schemes for the graphics processing units (GPUs) further reduced the computational time by a factor of 10, resulting in a final system approximately 100

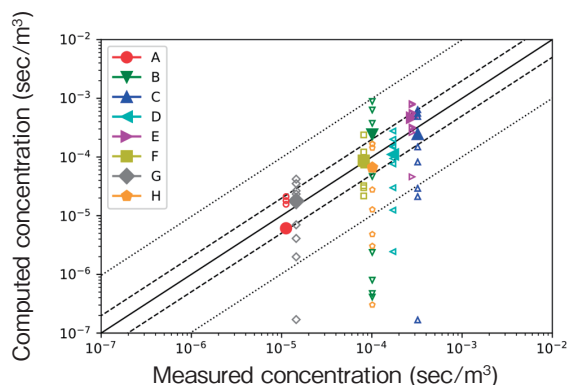


Fig.9-3 Mean concentration (scatter plots)

Open and solid symbols denote ensemble and ensemble-averaged data, respectively. The dashed and dotted lines represent factor-of-two and factor-of-ten agreement with the observations, respectively.

times faster than other state-of-the-art methods, enabling faster-than-real-time simulations.

In the second developed solution, a probabilistic evaluation method was employed to improve accuracy of simulations for turbulent plume dispersion. In high-resolution simulations, turbulence causes large fluctuations in the time series of measurement instruments, leading to large uncertainty. Such uncertainty was reduced by a probabilistic evaluation based on ensemble calculations of multiple cases with slightly different initial values.

The CityLBM was validated against the field experiments performed during the JU2003* campaign conducted in the city center of Oklahoma City, as shown in Fig.9-2. Although the concentrations for each ensemble case (white symbols) were widely dispersed with the observed concentrations (black lines), the mean ensemble values (fill-in symbols) achieved the standard accuracy for environmental assessment in more than 70% of all observations (8 observation points \times 3 time periods), as shown in Fig.9-3. These technological innovations thus allowed a real-time ensemble calculation that reduced the difference between simulated and experimental results to within a factor of two.

This research was supported in part by the Japan Society for the Promotion of Science (JSPS) KAKENHI Grants-in-Aid for Scientific Research (C) (No.JP19K11992, JP17K06570), (B) (No.JP17H03493) and the Ministry of Education, and the Joint Usage/Research Center for Interdisciplinary Large-scale Information Infrastructures in Japan (Project ID: jh200050-NAH).

(Naoyuki Onodera)

* Leach, M. J., Final Report for the Joint Urban 2003 Atmospheric Dispersion Study in Oklahoma City: Lawrence Livermore National Laboratory Participation, UCRL-TR-216437, 2005, 94p.

Reference

Onodera, N. et al., Real-Time Tracer Dispersion Simulations in Oklahoma City Using the Locally Mesh-Refined Lattice Boltzmann Method, *Boundary-Layer Meteorology*, vol.179, issue 2, 2021, p.187–208.

9-2 Exascale CFD Simulations on Fugaku and Summit

— Development of Mixed-Precision Matrix Solvers for Many-Core CPUs and GPUs —

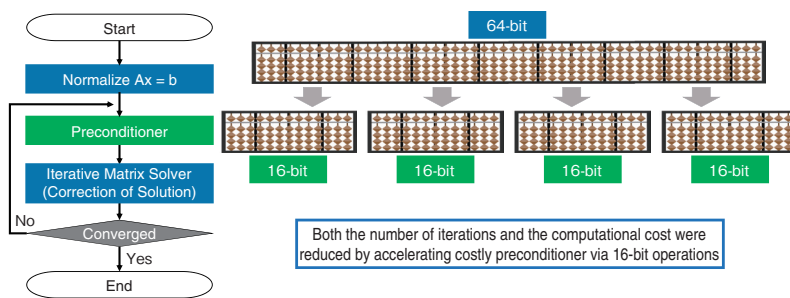


Fig.9-4 Schematic of a mixed-precision matrix solver

An iterative matrix solver for the linear system $Ax = b$ is shown. The preconditioner is accelerated by computing four operations at once using 16-bit operations (green), which are newly supported on Fugaku. The remaining part of the iterative solver is computed using 64-bit operations (blue). The picture shows a Japanese abacus, which is divided into four parts.

Computational fluid dynamics (CFD) simulations on exascale supercomputers (i.e., supercomputers capable of processing 10^{18} FLOPS), such as Fugaku, have been widely used in various scientific and engineering fields, including nuclear engineering. Computational algorithms for exascale computers are essential for processing such extreme-scale CFD simulations efficiently. In this work, a mixed-precision matrix solver, vital to CFD simulations, was developed in collaboration with Riken. The solver was developed using 16-bit operations, which are newly supported on the many-core CPU-based computer Fugaku (Riken). The solver was then implemented on the GPU-based computer Summit (Oak Ridge National Laboratory). It was demonstrated that the solver enables high-performance computing on exascale computers based on many-core CPUs and GPUs.

CFD simulations often compute a linear system $Ax = b$, which is given by discretizing the time development of fluid models. Here, a matrix A is an $N \times N$ sized sparse matrix given by the CFD scheme, b represents a vector given by variables at the current time step, x represents the solution vector for variables in the next time step, and N represents the number of grids. This type of large sparse matrix is normally computed using iterative solvers, which require several thousand iterations per time step in extreme-scale CFD simulations. The convergence may be improved by using a preconditioner, which converts the problem by multiplying the system by a preconditioning matrix M , so that the converted problem $M^{-1}Ax = M^{-1}b$ has better mathematical properties. Here, M is an approximate solution of A that can be represented in arbitrary precision. We constructed a mixed-precision solver, in which the preconditioner is computed in 16-bit operations, while the remaining part of the iterative solver is processed in 64-bit operations, which are the standard

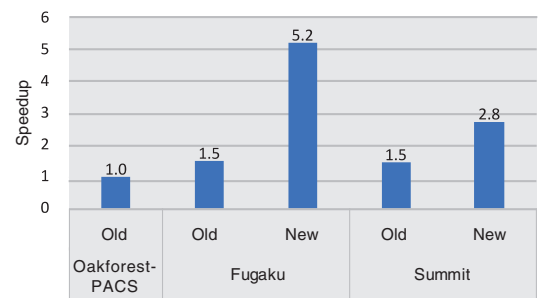


Fig.9-5 Computational performance of a mixed-precision matrix solver

Speedups of matrix solvers in plasma CFD simulations (about 100 billion grids) are shown for 1440 CPUs on Oakforest-PACS and Fugaku and 1440 GPUs on Summit.

precision in scientific computing; the proposed solver is shown schematically in Fig.9-4. Although 16-bit operations have been widely used in machine learning on GPUs, their use on CPUs was first supported on Fugaku. 16-bit operations can accelerate computation because four times the operations can be processed at once compared with 64-bit operations. Additionally, the problem $Ax = b$ was normalized to avoid accuracy degradation, which is a common issue when using 16-bit operations, and the number of iterations was reduced by an order of magnitude.

We then conducted plasma CFD simulations with about 100 billion grids using 1440 processors on Fugaku and Summit. In Fig.9-5, the resulting computing performance is compared with the conventional many-core CPU-based computer Oakforest-PACS (Univ. Tokyo/Univ. Tsukuba). Here, the performance of CFD simulations is mainly determined by the memory bandwidth; both Fugaku and Summit have a memory bandwidth approximately two times higher than Oakforest-PACS. Further, the performance improvement of the developed solver exceeded that of the hardware. Using the proposed methodology, Fugaku and Summit solved the system approximately 5.2 times and 2.8 times faster, respectively, whereas the conventional solver showed only 1.5 times speedup. These results demonstrate the high performance of the developed solver on many-core CPUs and GPUs.

This work was supported by MEXT as the Program for Promoting Research on the Supercomputer Fugaku “Exploration of Burning Plasma Confinement Physics” (hp200127) and Oak Ridge Leadership Computing Facility (OLCF) Director’s Discretion Project “Exascale CFD Simulations at JAEA (CSC367)”.

(Yasuhiro Idomura)

Reference

Idomura, Y. et al., Acceleration of Fusion Plasma Turbulence Simulations Using the Mixed-Precision Communication-Avoiding Krylov Method, Proceedings of International Conference for High Performance Computing, Networking, Storage and Analysis (SC), online, U. S. A., vol.1, 2020, p.1318–1330.

9-3 Theoretical Prediction of “Fermi Arc”

— Development of Novel Method for Analyzing Strongly Correlated Electrons in Heavy-Element Compounds —

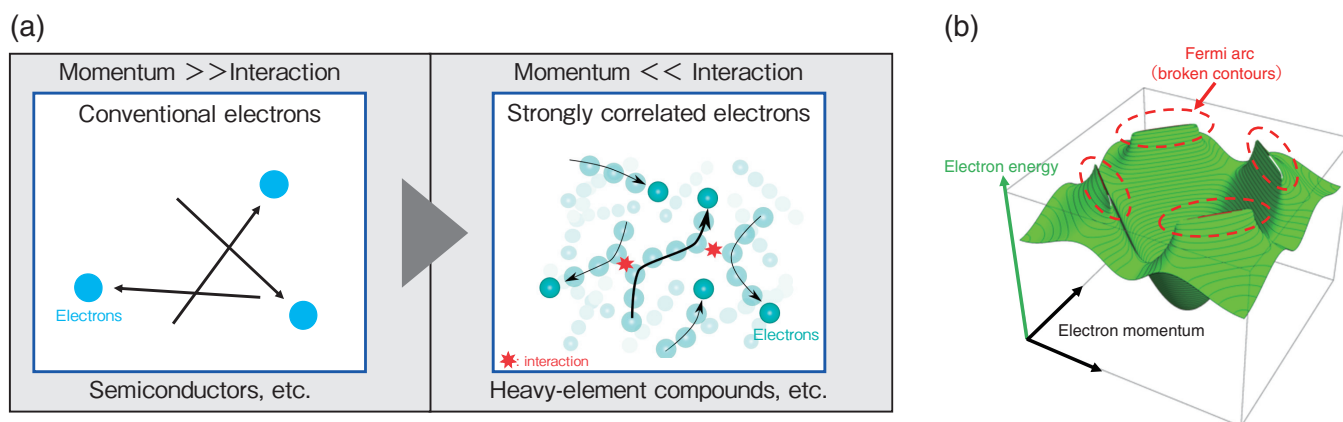


Fig.9-6 Simple descriptions of strongly correlated electrons

Methods for analyzing weakly correlated electrons were well established in the 20th century (Fig.9-6(a), left: blue circles are electrons) semiconductors, etc. It is hard to analyze strongly correlated electrons in heavy-element compounds (Fig.9-6(a), right: light blue circles indicate electrons, red indicates interactions). By extending the equations of quantum mechanics and allowing imaginary numbers to appear in the coefficients of the equations, the complex motion can be accurately captured. As a result, we can theoretically predict the appearance of a “Fermi arc” in the energy behavior of electrons (Fig.9-6(b)).

Many of the properties of matter can be explained by the behavior of electrons in matter. Electrons sometimes exhibit strange behaviors. For example, superconductivity, in which electrical resistance suddenly drops to zero, is one such example. By calculating the motion of electrons using quantum mechanics, it is possible to theoretically predict such phenomena. By taking advantage of these properties, various innovative technologies have been developed, such as maglev and MRI technology. The electrons in the copper oxide high-temperature superconductor interact strongly with each other. However, due to these strongly correlated electrons, the phenomenon cannot be reproduced by the conventional calculation method (Fig.9-6(a)). Such materials with strongly correlated electrons are not only high-temperature superconductors but also heavy-element compounds.

Good theoretical ways to analyze strongly correlated electrons might discover unknown materials that exhibit superior properties such as high-temperature superconductivity. Researchers around the world have been developing new computational methods.

In this study, we studied the behavior of strongly correlated electrons in heavy-element compounds. We focused on the

fact that there are two kinds of electrons in heavy-element compounds, weakly and strongly correlated electrons. We succeeded in capturing the motion of electrons by using a different quantum mechanical method. As a result, we can theoretically predict a unique phenomenon (a quantum phenomenon called “Fermi arc”) that has not been found in heavy-element compounds. (Fig.9-6(b)).

The Fermi arc is a region where the contour line representing the electron energy level appears to be broken. Fermi arcs have been observed in copper oxide high-temperature superconductors by angle-resolved photoemission spectroscopy, but have not been found in heavy-element compounds. Contour lines are represented as continuous lines, but by extending equations of quantum mechanics and allowing imaginary numbers to appear in the coefficients of the equations, such shredded regions appear.

We might discover novel innovative materials with the use of the developed theory in the future.

This work is partially supported by the Japan Society for the Promotion of Science (JSPS) KAKENHI (No.JP15K00178, JP18K03552, JP18H04228, and JP16H00995).

(Yuki Nagai)

Reference

Nagai, Y. et al., DMFT Reveals the Non-Hermitian Topology and Fermi Arcs in Heavy-Fermion Systems, *Physical Review Letters*, vol.125, issue 22, 2020, 227204, 7p.

9-4 Prevention of Hydrogen Embrittlement in Aluminum Alloys

— Identification of the Intermetallic Compounds that Take Away Hydrogen from Aluminum Lattice —

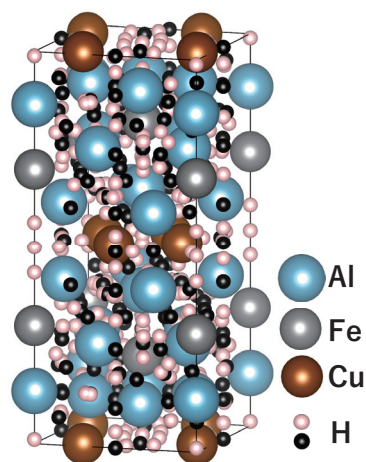


Fig.9-7 Crystal structure of an Al_7FeCu_2 compound and position of hydrogen atoms

Hydrogen (H) atoms can take two positions: the light-colored sphere lies at the vertex of the Voronoi polyhedron centered on the lattice points of Al, Fe, and Cu atoms, and the black sphere lies at the center of the plane of the polyhedron.

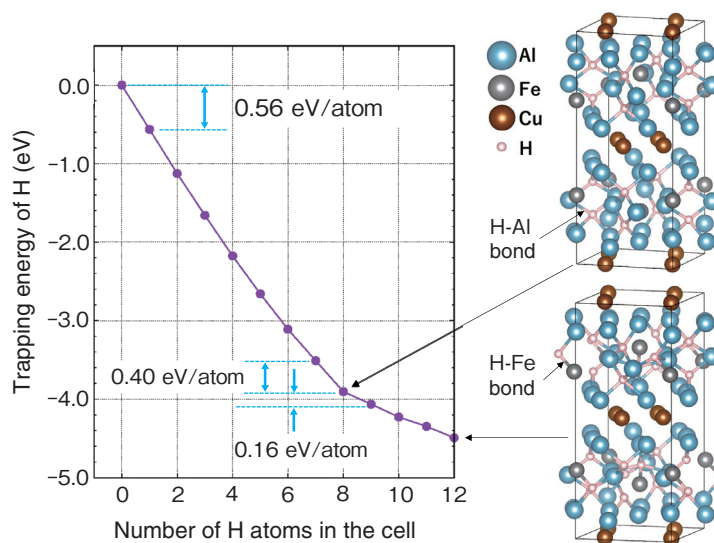


Fig.9-8 Hydrogen storage capacity of Al_7FeCu_2 compounds in aluminum

Initially, absorbed H atoms have a considerable trapping energy of 0.56 eV/atom in the cell. Because this decreases with the number of H atoms absorbed, approximately eight hydrogen atoms are expected to be absorbed in a cell of forty Al, Fe, and Cu atoms.

Although aluminum alloys have been commercially used for decades, significant improvements to their strength have not been made in many years. It has long been known that the strength of aluminum alloys, such as duralumin, which is used in aircraft bodies, has been improved by adding more zinc elements several ten years ago. However, adding alloying elements in this fashion tends to produce high-strength aluminum alloys that are susceptible to fracture due to hydrogen embrittlement because hydrogen penetrates the material during manufacturing. Hydrogen is the smallest element and thus can move quickly inside an aluminum lattice. Further, clarifying the behavior of hydrogen inside a lattice is difficult; the impact of hydrogen on the deformation and fracturing of an alloy has not been characterized well. However, reducing the hydrogen concentration in an aluminum alloy could prevent hydrogen embrittlement.

Thus, a compound that absorbs hydrogen in aluminum alloys and increases its concentration could prevent hydrogen embrittlement of aluminum lattice, because it reduces the content of hydrogen in aluminum lattice. Using first-principles calculations to investigate various compounds' ability to absorb

hydrogen, we discovered that an Al_7FeCu_2 compound strongly absorbs hydrogen.

The crystal structure of the Al_7FeCu_2 compound and the possible interstitial sites where hydrogen atoms can be absorbed are shown in Fig.9-7. Here, a Voronoi polyhedron division method was used to find the positions where hydrogen atoms are likely to enter. Next, the positions that could trap hydrogen atoms firmly were found by calculating the trapping energy from first-principles calculations. Furthermore, as shown in Fig.9-8, the amount of hydrogen absorbed in the cell was calculated.

Experimental work confirmed the effect of suppressing hydrogen embrittlement by increasing the Al_7FeCu_2 content in an aluminum alloy. Therefore, we submitted a patent application in Japan with Kyushu University detailing this embrittlement prevention method and alloy that is less susceptible to hydrogen embrittlement (Japanese Patent Application No.2020-96333).

This research was supported by a joint industry-academia basic research program (No.JPMJSK1412) of the Japan Science and Technology Agency (JST).

(Masatake Yamaguchi)

Reference

Yamaguchi, M. et al., Hydrogen Trapping in Mg_2Si and Al_7FeCu_2 Intermetallic Compounds in Aluminum Alloy: First-Principles Calculations, Materials Transactions, vol.61, issue 10, 2020, p.1907-1911.

Development of Technology and Human Capacity Building in the Nuclear Nonproliferation and Nuclear Security Fields to Support the Peaceful Use of Nuclear Energy

The Integrated Support Center for Nuclear Nonproliferation and Nuclear Security (ISCN) has conducted numerous technological and human resource development activities related to nuclear nonproliferation and security in cooperation with affiliated domestic and overseas institutions toward a world without the threat of nuclear weapons or nuclear terrorism, as summarized in Fig.10-1.

Technology Development for Applications in Japan and abroad

Numerous technologies are being developed to strengthen nuclear nonproliferation and security in line with domestic and international trends. A current project on nuclear material detection and measurement includes the development of a nondestructive assay technology to measure nuclear material retaining high radiation levels using an external pulsed neutron source and wide area monitoring using radiation imaging to strengthen nuclear security at large-scale events. Nuclear forensics technology used to identify the origin and processing history of nuclear materials used in criminal acts has been improved. Small, low-cost detectors for first responders following an act of nuclear terrorism and forensic nuclear signature analyzers using artificial intelligence (AI) are also under development. These developments help to improve nuclear forensic capabilities through international joint sample analysis exercises. Furthermore, methodologies to evaluate and reduce the attractiveness of nuclear or radioactive material for anti-nuclear terrorism are being developed in collaboration with the United States of America (US).

Policy Research Based on Technical Expertise

Based on requests from related administrative agencies, the factors affecting denuclearization have been studied through case studies of the following countries: South Africa, Ukraine, Belarus, Kazakhstan, Libya, Iran, Iraq, and North Korea. The factors include the incentives for developing nuclear weapons, situations at home and abroad, technological progress, and effects of sanctions (Topic 10-1). The technical procedures related to the treatment and disposal of nuclear materials available for nuclear weapons, deactivation of their manufacturing facilities, and verification methods are also investigated and examined in a view of the peaceful use of nuclear energy.

Capacity Building Support

ISCN has conducted capacity building support activities targeting Asian countries since 2011. As of March 2021, about 4,900 participants mainly from Asian countries including Japan have joined ISCN training activities on nuclear nonproliferation (safeguards) and nuclear security. In fiscal 2020, even under the influence of COVID-19 pandemic, we turned to the online method mainly for overseas, and continued to support capacity building by conducting the world's first four overseas online training in this field. ISCN's capacity building support activities have contributed to human-resource development in Asia and have drawn high praise internationally and domestically.

Contributions to the International Verification Regime for CTBT

JAEA has been operated the international monitoring system of the Comprehensive Nuclear-Test-Ban Treaty (CTBT) and a related national data under provisional operation to establish a global verification regime for nuclear testing. Additionally, based on the voluntary contribution of the Government of Japan to the CTBT Organization (CTBTO) in February 2017, a joint radioactive noble-gas measurement project between JAEA and the CTBTO has begun in Horonobe-Cho, Hokkaido and Mutsu City, Aomori in 2018 for strengthening the CTBTO's capability of detecting nuclear tests. This project aims to monitor the behavior of background radioactive xenon in East Asia in more detail by adding two temporary monitoring stations. This project has been agreed to extend its duration until March 2022.

Support for JAEA's Transportation of Nuclear Fuels and Procurement of Research Reactor Fuels

ISCN coordinates and supports JAEA's research and development centers by procuring and transporting the necessary fresh fuel for research reactors and then transporting the spent fuel. ISCN has been contributing to the Global Threat Reduction Initiative (GTRI), which has been strengthening global nuclear security by promoting the systematic return of highly enriched uranium to the US.

Efforts to Promote Public Understanding on Nuclear Nonproliferation and Nuclear Security

ISCN promotes the understanding of nuclear nonproliferation and nuclear security at home and abroad by delivering the ISCN Newsletter containing articles on international trends and analyses of nuclear nonproliferation and nuclear security and ISCN activities, and by holding the International Forum on Peaceful Use of Nuclear Energy.

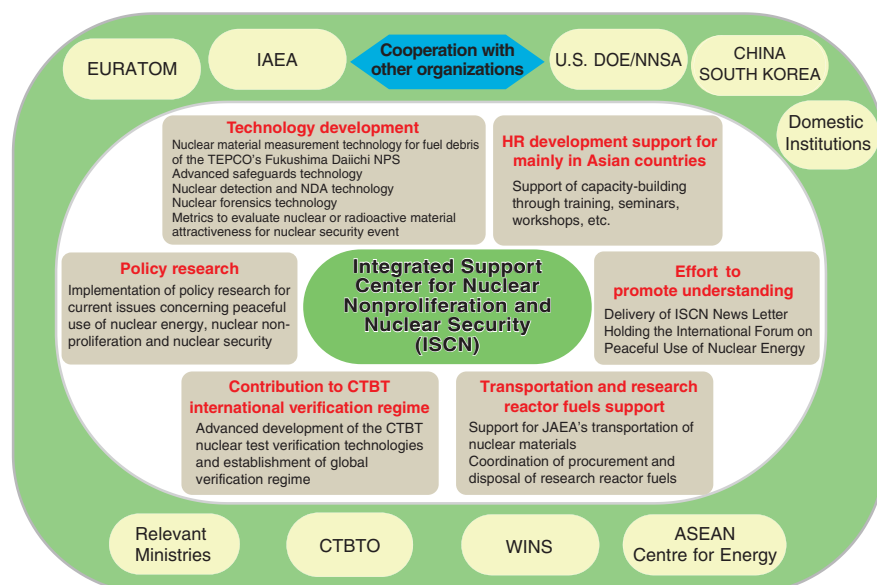


Fig.10-1 Summary of ISCN's activities and affiliated institutions

ISCN has played an active role in strengthening nuclear nonproliferation and nuclear security in cooperation with affiliated domestic and overseas institutions.

10-1 Toward a World without Nuclear Weapons and Nuclear Terrorism

— Case Study and Factor Analysis of Denuclearization —

Table 10-1 Characteristics of denuclearization and related denuclearization factors

	Countries	Progress of nuclear development / Denuclearization methods (Denuclearization factors: (3) and (6))		Characteristics of denuclearization (Related major denuclearization factors)	
		Nuclear weapons, etc.	Nuclear weapon usable materials		
(A)	South Africa	Possessed 6 self-made nuclear explosive devices / Disposed by itself	HEU has been stored	“Self-contained denuclearization”	(1) ~ (3), (6) ~ (8)
	Iraq	Nuclear weapon program was abandoned at planning stages	Unacquired	Denuclearization that had to be accepted	(2), (5), (7)
	Libya	Nuclear weapon program was abandoned at planning stages	Unacquired	Prompt denuclearization led by the US and UK, in exchange of sanction relief	(2) ~ (8)
(B)	Ukraine	Inherited nuclear weapons from the former Soviet Union, but later transferred to Russia	HEU was transferred to Russia, although partial HEU was left.	Denuclearization in exchange of national security	(1) ~ (3), (5) ~ (8)
	Kazakhstan				
	Belarus				
(C)	DPRK	Already conducted 6 nuclear tests / Estimated to have multiple nuclear warheads	Possess HEU / plutonium	Denuclearization was agreed in the Agreed Framework and during some Six-Party Talks process, without success.	(1) ~ (8)
	Iran	Nuclear weapon program was abandoned at planning stages	Unacquired (before JCPOA)	Joint Comprehensive Plan of Action (JCPOA)	(1) ~ (8)

Toward realizing a world without nuclear weapons and terrorism, we conducted a factor analysis on the past cases for examining the elements for successful future denuclearization.

Three classes of countries were considered: (A) countries that had completely denuclearized, (B) countries that inherited nuclear weapons but later transferred them to other countries, and (C) countries where denuclearization is being pursued. As summarized in Table 10-1, their history of nuclear weapon development and denuclearization, nuclear capabilities, denuclearization methods, etc., were then investigated. For example, Iraq, which had secretly engaged in uranium enrichment and nuclear weapons programs, had to terminate their weapons of mass destruction (WMD) program and dispose of their WMDs after their defeat in the Gulf War in accordance with United Nations Security Council Resolution (UNSCR). With cooperation and support from the United Nations Special Commission on Iraq (UNSCOM), the International Atomic Energy Agency (IAEA) verified Iraq’s clandestine nuclear activities. Libya also secretly engaged in uranium enrichment and nuclear weapons programs without having nuclear development capabilities. However, Libya abandoned this program in exchange for sanction relief because the Libyan economy had been severely exhausted due to the imposed sanctions. The subsequent removal of uranium-enrichment-related items was promptly and successfully led by the US and United Kingdom (UK).

Based on this case study, eight key factors demonstrated to influence denuclearization were extracted: (1) motivation for nuclear development or maintaining inherited nuclear weapons, (2) domestic and international circumstances at the time of denuclearization, (3) progress of nuclear development, (4) effects of sanctions, (5) international framework for

denuclearization, (6) denuclearization methods, (7) verification methods and verifier, and (8) incentives for denuclearization.

Finally, the relationship between and timeline of these denuclearization factors required to help the international community lead successful denuclearization efforts were studied. First, pushing a country toward denuclearization requires incentives for denuclearization (i.e., factor 8) while considering their motivation for nuclear development or maintaining their inherited weapons (i.e., factor 1) and the domestic and international circumstances (i.e., factor 2). In this context, providing national security and relieving sanctions could be effective incentives for denuclearization, especially if their economy has been severely damaged by international sanctions (i.e., factor 4). Next, international agreement and engagement with nuclear-weapon states (NWS) are necessary when detailing the denuclearization framework (i.e., factor 5). The selected denuclearization methods (i.e., factor 6) must include the effective, efficient, and prompt implementation of irreversible measures while considering the country’s progress of nuclear development and the domestic and international circumstances (i.e., factors 3 and 2, respectively). Thirdly, regarding the verification methods and verifier (i.e., factor 7), NWS should perform verification from the perspective of non-proliferation if the target country has nuclear weapons. Otherwise, the IAEA could perform verification using the measures implemented by the IAEA under the Comprehensive Safeguards Agreement and its Additional Protocol with its member states.

Further studies on denuclearization methods and verification methods will be conducted to continue efforts to lead to successful denuclearization.

(Makiko Tazaki)

Reference

Tazaki, M. et al., Research on Factor Analysis for Achieving Denuclearization, 4; Iraq: Characteristics of Iraq’s Denuclearization, Proceedings of 40th Annual Meeting of Institute of Nuclear Materials Management (INMM) Japan Chapter, Tokyo, Japan, 2019, p.93–96 (in Japanese).

JAEA R&D Review 2021-22

URL: <https://rdreview.jaea.go.jp/>

Published by

Japan Atomic Energy Agency in December 2021

Editorial Board

Chief editor: Michio Yoshizawa

Editors: Jin Iwatsuki, Yoshio Suzuki, Mitsuo Koizumi, Tadahiro Washiya, Kazuki Iijima,
Yutaka Udagawa, Naofumi Kozai, Hideo Harada, Yasuji Morita, Terufumi Yokota,
Kenji Sakai, Seiji Kitamura, Hiroyuki Sato, Hirotsugu Hamada, Takashi Mizuno,
Kazuhiko Sato

This publication is issued by Japan Atomic Energy Agency (JAEA) on a yearly basis.
Inquiries about availability and/or copyright of the contents in this publication should be addressed
to Institutional Repository and Utilization Section, JAEA Innovation Hub, JAEA.

Address: 2-4 Shirakata, Tokai-mura, Naka-gun, Ibaraki-ken 319-1195, Japan

Phone: +81-29-282-6387, **Facsimile:** +81-29-282-5920, **e-mail:** ird-seika_shi@jaea.go.jp

All Rights Reserved by JAEA ©2021

About the Cover Design

The cover design depicts white hexagons that are similar to a tortoise-shell pattern. This represents the ancient Japanese symbol of the desire for long life. Coincidentally, this is also the shape of the core fuel assemblies in the high-temperature engineering test reactor, “HTTR”.

The top left figure shows an image of an oxygen molecule passing through graphene (a net made of a single layer of carbon atoms). The bottom right figure shows an example of topographical and repository depth change calculated using the developed tool.

Synchrotron radiation experiments and computer simulations have revealed that only high-speed oxygen molecules existing in the atmosphere can permeate graphene, which is a single-layer net consisting of carbon atoms. This research is expected to be applied to the development of protective films to prevent rust and food corrosion. Further details can be found on page 62 in Chapter 5, Topic 5-6.

Topography and repository depth changes were calculated for multiple uplift rate settings. There are several patterns for changes in topography and repository depth. An estimation of the pattern to which the calculation result is close can be used to judge the impact to be focused on in safety assessment. Further details can be found on page 88 in Chapter 8, Topic 8-9.



Other Publications

Industrially applicable patented technology and know-how within the intellectual property owned by JAEA can be found on “JAEA Technology Seeds”.

The activity status of the whole agency, including CSR, can be found in the annual report, “Japan Atomic Energy Agency 2021 (Business Report FY2020)”.